Summer 7-15-2024

Exploration of Semiconductor Gain Medium, Resonator, Pump, and Frequency Stabilization for Laser Guide Star Applications

Mingyang Zhang
University of New Mexico - Main Campus

Mingyang Zhang

Candidate

Optical Science and Engineering

Department

This dissertation is approved, and it is acceptable in quality and form for publication:

Approved by the Dissertation Committee:

Alexander R. Albrecht

Victor Acosta

Garrett D. Cole

Daniel Feezell

Exploration of Semiconductor Gain Medium, Resonator, Pump, and Frequency Stabilization for Laser Guide Star Applications

by

Mingyang Zhang

B.Sc., Optical Information of Science and Technology,
Guizhou University, China, 2015

M.Sc. with distinction, Optics and Photonics,
Imperial College London, United Kingdom, 2016

DISSERTATION

Submitted in Partial Fulfilment
of the Requirements for the Degree of

Doctor of Philosophy

Optical Science and Engineering

The University of New Mexico
Albuquerque, New Mexico

July, 2024

Dedication

This dissertation is dedicated to my Ph.D. supervisor, Dr. Mansoor Sheik-Bahae, who profoundly influenced both my professional journey and personal development. Tragically, Dr. Sheik-Bahae passed away from lymphoma on July 10, 2023. His guidance was instrumental during my doctoral studies, and it is with deep regret that this dissertation was completed nearly a year after his passing, depriving him of the opportunity to read the final draft. His memory and impact, however, will forever resonate with me.

Acknowledgements

As I approach the completion of my Ph.D., I am profoundly grateful to several individuals whose support has been instrumental in my journey. First and foremost, I extend my deepest gratitude to my parents Jianqing and Lidong. Their unwavering support and understanding have been the cornerstone of my resilience and perseverance. As an only child, I am acutely aware of their longing and the sacrifices they have made, especially given that I have not been able to visit home for nearly six years due to visa issues. Despite their own longing, their encouragement during my moments of doubt was unconditional—they always reassured me to pursue what felt right, irrespective of the doctor title. Their love and support have been my greatest motivation to persevere through the challenges of this Ph.D.

I must also express my heartfelt thanks to Dr. Yang Jiang, who first introduced me to the field of optics. As a curious undergraduate with little knowledge of what lay ahead, Dr. Jiang not only welcomed me into his laboratory but also entrusted me with a significant project on designing and building a single longitudinal mode fiber laser. This opportunity opened the door to a whole new world for me, for which I am eternally grateful. Additionally, I would like to thank Dr. Michael Damzen. Despite my initial struggles with the English language, he welcomed me to undertake a project on LiDAR with him. His Laser Physics class was not merely an academic requirement—it was my favorite class, profoundly impacting my educational journey. Furthermore, gratitude is due to Dr. Jon Marangos and Dr. Dane Austin, who supervised my master's thesis on ultrafast spectroscopy. Working in their group, surrounded by fantastic equipment and brilliant minds, I not only honed my technical skills but also gained invaluable research experience.

During my Ph.D., I have been fortunate to receive guidance and support from many remarkable individuals, but none have had a more significant impact on me than Dr. Mansoor Sheik-Bahae. His patience and dedication to my development were truly extraordinary. I vividly remember times when I was stuck on a problem, and Dr. Sheik-Bahae would patiently sit with me, walking me through solutions on a piece of paper. When my Ti:Sapphire laser was

misaligned, he did not hesitate to join me in the lab to help rectify the issue. It was incredibly inspiring to see a scientist of his renown so deeply invested in the hands-on education of his students. Dr. Sheik-Bahae's support extended beyond academic mentorship; he was also a pillar of personal support during particularly challenging times. Following the unfortunate rise in racially charged sentiments due to the term "Chinese Virus," I faced numerous racial challenges. Dr. Sheik-Bahae shared his own experiences as an Iranian, offering empathy and understanding, and he was profoundly protective of his students' well-being. Reflecting on my Ph.D. journey, I realize that I have spent more time with Dr. Sheik-Bahae than with my own parents over these years. His influence on both my professional and personal life is immeasurable, and it is impossible to enumerate all the ways he has helped me grow and thrive.

I am deeply grateful to Dr. Alexander Albrecht, especially during the difficult period following Dr. Sheik-Bahae's passing. His adept leadership and support were invaluable, and I deeply appreciate his stepping in as the chair of my dissertation committee under these unforeseen circumstances. Before meeting Dr. Albrecht, my knowledge was primarily in ultrafast lasers, with little understanding of semiconductor lasers. His thorough tutorial on semiconductor lasers enabled me to shift the focus of my dissertation from ultrafast laser-based THz generation to semiconductor lasers, especially when COVID-19 limitations impacted my access to the Regen Amplifier. Additionally, I am thankful for his guidance in honing my photography skills, which has fueled my ongoing passion to pursue part-time photography.

I am immensely grateful to Dr. Garrett Cole, whose support has been fundamental to the success of my project. Without the epitaxial growth and fabrication contributions from his team, progressing in my research would have been unfeasible. When I encountered difficulties with locking my laser to sodium cells, Dr. Cole promptly arranged for his colleague, Dr. Gar-Wing Truong, to come to Albuquerque and assist in constructing the entire locking system. Moreover, following Dr. Sheik-Bahae's passing, I faced considerable personal and professional challenges, to the point where I doubted my ability to continue my academic journey. During this critical time, Dr. Cole's encouragement was instrumental in helping me persevere and consider a future in academia. His support not only sustained my project but also my academic aspirations.

I would like to express my deep gratitude to Dr. Victor Acosta. His courses have greatly enhanced my knowledge, particularly in optics lab skills and Lumerical FDTD simulations. I am especially appreciative of his willingness to serve on my dissertation committee, even though the topic slightly deviates from his primary research focus. Additionally, Dr. Acosta has been incredibly supportive of my career aspirations, providing invaluable advice as I explored postdoctoral opportunities in quantum optics and integrated photonics. His efforts to connect

me with his former supervisor at UC Berkeley went above and beyond my expectations. I am profoundly thankful for his guidance and support.

I would like to extend my heartfelt thanks to Dr. Daniel Feezell. When I consulted Dr. Sheik-Bahae about whom to invite to my dissertation committee, Dr. Feezell was the first person he recommended. Dr. Feezell possesses deep expertise in semiconductor lasers and LEDs and has provided numerous valuable insights concerning both my dissertation and my future career prospects. Additionally, Dr. Feezell is an accomplished rock climber. Every time I encounter him at the climbing gym, he is tackling routes that are beyond my reach, especially since my pulley injury. His skill and enthusiasm for climbing are truly inspiring.

I also want to thank Dr. Michael Hasselbeck. After my first year working with Dr. Jean-Claude Diels, I learned that the continuous funding I had been promised was no longer available. This was particularly disheartening, as I had chosen this program over others in the US and Europe based on assurances of stable funding and compelling projects. Faced with uncertainty, I considered transferring to another university. During this challenging time, I was a teaching assistant for Dr. Hasselbeck, who became aware of my situation. He graciously facilitated my transition to Dr. Sheik-Bahae's group. Without his intervention, I would not have dared to approach such a distinguished professor as Dr. Sheik-Bahae, whose renowned z-scan paper had already garnered over 9,000 citations (and has since surpassed 10,000). Dr. Hasselbeck's support was instrumental in shaping the direction of my Ph.D. journey, for which I am deeply thankful.

I must also express profound gratitude to Dr. Davide Priante and Dr. Azzurra Volpi, both of whom were postdocs who significantly assisted me in the laboratory. I acquired nearly all of my cleanroom fabrication skills under the guidance of Dr. Priante. Before meeting Dr. Volpi, I was completely unfamiliar with the concept of laser cooling. Beyond their professional support, they played a critical role in a life-saving moment for which I am eternally thankful. While snowboarding with them at Sandia Peak, I was involved in an accident that left me unconscious. They quickly found me and called 911, actions that were crucial to my survival. The accident resulted in permanent memory loss and ongoing challenges with memory retention, which notably affected my academic performance, including a particularly difficult period during my graduate quantum mechanics II course that few months. Despite these challenges, I am alive and deeply grateful for their swift and life-saving response.

I would like to express my heartfelt gratitude to my lab mate and roommate, Dr. Nathan Giannini-Hutchin, for his substantial support both personally and professionally. Nathan joined my project at a critical moment when I felt particularly lost and his involvement prevented

me from being the sole person working on it. I am also grateful for the wonderful times we spent visiting national parks and attending Comic Con in Washington with his sister, Kassie. Additionally, I appreciate his efforts in proofreading this dissertation and providing many invaluable suggestions.

I am immensely grateful to Dr. Kevin Malloy for his dedication in sitting with me to review my dissertation word by word, offering numerous valuable suggestions, and assisting in the reorganization of my defense slides. I am grateful for the meticulous proofreading and insightful comments provided by Dr. Hermann Kahle. I really appreciate all the help from Dr. Gar-Wing Truong on laser frequency stabilization. Additionally, I would like to express my appreciation to all the professors who have provided generous guidance and support as I approached the completion of my Ph.D., particularly Dr. Ivan Deutsch, Dr. Francisco Elohim Becerra, Dr. Stephen Boyd and Dr. James Thomas. I would like to extend a special thank you to Dr. Robert Johnson's group at the Air Force Research Laboratory. Their support has been invaluable to my project.

I would like to extend my heartfelt thanks to Dr. Sadhvikas Addamane for overseeing the MBE sample growth at Sandia National Laboratories. His contributions were crucial for several projects I was involved in, including the laser guide star, quantum dot laser, and meta-material enhanced laser. Additionally, I am grateful for the access to the cleanroom and the state-of-the-art equipment provided during my Ph.D. at the Center for Integrated Nanotechnologies. The availability of resources such as e-beam lithography, SEM, and sputtering greatly enhanced my research experience. This work was performed, in part, at the Center for Integrated Nanotechnologies, an Office of Science User Facility operated for the U.S. Department of Energy (DOE) Office of Science by Los Alamos National Laboratory (Contract 89233218CNA000001) and Sandia National Laboratories (Contract DE-NA-0003525).

I would like to express my gratitude to my lifelong friend, Peiyuan, and extend my apologies for being unable to attend his son's baby shower. Additionally, I regret not being able to attend my cousin Ran's wedding in China, another cousin Laimeng's wedding in Japan, and my best friend, Dr. Yuchen Xiang's wedding in Singapore. Prior to beginning my Ph.D., I never anticipated that I would remain in the United States for such an extended period, causing me to miss these once-in-a-lifetime events.

I want to extend my deepest thanks to all my friends who supported me throughout my Ph.D. journey. I faced severe depression that required medical treatment and nearly led me to drop out during COVID when I had to change my dissertation project several times. The joy and companionship you all provided were crucial to me. Although there are too many to name

individually, I must highlight a few: my roommate Dr. Xuefeng Li, my travel buddies Dr. Andrew Zhao and Dr. Changhao Yi; my swimming buddy Dr. Birendra Dhanasingham; my gym mate Dr. Shenghan Song; my snowboarding partners Dr. Cody Basset, Dr. Sam Slezak, and Dr. Austin Daniel; my shooting mate Dr. Yechuan Chen; and my hunting buddy Hutchins-Delgado. I am also grateful to my former and current research group members, Dr. Aram Gragossian, Dr. Denis Seletskiy, Dr. Zhou Yang, Dr. Shawn Hackett, Dr. Seth Melgaard, Dr. Saeid Rostami, Jackson Koch, Trevor Rubin, and Cameron Richards.

I also appreciate Dr. Lynn Yu, Dr. Ning Hsu, and Dr. Xuemei Wang for their efforts in helping me explore job opportunities at Apple, QuEra, and GlobalFoundries, I am immensely thankful for their kindness and support even though I decided to spend a few more years in academia. To all those individuals I have not had the chance to mention by name, I owe a tremendous debt of gratitude for your guidance, patience, and belief in my potential. Thank you for your invaluable support in navigating this challenging yet rewarding academic journey.

Last but not least, I would like to thank the University of New Mexico Graduate Online Writing Lab for proofreading my dissertation and providing recommendations for improvement. Following their suggestions, I also used Grammarly and ChatGPT to enhance my grammar and language in this dissertation. Although there were costs associated with both services, I find it essential to acknowledge their value as their assistance was worth every penny.

Exploration of Semiconductor Gain Medium, Resonator, Pump, and Frequency Stabilization for Laser Guide Star Applications

by

Mingyang Zhang

B.Sc., Optical Information of Science and Technology, Guizhou University, 2015
M.Sc. with distinction, Optics and Photonics, Imperial College London, 2016

Ph.D., Optical Science and Engineering, University of New Mexico, 2024

ABSTRACT

Laser Guide Star (LGS) systems are essential for adaptive optics in ground-based astronomical observation. This dissertation demonstrates the feasibility of semiconductor-based LGS systems using the membrane external-cavity surface-emitting laser (MECSEL) platform, employing multiple quantum wells. Various laser cavity configurations were analyzed through simulations and experiments. The in-well pumping method was explored to reduce the quantum defect and address thermal limitations. Multi-pass pumping schemes were designed with Zemax modeling and demonstrated experimentally. To simplify multi-pass pumping, the hybrid-MECSEL (H-MECSEL) design was introduced. COMSOL modeling studied thermal management and thermal lensing effect.

The H-MECSEL achieved approximately 30 W of output power at 1178 nm, frequency-doubled to over 10 W at 589.2 nm with TEM_{00} beam profile and 7 MHz linewidth. Hyperfine transitions within sodium D-lines were resolved using saturated absorption spectroscopy and dither-locking was implemented, stabilizing the H-MECSEL to the sodium D_{2a} line over an hour with watt-level output power. Allan deviation calculations confirmed the stabilization efficacy.

Table of Contents

List of Figures

List of Tables

Chapter 1

Introduction

This dissertation explores membrane external-cavity surface-emitting lasers (MECSELs) [1, 2] for Laser Guide Star (LGS) applications [3]. It builds upon the foundational work of previous doctoral students [4, 5] supervised by Dr. Mansoor Sheik-Bahae [6]. Dr. Zhou Yang established the foundation for the progression from Vertical External-Cavity Surface-Emitting Lasers (VECSELs) to MECSELs [4], which form the backbone of the laser architecture addressed in this research. Dr. Shawn Hackett, former Engineering Section Chief at Starfire Optical Range (SOR), which was at the forefront of pioneering LGS technology, provided insights into the advantages of semiconductor-based lasers over existing LGS systems and proposed methodologies for their integration into current frameworks [5]. Building on the groundwork laid by Drs. Yang and Hackett, this study leverages their solutions to numerous growth and fabrication challenges, thereby advancing the integration of MECSELs in LGS applications. My co-worker Dr. Davide Priante made significant contributions to the experimental work that will be discussed in Chapters 3 and 5. His efforts were particularly valuable when my research focus was on ultrafast phenomena, including THz generation, metamaterial for group delay dispersion compensation, and Kerr lens mode locking.

This dissertation is structured to thoroughly examine the implementation and innovation of MECSELs for LGS systems. Chapter 1 delineates the motivation for developing a semiconductor-based LGS system, reviews the history of semiconductor lasers, and articulates the necessary parameters for constructing an LGS. Chapter 2 elucidates the foundational aspects of MECSEL technology utilized in this project, covering topics such as the design of the active region, laser resonator configurations, approaches to laser linewidth narrowing, and the implementation of frequency doubling techniques. Chapter 3 presents experimental investigation of an 808 nm pumped eleven quantum well MECSEL, which has insufficient output power to meet the design criteria for LGS systems.

Chapter 4 proposes an in-well pumping strategy to reduce the quantum defect, and introduces several laser beam circulator designs intended to address the challenges of low absorption associated with the in-well pumping. ZEMAX [7] was used for the design of all beam circulators, saving considerable time in experimental verification. Chapter 5 discusses the experimental investigation of 1070 nm in-well pumped twenty quantum well MECSELs, which demonstrated promising output power while the output beam profile is distorted due to challenges in constructing the multi-pass pumping configuration.

Chapter 6 proposes a modified MECSEL design, hybrid membrane external-cavity surface-emitting lasers (H-MECSELs), that simplifies the multi-pass pumping design while preserving its superior heat dissipation capabilities, with thermal analysis conducted using COMSOL [8] software to assess the thermal lens effect in H-MECSEL for integration into the laser cavity design. Chapter 7 presents the experimental demonstration of the efficacy of the H-MECSEL design, and Chapter 8 further investigates the linewidth narrowing and frequency doubling to achieve the targeted wavelength for the LGS system.

Chapter 9 explores an active laser frequency stabilization method, detailing the experimental procedures including frequency reference preparation, feedback loop construction, and long-

term locking mechanisms. Finally, Chapter 10 summarizes the findings of this dissertation and projects the future prospects of semiconductor-based LGS systems and other potential applications where MECSEL technology may prove advantageous.

A significant portion of the data analysis and the coding of the cavity design script were conducted using MATLAB [9] through the entire dissertation. VERTICAL [10] was used to verify semiconductor structure designs provided by coauthors for this dissertation project (this software was not available anymore and was formerly distributed by GORE PHOTONICS). FUSION 360 [11] played a role in this dissertation project by enabling the visualization of experimental setups in advance of physical construction. Lastly, LABVIEW [12] was employed to automate several experimental procedures and data collection tasks, particularly in laser frequency stabilization experiments.

1.1 Motivation and Laser Guide Star Systems

The most advanced telescope systems currently in use are space telescopes like the James Webb Space Telescope [13]. They offer unique advantages due to their location, providing an unobstructed view with long observational windows. However, these telescopes are very expensive, and maintenance and upgrades are challenging, which limits their lifespan. On the other hand, ground-based telescopes are cost-effective and easy to maintain and upgrade. However, they suffer from atmospheric turbulence and observational constraints such as bad weather. While there is no effective solution for weather-related constraints, atmospheric interference can be mitigated using adaptive optics (AO) systems. An image of Saturn in Fig. 1.1 (a) was captured by the James Webb Space Telescope, while a photography of Jupiter in Fig. 1.1 (b) was taken by the Gemini North Telescope, utilizing an AO system to achieve such high resolution. Due to budget constraints and the advantages of ground-based telescopes

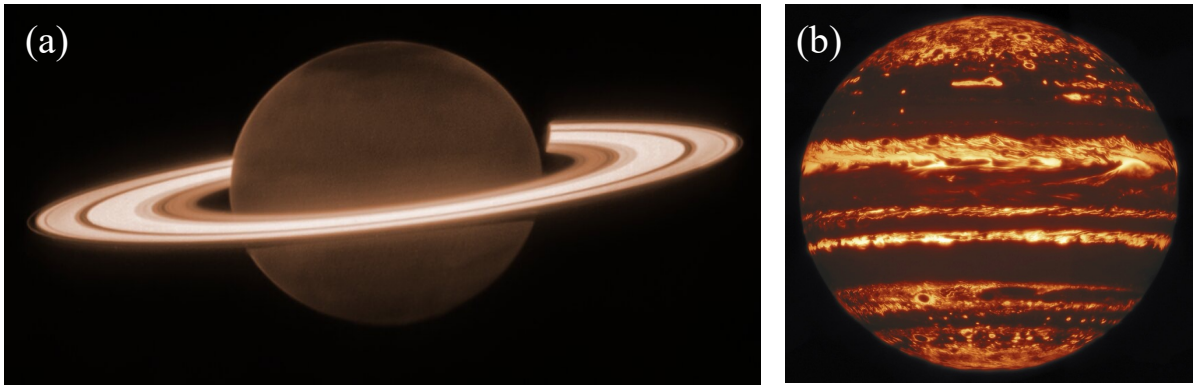

Fig. 1.1 (a) Photography of Saturn taken by the James Webb Space Telescope [14]. (b) Photography of Jupiter taken by the Gemini North Telescope [15].

in observing low orbit satellites and unidentified crafts, there is a high demand for achieving high-resolution images from ground telescopes.

Atmospheric turbulence, the irregular flow of air within the Earth's atmosphere, is induced by local temperature variations in the air, which are influenced by factors such as solar radiation, human activities, and wind dynamics [16]. These temperature fluctuations alter the refractive index, thereby introducing aberrations into the images captured by ground-based telescopes, which significantly limit the imaging resolution. This necessitates the development of effective aberration correction techniques for ground-based telescopes. In 1982, Dr. William Happer pioneered the development of an AO system utilizing sodium LGS to address this need [3]. The system operates by targeting the naturally occurring sodium layer in the mesosphere, located between 90 and 100 km in altitude, using a laser beam to generate an artificial laser beacon, which aids in correcting atmospheric distortions. Air density varies with altitude, decreasing exponentially as altitude increases. It is generally accepted that 100 km from sea level marks the boundary of space [17], and it is reasonable to assume that the thin air above the sodium layer contributing minimally to turbulence. In addition, a laser beam can traverse the sky within a very short time frame, and the beam profile of laser light is well-defined and can be measured

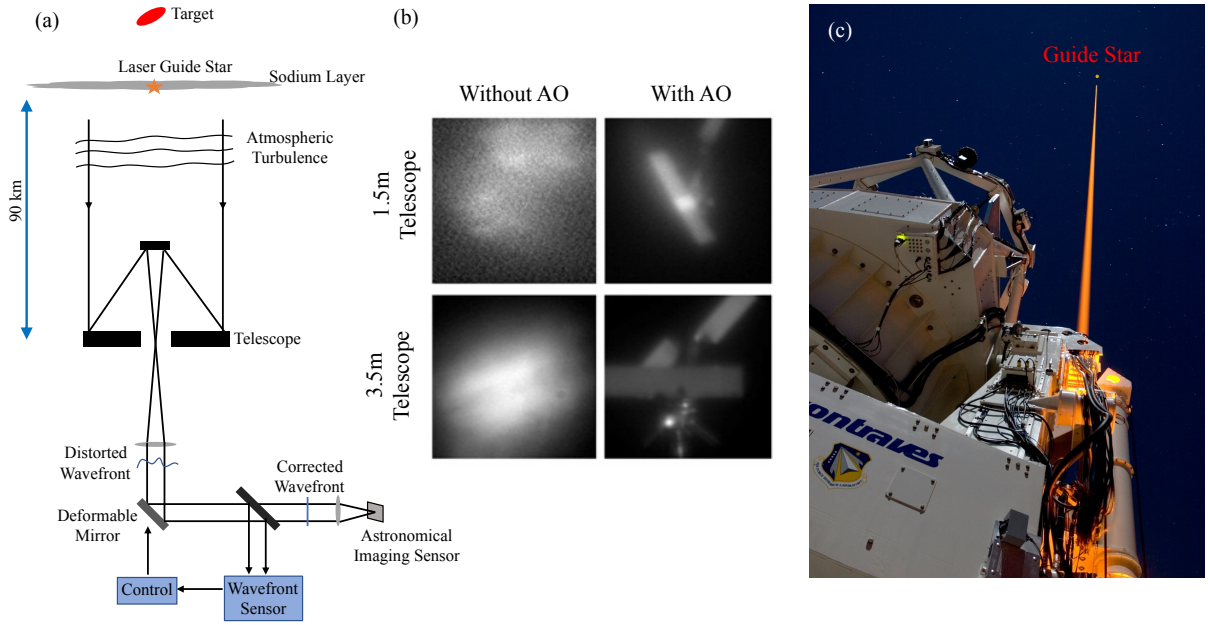

Fig. 1.2 (a) Schematic diagram of the AO system for aberration correction in ground-based observations using LGS [20]. (b) Comparative images of the SEASAT satellite captured by two ground-based telescopes with different aperture sizes, with and without the use of AO [21]. (c) Photograph of the LGS system at Kirtland Air Force Base in Albuquerque, NM, USA [22].

in real-time. Furthermore, the back-scattering of laser light at a wavelength of sodium D_2 transition (589.1583264 nm [18]) is sufficiently strong to serve as an artificial reference [3].

An AO system is depicted in Fig. 1.2 (a) for aberration correction in ground-based observations. This system generates a guide star within the sodium layer near the position of a targeted celestial body or spacecraft. The Shack-Hartmann wavefront sensor measures the distortion of the wavefront caused by atmospheric turbulence in the image of the LGS observed by the telescope [19]. The data from these wavefront distortions are utilized to manipulate a deformable mirror, which comprises numerous independently adjustable segments. These adjustments correct the aberrations caused by atmospheric turbulence, subsequently allowing the corrected wavefront image of the target of interest to be captured by an imaging sensor.

Images of the SEASAT satellite are displayed in Fig. 1.2 (b), as captured by two ground-based telescopes with different aperture sizes (1.5 m and 3.5 m diameter), versions with and

without the AO system, are displayed. Without AO, the larger 3.5 m diameter telescope struggles to resolve the satellite clearly; however, with AO, even the smaller 1.5 m diameter telescope is able to produce a reasonably sharp image of the SEASAT satellite [21]. A photograph of the LGS system at Kirtland Air Force Base in Albuquerque is included in Fig. 1.2 (c) [22]. This photograph showcases a bright yellow beam, a result of Rayleigh scattering, and a bright yellow guide star, created by fluorescence in the sodium layer. The gap between the laser beam and the guide star occurs because the air is too thin at that altitude to create sufficient Rayleigh scattering beyond approximately 30 km [23].

Collecting accurate aberration information is crucial for AO systems. Although a natural star near the object of interest can serve as a reference, it is not always available. The requirements for such a standard reference for AO include being sufficiently high to capture all atmospheric turbulence data and having the capability to move quickly to the area of interest. Additionally, the reference must have a well-known shape and be bright enough for observation by a ground-based telescope. Those requirements can all be met by using LGS.

Very few dye laser-based LGS systems remain in use today, even though the first LGS was constructed using a dye laser [3]. The costly and hazardous maintenance requirements of dye lasers have deterred significant new investments in further developing dye laser-based LGS systems. Numerous researchers are dedicated to developing alternative techniques for LGS [24]. One such technique is sum frequency generation (SFG). The schematic diagram of an SFG LGS system at SOR, which employs two emission lines of Nd:YAG lasers at 1064 nm and 1319 nm, is depicted in Fig. 1.3. Both high-power Nd:YAG lasers at these wavelengths are frequency stabilized, and their outputs are combined and directed into a cavity containing a lithium triborate (LiB_3O_5 or LBO) crystal for SFG, yielding 589 nm light via the $\chi^{(2)}$ effect. However, this method results in a very narrow linewidth (1-500 kHz); achieving a linewidth of 1 MHz

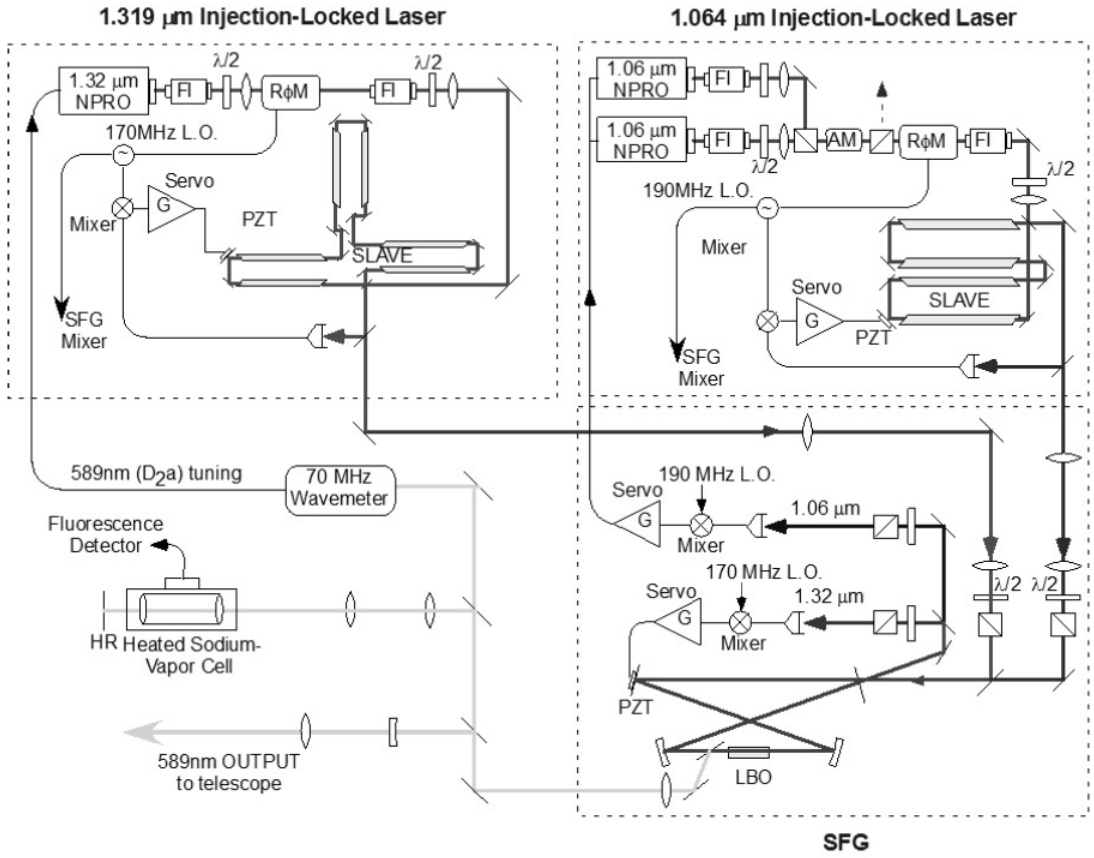

Fig. 1.3 Schematic diagram depicting the Nd:YAG SFG-based LGS system at SOR [25].

entails significant maintenance efforts including routinely cavity alignment [5]. Moreover, the bulky size of this setup makes it impractical for adaptation to mobile telescopes.

Raman fiber amplifier (RFA) LGS is another technique that widely adopted by observatories. An RFA-based LGS system is depicted in Fig. 1.4, where a 1178 nm distributed feed back (DFB) diode seed laser (with isolator) is injected into the system for multi-stage Raman fiber amplification. Subsequently, the amplified laser is directed to a frequency-doubling cavity with an nonlinear crystal to generate 589 nm light. The RFA LGS system encounters power limitations due to stimulated Brillouin scattering (SBS) within the fiber, necessitating multi-stage amplification to attain the required output for LGS application [26], which significantly

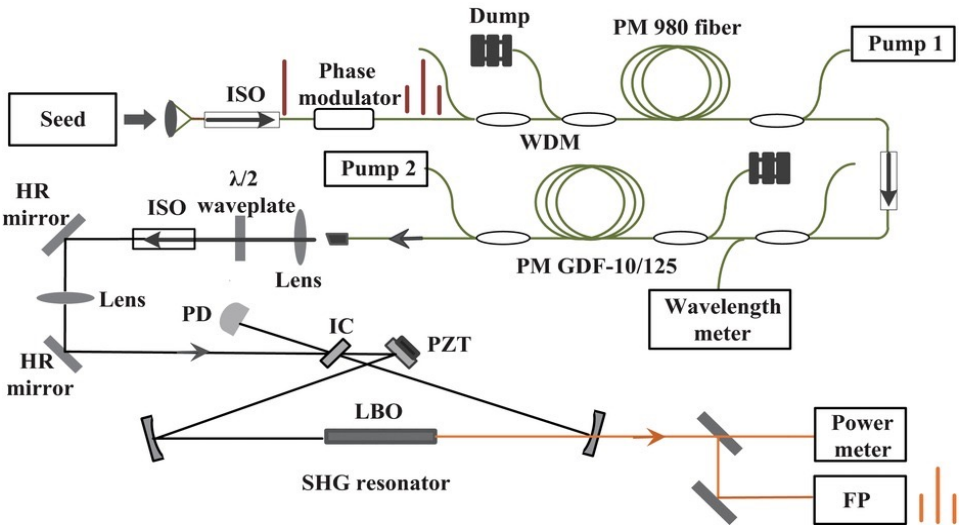

Fig. 1.4 Schematic diagram of an RFA-based LGS system [27].

escalates the cost of constructing such systems. Such RFA LGS systems are commercially available, typically priced in the range of a few million US dollars.

There is a growing interest in alternative platforms for developing a size, weight, and power (SWaP) optimized LGS, given the constraints of current LGS systems. One such platform is the semiconductor laser, which, due to its potential in wavelength engineering [28], can achieve this challenging wavelength more straightforwardly compared to other methods. Semiconductor disk lasers (SDLs), with an active region thickness at the micrometer level, have demonstrated high power outputs exceeding 100 W [29] and watt-level power at the targeted 589 nm [30]. Thus, SDLs are a promising alternative to the currently used LGS systems.

1.2 Design Criteria for Laser Guide Stars

Before designing and building a semiconductor-based LGS, it is essential to clarify the required parameters. These requirements include the transverse beam profile, laser wavelength, output power, and laser linewidth. A laser guide star requires the TEM_{00} mode because it provides a

beam with the highest spatial coherence and a Gaussian intensity profile, which are essential for creating an artificial star in the atmosphere. This mode ensures accurate wavefront sensing and correction of atmospheric distortions, leading to clearer astronomical images [31].

The wavelength required for LGS corresponds to the atomic transition of sodium atoms in the atmosphere. Sodium (Na), an alkali metal with atomic number of 11, primarily has all but one of its electrons in a closed shell configuration. The single valence electron resides in the third principal shell (principal quantum number $n = 3$), occupying an s-subshell with spherical symmetry (orbital angular momentum quantum number $l = 0$), and has an orientation described by the magnetic quantum number $m = 0$. The spin quantum number is $s = \frac{1}{2}$, and the total electron angular momentum quantum number $J = \frac{1}{2}$. Sodium has only one stable isotope, ^{23}Na, which constitutes 100% of atmospheric sodium. This isotope has a nuclear spin angular momentum quantum number $I = \frac{3}{2}$, resulting in possible total angular momentum quantum numbers of the ground state $F = 1$ or $F = 2$, due to magnetic interactions between the electron and nuclear magnetic dipole moments [32].

The first excited state of sodium retains the same principal quantum number (n), but with an increased electron orbital angular momentum quantum number $l = 1$. The possible total electron angular momentum quantum numbers for this state are $J = \frac{1}{2}$ and $\frac{3}{2}$. These states are further split due to interactions between the total electron magnetic moment and the nuclear magnetic moments [32]. The lower $J = \frac{1}{2}$ state divides into two hyperfine states with $F = 1$ and $F = 2$, while the upper $J = \frac{3}{2}$ state splits into four hyperfine states with $F = 0$, $F = 1$, $F = 2$, and $F = 3$. The sodium hyperfine structure, as depicted in Fig. 1.5, includes transitions such as the $3^2S_{\frac{1}{2}}$ to $3^2P_{\frac{1}{2}}$ D_1 transition requiring a $\sim$589.76 nm (vacuum) laser wavelength, and the $3^2S_{\frac{1}{2}}$ to $3^2P_{\frac{3}{2}}$ D_2 transition requiring a $\sim$589.16 nm (vacuum) laser wavelength [33]. Specifically, the sodium D_{2a} transition ($3^2S_{\frac{1}{2}}$ with $F = 2$ to $3^2P_{\frac{3}{2}}$) exhibits the highest absorption at a laser wavelength of 589.1591 nm, with three possible hyperfine transitions from $F = 2$ to

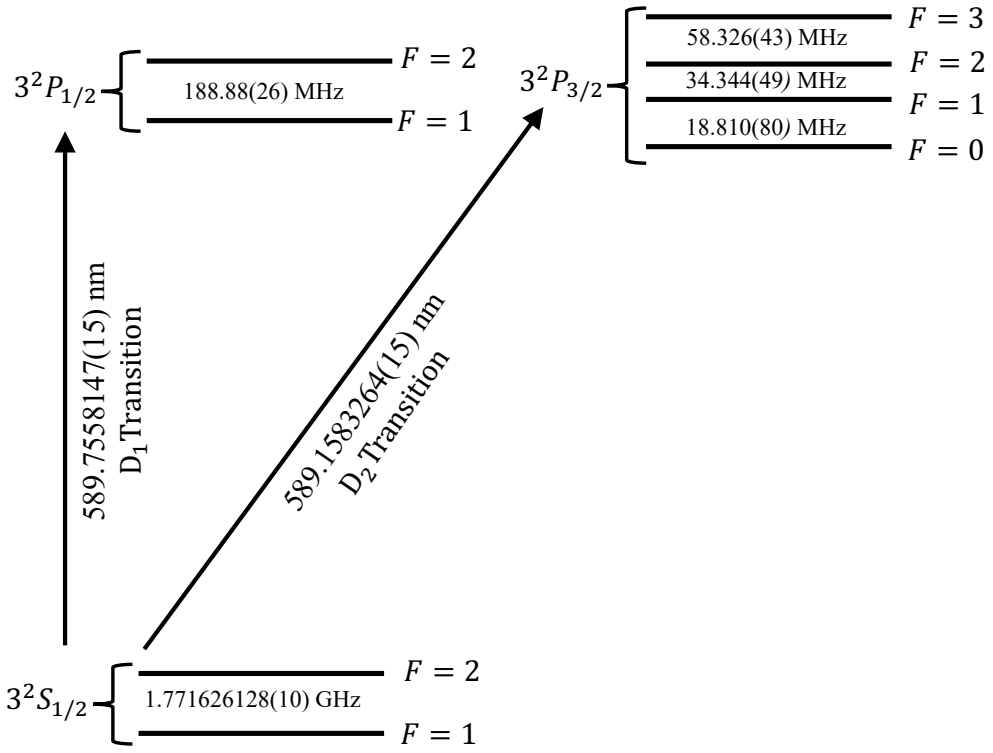

Fig. 1.5 Hyperfine structure for sodium D lines [18]. The required laser wavelengths corresponding to D_1 and D_2 transitions are ∼589.76 nm and ∼589.16 nm, respectively.

$F' = 1, 2, 3$ [34]. For optimal absorption, the laser wavelength needs to be precisely tuned to 589.16 nm for LGS applications.

The number of photons that return to a ground-based telescope can be quantitatively described by the following equation [3]:

$$\Delta N = N_{\mathrm{t}} \varepsilon_{\mathrm{s}} \frac{r_0^2}{4H^2}, \tag{1.1}$$

where N_{t} represents the number of transmitted photons, ε_s is the fraction of scattered photons, which can be expressed in terms of the peak cross section σ_{peak} and the sodium column density ρ_{Na} as

$$\varepsilon_s = \sigma_{\mathrm{peak}} \int dz[\mathrm{Na}] \approx \sigma_{\mathrm{peak}} \rho_{\mathrm{Na}}, \tag{1.2}$$

and r_0 is Fried's coherence length, which is defined as [35]:

$$r_0 = \left(0.423k^2 \int_{\text{path}} C_n^2(z)dz\right)^{-0.6}, \tag{1.3}$$

where k is the wave number, $C_n^2(z)$ denotes the strength of atmospheric turbulence along the path z, and H is the altitude of the sodium layer. Assuming $\varepsilon_s = 10\%$, a good seeing condition with $r_0 = 10\,\text{cm}$ [22], and $H = 90\,\text{km}$, the resulting ratio of returned to transmitted photons is

$$\frac{\Delta N}{N_\text{t}} = 3.09 \times 10^{-14}.$$

This formulation provides a fundamental understanding of the efficiency of photon return in a sodium LGS system under given atmospheric conditions.

The Shack-Hartmann wavefront sensor, illustrated in Fig. 1.6, is frequently employed by AO systems to gather data on wavefront distortions. This sensor features an array of lenslets, with each lenslet directing the light within its aperture onto a specific sub-aperture on the sensor. Each sub-aperture contains numerous pixels, facilitating precise measurement of the focus spot's position for each lenslet. When the wavefront is distorted, the position of the focus spot deviates from the sub-aperture's center. The displacement data from these focus spots are utilized to generate feedback signals for the deformable mirrors, thus enabling the active correction of aberrations by adjusting various segments of the mirror. This capability for real-time wavefront distortion measurement provides the AO system with the necessary feedback to control actuators that adjust the deformable mirror segments, effectively compensating for these distortions.

For the light collected by each lenslet, assuming a minimum signal-to-noise ratio (SNR) of 35 is required for adequate signal capture within its dedicated sensor area, and employing a

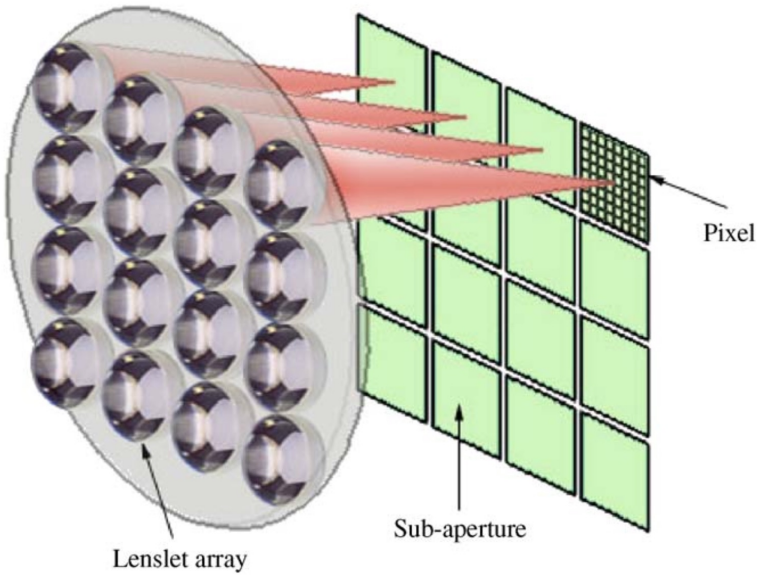

Fig. 1.6 Shack Hartmann wavefront sensor features an array of lenslets, with each lenslet directing the light within its aperture onto a specific sub-aperture on the sensor [36].

quantum efficiency ($\eta_{\mathrm{PD}} = 50\%$) for the sensor, the equation

$$\sqrt{\eta_{\mathrm{PD}} \Delta N} = 35,$$

determines that the required minimum number of transmitted photons is

$$N = 7.94 \times 10^{16}.$$

With photons at ~589.16 nm having a photon energy of $h\nu = 3.37 \times 10^{-19}$ J, a continuous-wave (CW) LGS must provide a minimum output power of 27 mW per lenslet. Typically, AO systems have significantly more lenslets within the sensor than the number of actuators within the deformable mirror. The extra lenslets serve primarily to robustly estimate the wavefront, but they do not contribute to aberration correction due to the insufficient number of actuators

to provide enough correction degrees of freedom. For a single conjugate AO system for an 8-m diameter telescope, approximately 190 useful actuators are required within the deformable mirror for effective aberration correction [37, 38]. Using 200 actuators for this calculation, the LGS operating at the sodium D_{2a} transition requires a minimum power of

$$P_{\min} = 5.4\,\mathrm{W}.$$

Based on these calculations, the design goal for the LGS system is set to 10 W at ∼589.16 nm to account for potential issues such as transmission losses over 90 km of air and variations in the laser output frequency from the maximum absorption wavelength. However, this estimate is conservative. Optimized CW LGS systems can achieve a 20% backscattering efficiency, significantly higher than the 10% used in the initial calculation [39]. Furthermore, commercially available silicon-based photodetectors typically have a quantum efficiency closer to 70%, rather than the 50% assumed. Additionally, an SNR of 35 can be effectively reduced to 10-20 for adequate photon counting in practical applications.

The saturation intensity of LGS for sodium atoms in the atmosphere is another parameter that needs to be considered during the design phase. This can be calculated using the natural linewidth of the sodium atom's lifetime. The velocity of sodium atoms is influenced by the temperature, that temperature is around 200 K in the mesosphere, where laser guide stars are created [40]. There are multiple velocity groups of sodium atoms in mesosphere, for each velocity group with a natural lifetime (τ_{n}) of 16 ns, the natural linewidth can be calculated as

$$\Delta\nu_{\mathrm{n}} = \frac{1}{2\pi\tau_{\mathrm{n}}} \approx 10\,\mathrm{MHz},$$

and if the laser linewidth is narrower than this natural linewidth, the same velocity group of atoms will be consistently engaged and may become depleted [3]. This before mentioned

saturation intensity can be derived from

$$I_{\text{sat}}\sigma_{\text{peak}} = \frac{1}{\tau_{\text{n}}}, \tag{1.4}$$

where $\sigma_{\text{peak}} = 1.1 \times 10^{-9}$ cm^2 is the peak cross section for the natural linewidth at the sodium D_2 line [3], then the saturation intensity is

$$I_{\text{sat}} = 5.68 \times 10^{16} \text{ photon} \cdot \text{s/cm}^2 \approx 19 \text{ mW/cm}^2.$$

For a circularly polarized beam, the experimental saturation intensity is one-third of this theoretical value at 6.4 mW/cm^2, and even lower for a linearly polarized beam [22]. Assuming a conservative saturation intensity of 2.2 mW/cm^2 for a linearly polarized beam and a LGS diameter of 1 m [22], the saturation power is calculated to be 17.3 W. The designed system for this dissertation will not approach this saturation power, ensuring optimal absorption efficiency with a laser linewidth under 10 MHz. While a frequency chirping system is not required for this project, scanning the laser wavelength to engage more than one velocity group of sodium atoms is advisable to avoid saturation in future versions of semiconductor-based LGS systems with output powers exceeding 20 W based on the calculation mentioned above [41].

1.3 Progress in Semiconductor Laser Technology

The term "laser" originates from the acronym for "light amplification by stimulated emission of radiation," which succinctly encapsulates its defining characteristic: the amplification of light through stimulated emission. This foundational principle of laser operation was discovered by Albert Einstein in 1916 [42]. Nicolay Gennadiyevich Basov and Aleksandr Mikhailovich Prokhorov made seminal theoretical contributions to quantum electronics which has led to the

construction of oscillators and amplifiers based on the maser-laser principle in 1950s [43, 44]. Almost concurrently, the team led by Charles Hard Townes developed the first operational device that utilized Einstein's theories in practice, specifically as a microwave amplifier [45–47]. Basov, Prokhorov, and Townes were awarded the Nobel Prize in 1964 for their contributions to the laser-maser principle [48].

As a subsequent advancement to extend the application from microwaves to infrared and visible light, the first operational laser, employing a flash lamp and a ruby rod with silver-coated facets, was successfully demonstrated in 1960 by Theodore Maiman [49]. Shortly after, in 1962, several groups almost simultaneously demonstrated the first semiconductor laser [50–52]. In its initial iterations, semiconductor lasers were homojunction devices, characterized by high laser threshold and the necessity for liquid nitrogen cooling, rendering them impractical for real-world applications. However, in 1963, Herbert Kroemer proposed the heterojunction structure, which was experimentally realized by Zhores Alferov in 1970 [53, 54]. This development enabled semiconductor lasers to operate at room temperature with CW output. Alferov and Kroemer received the Nobel Prize in 2000 for their pioneering work on semiconductor heterostructures [55].

The edge-emitting laser (EEL) is the predominant type of semiconductor laser, typically electrically pumped, with its laser resonator formed by cleaved facets (sometimes coated). While EELs achieve high output power, they sacrifice beam quality [56]. In contrast, the vertical-cavity surface-emitting laser (VCSEL) that emits light perpendicular to the wafer surface has better beam profile [57]. VCSELs utilize Distributed Bragg Reflectors (DBRs) [58] on both sides of the quantum well active region to construct the laser cavity [59] and are also commonly electrically pumped. Despite the enhanced beam profile of VCSELs, achieving uniform carrier injection for large cavity modes poses a challenge, thereby limiting the output power of VCSEL devices. Individual VCSELs typically operate at power levels in the 1-10 mW

range [60]. The limited output power of VCSELs output falling short of the requirements for LGS applications.

Optical pumping enabled the enlargement of the active region while maintaining uniform carrier injection, facilitating high-power output with a single transverse mode [61]. This concept was proposed in 1966 [62] but was only experimentally demonstrated after advancements in diode laser technology three decades later [61, 63]. The advent of the first vertical external-cavity surface-emitting laser (VECSEL), boasting a TEM_{00} transverse mode with over 0.5 W output, marked a significant milestone [61]. In this configuration, one of the cavity mirrors was comprised of a DBR grown adjacent to the quantum well active region, while an external mirror served as the other cavity mirror. Typically, a diode laser was employed to pump VECSELs, and the utilization of an external cavity mirror ensured a TEM_{00} beam profile. In multi-transverse mode operation, which typically yields higher output than TEM_{00} mode, a single VECSEL device has achieved over 100 W output power [29]. However, optical pumping's drawback lies in its wall-plug-to-laser efficiency, which is inferior to that of electrically pumped lasers. Nonetheless, this efficiency is not the primary concern for many applications, such as LGS.

Researchers have achieved numerous successful outcomes using VECSELs for LGS applications. High power output near 1178 nm was demonstrated [64], and an output exceeding 5 W at 589 nm has been demonstrated [30], while another group achieved 20 W yellow output around 588 nm [65]. Despite the use of diamond heat spreaders, all those outputs were thermally limited, indicating the need for better thermal management platforms to demonstrate a high-power semiconductor-based LGS. Due to small refractive index contrast for semiconductor material for DBRs, normally tens of DBR pairs are required to achieve high reflectance. The large thickness and number of layers in DBRs result in high thermal resistance, which hinders effective heat dissipation [66, 67]. In addition, the lattice mismatch between the substrate and DBR poses significant hurdles during VECSEL wafer growth, hindering the production of

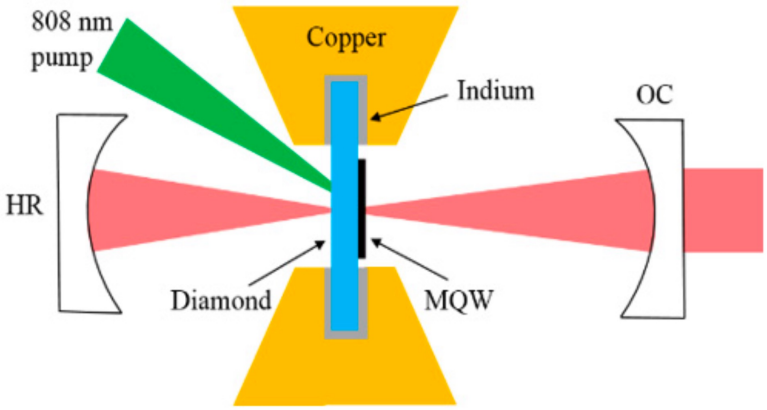

Fig. 1.7 Schematic representation of a MECSEL setup [1].

high-quality VECSEL samples across various desired wavelengths like in GaN system and InGaP system [68, 69].

A proposed solution involves the complete elimination of DBRs and the exclusive use of external mirrors [1, 2] and/or gratings [70, 71] to form the resonator, resulting in a novel structure termed MECSEL [1, 2]. Figure 1.7 is a schematic diagram of MECSEL. The multi-quantum well (MQW) active region is directly bonded to a single-crystalline diamond heat spreader, and then the bonded sample is mounted on a copper heat sink with indium to enhance thermal contact [1]. An 808 nm diode laser serves as the pump, with two external mirrors employed for the formation of the laser resonator, one is a high reflectance (HR) mirror, another is output coupler (OC). The advantages of the MECSEL platform include superior thermal management capability due to the absence of a DBR [4, 66, 67, 72], and the potential for easier wafer growth since there is no DBR adjacent to the active region [2]. With improved thermal management, more affordable and available silicon carbide (SiC) can be used as a heat spreader instead of diamond, enabling wafer-scale fabrication. Besides those advantages, MECSEL also has less better wavelength tunability compared with VECSEL [73]. Like VECSELs, MECSELs provide access to the cavity, enabling laser linewidth narrowing [74], intracavity frequency

doubling [75], and active frequency stabilization [76]. These attributes collectively position the MECSEL as an ideal candidate for constructing compact and budget-friendly LGSs.

An emerging platform, the photonic-crystal surface-emitting laser (PCSEL) [77], has shown potential to achieve high power output with good beam profile. The two-dimensional photonic crystal structure allows a much larger active area compared with VCSELs while maintaining single-mode operation with suitable design [78]. Even blue-violet wavelengths can be achieved by PCSEL with more straightforward current injection [79]. They offer potential for on-chip integration [80], ultralow thresholds [81], and high beam quality with a small divergence angle [82, 83]. Additionally, they can be mass-produced on commercial epitaxial wafers [84]. There was even a report last year of a CW single-mode PCSEL at over 50 W [85], highlighting the great potential of this platform.

However, the output beam quality deteriorates with increased power [82], and the current output power record has an M^2 value of 2.4 [85], which is unsuitable for LGS applications that need to project the laser up to the sodium layer around 90 km above the ground. While PCSELs may become viable for LGS with technical advancements, they are not yet mature enough. Currently, MECSEL is the most suitable candidate.

1.4 Conclusion

This chapter highlighted the important role of the LGS system in astronomical observation, and introduced the current LGS systems and the motivation to build a semiconductor-based LGS. Parameters necessary for the LGS, such as laser wavelength, output power, and laser linewidth, were computed. It was determined that it is essential to construct a MECSEL emitting at $\sim$589.16 nm with a TEM_{00} transverse mode, capable of exceeding 10 W output power and maintaining a linewidth narrower than 10 MHz. Furthermore, the laser requires frequency

stabilization at the sodium D_2 transition to optimize absorption efficiency. While integrating a frequency chirping system would aid in mitigating sodium atom saturation in LGS systems exceeding 20 W, it is not essential for this 10 W LGS configuration.

The next chapter will delve into the design of the MECSEL, focusing on the laser resonator configuration, quantum well active region, and the methodologies for implementing laser linewidth narrowing and frequency doubling.

Chapter 2

Membrane External-Cavity Surface-Emitting Laser

After clarifying the parameters necessary for the MECSEL to be utilized in the LGS system in Chapter 1, the subsequent task involves designing the laser to meet these established requirements. This chapter will explore the design process of the MECSEL gain structure, employing basic equations to outline the initial design considerations. This chapter will also detail the configuration of the laser resonator, incorporating a custom developed MATLAB script to optimize the resonator design. Additionally, this chapter will discuss the techniques implemented for linewidth narrowing and intracavity frequency doubling, which are essential for achieving the target wavelength of 589 nm from a fundamental wavelength of 1178 nm in the MECSEL.

2.1 Gain Structure Design

The gain medium, laser resonator, and pump are the three fundamental components required to construct a laser, and semiconductor lasers are no exception. The semiconductor thin disk, which serves as the gain medium is the key component for MECSEL. The heat spreader sandwich plays a pivotal role in the device's performance via optimized heat extraction. This structure, often referred to as the MECSEL gain chip, is composed of several key elements: the quantum well active region, which provides the necessary gain; window layers, which serve to prevent surface recombination; and directly bonded heat spreaders that effectively dissipate heat.

A simplified band diagram of the optically pumped MECSEL gain structure is presented in Fig. 2.1. The horizontal axis of this diagram indicates the position along the wafer's growth direction, where the MECSEL gain structure is situated in air. The vertical axis represents the energy levels at different layers, with the upper band corresponding to the conduction band and the lower band to the valence band. Within the gain structure, the quantum wells are positioned at the anti-nodes of the laser's optical standing wave to maximize gain, a configuration known as the resonant periodic gain structure or RPG structure [86]. In this setup, a pump photon with energy E_{pump} from pump laser (blue) is absorbed at the barrier layer, exciting an electron from the valence band to the conduction band, and leaving a hole at valence band. The free carriers diffuse from the barrier layers to the quantum wells, and subsequently recombine within the quantum wells, emitting a photon with energy E_{laser}. The resulting laser output (red) is directed perpendicular to the surface of the MECSEL, emanating in both directions. To further enhance performance, high bandgap energy window layers are grown between the quantum well active region and the air. These layers are essential for preventing surface recombination.

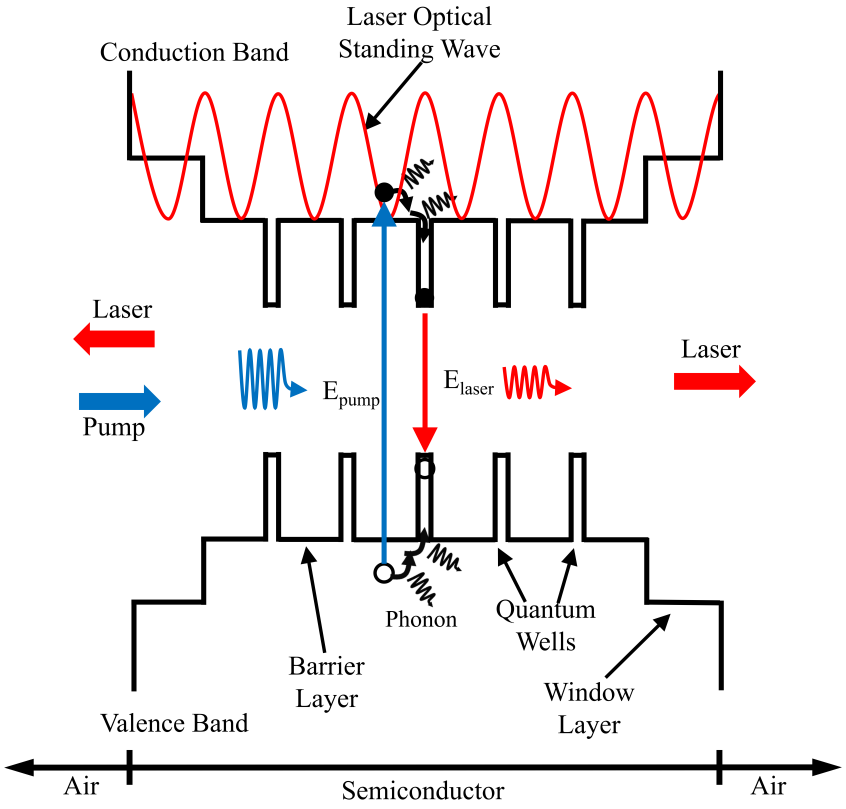

Fig. 2.1 Schematic diagram of the MECSEL gain structure with laser optical standing wave.

The gain medium in a laser device provides the necessary energy levels for emitting specific wavelengths. In this process, electrons within the active media are initially excited from lower energy states to higher ones either through electrical injection or optical pumping. The carriers then diffuse and thermalize to lower energy levels while emitting phonons, and these free carriers subsequently return to initial energy states via stimulated emission, facilitated by the feedback mechanism of the laser resonator. The energy of the emitted photons is given by:

$$E_{\text{photon}} = E_{\text{upper}} - E_{\text{lower}},$$

where E_{upper} represents the energy level of the upper state, and E_{lower} denotes that of the lower state. The wavelength, λ, of the emitted light can then be calculated using the equation:

$$\lambda = \frac{hc}{E_{\text{photon}}}, \tag{2.1}$$

where h is Planck's constant, and c is the speed of light in vacuum.

In scenarios where optical pumping is utilized, the pump photon typically possesses a shorter wavelength—and consequently higher energy—than the emission photon, unless nonlinear effects are being employed to alter this relationship. For a wavelength of 589 nm that is targeted for LGS applications, there are significant challenges associated with fabricating a MECSEL that can directly emit at this wavelength. Although a recent study demonstrated a direct output of 0.87 W at 589 nm from an Indium gallium phosphide (InGaP) quantum well semiconductor laser using electron injection [87], this power is insufficient for LGS requirements. Given the constraints related to manufacturing challenges and the requisite output power, the dissertation will focus on designing and fabricating a MECSEL that operates at 1178 nm. Available pump laser wavelengths in the laboratory, such as 808 nm and 1070 nm, will be utilized to construct the 1178 nm MECSEL. This wavelength will then be converted to 589 nm using second harmonic generation (SHG).

The bandgap energy versus lattice constant for commonly used III-V semiconductor compounds at room temperature is shown in Fig. 2.2. On this diagram, solid lines represent ternary compounds with a direct bandgap, which are alloys of the binary compounds at each line's endpoints. The dashed lines highlight regions where the bandgap is indirect. Additionally, the areas enclosed by lines between various binary compounds represent quaternary compounds, noted for their greater flexibility in bandgap energy engineering while maintaining lattice matching between layers [88]. From this diagram, indium gallium arsenide (InGaAs) and indium gallium

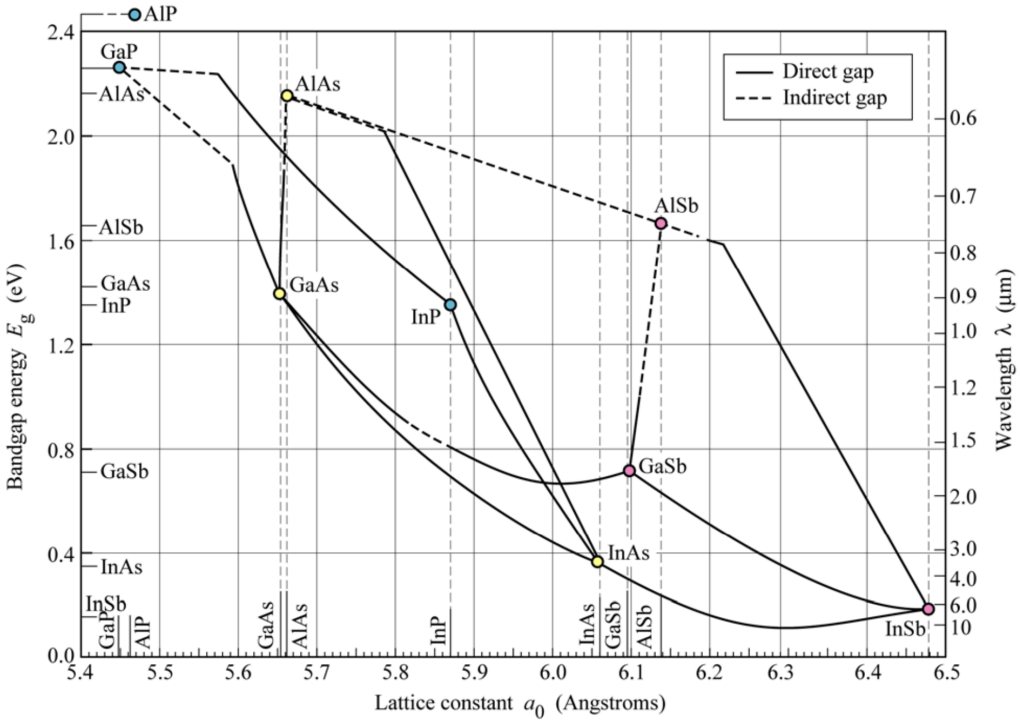

Fig. 2.2 Bandgap energy versus lattice constant for commonly used III–V compounds at room temperature for semiconductor design [88].

arsenide phosphide (InGaAsP) are suitable candidates for applications requiring a bandgap energy corresponding to 1178 nm. Given the difficulty in InGaAsP quaternary compound growth due to the large discrepancy in size between In and P atoms, InGaAs has been selected for the quantum well fabrication. Furthermore, gallium arsenide (GaAs) has been chosen as the material for the barrier layers.

The energy diagram for a quantum well with thickness L_z is illustrated in Fig. 2.3. The horizontal axis represents the wafer growth direction, and the vertical axis displays the energy levels within the quantum well structure. The bandgap energy of the quantum well is denoted as E_g, and the well exhibits an energy potential of ΔE_c in the conduction band and ΔE_v in the valence band. In the conduction band, the first three quantized energy levels are labeled E_{1c}, E_{2c}, and E_{3c}. These represent the confined energy states due to the quantum confinement effect

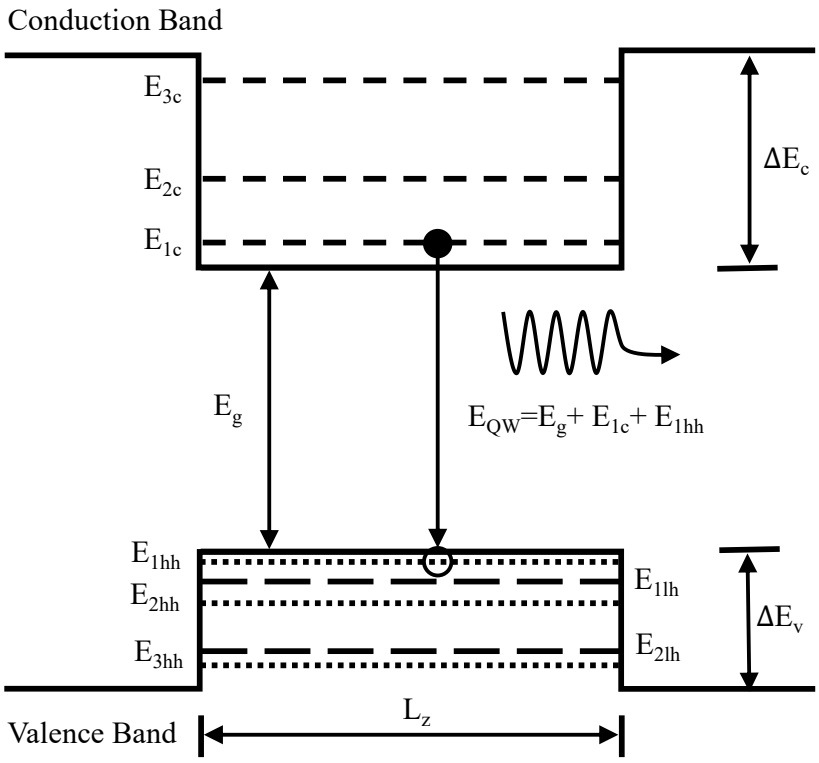

Fig. 2.3 Energy diagram of a quantum well structure with thickness of L_z [89].

within the well. Similarly, in the valence band, the energy levels for heavy holes (represented by dotted lines) and light holes (represented by long dashed lines) are indicated. The first few quantized energy levels for heavy holes are E_{1hh}, E_{2hh}, and E_{3hh}, while those for light holes are E_{1lh} and E_{2lh}. The transition from the first conduction band energy level (E_{1c}) to the first heavy hole valence band energy level (E_{1hh}), results in the emission of light. The photon energy associated with this transition can be expressed by the following equation:

$$E_{QW} = E_g + E_{1c} + E_{1hh}.$$

The energy levels of carriers confined within a quantum well can be quantitatively described by considering their quantized nature and the energy of these quantized levels is expressed by:

$$E_z = \frac{h^2 {k_z}^2}{8\pi^2 m^*}, \tag{2.2}$$

where m^* represents the effective mass of the carriers of interest (either electrons or holes), and k_z is the quantization wave vector defined as:

$$k_z = \frac{l\pi}{L_z}, \quad l = 1,2,3,\ldots \tag{2.3}$$

where l is the integer quantum number which corresponds to the n^{th} energy level of the electrons or holes [90]. For a 7 nm thick InGaAs quantum well, the effective masses for electrons ($0.067m_e$) and heavy holes ($0.45m_e$) from GaAs were utilized as an approximation [91], where m_e is the electron's rest mass. Using these values, the confined energies for the first quantized levels were calculated to be $E_{1c} = 115\,\text{meV}$ for electrons and $E_{1hh} = 17\,\text{meV}$ for heavy holes.

The temperature dependency of the bandgap energy for semiconductors needs to be considered in the design of MECSELs. This dependency can be accurately modeled using Varshni's empirical formula [92]:

$$E_g(T) = E_{g,0} - \frac{\alpha T^2}{\beta + T}, \tag{2.4}$$

where $E_{g,0}$ is the bandgap energy at 0 K, and α and β are coefficients that encapsulate the temperature dependence of the bandgap energy that expressed in units of [eV/K] and [K], respectively. There will be a shift in the emission wavelength due to temperature-induced changes in the bandgap energy. For MECSEL applications, increasing the pump power can enhance the output power up to the thermal rollover point. Beyond the thermal rollover point

approximately 90 °C to 110 °C [67, 93, 94], further increases in pump power lead to excessive heating and a subsequent decrease in performance due to increased internal losses.

To design a laser that emits the desired wavelength at maximum output power, it is necessary to account for the temperature-related changes in the bandgap energy from room temperature to the rollover temperature. This change is quantified by:

$$\Delta E_{\mathrm{g,T}} = \frac{\alpha {T_{\mathrm{RT}}}^2}{\beta + T_{\mathrm{RT}}} - \frac{\alpha {T_{\mathrm{RO}}}^2}{\beta + T_{\mathrm{RO}}}, \tag{2.5}$$

where T_{RT} represents room temperature and T_{RO} denotes the rollover temperature. Assuming a temperature differential of 70 K between these two states, the change in the bandgap energy can be calculated. Using $\alpha = 6 \times 10^{-4}$ eV/K and $\beta = 408$ K [95], the change is:

$$\Delta E_{\mathrm{g,T}} = -29\,\mathrm{meV}.$$

Consequently, a laser designed to emit at 1178 nm at the rollover point would emit at approximately 1150 nm at room temperature to accommodate this shift.

To ensure that a 1178 nm laser operates effectively, the photon energy associated with this wavelength, $E_{1178\,\mathrm{nm}}$, is calculated to be 1.053 eV. The design target for the bandgap energy of the InGaAs quantum well at 300 K is then derived by incorporating the effects of quantized energy levels within the quantum well and the temperature-dependent change in bandgap energy:

$$E_{\mathrm{design}} = E_{1178\,\mathrm{nm}} - E_{1\mathrm{c}} - E_{1\mathrm{hh}} + \Delta E_{\mathrm{g,T}} = 0.892\,\mathrm{eV},$$

where $E_{1\mathrm{c}}$ and $E_{1\mathrm{hh}}$ are the confined energy levels of the electrons and heavy holes, respectively, in the quantum well, and $\Delta E_{\mathrm{g,T}}$ represents the shift in bandgap energy due to temperature effects.

The bandgap energy of the $In_{1-x}Ga_xAs$ alloy at 300 K, as a function of the gallium composition x, is modeled by the equation [96]:

$$E_g(x) = 0.36 + 0.629x + 0.436x^2. \tag{2.6}$$

Using this model, the composition x of gallium necessary to achieve the desired bandgap energy at room temperature was initially calculated to be approximately 0.6. During the wafer fabrication phase, a 6 nm thick $In_{0.38}Ga_{0.62}As$ quantum well was used with slightly adjusting the gallium content to 0.62. This composition adjustment was found to yield superior performance and closely aligning with the theoretical calculations.

GaAs serves as an barrier layer material for InGaAs quantum wells, primarily due to its favorable optical properties and compatibility with existing fabrication processes. GaAs is chosen because it can absorb photons from a 808 nm diode laser, which is readily available in the laboratory, and it is transparent to the 1178 nm emission photons from the quantum well. GaAs is a commonly used substrate material in semiconductor manufacturing, which simplifying the wafer fabrication process significantly. Mismatch in lattice constants can lead to defects during the epitaxial layer growth, potentially resulting in poor-quality samples and reduced device performance [97]. To address potential strain issues between the InGaAs and GaAs layers, gallium arsenide phosphide (GaAsP) is employed as a strain-compensation material [98]. This approach is supported by the effectiveness of $GaAs_{0.94}P_{0.06}$ buffer layers placed at the node positions of the RPG structure, which aids in strain compensation during the wafer growth process with minimal absorption from GaAsP. For the RPG structure, precise calculation of the refractive indexes of each layer is essential to determine the correct thickness of each layer during wafer growth. The Sellmeier equation, which has been thoroughly studied and is documented for commonly used semiconductor compounds, provides a reliable method

for calculating these refractive indexes [99]. At the specific wavelength of 1178 nm, the refractive indexes for GaAs and InGaAs were calculated to be $n_{\mathrm{GaAs}}(1178\,\mathrm{nm}) = 3.355$ and $n_{\mathrm{InGaAs}}(1178\,\mathrm{nm}) = 4.008$.

Calculating the optimal number of quantum wells is important for achieving the desired threshold and output slope efficiency in MECSELs. The maximum number of quantum wells is constrained by the challenges in managing strain compensation during wafer growth [100]. The gain g, measured in cm^{-1}, is influenced by the carrier density N [cm^{-3}] and can be expressed as [61]:

$$g = g_0 \ln\left(\frac{N}{N_0}\right), \tag{2.7}$$

where g_0 is the gain parameter and N_0 is the transparency carrier density—the electron-hole concentration at which absorption equals emission. The threshold condition for MECSEL operation, similar to other lasers, is given by [101]:

$$R_1 R_2 T e^{2\Gamma g_{\mathrm{th}} L_{\mathrm{QW}}} = 1, \tag{2.8}$$

where R_1 and R_2 are the reflectivities of the cavity mirrors, T represents the transmission factor of the laser cavity (accounting for all intracavity losses), Γ is the longitudinal confinement factor indicating the proportion of mode energy contained within the active region, g_{th} is the threshold gain, and L_{QW} is the total thickness of all quantum wells.

Below the lasing threshold, the carrier density in the active medium of a laser can be written as

$$N = \frac{\eta_{\mathrm{abs}} P_{\mathrm{pump}}}{E_{\mathrm{pump}} L_{\mathrm{QW}} A_{\mathrm{p}}} \tau(N), \tag{2.9}$$

where η_{abs} is the absorption efficiency for the pump, follows the Beer-Lambert Law as

$$\eta_{\text{abs}} = 1 - e^{-\alpha d}, \tag{2.10}$$

with d being the material thickness and α the absorption coefficient, P_{pump} denotes the pump power, E_{pump} is the energy of the pump photons, A_{p} is the area of the pump mode, and $\tau(N)$ represents the carrier lifetime, which depends on the carrier density N and is given by:

$$\frac{1}{\tau(N)} = A + BN + CN^2, \tag{2.11}$$

where A, B, and C are the Shockley-Read-Hall (SRH), radiative, and Auger recombination coefficients, respectively [101]. The threshold for lasing, in terms of carrier density and pump power, can be derived from:

$$N_{\text{th}} = N_0 (R_1 R_2 T)^{-\frac{1}{2\Gamma g_0 L_{\text{QW}}}}, \tag{2.12}$$

and

$$P_{\text{th}} = N_{\text{th}} \frac{E_{\text{pump}} L_{\text{QW}} A_{\text{p}}}{\eta_{\text{abs}} \tau(N_{\text{th}})}. \tag{2.13}$$

These equations define the minimum carrier density N_{th} and pump power P_{th} needed to reach the lasing threshold. The output power of the laser, P_{laser}, is then described by the relationship:

$$P_{\text{laser}} = (P_{\text{pump}} - P_{\text{th}}) \eta_{\text{diff}}, \tag{2.14}$$

where η_{diff} represents the differential efficiency of the laser system, define as [102]

$$\eta_{\text{diff}} = \eta_{\text{abs}} \cdot \eta_{\text{geo}} \cdot \eta_{\text{q}} \cdot \eta_{\text{out}} \cdot \eta_{\text{rad}}, \tag{2.15}$$

incorporating absorption efficiency η_{abs}, geometrical efficiency η_{geo}, quantum efficiency (η_{q}), output efficiency (η_{out}), and radiative efficiency (η_{r}). These efficiencies are further defined as:

$$\eta_{\text{abs}} = \frac{P_{\text{abs}}}{P_{\text{pump}}} = \frac{P_{\text{pump}} - P_{\text{r}} - P_{\text{t}}}{P_{\text{pump}}} \tag{2.16}$$

where P_{abs} is the absorbed pump power, P_{r} is the reflected pump power from all interfaces, and P_{t} is the transmitted pump power.

$$\eta_{\text{geo}} = \frac{A_{\text{l}}}{A_{\text{p}}}, \tag{2.17}$$

where A_{l} is the area of the laser mode.

$$\eta_{\text{q}} = \frac{\lambda_{\text{pump}}}{\lambda_{\text{laser}}}, \tag{2.18}$$

$$\eta_{\text{out}} = \frac{\ln(R_2)}{\ln(R_1 R_2 T)}, \tag{2.19}$$

and

$$\eta_{\text{r}} = \frac{BN_{\text{th}}}{A + BN_{\text{th}} + CN_{\text{th}}{}^2}. \tag{2.20}$$

Table 2.1 presents the parameters used to determine the optimal number of quantum wells for a 1178 nm MECSEL. With an output coupling efficiency of 2% and a pump power of 100 W at 808 nm, the impact of varying the number of quantum wells on the output power was analyzed. Each barrier layer was maintained at a thickness of 82 nm, while the quantum well thickness was set at 6 nm. The resultant maximum output power, as a function of the number of quantum wells ranging from 0 to 20, was graphically represented in Fig. 2.4. The calculation indicates that increasing the number of quantum wells beyond 10 may slightly enhance the maximum output power achievable with a fixed pump power. However, while adding more quantum wells can theoretically improve performance, practical challenges such

Table 2.1 Parameters for MECSEL threshold and output power calculations [103].

Parameter	Description	Value	Unit
g_0	gain parameter	2000	cm^{-1}
N_0	transparency carrier density	1.7×10^{18}	cm^{-3}
Γ	longitudinal confinement factor	2.0	-
L_z	quantum well thickness	7.0	nm
R_1	mirror 1 reflectivity	0.999	-
T	round trip transmission factor	0.98	-
λ_{pump}	pump wavelength	808	nm
λ_{laser}	emission wavelength	1178	nm
A_p	area of pump spot	3.14×10^4	μm^2
α	GaAs absorption coefficient at 808 nm	1	μm^{-1}
A	SRH recombination coefficient	1×10^7	s^{-1}
B	radiative recombination coefficient	1×10^{-10}	$cm^3 s^{-1}$
C	Auger recombination coefficient	6×10^{-30}	$cm^6 s^{-1}$

as increased internal optical losses and non-uniformities can negate these benefits [104]. More importantly, in the RPG configuration, quantum wells are positioned at the anti-node of the cavity standing wave, with barriers placed between adjacent quantum wells. As the number of quantum wells increases, the total thickness of these barriers also increases. Assuming an absorption coefficient of $1\,\mu m^{-1}$ and each barrier layer being 170 nm thick, the incident pump power decreases by approximately 15% after passing through each barrier layer. Consequently, if the number of quantum wells is too large, there will be almost no pump power available at the last few layers, resulting in non-uniform pumping. If the active region of a laser contains fewer than four quantum wells, it has been calculated that the laser threshold exceeds 100 W, making such a configuration inefficient for practical purposes. Analysis has shown that the maximum output power reaches 26.4 W when the number of quantum wells is increased to eleven. Beyond this point, adding additional quantum wells provides only small gains in output power, and considering the quantum well that not receive enough pump will result in absorption of 1178 nm, more quantum wells may not be beneficial. Considering the intracavity losses

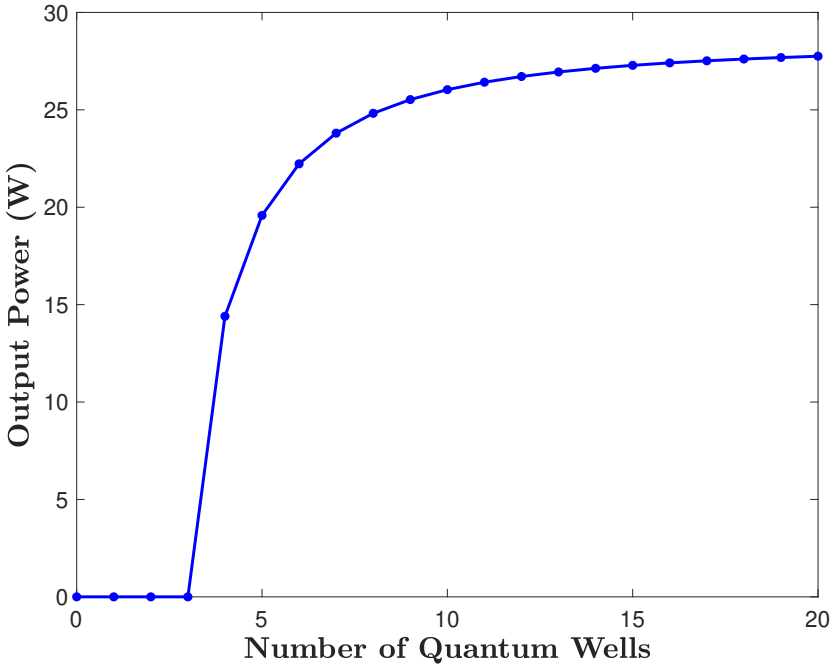

Fig. 2.4 Maximum output power at 1178 nm with 2% output coupler versus number of quantum wells in MECSELs using 100 W pump at 808 nm.

associated with linewidth narrowing and frequency doubling, estimating to about 60% from the free-running output at fundamental wavelength to SHG output, an eleven quantum well MECSEL can potentially produce over 10 W at 589 nm based on the theoretically calculated value of 26.4 W. A MECSEL gain chip featuring an eleven quantum well structure, optically pumped at 808 nm, was fabricated to validate these theoretical predictions.

The designed MECSEL structure was produced by a commercial growth foundry (21 SEMICONDUCTORS, Stuttgart, Germany) using metal-organic chemical vapor deposition (MOCVD) on a GaAs substrate. The structure includes $In_{0.49}Ga_{0.51}P$ window layers on both sides of the multi-quantum well gain region to prevent surface recombination. To facilitate subsequent substrate removal, a 250 nm thick $Al_{0.92}Ga_{0.08}As$ etch stop layer was grown between the GaAs substrate and the window layer. This composition was specifically selected for its high selectiv-

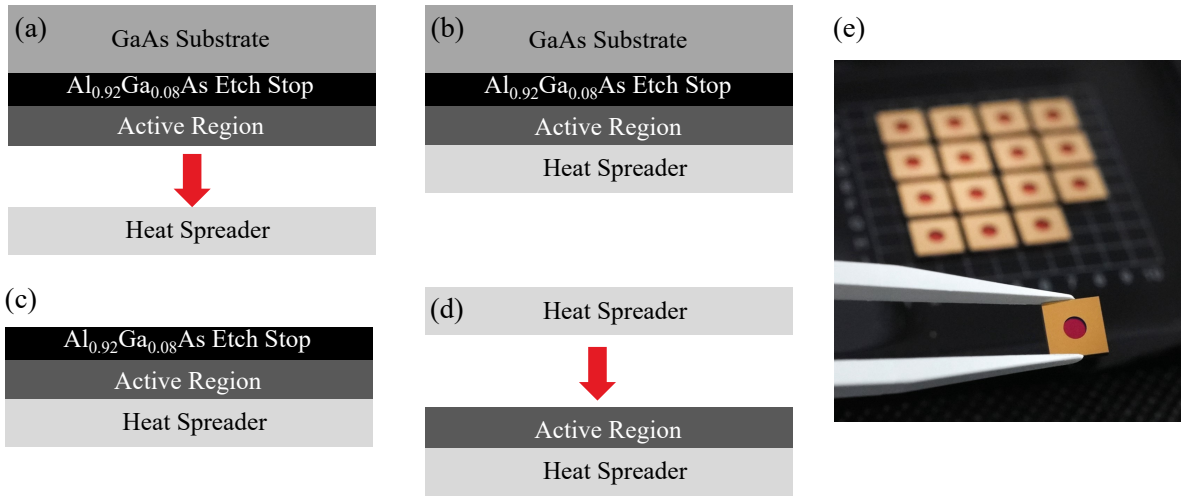

Fig. 2.5 MECSEL gain chip fabrication process. (a) The first surface bonding, (b) GaAs substrate etching, (c) AlGaAs etch stop etching, (d) the second surface bonding, and (e) a photography of a complete MECSEL gain chip (Credit: Dr. Garrett Cole).

ity in GaAs etching followed by HF-based wet etching. The multi-quantum well structure was then sandwiched between two 500 µm thick, double-side polished single-crystalline 4H-SiC heat spreaders utilizing a plasma-activated low-temperature direct bonding technique. This process was performed by our collaborators from THORLABS CRYSTALLINE SOLUTIONS [105].

Fabrication of the MECSEL gain chips begins with the thorough cleaning of both the epitaxial structure and the SiC substrate to ensure that all surfaces are free of contaminants and debris. Subsequent oxygen plasma activation ensures that the surfaces are chemically reactive for achieving a strong bond. After the cleaning and activation steps, the materials are carefully aligned and contacted at either the chip or wafer scale as shown in Fig. 2.5 (a). Pressure is applied to the stack to enhance the initial bond strength, with processes carried out in both ambient and vacuum, followed by post-bond annealing to set the bond. Once annealing is complete, the GaAs growth wafer as seen in Fig. 2.5 (b) is selectively removed using H_2O_2:NH_4OH-based wet chemical etching (NH_4OH:H_2O_2=1:30). As shown in Fig. 2.5 (c), the substrate removal process terminates on the $Al_{0.92}Ga_{0.08}As$ etch stop layer, which is stripped

using dilute HF acid (HF:H_2O=1:20). This leaves only the multi-quantum well epitaxial layers, capped by the $In_{0.49}Ga_{0.51}P$ window layers, bonded on the surface of the first SiC substrate. Following this, the surface of the transferred epitaxial material and the bare SiC are again cleaned and activated in preparation for a second bonding process as shown in Fig. 2.5 (d). This process involves similar steps of initial contact, pressure application, and another round of annealing, thereby integrating the epitaxial active region between two SiC substrates to act as high thermal conductivity transparent heat spreaders for the MECSEL gain chips. Finally, any required metal or dielectric layers are applied to the SiC/epi/SiC stack (for example, AR coatings are applied using plasma-enhanced chemical vapor deposition (PECVD), while Ti/Au or Cr/Au films are evaporated for improved thermal contact to the copper heat sink), and wafer-scale bonds are diced to yield individual gain chips. Photography of a complete gain chip is shown in Fig. 2.5 (e).

2.2 Laser Resonator Design

The laser resonator, or laser cavity, provides essential feedback and enhances stimulated emission. In the case of a MECSEL, the design differs from commonly semiconductor lasers that typically incorporate DBRs adjacent to the active region. Instead, MECSELs rely entirely on external mirrors for feedback as they do not integrate a DBR within their structure. This aspect aligns MECSELs more closely with solid-state lasers, where external mirrors predominantly form the resonator. This configuration enhances the flexibility in cavity design, allowing adaptation to a wide range of output requirements. Consequently, MECSELs offer unparalleled versatility, capable of accessing a broad spectrum of wavelengths [1, 2, 106–111], achieving high output powers [109, 112–114], and facilitating intracavity processes such as linewidth

narrowing [20, 74–76, 115], nonlinear wavelength conversion [75, 76, 115], and frequency stabilization [75, 76].

The schematic diagram presented in Fig. 2.6 showcases a MECSEL specifically designed for LGS applications. This design employs a V-cavity configuration that includes two plane end mirrors and a concave folding mirror. In this setup, the use of two plane cavity end mirrors simplifies the overall cavity design, particularly enhancing intracavity processes such as frequency doubling. This configuration is advantageous because it ensures the highest beam intensity at the plane mirror within the shorter arm, and a nonlinear crystal will be placed in this arm near the cavity beam waist. Additionally, the presence of a plane wavefront at this mirror facilitates optimal overlap between the fundamental and the nonlinear conversion beams. A curved folding mirror is utilized for maintaining the stability of the laser cavity. This mirror is high-reflection (HR) coated at 1178 nm to reflect the fundamental wavelength within the cavity, and anti-reflection (AR) coated at 589 nm to facilitate the output of yellow light, effectively functioning as the output coupler (OC) for the system. Furthermore, a birefringent filter (BRF) [116] and an etalon are positioned on the MECSEL gain chip arm to narrow the laser's output linewidth. On another arm, a nonlinear frequency doubling LBO crystal along with a piezoelectric transducer (PZT) for wavelength stabilization are installed.

The resonator design must fulfill three criteria to ensure optimal performance. First the laser cavity needs to be stable under various operational conditions including the development of a thermal lens from parasitic heating. Secondly, the cavity length must be sufficient to accommodate all intracavity elements, including filters and nonlinear crystals, ensuring that they function effectively without spatial constraints. Lastly, the beam size within the cavity must be carefully managed to ensure good overlap and efficient interaction at the MECSEL gain chip and the LBO crystal for high nonlinear conversion efficiency. To achieve these objectives,

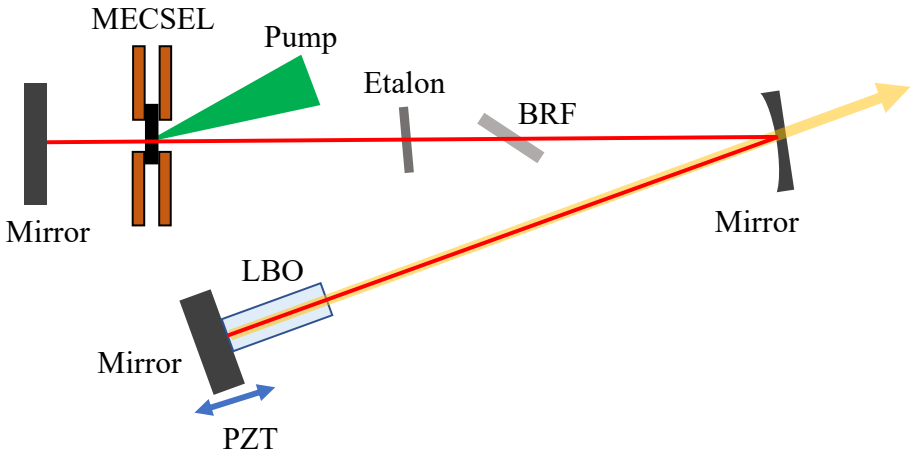

Fig. 2.6 Schematic diagram of a V-configuration MECSEL for LGS applications. Etalon and BRF are used for single longitudinal mode selection, LBO crystal is used for intracavity frequency doubling, and PZT is used for laser frequency stabilization.

the cavity configuration is carefully analyzed using Gaussian beam solutions of the paraxial wave equation and ray transfer matrix analysis.

In terms of properly designing a laser cavity, the behavior of a laser beam within the cavity can be accurately described using Gaussian beam solutions derived from the paraxial wave equation, as outlined in Table 2.2 [101]. In this model, z represents the on-axis distance from the Gaussian beam waist, while x and y specify the distances from the optical axis, collectively describing the in-plane position r. The constant c stands for the speed of light, ε_0 denotes the vacuum permittivity, A is an intensity-related constant, and λ is the wavelength of the laser.

In addition to Gaussian beam analysis, ray transfer matrix analysis, also known as the ABCD matrix method, is utilized for ray tracing calculations under the paraxial approximation. This technique involves representing each optical element within the system by a 2×2 matrix. To analyze the entire optical system, the matrices of individual elements are multiplied in a sequence from the last to the first element encountered by the light, forming what is known as the ABCD matrix of the system. Table 2.3 lists some commonly used matrices, which are

Table 2.2 Gaussian beam solutions of the paraxial wave equation.

Parameter	Equation
intensity	$I(r) = \frac{c\varepsilon_0}{2}\lvert A\rvert^2 e^{-\frac{2(x^2+y^2)}{w^2(z)}}$
spot size	$w(z) = w_0\sqrt{1+\frac{z^2}{Z_0^2}}$
radius of curvature	$R(z) = z + \frac{Z_0^2}{z}$
Rayleigh range	$z_0 = \frac{\pi w_0^2}{\lambda}$
divergence angle	$\theta = \frac{\lambda}{\pi w_0}$

essential for predicting how the laser beam will interact with various optical components. This dual approach, combining Gaussian beam solutions and ABCD matrix analysis, provides a comprehensive framework for understanding and optimizing the propagation of light through the laser cavity.

Table 2.3 Commonly used matrices in ray transfer matrix analysis.

Parameter	Equation
free space propagation	$\begin{bmatrix} 1 & d \\ 0 & 1 \end{bmatrix}$
refraction at a flat interface	$\begin{bmatrix} 1 & 0 \\ 0 & \frac{n_1}{n_2} \end{bmatrix}$
reflection from a curved mirror	$\begin{bmatrix} 1 & 0 \\ -\frac{2}{R} & 1 \end{bmatrix}$
propagation through thin lens	$\begin{bmatrix} 1 & 0 \\ -\frac{1}{f} & 1 \end{bmatrix}$

In these matrices, d represents the distance traveled in free space or within a medium of constant refractive index. For flat interfaces between two different materials, n_1 and n_2 denote the refractive indices of the initial and final materials, respectively. In the context of mirrors, R specifies the radius of curvature (ROC) for normal incidence. When a mirror is placed at an incidence angle θ, the tangential plane's radius R_t is adjusted to $R\cos\theta$ and the sagittal plane's radius R_s to $R/\cos\theta$. For thin lenses, f indicates the focal length.

Upon calculating the ABCD matrix of the laser cavity, represented as $\begin{bmatrix} A & B \\ C & D \end{bmatrix}$, the stability of the cavity can be determined using the criterion:

$$-1 \leq \frac{A+D}{2} \leq 1. \tag{2.21}$$

If this condition is not met, the cavity is defined as unstable. A stable laser cavity is characterized by its ability to reproduce the same beam properties, including wavefront and beam size, after each round trip. This implies that the wavefront should have the same radius of curvature as the cavity end mirrors at their respective positions. However, there is no necessity for the cavity beam's wavefront to match the folding mirror's curvature.

The q parameter, crucial for ray tracing calculations within the cavity, is defined as:

$$\frac{1}{q(z)} = \frac{1}{R(z)} + i\frac{\lambda}{\pi w_0}, \tag{2.22}$$

where $R(z)$ is the radius of curvature of the wavefront at position z, and λ is the laser wavelength [101].

The final q parameter, q_f, after traversing through the optical system is given by:

$$q_\mathrm{f} = \frac{Aq_\mathrm{i} + B}{Cq_\mathrm{i} + D}, \tag{2.23}$$

where q_{i} is the initial q parameter before the system, and A, B, C, and D are elements of the ABCD matrix. For a stable cavity, where q_{i} equals q_{f} after one complete round trip, the beam size $w(z)$ within the cavity can be expressed as

$$w(z) = \sqrt{\frac{-\lambda B}{\pi\sqrt{1-(\frac{A+D}{2})^2}}}. \tag{2.24}$$

This expression illustrating that the beam size is dependent on the cavity design, specific positions within the cavity, and the wavelength of the laser.

In the design of a V-cavity configuration, two plane end mirrors and a concave folding mirror with a ROC of 500 mm are employed. The stability of the laser cavity was systematically evaluated by varying the lengths of both cavity arms from 0 to 1 meter. The arm containing the gain medium is referred to as the gain chip arm, while the arm intended for the placement of the LBO crystal is designated as the LBO arm, as illustrated in Fig. 2.7. The stability regions within this configuration are indicated by the colored areas in Fig. 2.7, where the condition $-1 \leq \frac{A+D}{2} \leq 1$ is satisfied, denoting a stable cavity. Conversely, the white areas represent regions where the cavity is unstable. With the gain chip arm set to a length of 520 mm and the LBO arm to 345 mm, and an opening angle of 15° between the two arms (corresponding to a 7.5° incidence angle at the folding mirror), the beam size within the laser cavity was calculated. These beam size calculations are depicted in Fig. 2.8, with negligible deviation between tangential and sagittal planes. This intracavity beam size analysis was run via a custom MATLAB script based on transfer matrix calculations. This script not only facilitated the design of this specific cavity but was also utilized in the design process for all laser cavities discussed throughout this dissertation.

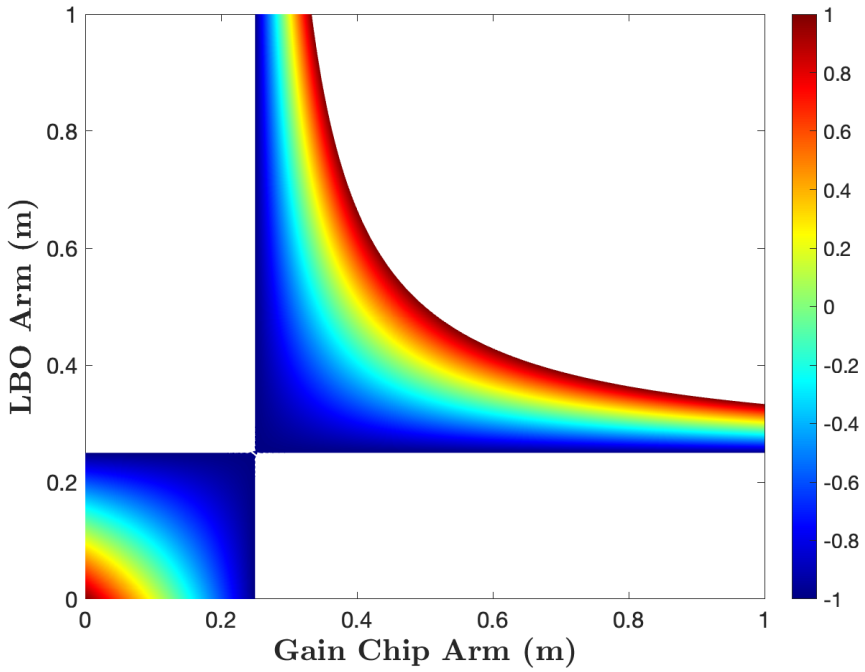

Fig. 2.7 The cavity stabilization calculation for a V-cavity configuration with two plane end mirrors and a ROC = 500 mm folding mirror.

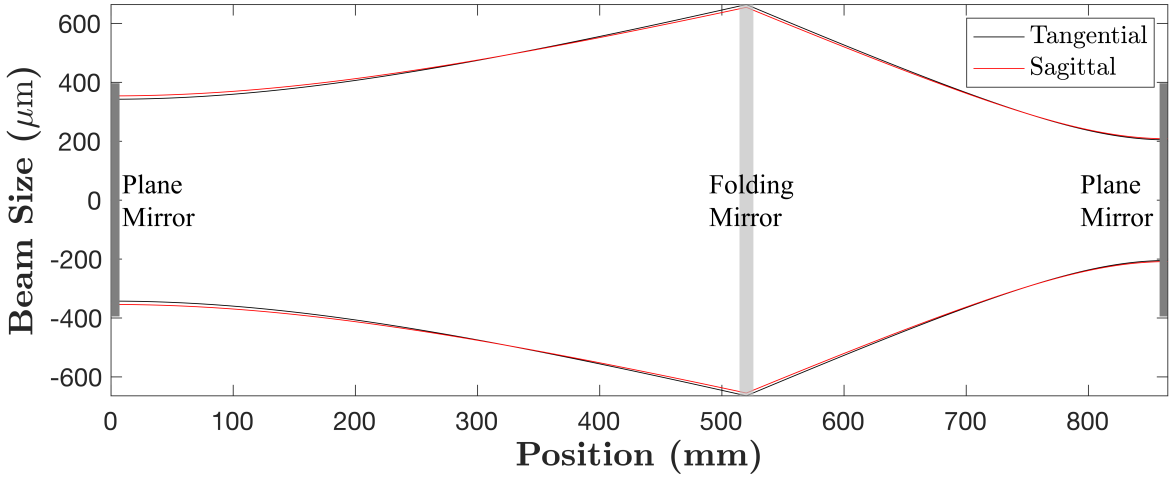

Fig. 2.8 The beam size calculation for a V-cavity configuration on tangential (blue) and sagittal (red) planes with two plane end mirrors and an ROC = 500 mm folding mirror, the angle between two cavity arms is 15°.

2.3 Laser Linewidth Reduction

The actual laser output wavelength might deviate from the ideal 1178 nm for the the designed MECSEL system, necessitating the use of intracavity optics like crystalline quartz BRF for precise wavelength tuning [117]. BRFs are typically positioned at Brewster's angle within the cavity to minimize intracavity loss. Figure 2.9 illustrates the reflectance of a single crystalline quartz BRF at 1178 nm across various incidence angles. The graph differentiates the reflectance for transverse-electric (TE) polarization, shown in red, and transverse-magnetic (TM) polarization, shown in blue, with a refractive index of quartz noted as $n(1178\,\mathrm{nm}) = 1.5326$ [118]. From the data in Fig. 2.9, it is evident that the reflectance for the TM beam approaches zero at an angle of 56.88°, identified as Brewster's angle for 1178 nm. Positioning the BRF at this angle within the laser cavity ensures that the output is predominantly P-polarized. This polarization preference occurs because s-polarized light experiences higher intracavity loss with non-zero reflectance from BRF at Brewster's angle.

The wavelength tuning capability of a BRF is primarily facilitated through a wavelength-dependent phase retardation, which can be mathematically described by the following equation [119]

$$\delta = \frac{\pi(n_\mathrm{o} - n_\mathrm{e})d\sin^2\zeta}{\lambda\sin\theta}, \tag{2.25}$$

where $(n_\mathrm{o} - n_\mathrm{e})$ represents the difference between the ordinary (n_o) and extraordinary (n_e) refractive indices of the BRF, d is the thickness of the BRF plate, θ is the incidence angle, ζ is the polar angle, and λ is the wavelength of the incident light. At Brewster's angle the retardation δ amounts to an integer multiple of the wavelength, leading to a condition where the polarization state is TM at both interfaces of the BRF and the transmission is maximized. Conversely, wavelengths that do not fulfill this condition undergo polarization changes between

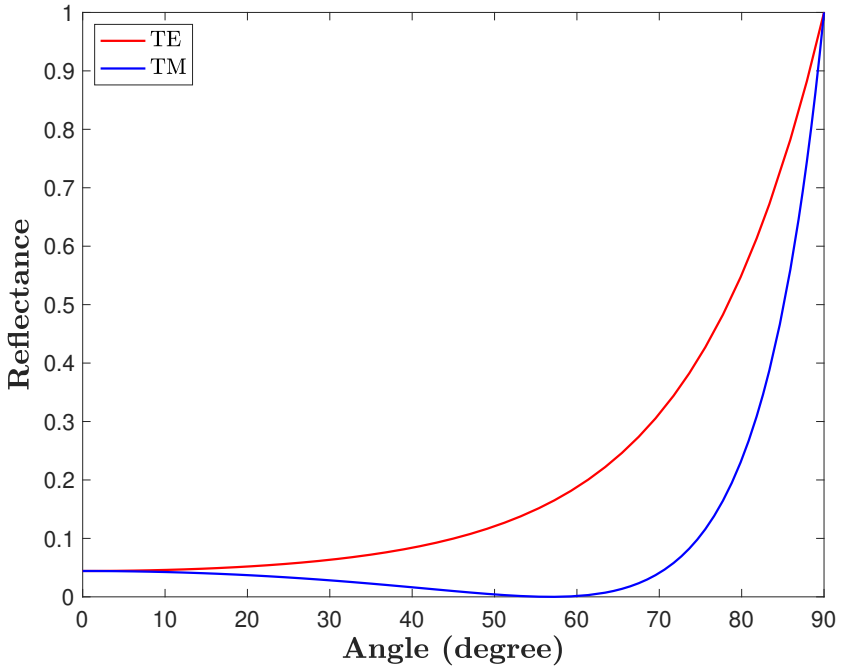

Fig. 2.9 Reflectance of a single crystalline quartz BRF at 1178 nm as a function of incidence angle for TE (red) and TM (blue) polarization.

the two interfaces, incurring additional intracavity losses, and thus are less likely to achieve lasing.

The central wavelength at which the BRF operates most effectively can be expressed as [117]

$$\lambda = \frac{(n_e - n_o) d \sin^2 \zeta}{m \sin \theta}, \tag{2.26}$$

where m is an integer that denotes the order of the mode and the free spectral range (FSR) of the BRF, which defines the wavelength spacing between successive resonant peaks of the filter, as described by [117]

$$\Delta\lambda = \frac{\lambda^2 \sin \theta}{(n_e - n_o) d \sin^2 \zeta}. \tag{2.27}$$

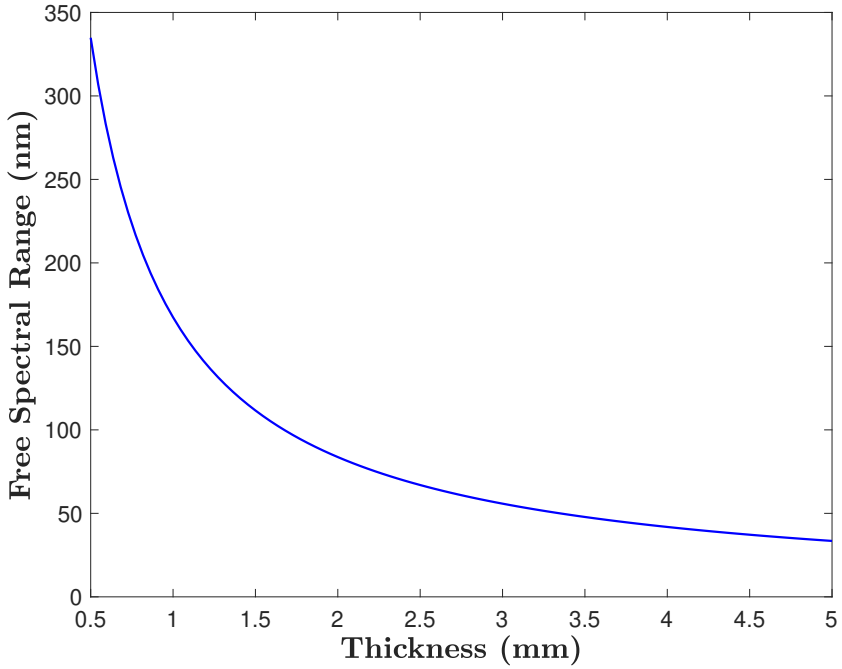

Fig. 2.10 Free spectral range of a quartz BRF versus plate thickness at Brewster's angle for 1178 nm incident light.

The FSR of a BRF is influenced by the filter's thickness, as well as the difference in the ordinary and extraordinary refractive indices ($n_e - n_o$) of the material used. For incident light at 1178 nm, this difference is 0.0087 for a quartz BRF [118]. The FSR of a quartz BRF at Brewster's angle for 1178 nm light varies as a function of the BRF plate's thickness as shown in Fig. 2.10. For example, a 2 mm thick quartz BRF results in an FSR of 83.7 nm. As the thickness increases to 4 mm, the FSR decreases to 41.9 nm. This FSR limits the BRF's maximum wavelength tuning ability. However, a smaller FSR is advantageous for finer wavelength adjustment, making it possible to achieve more precise tuning within a narrower range. This is particularly beneficial in applications requiring high spectral resolution or when targeting specific narrowband emissions as in LGS applications. Additionally, thicker BRFs are generally easier to manufacture and can offer greater robustness and reduced susceptibility to manufacturing imperfections. Therefore,

selecting the appropriate thickness of the BRF is balanced between the desired wavelength tuning range and the quality and precision of the laser output.

In a MECSEL setup, the laser typically operates in multi-longitudinal mode under free-running conditions, particularly when aiming for high output power levels [113, 112]. However, for applications requiring higher spectral purity, such as LGS operations, it is essential to narrow the linewidth to achieve a single longitudinal mode with a linewidth of less than 10 MHz (Full Width at Half Maximum, FWHM). Achieving single longitudinal mode operation typically requires more than just one BRF. To refine the mode selectivity and reduce the number of supported modes, additional intracavity optical elements are necessary.

One effective element for enhancing mode selectivity is the intracavity Fabry–Pérot (FP) etalon. The FP etalon works by exploiting the interference effect within its structure. This interference effect depends on the phase change that occurs within the etalon, which is wavelength-dependent. The FP etalon's thickness and refractive index are key factors in determining the selectivity of the modes it supports. Additionally, an extra BRF can be incorporated to form the Lyot-Ohman filter [120] to further narrow the laser output linewidth. Precise control over the laser's operating temperature and pump power is also essential. These factors help to stabilize the laser's operating conditions, reduce mode hopping, and enhance overall mode stability.

For this dissertation project, an FP etalon was employed alongside the wavelength-tuning BRF. A schematic diagram of FP etalon is shown in Fig. 2.11, two surfaces of the etalon have surface reflectivities r_1, r_2 and round trip phase shift of 2ϕ. For incident electric field E_{inc}, the transmitted signal after both surfaces can be written as

$$E_{\text{trans}} = (1-r_2)\cdot(1-r_1)\cdot e^{-i\phi}\cdot E_{\text{inc}} + (1-r_2)\cdot r_1\cdot r_2\cdot(1-r_1)\cdot e^{-i3\phi}\cdot E_{\text{inc}} + \cdots, \quad (2.28)$$

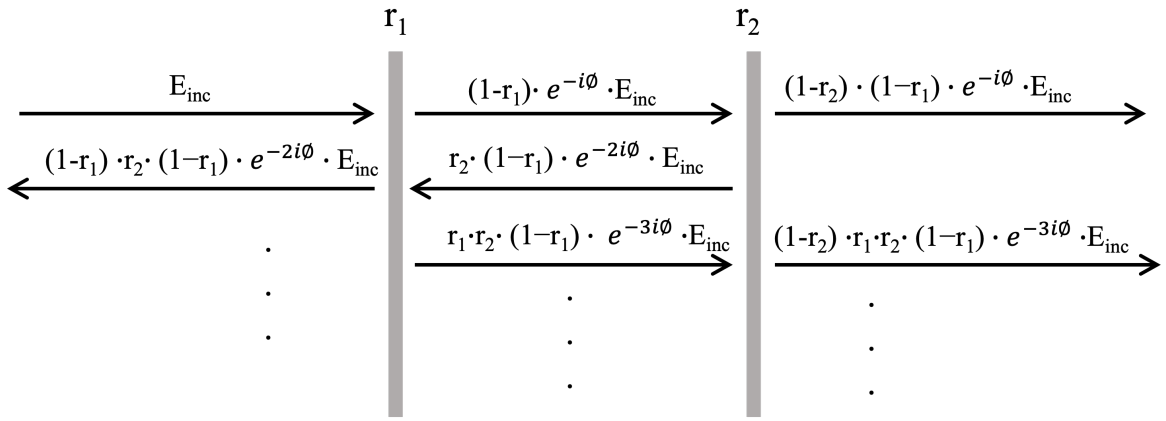

Fig. 2.11 Illustration of transmission and reflection of an etalon with surface reflectivities r_1, r_2 and round trip phase shift of 2ϕ with normal incidence light E_{inc}.

and round trip phase change 2ϕ is

$$2\phi = \frac{4\pi nl cos\theta}{\lambda}, \tag{2.29}$$

where n is the refractive index of the etalon, θ is the incident angle, l is the etalon thickness, and λ is the light wavelength. Using geometric series summation formula, Eq. 2.28 can be written as

$$E_{\text{trans}} = \frac{(1-r_1)(1-r_2)e^{-i\phi}}{1-r_1 r_2 e^{-2i\phi}} E_{\text{inc}}. \tag{2.30}$$

Using Euler's formula, the transmission of the incident light is

$$T = \frac{E_{\text{trans}} E^*_{\text{trans}}}{E_{\text{inc}} E^*_{\text{inc}}} = \frac{(1-r_1)^2(1-r_2)^2}{1-2r_1 r_2 cos(2\phi)+r_1^2 r_2^2}, \tag{2.31}$$

for a lossless etalon with identical surfaces, this equation can be simplified into

$$T = \frac{(1-r)^4}{1-2r^2 cos(2\phi)+r^4}, \tag{2.32}$$

and when $cos(2\phi) = 1$, the transmission is unity. As the phase shift ϕ is wavelength related, the FP etalon can be used to select the laser output wavelength.

Specifically, a 100 µm thick Yttrium Aluminum Garnet (YAG) etalon was used. This etalon has a surface reflection of 8.35% between YAG (n=1.8126 at 1178 nm [121]) and air, Fig. 2.12 demonstrates how transmission varied as a function of wavelength near 1178 nm under normal incidence (just for demonstration not the experimental case). The FSR of this etalon is 3.77 nm (FSR$\approx \frac{\lambda^2}{2lcos(\theta)}$), allowing for 100% transmission peaks. These peaks can be precisely aligned to 1178 nm either by adjusting the incidence angle or by changing the temperature of the etalon, enabling fine-tuning of the laser output to achieve the desired wavelength with high efficiency.

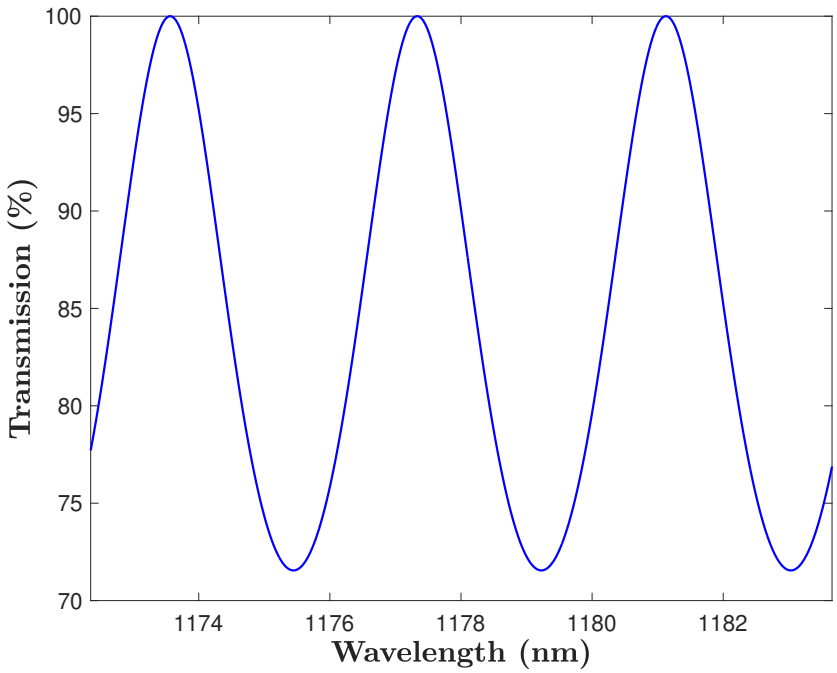

Fig. 2.12 Transmission versus wavelength at room temperature for a 100 µm thick YAG etalon at normal incidence [122].

2.4 Laser Frequency Conversion

Achieving 589 nm emission from the fundamental 1178 nm wavelength of the MECSEL involves nonlinear conversion through SHG, which relies on the conversion crystal's nonlinear susceptibility. Nonlinear optical effect arises from the interaction between matter and an electromagnetic field. At low intensities, the electrons are displaced slightly from their equilibrium positions, and this small displacement results in a linear restoring force, hence the linear relationship between induced polarization P and the applied electric field E, expressed as [123]

$$P = \varepsilon_0 \chi^{(1)} E, \tag{2.33}$$

where ε_0 represents the permittivity of free space and $\chi^{(1)}$ is the linear susceptibility describing the material's response. In this regime, the incident light field induces oscillations in the electric dipoles of the medium at the same frequency as the field, resulting in the emission of electric field at this frequency.

However, when the intensity of the incident field is sufficiently high, the displacement of electrons is large enough to cause nonlinear restoring forces. As a result, the induced polarization includes nonlinear terms, represented as [123]

$$P = \varepsilon_0(\chi^{(1)} E + \chi^{(2)} E^2 + \chi^{(3)} E^3 + \ldots), \tag{2.34}$$

where $\chi^{(2)}$ and $\chi^{(3)}$ are the second-order and third-order nonlinear susceptibilities, respectively. These higher-order terms lead to the generation of new frequencies through processes such as second-harmonic generation, sum-frequency generation, and other nonlinear optical phenomena, which result from the interaction between the medium and the electric field.

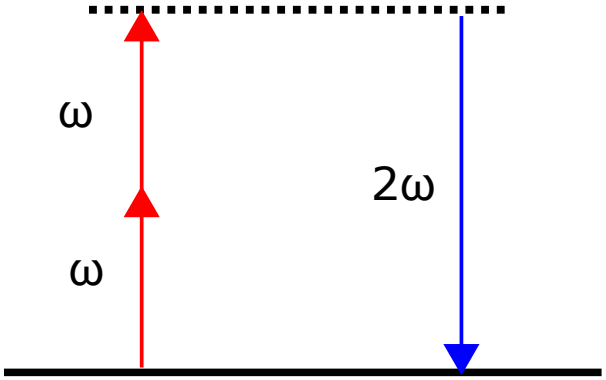

Fig. 2.13 A simple conceptual overview of the SHG process [124].

In the SHG nonlinear process, two photons with frequency ω combine to form a single photon with frequency 2ω. The solid line in Fig. 2.13 is ground state and the dashed line represents a virtual state, where no energy is stored. The conservation of energy and momentum for this process can be expressed as follows:

$$\hbar\omega + \hbar\omega = \hbar 2\omega, \tag{2.35}$$

and

$$\hbar k_\omega + \hbar k_\omega = \hbar k_{2\omega}. \tag{2.36}$$

Given that $k_\omega = n_\omega \frac{\omega}{c}$ and $k_{2\omega} = n_{2\omega}\frac{2\omega}{c}$, where n_ω and $n_{2\omega}$ are the refractive indices for the fundamental and SHG wavelengths, respectively. The phase-matching condition required for efficient SHG is $n_\omega = n_{2\omega}$. This ensures that the wave vectors are appropriately aligned to facilitate the nonlinear interaction.

The nonlinear conversion efficiency of SHG can be described by the equation [123]:

$$\eta_{\mathrm{SHG}} = \frac{2\omega^2 d_{eff}^2 l^2}{n_{2\omega} n_\omega^2 c^3 \varepsilon_0} \mathrm{sinc}^2\left(\frac{1}{2}\Delta k l\right) I^2(\omega), \tag{2.37}$$

where ω represents the frequency of the fundamental light, d_{eff} is the effective coupling coefficient, $\Delta k = \frac{2\omega}{c}(n_{2\omega} - n_{\omega})$ is the phase mismatch between the two wavelengths, l is the length of the nonlinear crystal, and $I(\omega)$ is the intensity of the fundamental wavelength.

Effective phase matching within the crystal is important for optimizing SHG efficiency and can be achieved by adjusting the crystal's temperature or its orientation, ensuring that the optical axis is aligned with the laser beam. Additionally, reducing the laser beam size within the nonlinear crystal is essential to maximize the intensity at the fundamental frequency, which is important for achieving high SHG conversion efficiency according to Eq. 2.37. In a high-Finesse laser cavity, the intra-cavity power can be orders of magnitude higher than the maximum output power, leading to significantly enhanced nonlinear conversion efficiency with increased fundamental wavelength intensity with intra-cavity frequency doubling. Using a longer nonlinear crystal can be advantageous for optimal results as it can also increase the nonlinear conversion efficiency.

There are two primary methods of achieving phase matching in nonlinear optics. The first is critical phase matching, which involves orienting the nonlinear crystal at a critical angle where the refractive indices for the fundamental and SHG wavelengths are equal. However, this method can lead to issues such as beam walk-off, where the Poynting vector (direction of energy propagation) does not align with the wave vector, especially in longer crystals [123]. The second method, non-critical phase matching (NCPM), involves controlling the crystal temperature to equalize the refractive indices at the fundamental and SHG wavelengths. NCPM avoids the beam walk-off problem and is particularly suitable for LGS applications, where a LBO crystal is used.

In these experiments that will be discussed in this dissertation, a plane end mirror was used to produce a plane wavefront, and the waist of the laser cavity mode that yields the highest

intensity. Thus, the LBO crystal was placed in this position, adjacent to this planar cavity end mirror to maximize the nonlinear conversion efficiency.

2.5 Conclusion

In this chapter, the design and operational principles of the MECSEL gain structure were explored. The design for this dissertation project employs InGaAs quantum wells with GaAs barriers, arranged in a resonant periodic gain structure, complemented by GaAsP strain compensation layers and InGaP window layers. Calculations demonstrated that an array of eleven quantum wells could potentially yield an output power of 26.4 W in free-running operation, satisfying the output power requirements outlined in Chapter 1. Next, the resonator design was analyzed through ray tracing matrix analysis, employing a V-cavity configuration that incorporates linewidth narrowing elements in the gain chip arm and second harmonic generation along with a PZT actuator for frequency stabilization in the LBO arm. Intracavity beam size simulations were performed using MATLAB, providing a detailed visualization of the expected beam size. Furthermore, strategies for linewidth narrowing, particularly the use of a quartz birefringent filter and a YAG Fabry-Pérot etalon, were thoroughly reviewed. Additionally, non-critical phase matching intracavity frequency doubling using an LBO crystal was discussed. This nonlinear crystal will be employed for SHG to produce the targeted 589 nm output from 1178 nm fundamental wavelength.

Building upon the design principles covered, an eleven quantum well MECSEL was constructed with 808 nm barrier pumping, and the detailed experimental setup and the results obtained will be discussed in the next chapter.

Chapter 3

Barrier Pumped MECSEL

In this chapter, building upon the MECSEL design principles introduced in Chapter 2 and the LGS design criteria mentioned in Chapter 1, an eleven quantum well MECSEL structure with a linear laser resonator was developed. Barrier pumping was utilized as a straightforward implementation strategy for building a semiconductor-based LGS. The investigation commenced with a study of the thermal rollover effect. Subsequently, a record free-running output power and the study of wavelength tuning to 1178 nm will be discussed. The experimental results presented in this chapter were originally documented in [113], and this chapter will provide a more detailed reevaluation.

3.1 Eleven Quantum Well Gain Chip

Aiming to achieve high output power at 1178 nm, the MECSEL active region comprises eleven quantum wells of $In_{0.38}Ga_{0.62}As$, each 6 nm thick, arranged in a RPG structure. As discussed in Chapter 2, these quantum wells are sandwiched between GaAs barriers, with strain-compensating $GaAs_{0.94}P_{0.06}$ layers integrated to balance strain energy between the InGaAs and

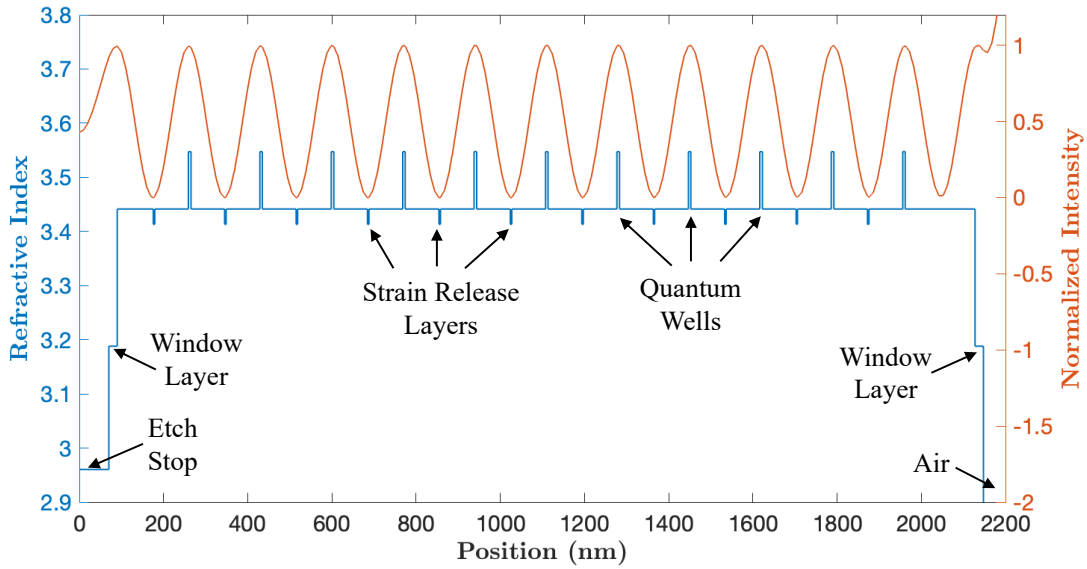

Fig. 3.1 An eleven quantum well MECSEL sample design. The blue line is for refractive index and the orange line is for normalized intracavity intensity.

GaAs materials. Additionally, 20 nm thick $In_{0.49}Ga_{0.51}P$ window layers are placed on both sides of the active region. A 250 nm thick $Al_{0.92}Ga_{0.08}As$ etch-stop layer was incorporated between the GaAs substrate and the membrane, tailored for selective wet etching to facilitate substrate and etch stop removal. The refractive index profile and normalized field of an eleven quantum well MECSEL gain structure is similar to the design in [1] and [65], as extracted from the design software Vertical, are depicted in Fig. 3.1. The gain structure was fabricated using MOCVD by 21 SEMICONDUCTORS. The detailed structure and progression of the sample preparation are illustrated in Fig. 3.2. The initial MOCVD-grown eleven quantum well MECSEL structure on a GaAs substrate is illustrated in Fig. 3.2 (a).

Post-fabrication, the sample was encapsulated between two 500 µm thick double-side polished single-crystalline 10 mm×mm 4H-SiC heat spreaders through a plasma-activated, low-temperature direct bonding technique [105] as detailed in Chapter 2. This encapsulation was completed with the removal of the substrate [105], carried out by our collaborators at

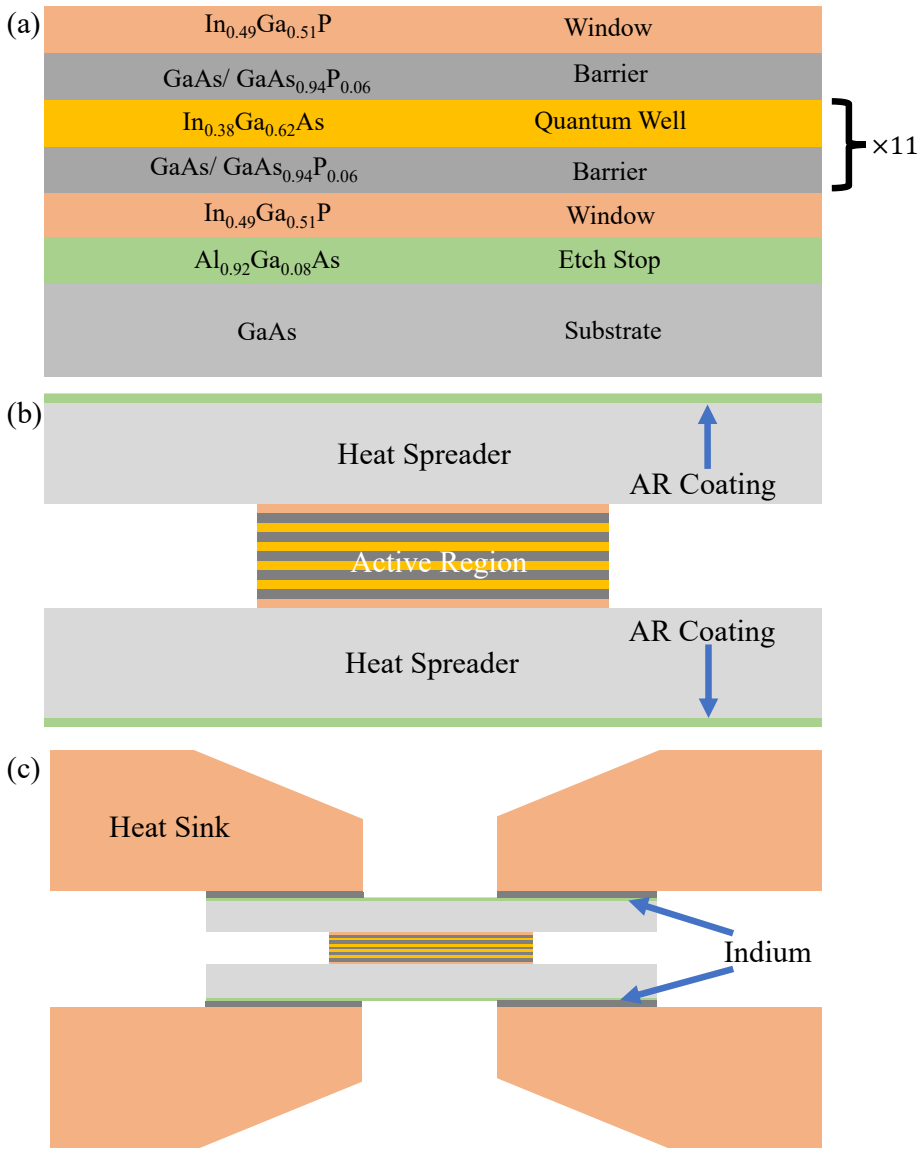

Fig. 3.2 Schematic of (a) MOCVD-grown eleven quantum well MECSEL gain structure on GaAs growth substrate. (b) Sandwich-bonded sample after substrate removal between two AR-coated SiC heat spreaders, and (c) sample mounted between two copper heat sink plates with indium in between.

THORLABS CRYSTALLINE SOLUTIONS. The gain heat spreader sandwich with AR coating is shown in Fig. 3.2 (b).

For testing, the completed gain chip was clamped between two water-cooled copper heat sinks, each featuring a central aperture with a diameter of 2.2 mm to permit the transmission of the laser beam. To enhance thermal contact between the sample and the copper mounts, a 50 µm thick layer of indium foil was interposed, which compresses upon assembly to form a thinner layer. The mounted gain chip is displayed in Fig. 3.2 (c).

3.2 Laser Resonator

The experimental setup for optically pumping the mounted MECSEL sample was arranged to ensure optimal alignment and focus of the pump beam. Utilizing a diode laser emitting at 808 nm for barrier pumping, the pump light was guided via a 400 µm diameter core fiber and then focus onto the sample with two identical plano-convex lenses, each with a 50 mm focal length, were positioned as depicted in Fig. 3.3 (a).

The pump beam (illustrated in green) at a 25-degree angle to the surface of the sample. Due to the oblique angle of incidence, the focused spot of the pump beam was slightly elliptical, being 10% larger in one axis than the other (radius of 200 µm and 220 µm). Ideally, this ellipticity could be corrected using cylindrical lenses to produce a more uniform pump spot on the sample; however, this adjustment was not implemented in the current setup due to the limited availability of appropriate optics in the laboratory. To explore the potential for wavelength tuning, a 2 mm thick quartz BRF was later incorporated into the cavity, as depicted in Fig. 3.3 (a). This addition aimed to examine both the tunable wavelength range and the maximum achievable output power at 1178 nm.

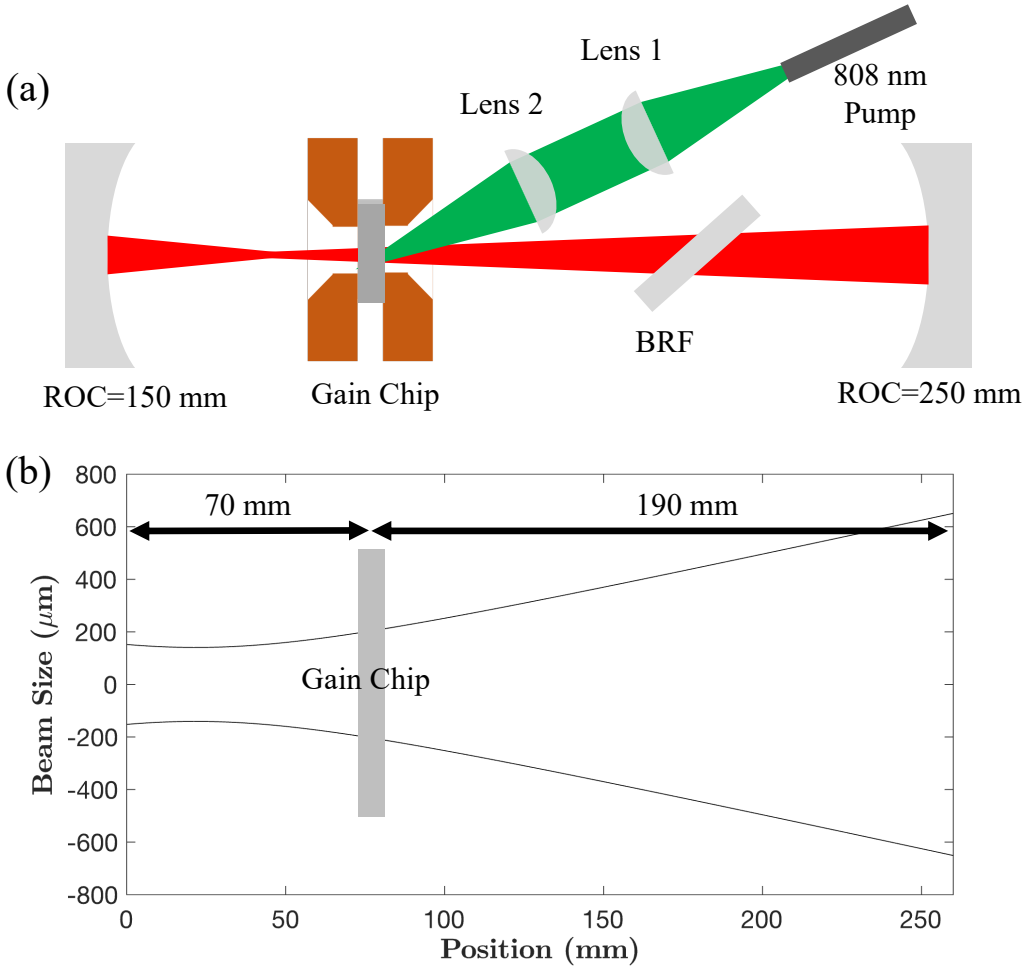

Fig. 3.3 (a) Schematic of a linear cavity for eleven quantum well MECSEL gain chip. (b) Intracavity mode size calculation across the linear cavity for the eleven quantum well MECSEL gain chip.

The calculated intracavity laser beam size within the resonator is illustrated in Fig. 3.3 (b), providing a visual representation of the beam propagation and interactions within the cavity. In the experimental configuration, a linear laser cavity was established using two mirrors with radii of curvature (ROC) of 150 mm and 250 mm, respectively. The total cavity length was set at 260 mm to ensure optimal resonance conditions, aligning the cavity mode size with the pump beam for maximum efficiency on the MECSEL gain chip. The MECSEL gain chip itself was positioned 70 mm from the ROC=150 mm mirror. At this point, the cavity beam

was calculated to have a radius of 190 µm, closely matching the pump beam radius of 200 µm, thereby optimizing the overlap between the pump and the lasing mode volumes.

3.3 Experimental Results

3.3.1 Thermal Rollover

Thermal rollover is a well-known phenomenon in semiconductor lasers where the output power begins to decrease after reaching a certain temperature as the pump power continues to increase. This effect is primarily attributed to the excessive heat generated within the semiconductor active region, which adversely affects the laser's performance [94]. As the temperature rises, several processes occur, including increased carrier leakage and internal optical absorption loss [125], reduction in bandgap energy [92], and the impact of thermal lensing [114]. These factors collectively degrade the efficiency and output power of the laser, necessitating effective thermal management strategies to mitigate these effects.

Decreasing the chiller temperature is an effective method for delaying the onset of thermal rollover, as it allows the MECSEL gain chip to avoid reaching the limiting rollover temperature. In this study, utilizing a gain chip and laser resonator designed earlier in this chapter with a 3% overall output coupling efficiency, the impact of chiller temperature on output power was investigated, as shown in Fig. 3.4 with 808 nm barrier pumping. The results clearly demonstrate that after the thermal rollover point is reached, further increases in pump power do not enhance laser output. Lowering the chiller temperature setting can delay the thermal rollover point, resulting in higher output power. For example, the maximum output power from the same sample increased nearly fourfold when the chiller temperature was reduced from 18 °C to 4 °C. Operating beyond the thermal rollover point can potentially damage the sample. Consequently,

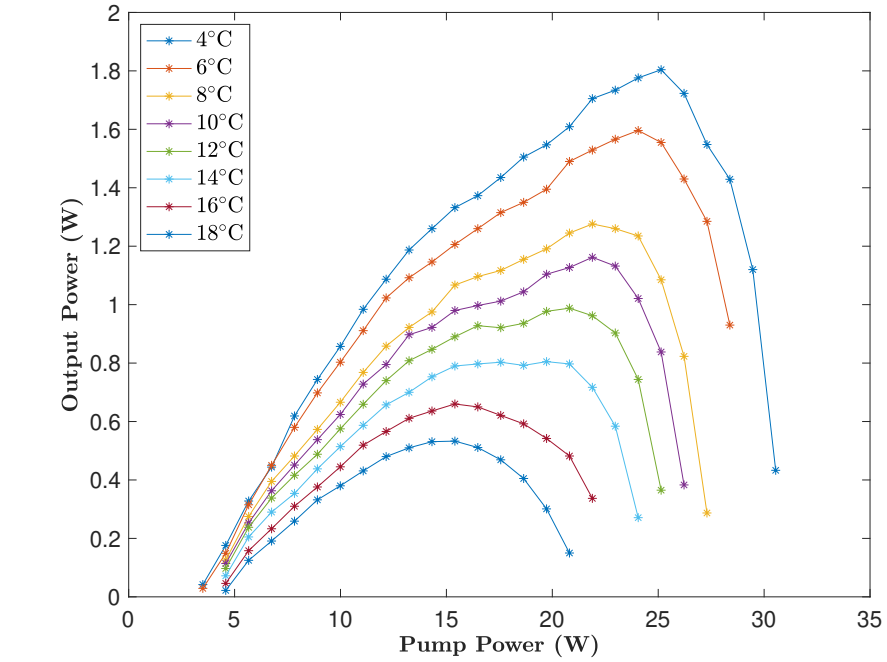

Fig. 3.4 Output power versus pump power with various of chiller temperature settings.

some subsequent experiments discussed later in this dissertation were terminated upon signs of thermal rollover. The experiments were halted to prevent further increases in pump power to protect the sample, thus the output power at these points is described as being thermally limited.

3.3.2 Free Running Operation

In the experiments, the output power of the MECSEL was studied also with different chiller temperature settings with a total 2% output coupling. The experimental results were plotted in Fig. 3.5 (a), showing that with the decrease of the chiller temperature, both the slope efficiency, which is defined as the slope of laser output power versus pump power (minus threshold), and the thermal rollover point of the output power improved. Specifically, the slope efficiencies, extracted using a linear fit from experimental data, improved from 25.4% at 10 °C to 27.7% at

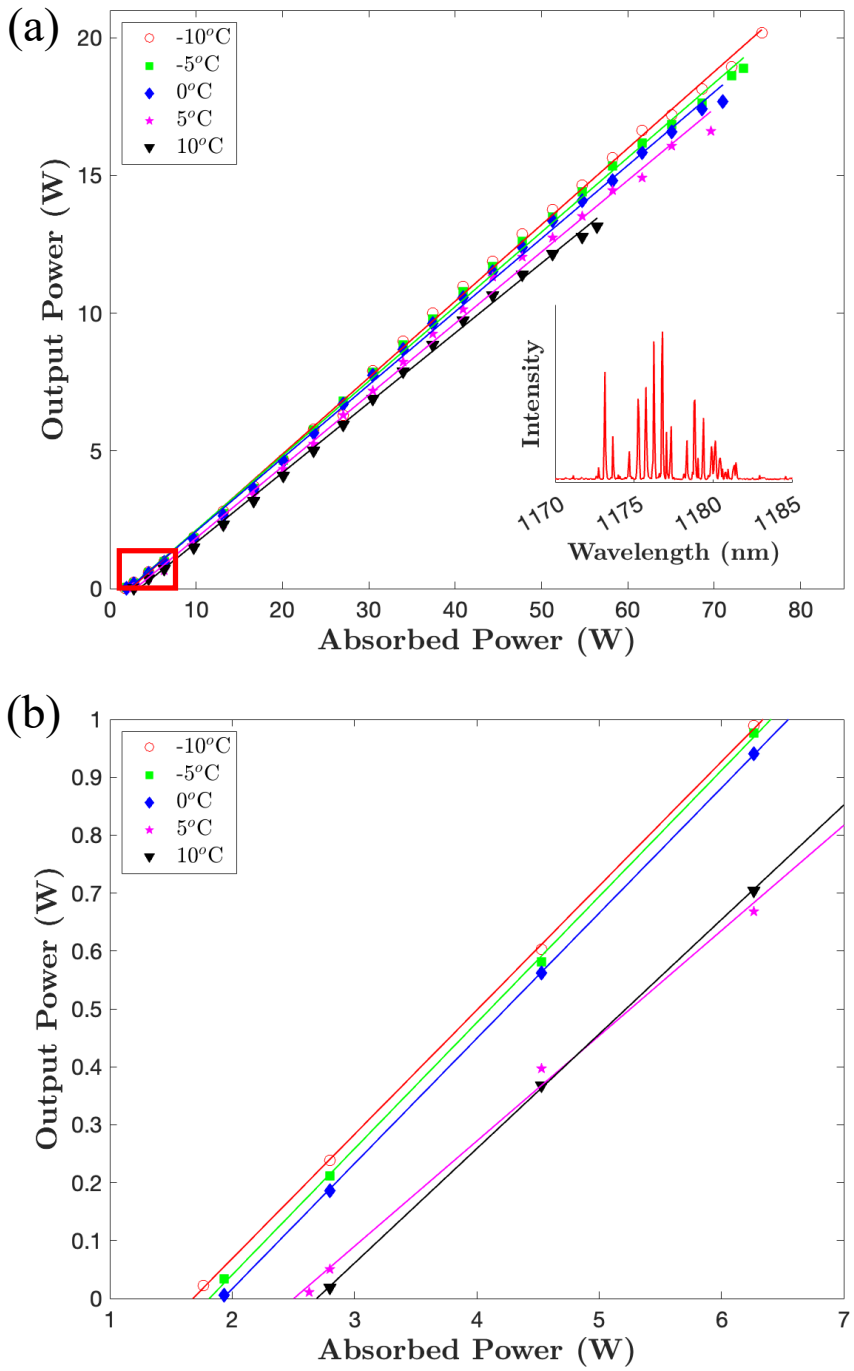

Fig. 3.5 (a) Output power as a function of absorbed pump power with different chiller temperatures, the inset illustrates the spectrum measured at $-10\,^{\circ}\mathrm{C}$ with 40 W absorbed pump power. (b) Laser threshold with different chiller temperatures.

$-10\,^{\circ}$C, and the thermal limitation point increased from 13.2 W at 10 °C to 20.2 W at -10 °C. These results demonstrated that further reductions in chiller temperature could potentially enhance the performance of the MECSEL by shifting the thermal limitation point to even higher output powers as expected. The lowest temperature achievable for the chiller used in these experiments was -10 °C, which is the practical limit of the current experimental setup. Also cooling at -10 °C presents significant challenges for practical applications like LGS. Condensation is a problem and requires nitrogen purging for cooling temperature below 10 °C, cooling temperature at 15 °C or even room temperature is more favorable. The inset of Fig. 3.5 (a) presents a spectrum measured at -10 °C with 40 W of absorbed 808 nm barrier pump power. This spectrum centered around 1178 nm with a FWHM of 6 nm demonstrates the multi-longitudinal mode operation without BRF and etalon for linewidth narrowing, and was captured using an optical spectrum analyzer (OSA). This experiment set a record of 20.2 W output power for a MECSEL at 1178 nm and across all wavelengths for MECSELs, as documented in the literature [113].

The laser threshold across different chiller temperatures was detailed in Fig. 3.5 (b). The data indicates that while the threshold power remains relatively stable, there is a noticeable increase as the chiller temperature rises. This can be explained by improved gain of quantum wells and reduced carrier leakage at lower temperature. Due to the slow start in VECSELs and MECSELs as also reported by other researchers [107], the slope efficiency near the threshold is lower than the overall slope efficiency. Specifically, the slope efficiencies were measured at 19.8% at 10 °C and 21.5% at -10 °C. This decrease in slope efficiency was due to the laser threshold not being achieved across the entire lasing area at low pump power levels.

3.3.3 Linewidth Narrowed Output

Single longitudinal mode operate at the wavelength of sodium D_{2a} transition is necessary for LGS applications. A 2 mm thick quartz BRF mounted on a rotation mount was placed within the laser cavity at Brewster's angle to facilitate wavelength tuning and linewidth narrowing. The resulting output spectra were measured at an absorbed pump power of 46 W with a chiller temperature of 5 °C, by carefully adjusting the orientation of the BRF. The data, depicted in Fig. 3.6, revealed a maximum spectral tuning range of 75 nm, extending from 1119 nm to 1194 nm.

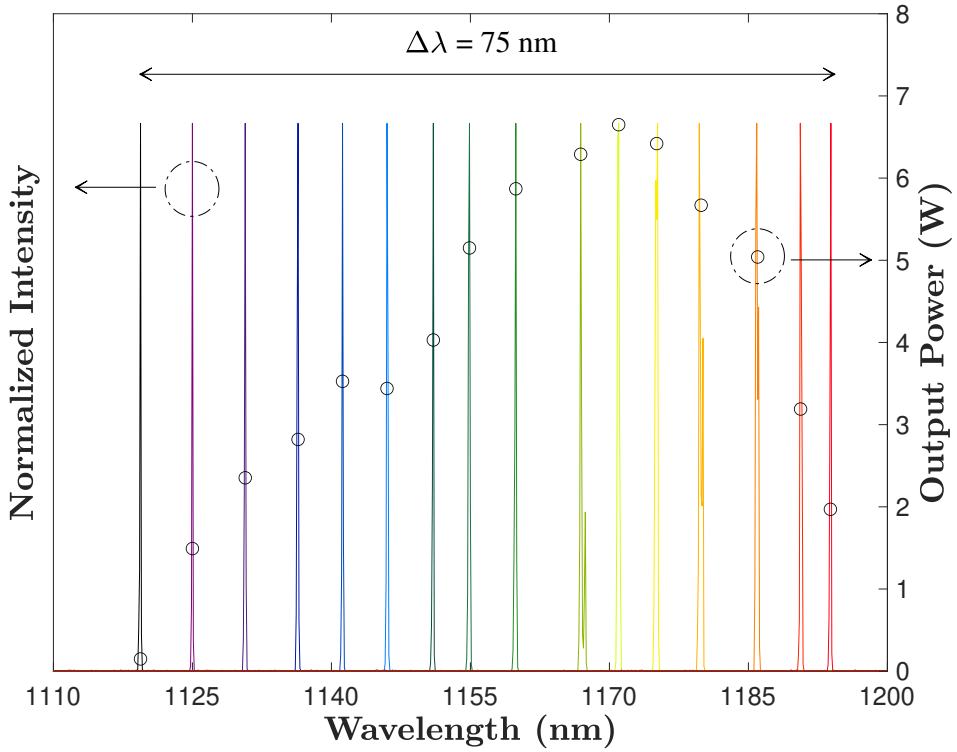

Fig. 3.6 Normalized spectra for eleven quantum well MECSEL gain chip by tuning a 2 mm thick quartz BRF with 46 W of absorbed pump power at 5 °C of chiller temperature.

The architecture of the MECSEL, unlike VECSELs with a DBR adjacent to the multi-quantum well structure, affords it certain advantages. In VECSELs, the active region's adjacency to one cavity node, stemming from the DBR, limits the mode selectivity. The MECSEL configuration, free from such spatial constraints relative to global cavity nodes, enhances the integrated gain factor—reported to be twice that of standard VECSELs—allowing for expanded wavelength tunability [4]. This attribute was underscored by the experimental tuning range of 75 nm, closely approaching the record 80 nm tuning range at 1160 nm for similar devices [126]. The FSR of 83.7 nm for a 2 mm thick quartz BRF at 1178 nm represents a theoretical upper limit to the tuning range, as illustrated in Fig. 2.10. Measurements of output power across different wavelengths under identical experimental conditions revealed peak performance at 1171 nm, attributable to the design optimization of the MECSEL for peak performance near 1178 nm at the thermal rollover point.

To tune the fundamental wavelength for frequency doubling precisely to 1178.32 nm, targeting the sodium D_{2a} transition to achieve 589.16 nm, angle tuning of the BRF was undertaken to achieve an output centered at 1178.32 nm with a linewidth (FWHM) of 0.3 nm. This spectrum is illustrated as the bottom-right inset of Fig. 3.7, as confirmed by an OSA with a resolution of 0.06 nm. To further narrow down the linewidth, integration of additional intracavity element such as a FP etalon was deemed necessary. The chiller temperature of -10 °C was used to evaluate the maximum output power achievable before reaching the thermal rollover, detailed in Fig. 3.7. The slope efficiency is 25.4%, reduced slightly from the free running efficiency of 27.7% due to increased intracavity loss, and peak output power of 12.8 W was achieved with an absorbed pump power of 67 W. The experiments also included a transverse mode assessment with a commercial beam profiler and a laser spectrum analysis with an OSA, both conducted at 65 W of absorbed pump power. The beam profiler captured a TEM_{00} Gaussian mode.

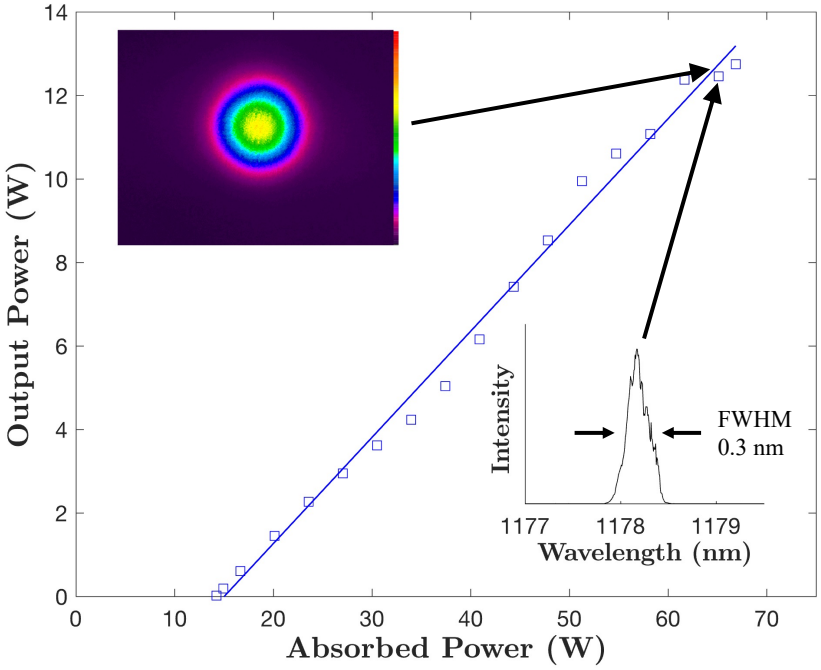

Fig. 3.7 Output power at 1178 nm versus absorbed pump power. The beam profile (top-left) and spectrum (bottom-right) were recorded at 65 W of absorbed pump power.

This BRF-involved experiment underscored the capability of MECSELs for broad wavelength tunability and highlighted their potential for further optimization. Despite achieving significant milestones, the results indicated several areas for potential improvements, such as in thermal management to enable higher output powers, integrating more intracavity elements for finer linewidth control, and implementing the frequency doubling process to achieve the targeted 589 nm output for practical LGS applications. Linewidth narrowing and frequency doubling could be implemented but would lead to insufficient output power with additional internal losses to meet LGS design criteria due to thermal limitations on this MECSEL setup.

3.4 Conclusion

In this chapter, an eleven quantum well MECSEL gain chip was designed and fabricated with the aim of developing a semiconductor LGS. A linear laser cavity was implemented to ensure good overlap between the pump and cavity mode. The thermal rollover effect was discussed prior to presenting the experimental results. The experiment achieved a record output power of 20.2 W at 1178 nm under free-running conditions with a slope efficiency of 27.7%, using a chiller temperature of -10 °C. Additionally, this configuration exhibited a wavelength tuning range of 75 nm. A 12.8 W output power was achieved at 1178 nm with a TEM_{00} beam profile. However, the actual output power achieved fell short of theoretical expectations due to thermal limitations, and further linewidth narrowing and frequency doubling were not implemented.

The subsequent chapter will introduce advanced methodologies to mitigate these thermal issues, focusing on in-well pumping techniques designed to reduce heat generation within the MECSEL gain chip. Additionally, innovative multi-pass pumping structures will be introduced to address challenges associated with low pump absorption often accompanying in-well pumping implementations.

Chapter 4

Low Quantum Defect Implementation

The design of the eleven quantum well MECSEL did not achieve the projected output power of 26.4 W under free-running operation. The inability to reach the higher output power was primarily due to thermal rollover [94]. This chapter addresses the challenges posed from thermal limitation with an in-well pumping method aimed at reducing the heat generated within the MECSEL gain chip. This method benefits from a reduced quantum defect, albeit at the cost of decreased absorption efficiency. Following the discussion of in-well pumping, the chapter will present three types of laser beam circulator designs. These designs are specifically developed to tackle the issue of low absorption resulting from the in-well pumping strategy by recycling the pump power. This chapter aims to provide viable solutions to the challenges faced in achieving high output power in MECSELs while managing the thermal dynamics within the laser structure. The laser beam circulator designs were originally documented in [127] and more detailed reevaluation will be given in this chapter.

4.1 In-Well Pumping

Heat mitigation presents a significant challenge in achieving high output power with a MECSEL. In conventional VECSELs, there are primarily two sources of heat generation within the gain structure. The first source pertains to the radiative efficiency in the active region, as described by Eq. 2.20. Free carriers that undergo Shockley-Read-Hall and Auger recombination processes generate heat. Due to carrier thermalization, the quantum defect q_{d} associated with radiative recombination results in the emission of phonons, which are quantized vibrations of the crystal lattice and also contributes to heat generation. The second source is the absorption of the pump light within the DBR structure, but it does not apply for MECSELs. For the purposes of this dissertation, the study primarily focusing on minimizing the quantum defect as a strategy to address thermal rollover and achieve high output power from the MECSEL platform for LGS applications.

The quantum defect in radiative recombination is a factor influencing the efficiency and thermal characteristics of the device. It can be quantitatively expressed as:

$$q_{\mathrm{d}} = 1 - \frac{\lambda_{\mathrm{pump}}}{\lambda_{\mathrm{laser}}}, \tag{4.1}$$

where λ_{pump} is the wavelength of the pump laser and λ_{laser} is the wavelength of the emitted laser light. This relationship highlights that the closer the pump and laser wavelengths are to each other, the smaller the quantum defect becomes. Therefore, by choosing a pump wavelength that is relatively close to the emission wavelength, the efficiency of the device can be improved while simultaneously reducing the heat generated due to quantum defect. The schematic diagram of barrier pumping for the experimental structure consisting of InGaAs quantum wells and GaAs barriers with InGaP strain compensation layers is depicted in Fig. 4.1 (a). In this configuration, pump photons with wavelength λ_{pump} are absorbed in the barrier, exciting electrons from the

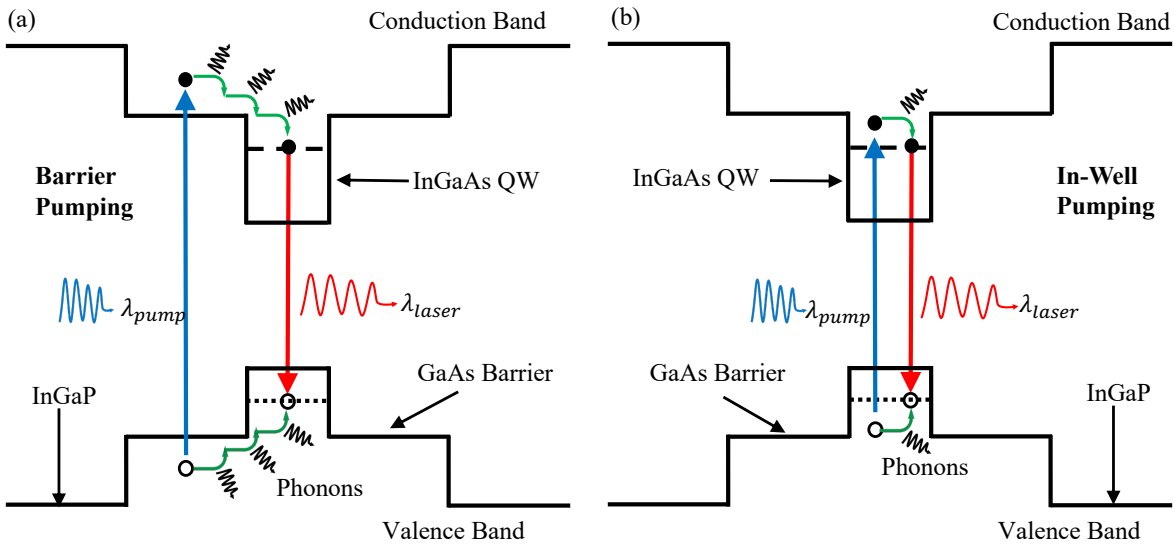

Fig. 4.1 Schematic diagrams of (a) barrier pumping and (b) in-well pumping.

valence band to the conduction band. These hot carriers thermalize to the band edge/ground state of the quantum well, where their recombination results in emitting photons at wavelength λ_{laser}. When charge carriers diffuse to lower energy levels, they release energy in the form of phonons. In contrast, the mechanism of in-well pumping is illustrated in Fig. 4.1 (b), where the pump photons are directly absorbed within the quantum well itself, and the emitted laser photons are also generated in the same layer. This in-well pumping method results in a smaller wavelength difference between the pump and the laser compared to the barrier pumping mechanism, and reduced emission of phonons given the reduced energy difference. For producing a 1178 nm laser output, the quantum defect is 31.4% when using barrier pumping with an 808 nm pump laser. However, this quantum defect can be significantly reduced to just 9.2% with in-well pumping utilizing a 1070 nm pump laser.

Although in-well pumping offers the advantage of a reduced quantum defect, it presents a challenge in terms of absorption efficiency. With 808 nm barrier pumping, the absorption coefficient of the GaAs barrier is approximately 1 μm^{-1} [128], with a slightly higher absorption

coefficient for InGaAs quantum wells [129]. However, when using 1070 nm in-well pumping, there is no absorption from the GaAs barrier, and the absorption coefficient for InGaAs quantum wells also decreases [129]. As described by the Beer-Lambert Law in Eq. 2.10, the absorption efficiency is directly proportional to the thickness of the absorption layer and the absorption coefficient. The absorption per pass with in-well pumping is significantly lower than barrier pumping due to the much smaller thickness of the quantum wells compared with the barriers [130]. To compensate for this reduced single-pass absorption, pump light recycling is necessary. The unabsorbed pump power is redirected through the same spot multiple times to increase the effective absorption length. Implementing such a pump beam circulation system is critical to achieving the required output power, particularly when the available pump power is limited.

4.2 Pump Beam Recycling

Multi-pass pumping with a laser beam circulator is a technique extensively utilized in thin disk lasers and laser amplifiers to enhance the efficiency by recycling unabsorbed pump power. An example of this approach is the parabolic mirror-based multi-pass pump structure for thin disk lasers, as depicted in Fig. 4.2. This setup includes a parabolic mirror featuring a central aperture that facilitates the construction of the laser cavity. Additionally, four deflection prisms are employed to redirect the collimated pump beam, which originates from an optical fiber, enabling multiple passes—typically 16 or 24—through the thin disk crystal [131]. A similar multi-pass pumping architecture has been adapted for experiments involving multi-pass in-well pumping in VECSELs [132]. This adaptation underscores the versatility and effectiveness of multi-pass pumping strategies across different laser platforms. However, despite its advantages in enhancing pump absorption, this type of structure presents significant challenges in terms

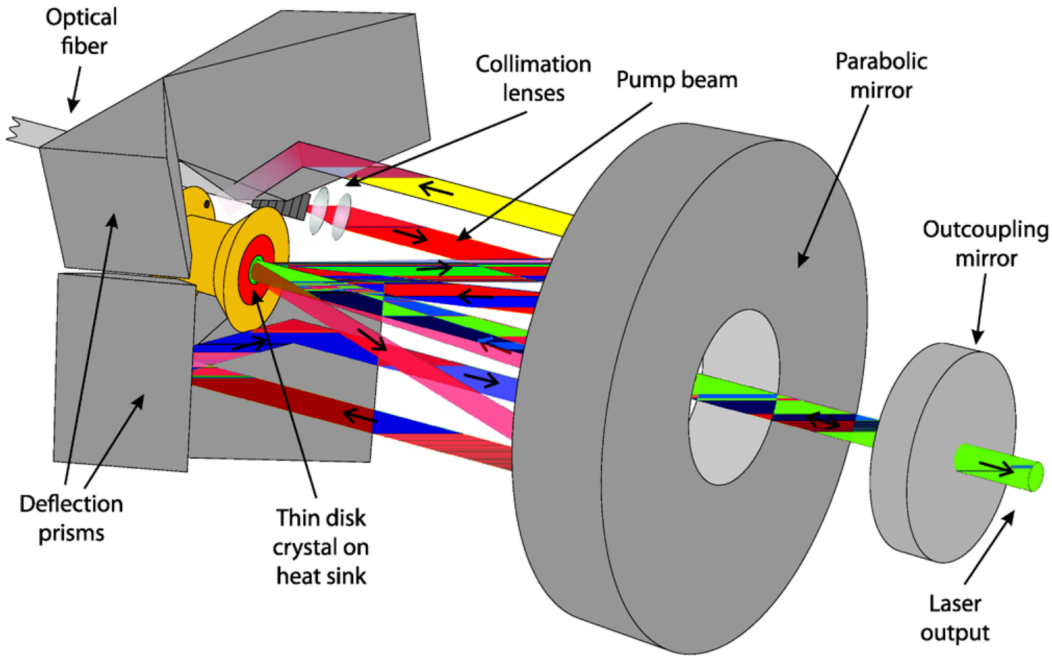

Fig. 4.2 Schematic diagram of a thin disk laser, thin crystal disk and and out-coupling mirror are used to build the laser cavity [131]. The pump configuration setup insists the thin disk crystal on the focal plane of a parabolic mirror and four deflection prisms.

of optical alignment and system compactness. The complexity of aligning multiple optical elements make this structure less ideal for applications where a compact and less cumbersome optical system is required. Those drawbacks require some innovative designs that simplify the optical alignment process while maintaining the benefits of multi-pass pumping in enhancing pump absorption for constructing a semiconductor-based LGS with in-well pumping.

4.2.1 Pump Beam Recycling with Parabolic Mirrors

The parabolic asymmetric confocal cavity (PACC) design, illustrated in Fig. 4.3, represents a new approach to laser beam circulation using two parabolic mirrors, as developed by the author and collaborators [127]. This design incorporates two parabolic mirrors with slightly different

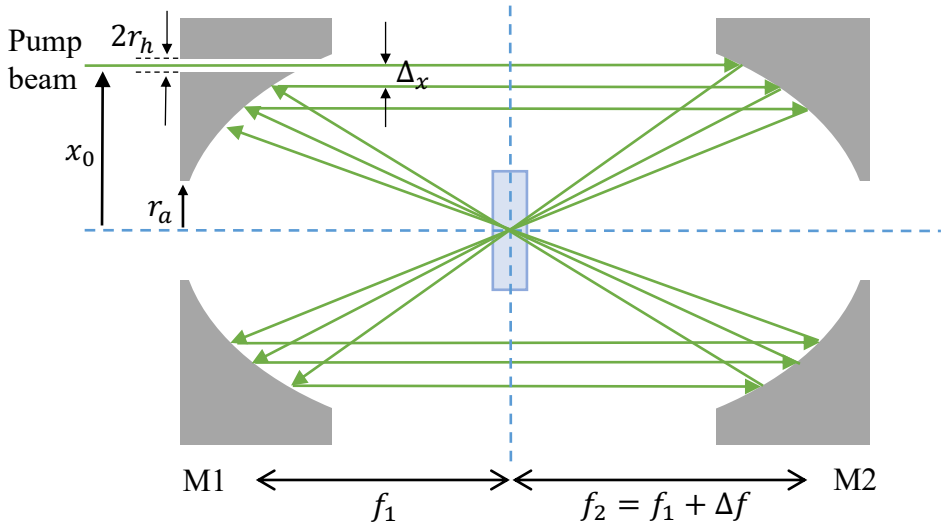

Fig. 4.3 Schematic diagram of a pump beam recycling setup with two parabolic mirrors with slightly different focal lengths. The transmissive sample is placed at the focus of both parabolic mirrors and the pump beam is injected from a hole on mirror M1.

focal lengths, each featuring a central aperture (r_a in radius) that is sufficiently large to allow the laser cavity beam to pass through unobstructed. In this configuration, the MECSEL gain chip is positioned at the confocal point of both mirrors, optimizing the overlap of pump spots. The first parabolic mirror, denoted as M1, includes an additional hole with a diameter of $2r_h$ located x_0 from the optical axis. This hole serves as the entry point for the pump beam, which is directed through this aperture and focused onto a plane indicated by a blue dashed line, representing the confocal plane of both mirrors.

Following its initial focus, the pump beam is then reflected off the second parabolic mirror (M2), where it becomes collimated and passes through the MECSEL gain chip. It subsequently refocuses onto the confocal plane by M1. After this refocusing, the beam is recollimated by M2, passing through the MECSEL gain chip once more and hitting M1 at a lateral shift Δx from the original pump beam entry point. This lateral shift is induced by the difference in focal lengths between the two mirrors (Δf in Fig. 4.3), where Δx is directly proportional to Δf. Each

reflection and passage through the MECSEL gain chip gradually absorbs more of the pump energy, with the beam continuing to circulate in this manner—being focused and recollimated in repeated round trips—until the pump energy is fully absorbed or the beam is either blocked or escapes from the circulating cavity. This design not only maximizes pump absorption efficiency but also simplifies the optical setup by minimizing the number of components needed, thereby enhancing overall system performance and stability for LGS applications.

The PACC design utilizing two parabolic mirrors for efficient laser beam circulation was computationally verified using Zemax ray tracing analysis of a Gaussian pump beam, as depicted in Fig. 4.4 (a). For this simulation, two parabolic mirrors, M1 and M2, were employed with focal lengths of $f_1 = 100\,\text{mm}$ and $f_2 = 101\,\text{mm}$, respectively. Each mirror featured a central aperture to facilitate the passage of the cavity laser beam that through the MECSEL gain chip positioned on the confocal plane. In the simulation, a gain module was placed in this confocal plane, incorporating a small opening with a radius of 1 mm, specifically designed to accommodate the MECSEL gain chip. A detector was positioned at this opening to analyze the pump beam's overlap on the MECSEL gain chip.

The simulation results, illustrated in Fig. 4.4 (b), demonstrated 33 passes of the pump beam through the MECSEL gain chip. The overlaid result of these 33 passes maintained a Gaussian shape similar to that of a single-pass incident beam, albeit with an increased amplitude. The excellent beam overlap achieved in this setup can be attributed to the intrinsic properties of the parabolic mirrors, which are capable of near aberration-free performance. This characteristic is pivotal in maintaining the quality and focus of the beam throughout multiple passes, thereby enhancing the efficiency of the pump process. Furthermore, the analysis suggested that the number of passes on the MECSEL gain chip could be increased by further reducing the difference in focal lengths between the two mirrors. This adjustment would allow for even greater absorption of the pump energy by the MECSEL gain chip, potentially leading to higher

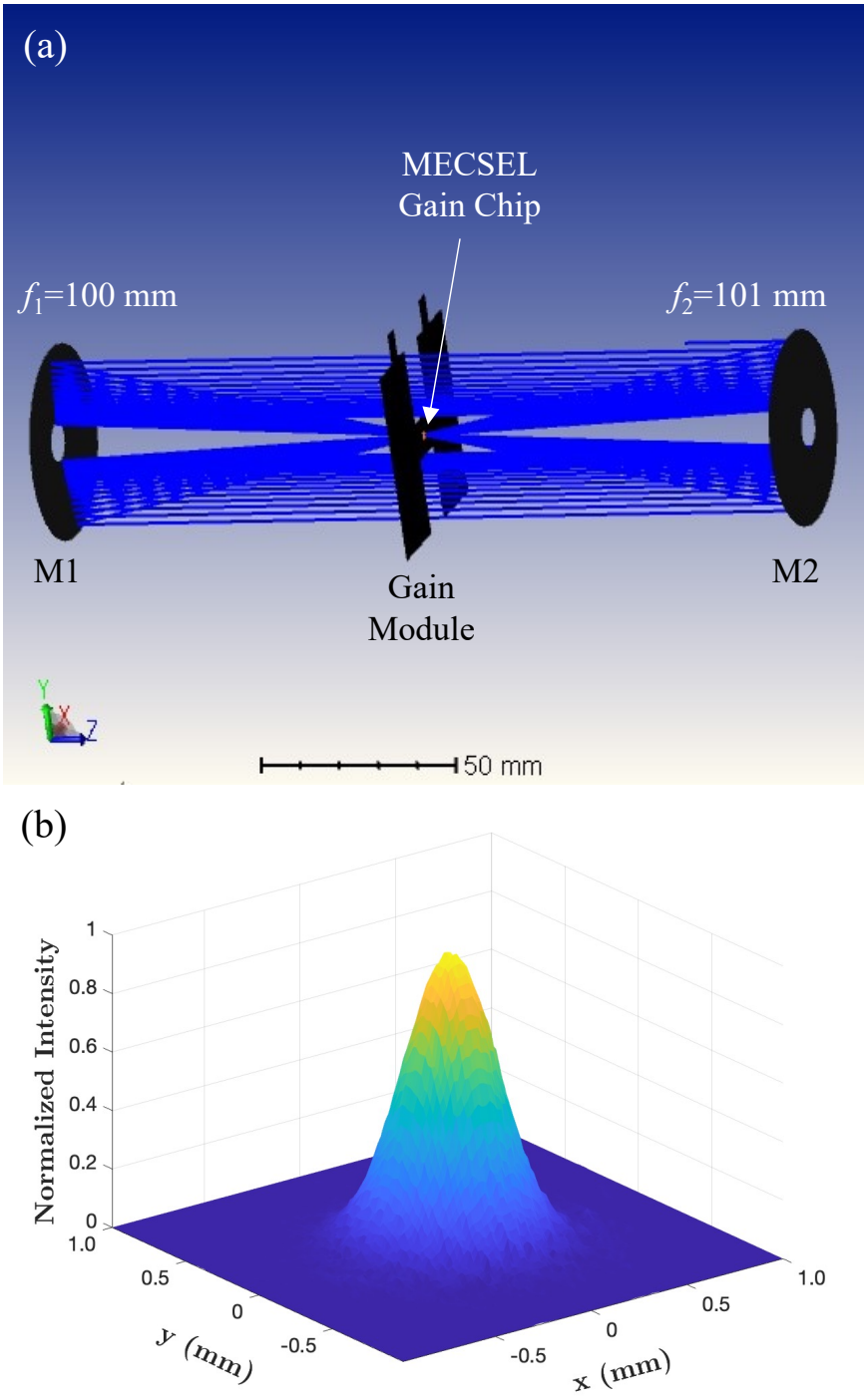

Fig. 4.4 (a) PACC setup consists of two parabolic mirrors of slightly different focal lengths in Zemax. (b) Overlapped pump beam profile on the MECSEL gain chip for 33 passes.

output powers and more efficient laser operation. The computational verification provided by the Zemax analysis underscores the feasibility and effectiveness of the PACC design, confirming its potential for practical applications in high-efficiency laser systems for LGS applications.

The PACC structure can be adapted to accommodate multiple pump sources, enhancing its capability to manage higher pump powers as a single pump source might not provide. This modified design, depicted in Fig. 4.5, incorporates the first parabolic mirror M1 equipped with multiple apertures. These holes are uniformly positioned x_0 away from the optical axis, allowing for the injection of multiple pump lasers from different apertures. The maximum number of pump lasers that can be effectively utilized in this setup is dictated by the focal length difference and the focal length of the second mirror (M2), calculated by the following equation [127]:

$$N_{\text{pump}} \approx \frac{\pi f_2}{\Delta f} = 10 \sim 30, \tag{4.2}$$

where f_2 is the focal length of the second parabolic mirror and Δf is the difference in focal lengths between the two mirrors. This configuration allows for a significant increase in the number of pump sources, potentially ranging from 10 to 30, depending on the specific dimensions and configurations of the mirrors involved.

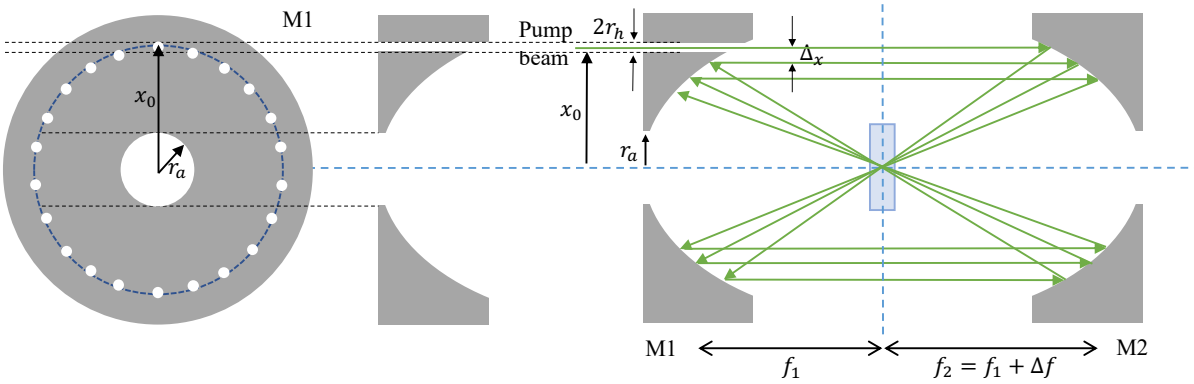

Fig. 4.5 Schematic diagram of PACC with multiple pump sources.

The effectiveness of this multi-beam PACC structure has also been verified through ray tracing analysis. The simulation results confirmed that good beam overlap on the MECSEL gain chip is achievable, which is crucial for ensuring efficient energy absorption and uniform pumping. However, adjustments to the heat sink are necessary to prevent it from obstructing the multi-pass pumping beams. This adjustment involves careful alignment and possibly redesigning the gain module to accommodate the geometry and paths of the multiple beams without interfering with their trajectories. Such a setup proves extremely useful in scenarios where a single pump source is insufficient to meet the power requirements of the system. By employing multiple pump lasers, the PACC design can significantly enhance the overall pump power available to the MECSEL, thereby improving the maximum possible output power.

Beyond its core role in multi-pass pumping for in-well pumped MECSELs, the PACC has broader implications for spectroscopy and signal amplification due to its ability to maintain multiple passes through a medium without altering the input beam shape [127]. This capability is particularly advantageous for a range of sophisticated spectroscopic applications. For transmission spectroscopy in gases, PACC can be employed by coupling the laser out of the cavity through a small hole as illustrated in Fig. 4.6 (a). This method is ideal for analyzing the absorption characteristics of various gases, providing essential spectral data for applications such as environmental monitoring and chemical analysis. In photo-acoustic spectroscopy, PACC increases the absorption of laser light in gases and aerosols and generating more sound waves. The increased interaction length with the sample, afforded by the multiple passes of the incident laser beam, amplifies the photo-acoustic signal, thereby improving the sensitivity and reliability of the measurements. PACC is also suitable for cavity ring-down spectroscopy, where the decay time of light within the cavity is measured after the introduction of a sample. The setup ensures multiple passes of light, increasing the effective path length and thus enhancing the sensitivity and accuracy of trace gas concentration measurements. For signal amplification, as shown in

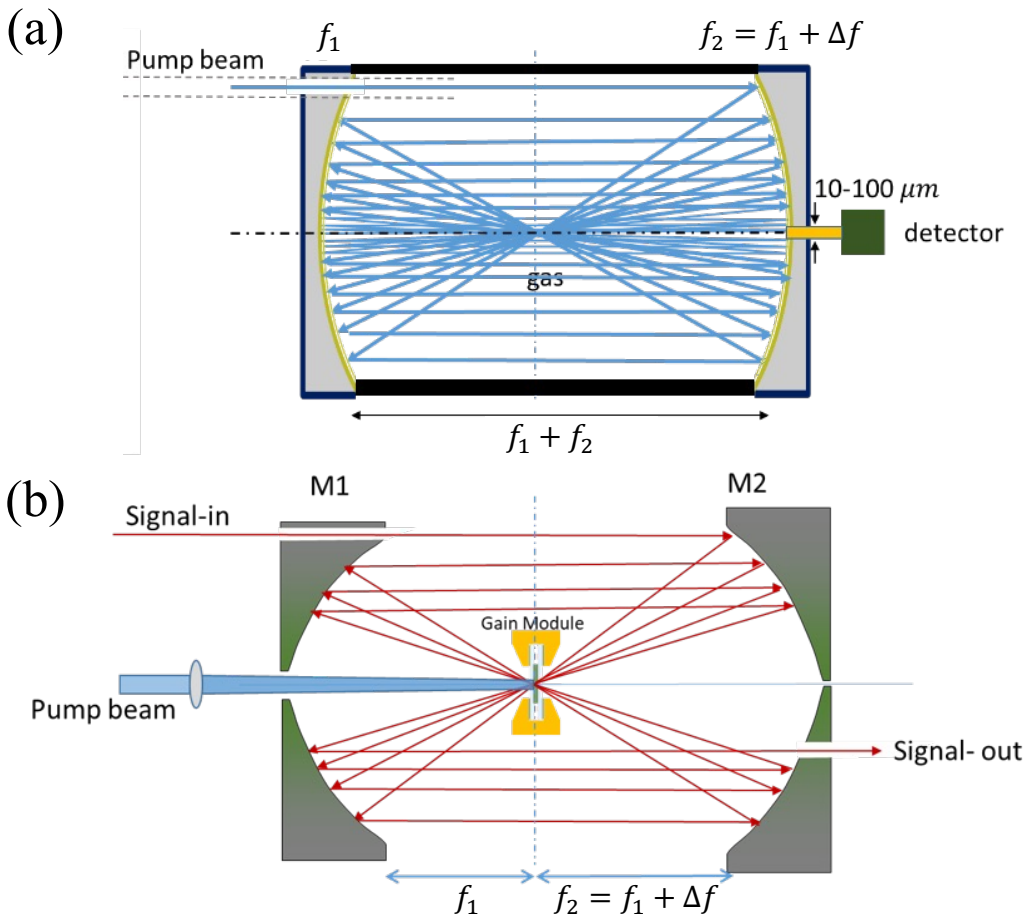

Fig. 4.6 Schematic diagram of PACC for (a) transmission spectroscopy in gases, and (b) signal amplification [127].

Fig. 4.6 (b), the input signal undergoes multiple passes through the gain medium. As a result, the signal is amplified upon exiting the gain medium.

Despite these promising applications, the practical implementation of PACC has been limited due to the high costs associated with custom-made parabolic mirrors, which are critical for constructing such cavities. This limitation prevented the experimental verification of PACC by the author for constructing a prototype MECSEL for LGS applications. Instead, alternative configurations using off-axis mirror-based laser beam circulator structures were explored.

4.2.2 Pump Beam Recycling with Off-Axis Parabolic Mirrors

All incident beams that are parallel to the symmetry axis of a parabolic mirror are reflected through the focus of the curve, with an angle θ between the incident and reflected light. This geometric principle underlies the design of off-axis parabolic (OAP) mirrors, which are a specialized type of mirror featuring a segment of a parabolic surface that is offset from the symmetry axis. An OAP mirror can focus parallel rays to a single point without introducing spherical aberration, which is a common issue with spherical mirrors and lenses. By using an off-axis segment, the OAP mirror avoids the obstruction caused by the light source or other components that would typically be placed along the axis in a traditional parabolic mirror setup. OAP mirrors can be effectively utilized in multi-pass pumping systems to ensure that beams are accurately redirected back into the gain medium, optimizing each pass to maximize energy absorption and minimize losses due to misalignment or beam spread. The precise focusing ability of OAP mirrors ensures that the laser beams remain tightly focused over multiple reflections, which is essential for maintaining the high optical intensities needed for effective pumping.

The design of an OAP mirror-based laser beam circulator, as illustrated in Fig. 4.7 (a), employs two OAP mirrors, M1 and M2. These mirrors are sections of two parabolic curves that have identical parent focal lengths, defined as the distance from the focus to the vertex of the parabola. In this configuration, the OAP mirrors are arranged such that their corresponding parent parabolic curves are oriented such that their symmetry axes and foci overlap. At this shared focal point, the reflective sample denoted as M3 is positioned. The design is such that the pump beam is initially focused by a lens onto a plane that not only is perpendicular to the symmetry plane of the two parabolas, but also intersects the common focus of the OAP mirrors. Once focused, the beam is collimated by the second OAP mirror M2, directing it precisely onto the sample M3. Upon striking M3, the beam is reflected toward M1, where it is again focused

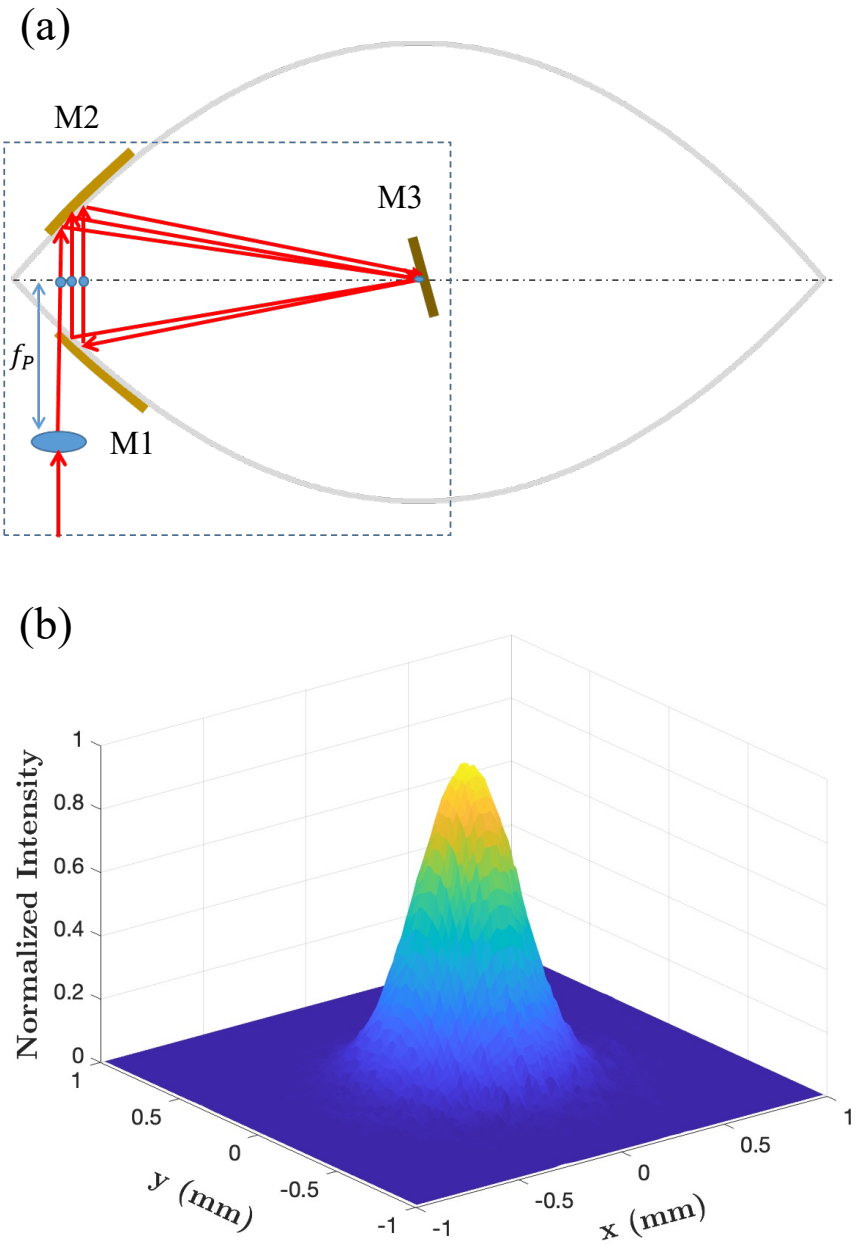

Fig. 4.7 (a) Schematic diagram of OAP mirror based laser beam circulator. (b) Beam profile of the overlapped beam on the sample for 30 passes.

back onto the focal plane, continuing the cycle. This cyclic process of focusing and collimation is repeated, with the beam traveling back and forth between the OAP mirrors until the pump energy is exhausted or exits the circulator. The slight shift introduced in each round trip is achieved by a small tilting angle of the sample M3. The effectiveness of this configuration in maintaining beam quality over multiple passes is depicted in Fig. 4.7 (b), where the beam profile on the sample after 30 passes is shown with a tilting angle of 1° from the symmetry axis. The overlapped beam profile demonstrates a near-perfect Gaussian shape, indicating minimal distortion and high efficiency in beam handling. The precision and quality of the beam can be enhanced by utilizing a larger segment of the parabola or by adjusting the tilting angle to be smaller, allowing for more passes overlapped on the sample.

According to the author's simulations, 90° offset angle will provide the best beam overlap on the sample. However, 1" diameter, 60° offset angle OAP mirrors with an aluminum coating and an effective focal length of 50.8 mm are commercially available. A Zemax simulation setup as illustrated in Fig. 4.8 (a) was constructed based on those off-the-shelf OAP mirrors. This setup incorporated two OAP mirrors M1 and M2, along with a detector positioned at the focus shared by both mirrors to analyze the pump beam profile on the sample M3, represented by a plane HR mirror in this scenario. While the lens focusing the pump beam onto the focal plane is omitted in the figure, its role is crucial in achieving the desired beam concentration. A photograph of the experimental setup using these OAP mirrors is shown in Fig. 4.8 (b). In this demonstration, a plane silver mirror served as a dummy sample to configure the beam circulator, and a He-Ne laser was employed to illustrate the setup's functionality. 14 pump spots are visible on M1, while a single spot on M3 represents the cumulative effect of 28 passes. This effective beam overlap is further quantified in the ray tracing analysis depicted in Fig. 4.8 (c). The beam profile appears slightly elliptical, which is expected given the 60° offset angle of the OAP mirrors.

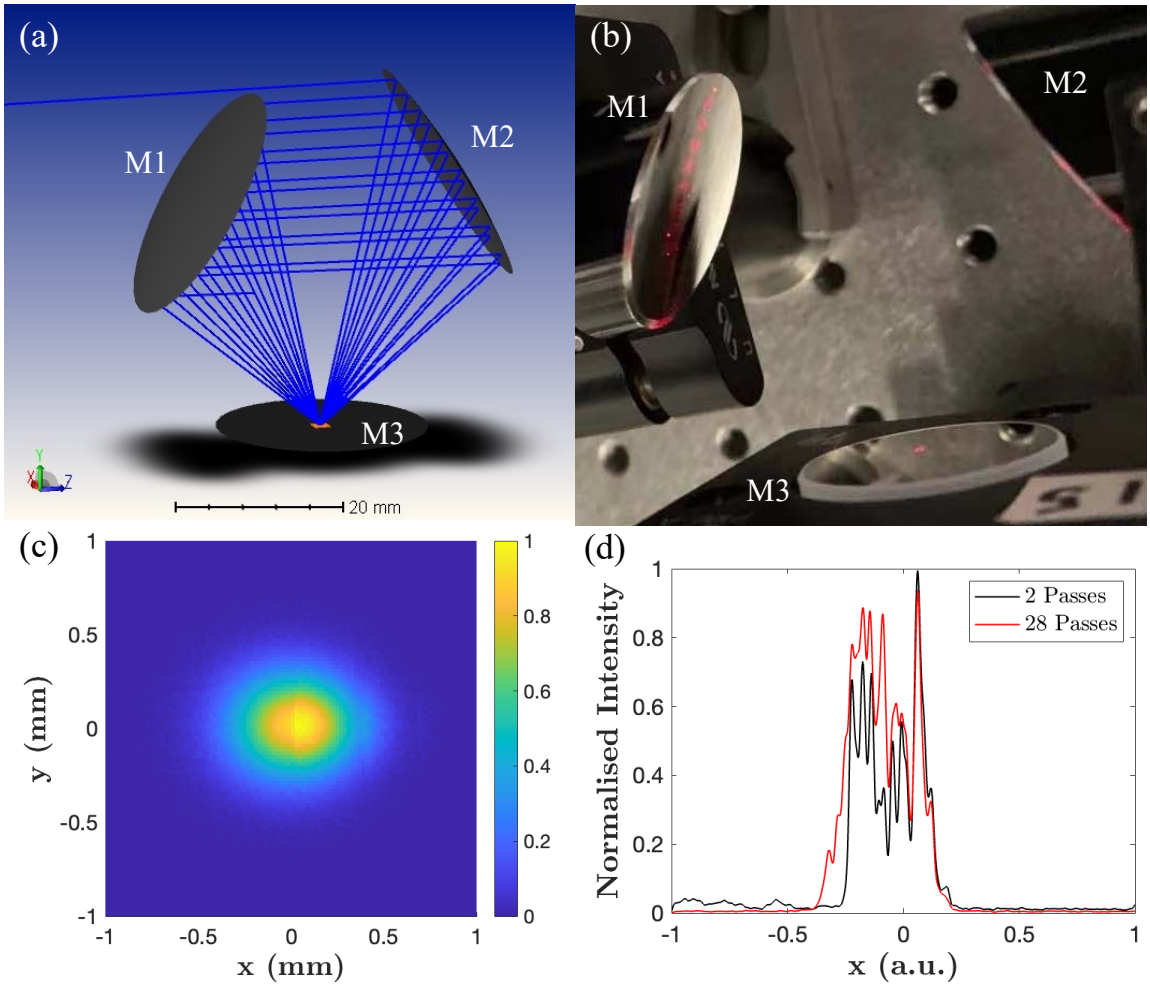

Fig. 4.8 (a) OAP based laser beam circulator in Zemax. (b) Experimental setup of the Zemax simulated design. (c) Beam profile of the sample for 28 passes using Zemax simulation. (d) Experimental result of beam on the dummy sample for 2 passes (black) and 28 passes (red).

Further analysis of the beam profiles on the dummy sample was conducted using a CCD camera, with results presented in Fig. 4.8 (d). The black and red lines represent the beam profiles after 2 and 28 passes, respectively, showing only a 6.6% increase in beam size (FWHM). This minimal expansion in beam size across numerous passes underscores the system's efficiency in maintaining beam integrity. The minimum observed number of overlapping passes on the sample was 2, inherent to the setup's reflective design. Additionally, fringe patterns noted in

the figures result from manufacturing imperfections in the OAP mirrors' substrates. Despite the promising results with a dummy sample and a He-Ne laser, the pursuit of this setup for further experimental work was curtailed by the unavailability of high-quality, large offset angle OAP mirrors with HR coating suitable for 1070 nm, the intended pump wavelength. However, the successful demonstration offers a solid foundation for potential future enhancements of the MECSEL LGS technology. The implementation of this OAP mirror-based circulator could substantially simplify multi-pass pumping structures and, given the inherent advantages of reflective over transmissive optics, represents a promising avenue for advancing LGS systems in observational astronomy. Two 90° OAP mirrors, coated for 1064 nm, were purchased and modified for constructing a multi-pass pumping setup. But due to the availability of gain chip in the lab, they were not used to build a real laser. The alternative configurations using aspheric lens-based laser beam circulator structures were also explored.

4.2.3 Pump Beam Recycling with Aspheric Lenses

Plane mirrors and aspheric lenses are types of optical elements that are commercially available, making the construction of pump beam recycling setups for multi-pass in-well pumping both budget-friendly and feasible for laboratory verification. Two distinct designs utilizing aspheric lens-based laser beam circulators have been developed and are depicted in Fig. 4.9. These designs were specifically tailored for multi-pass pumping applications in MECSELs.

Two aspheric lens-based pump beam recycling designs, optimized for multi-pass pumping in MECSEL applications, are detailed in Fig. 4.9. Design (a) is tailored for a transmissive sample, while design (b) is suited for a reflective sample. In the multi-pass structure depicted in Fig. 4.9 (a), the system employs two identical aspheric lenses (L1 and L2) coupled with four plane mirrors (M1 to M4) to facilitate effective beam circulation. Each aspheric lens, possessing a focal length f, features a central aperture that allows the laser cavity beam to pass through

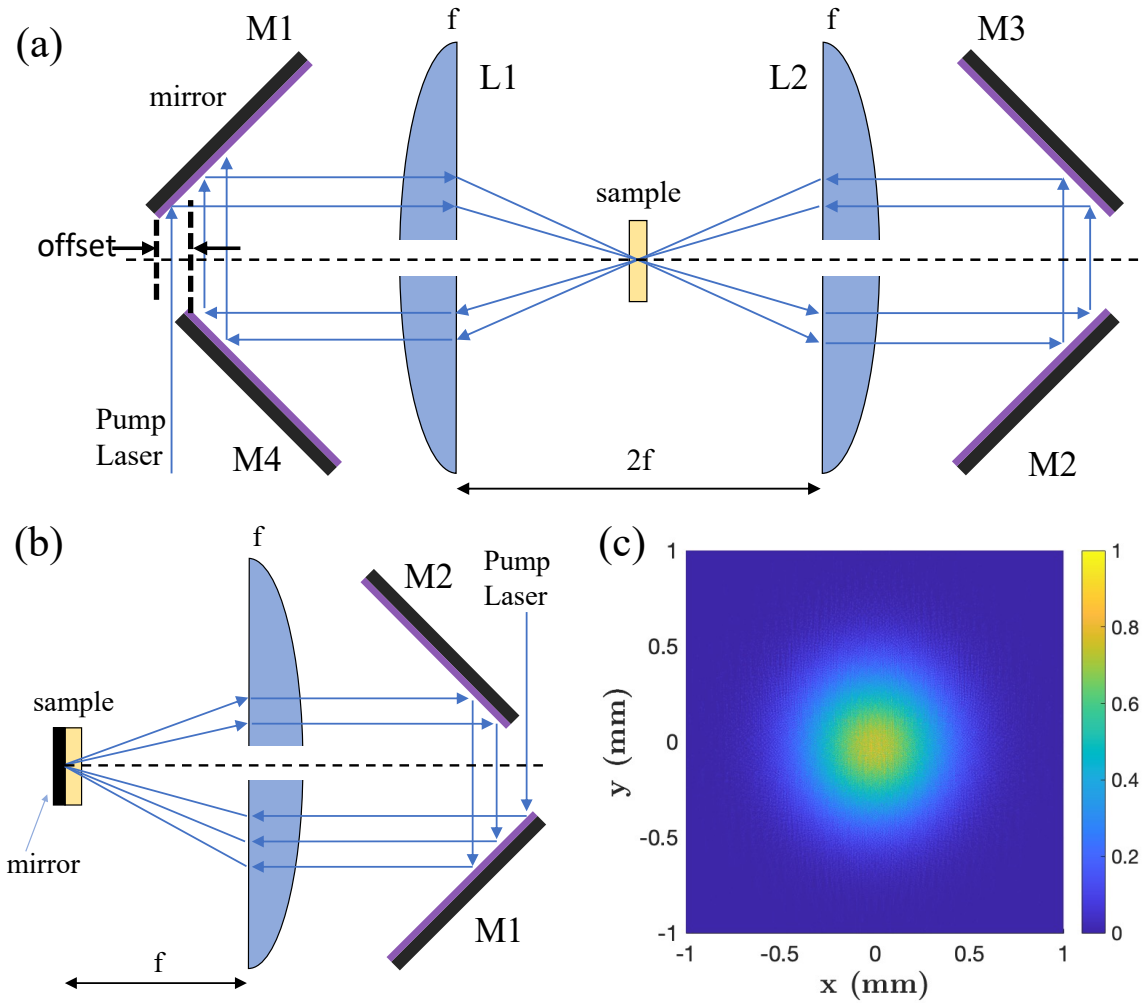

Fig. 4.9 Schematic diagrams of aspheric lens based multi-pass pumping structure, (a) is a design for transmissive sample and (b) is a design for reflective sample. (c) Beam profile on the reflective sample with 20 passes using ray tracing analysis.

unobstructed. The lenses are positioned 2f apart from one another, aligning the sample at the confocal point between them. The accompanying four plane mirrors are arranged into two retro-reflector pairs, with each pair designed to maintain an optical path length of 2f tracking the laser beam path from the exit point of one lens to the re-entry point of the same lens, facilitated by reflections off the plane mirrors. One mirror in a retro-reflector pair is slightly offset to introduce a lateral shift in the pump laser beam with each pass. To avoid focusing the beam too

tightly on the sample, a collimated beam is used at the sample position. This collimated beam ensures that the beam size remains roughly the same during different passes. Additionally, the pump beam on the sample is re-imaged back to its original position after each round trip. The pump laser is initially focused at an optical path length f from L1 at the offset gap between M1 and M4, and is then collimated by L1 into the 4-f system. The collimated beam then transits through the sample and is subsequently refocused by L2. Then the beam is reflected back to L2 by the a retro-reflector pair formed by M2 and M3, and the beam is recollimated through the sample again. This beam then undergoes refocusing by L1, and another retro-reflector pair (formed by M1 and M4) reflects it back to L1. The slight displacement between M1 and M4 introduces a lateral shift in the beam path with each pass. This cyclical process is designed to repeat until the pump beam is fully absorbed by the sample, blocked, or escapes the multi-pass structure.

The multi-pass design featuring a reflective sample, as in Fig. 4.9 (b), offers a more streamlined alternative to the transmissive setup by reducing the number of optical elements required by half. This design capitalizes on the reflective properties of the sample, eliminating the need for an additional set of optical elements typically used in the transmissive system. In this configuration, only one retro-reflector pair is necessary, and the lateral shift of the pump beam with each pass is ingeniously introduced by slightly tilting the sample. The effectiveness of this design was substantiated through Zemax simulations, the results of which are presented in Fig. 4.9 (c). For these simulations, a f=100 mm aspheric lens was utilized, with lens data including aberrations imported from THORLABS. The simulation output demonstrates that after 20 passes, the beam profile overlapped on the sample exhibits negligible deviation from that of a single pass, indicating the necessary beam stability and uniformity. The color coding in this figure represents the normalized intensity of the beam at various positions. Moreover, the simulations revealed the operational robustness of the two structures. While the transmissive

multi-pass structure exhibits some sensitivity to alignment and construction errors, the reflective design proves to be more robust, showing less susceptibility to experimental misalignments. This characteristic makes the reflective setup particularly advantageous for practical implementations where alignment precision might be challenging to maintain consistently. The practical implementation of the designs in Fig. 4.9 (a) and (b) have been successfully verified in experimental settings and the detailed examination and discussion of these aspheric lens-based circulator designs and their impact on the performance of MECSELs will be further explored later.

Aspheric lens based multi-pass pumping structures in Fig. 4.9, although effective, necessitate the modification of aspheric lenses by drilling a central hole to accommodate the laser cavity beam. This requirement can complicate the fabrication process and potentially affect the optical performance of the lenses. To circumvent this issue, an alternative design involving a ring circulator can be utilized, which avoids the need for modifying the lenses, while incorporating more elements into the setup. The design as illustrated in Fig. 4.10 (a), employs two identical aspheric lenses, each with a focal length f, and includes two plane mirrors, M1 and M3, along with a reflective sample denoted as M2. The arrangement is such that both lenses are positioned at a distance f from the reflective sample M2, and the optical path length between the lenses, with beam reflections from M3 to M1, is 2f. This setup is designed to form a 4-f system, ensuring that the pump beam spot is re-imaged onto the sample after completing a round trip.

In this configuration, the pump beam initially passes through a hole in the mirror M3 and is focused by lens that focus the pump laser with a focal length f_p onto a plane that is an optical path length f away from both aspheric lenses. After this focusing, the beam is directed towards M1, which reflects the beam to one of the aspheric lenses. This lens then collimates the beam onto the reflective sample M2. Importantly, the sample M2 is tilted at an angle θ from being parallel to the optical axis of the lens with focal length f_p, introducing a deliberate angular

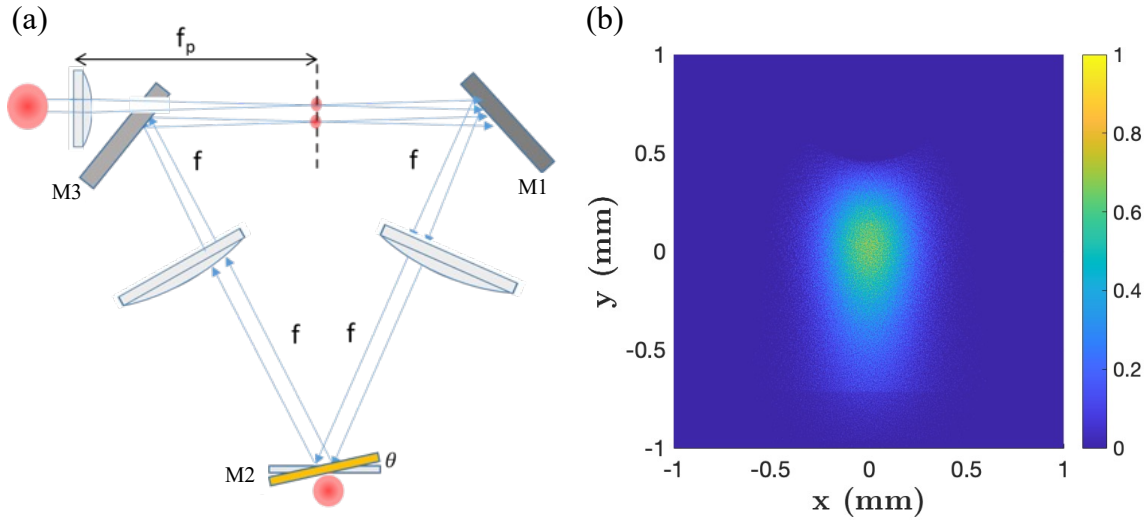

Fig. 4.10 (a) Schematic diagram of an aspheric lens based ring circulator [127]. (b) Beam profile on M3 for 40 passes.

displacement that aids in the circulation of the beam. Once the beam strikes the tilted sample M2, it is reflected and subsequently refocused at the same confocal plane after being reflected by mirror M3. This cycle of refocusing and recollimation repeats multiple times, allowing the pump beam to make numerous passes through the system until it is either fully absorbed by the sample, blocked, or escapes the confines of the ring circulator.

The ring circulator concept was rigorously tested using Zemax ray tracing simulations to determine its feasibility for practical applications. In optical design, the orientation of a lens can introduce various aberrations that significantly impact the performance of the system. Consequently, simulations were conducted for both orientations of the aspheric lenses to fully understand how these variations might affect the system's optical behavior. The simulation results indicated that the beam overlap at the sample position is highly sensitive to both the precise positioning and the tilting angle of the aspheric lenses and the plane mirrors. The simulations failed to identify any combination of parameters that could produce a Gaussian-shaped overlapped beam profile on the sample. Figure 4.10 (b) is the best overlapped beam

profile on M3 for 40 passes with the parameter sweep in Zemax. Due to the inability to achieve an optimal Gaussian beam profile and the overall sensitivity of the system to alignment, the decision was made not to pursue this particular design experimentally. The lack of a promising beam profile on the sample rendered the structure less suitable for constructing a multi-pass pumping structure. However, it is important to note that while the design may not be ideal for applications demanding precise beam control and shape, it possesses significant potential for spectroscopy-related applications. The ability of this structure to facilitate more than 100 passes makes it extremely valuable for spectroscopy, where extended interaction lengths can greatly enhance signal detection and analysis. This attribute could be particularly beneficial in environments where high sensitivity and extended path length are more critical than the specific beam shape, such as in gas absorption studies or complex material characterizations. Thus, while the ring circulator design may not have progressed for pump recycling, its applicative scope in spectroscopy presents a promising area for further exploration and development.

4.3 Conclusion

In this chapter, the in-well pumping method was explored as a strategy to minimize heat generation within the MECSEL gain chip by reducing the quantum defect. This approach necessitates pump beam recycling to address the significant challenge of low absorption associated with in-well pumping, attributable to the reduced thickness of the quantum well layers compared with the total thickness of the barrier layers. Various designs for pump beam recycling were examined to enhance the efficacy of in-well pumping. Parabolic mirror-based designs were studied through ray tracing analysis to assess their performance in circulating the laser beam effectively. Additionally, the OAP mirror-based pump beam circulator was introduced as having the simplest design among the circulators considered. Feasibility studies conducted via Zemax

and experimental validation using a He-Ne laser and a silver mirror supported the potential of this design. Furthermore, aspheric lens-based laser beam circulator were evaluated both computationally and experimentally, proving their suitability for constructing multi-pass in-well pump MECSEL systems for LGS applications. The detailed discussion and outcomes of these evaluations will be further elaborated in chapters 5, 6 and 7.

The following chapter will discuss the experimental implementation of in-well pumping of MECSELs to address the thermal limitations and achieve high output power for LGS applications.

Chapter 5

In-Well Pumped MECSEL

In this chapter, the discussion will focus on a twenty quantum well MECSEL structure employing in-well pumping, where the pump light is directly absorbed by the quantum wells. This approach is designed to reduce the quantum defect and associated thermal effects, thereby improving the laser output power. The experimental results presented in this chapter were originally documented in [112] and further detailed reevaluation will be discussed.

5.1 Twenty Quantum Well Gain Chip

The maximum output power of MECSELs is constrained by thermal limitations, which requires improved thermal management. MECSELs excel in heat dissipation compared to other SDL architectures due to the absence of a DBR directly attached to the active region. To further increase output power, it is essential to focus on minimizing heat generation within the active region. One promising approach is the implementation of in-well pumping [130], which decreases the quantum defect significantly compared to traditional barrier pumping methods.

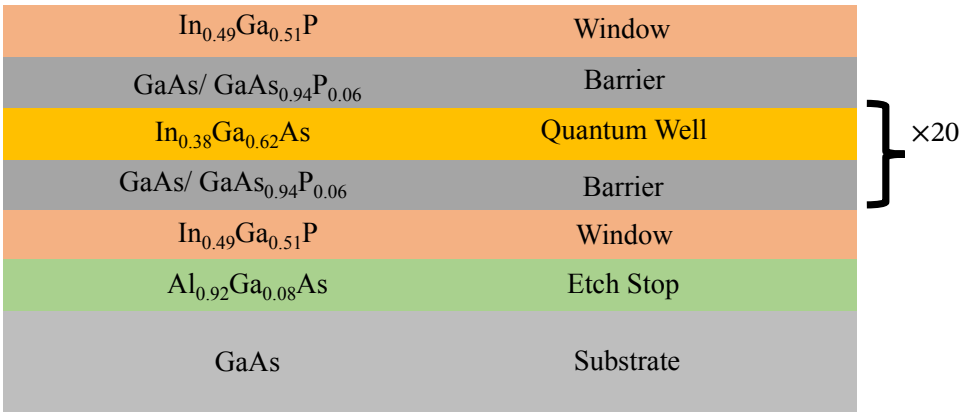

Fig. 5.1 Schematic of the MOCVD-grown twenty quantum well MECSEL wafer.

The twenty quantum well MECSEL is grown using a shower head MOCVD reactor, utilizing a GaAs substrate. This structure as depicted in Fig. 5.1, designed similarly to the previously mentioned eleven quantum well MECSEL, features an increased number of quantum wells aimed at augmenting the absorption per pass. For 808 nm barrier pumping, both InGaAs quantum wells and GaAs barriers absorb pump photons. In contrast, for 1070 nm in-well pumping, the absorption coefficient of InGaAs decreases, and GaAs barriers become transparent, resulting in no absorption. Given that the GaAs barriers are nearly 30 times thicker than InGaAs quantum wells and have comparable absorption coefficients [129], achieving similar absorption in a single pass for in-well pumping would require 30 times more quantum wells, as per Eq. 2.10. However, high-quality epitaxial growth with so many quantum wells is challenging, so twenty quantum wells were implemented to partially address the reduced absorption. A multi-pass pumping scheme, described in the previous chapter, will be used to further improve absorption efficiency. The InGaAs quantum wells and GaAs/GaAsP barrier layers form a RPG structure similar to Fig. 3.1. As in the previous structure, InGaP window layers were grown next to the active region to prevent surface recombination. The substrate removal and bonding process to 500 µm thick SiC heat spreaders were similar to the eleven quantum well MECSEL, and the external facets of the gain heat spreader sandwich were AR coated with SiO_2 (refractive index

of 1.45) via plasma-enhanced chemical vapor deposition (PECVD) at the central wavelength of 1070 nm. To finalize the assembly, the sample was secured between two water-cooled copper heat sink plates. A 50 µm thick indium foil was introduced between the sample and the copper plates to enhance thermal contact.

5.2 In-Well Pumping and Barrier Pumping

The experimental design for the twenty quantum well MECSEL incorporated a linear laser resonator configuration, mirroring the cavity setup used in the eleven quantum well MECSEL experiments. The resonator was structured with two 1% OCs, having ROCs of 150 mm and 250 mm, and an extended cavity length of 350 mm. This increase in cavity length was planned to accommodate a multi-pass pumping structure. The placement of the twenty quantum well MECSEL gain chip was calculated to be 163 mm from the ROC=150 mm mirror, setting the cavity mode to achieve a beam radius of approximately 190 µm at this position to align with the pump mode. The theoretical mode size across the cavity is illustrated in Fig. 5.2 (a). And the chiller temperature was set to 10 °C.

The twenty quantum well sample has an increased active region thickness of 3.56 µm. Using an absorption coefficient of 1 μm^{-1} for GaAs at 808 nm, over 97% of the pump is absorbed. This results in almost no pump power being available for the last few layers, leading to uneven carrier injection among the quantum wells. To address this issue, double-side barrier pumping can be implemented to achieve a more evenly distributed carrier injection [106]. To evaluate the performance differences between barrier and in-well pumping methodologies, the experimental setup was initially configured to test three distinct scenarios: single-side barrier pumping, double-side barrier pumping, and single-pass in-well pumping. The experimental setup is illustrated in Fig. 5.2 (b). For these tests, a fiber-coupled 808 nm diode laser served as the pump

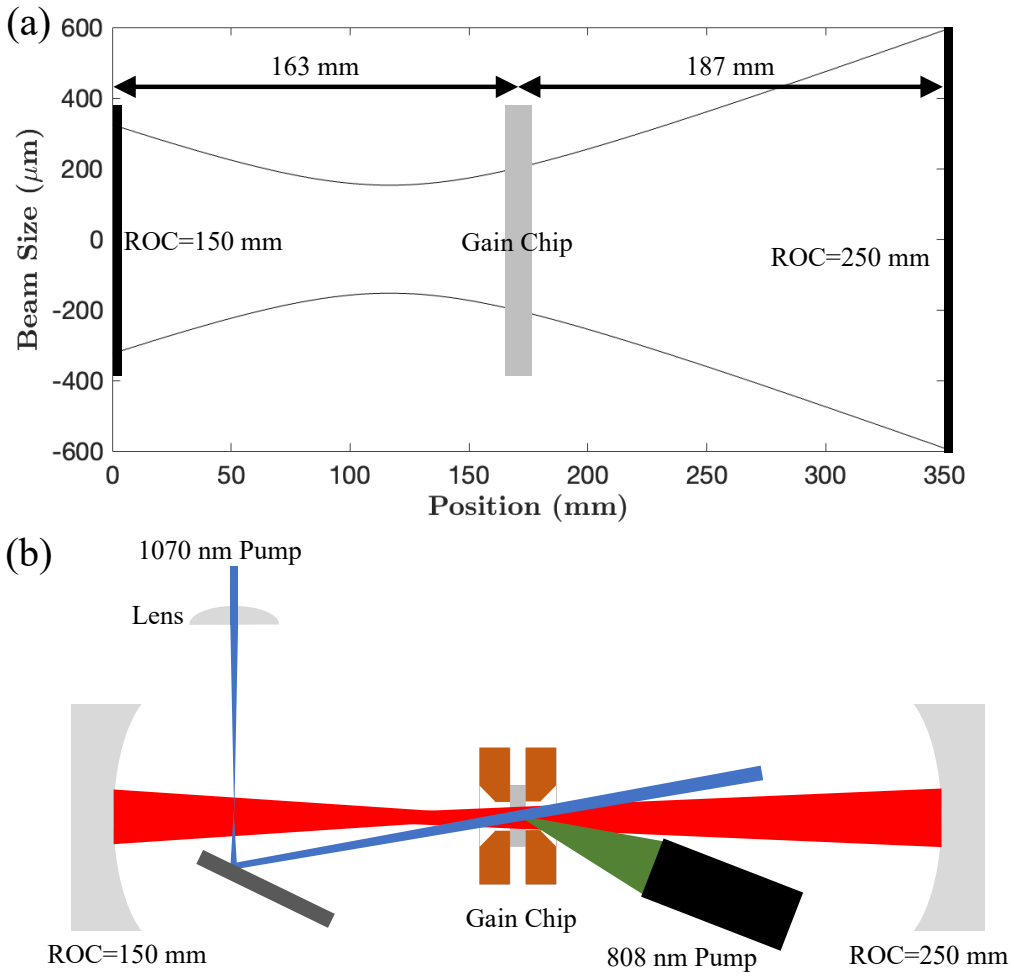

Fig. 5.2 (a) Mode size calculation across the cavity for the twenty quantum well MECSEL gain chip. (b) Experimental setup for 808 nm barrier pumping and 1070 nm in-well pumping comparison.

source for barrier pumping, while a 1070 nm fiber laser was employed for in-well pumping. In terms of pump beam configuration, both pumping strategies utilized a consistent pump beam radius of 200 µm. The gain chip remained stationary with an unchanged cavity mode size. To implement the double-side barrier pumping scenario, an additional 808 nm diode laser was introduced, and carefully aligned to ensure overlap with the existing 808 nm pump spot on the MECSEL gain chip. For a comprehensive comparison, output power measurements

were collected from both output couplers and aggregated. To accurately assess the efficiency and effectiveness between the barrier and in-well pumping strategies, especially given the inherently low absorption in in-well pumping, absorbed pump power was used in the analysis. This necessitated detailed measurements of incident, transmitted, and reflected pump power, ensuring precise determination of the absorbed pump power.

The experimental results for the twenty quantum well MECSEL are plotted in Fig. 5.3, showcasing the total output power as a function of absorbed pump power for three distinct pumping configurations. This twenty quantum well MECSEL gain chip achieved a 95% absorption of the incident 808 nm pump power, which matches the theoretical calculation (97%) and leaving only a negligible amount of transmitted pump power. The slope efficiencies for the single-side and double-side barrier pumping experiments were nearly identical, recorded at 21.6% and 22.4% respectively. Also the analysis of the laser threshold, detailed in the zoomed-in inset of Fig. 5.3, indicated a threshold of approximately 2 W for both barrier pumping scenarios. The experimental results of gain chip absorption confirm our concern that very little pump power remains available for the last few layers of the gain chip, which motivated the implementation of double-side barrier pumping. However, the double-side barrier pumping exhibited similar threshold and slope efficiency compared to single-side barrier pumping. This may be attributed to the high mobility of free carriers, allowing them to diffuse over large distances through carrier tunneling [133] or with the aid of additional thermal energy [134]. The double-side barrier pumping achieved a maximum output power of 18 W with 85 W of absorbed pump power before reaching the thermal limitation. These results outperformed the previously discussed eleven quantum well MECSEL shown in Fig. 3.5 (a), achieved an output power of 13.2 W under the same chiller temperature.

The in-well pumping experiment, conducted under the same setup conditions as the barrier pumping tests, showcased a comparable threshold. The slope efficiency for in-well pumping

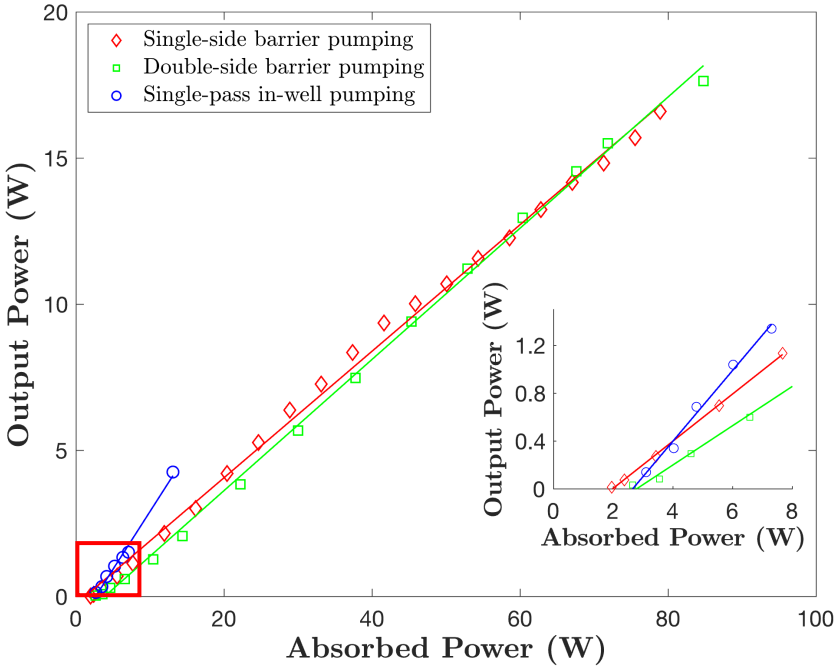

Fig. 5.3 Output power versus absorbed pump power for the twenty quantum well MECSEL at 10 °C chiller temperature with three different scenarios. The laser threshold is detailed in the inset.

reached 39.5%, significantly outperforming the barrier pumping methods. This increase in efficiency is attributed to the decrease in quantum defect in the in-well pumping scenario. Additionally, the superior beam quality of the 1070 nm fiber laser, with an $M^2 < 1.05$ compared to the top hat output for the 808 nm diode laser, contributed to a more effective mode overlap between the pump and cavity mode. Furthermore, pump photon absorption and free carrier recombination in the same layer reduce losses from carrier diffusion, having a positive impact on slope efficiency. Also in the single-pass in-well pumping experiment, the maximum output power is pump power limited primarily due to the low absorption rate of the incident 1070 nm pump light—only 9.5%. This underscores the necessity for a multi-pass pumping scheme to recycle the pump beam efficiently, thereby enabling higher output power from the limited pump power available [132].

5.3 Multi-Pass In-Well Pumping

While in-well pumping reduces the quantum defect, enhancing device efficiency, it introduces a challenge due to the significantly thinner quantum well layers compared to barrier layers, leading to insufficient absorption of the pump power as mentioned in Chapter 4. Given the thickness of the quantum wells and the finite number of wells that can be practically fabricated in good quality, a strategy to recycle unabsorbed pump power becomes essential for optimizing the efficiency of in-well pumped MECSELs.

In the experimental setup depicted in Fig. 5.4 (a), a multi-pass pumping structure was incorporated into the existing laser cavity configuration, featuring two sets of retro-reflectors and two 1" diameter aspheric lenses each with a focal length of 50 mm and anti-reflective coating at 1070 nm. To facilitate the passage of the intra-cavity laser beam, a 1.5 mm diameter hole was drilled at the center of each lens. These lenses were positioned 50 mm from the MECSEL gain chip, with the retro-reflectors similarly spaced 50 mm from the adjacent aspheric lens. To maintain the desired pump beam size and avoid overly tight focusing of the high-quality output from the 1070 nm pump fiber laser, a 200 mm focal length lens was used to focus the pump beam between two plane mirrors. Following reflection, the beam was collimated by the first aspheric lens, traversed the gain chip sample with a beam radius of 250 µm, and then refocused by the second aspheric lens. A retro-reflector then redirected the beam back through the system, with each pass slightly shifting the beam laterally to facilitate multiple interactions with the gain medium, achieving up to ten passes in this setup.

The multi-pass in-well pump beam profile on the MECSEL gain chip as simulated using Zemax is displayed in Fig. 5.4 (b). The simulation predicted an elliptical beam profile, and parameter adjustments within the software demonstrated the challenge of correcting this distortion to optimize beam overlap on the sample for more than ten passes. The difficulty of

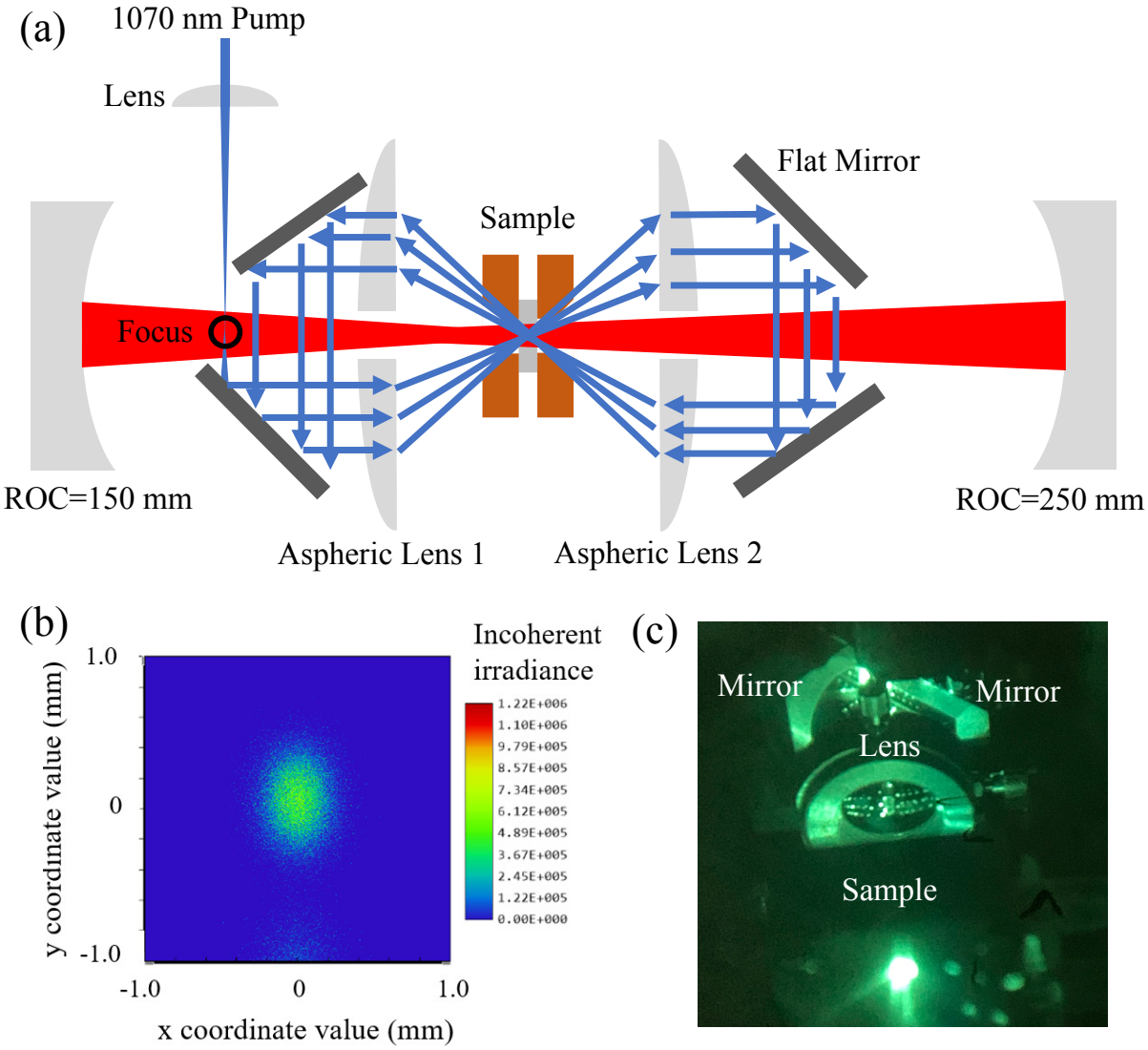

Fig. 5.4 (a) Schematic diagram of multi-pass pumping structure and laser cavity for the twenty quantum well MECSEL gain chip. (b) Pump beam profile on the sample calculated with experimental parameters using ray tracing analysis [112]. (c) Photo of multi-pass beam spots on aspheric lens 1 and two plane mirrors taken with an infrared (IR) viewer.

alignment precluded attempts at achieving more passes within this experimental framework. Multiple pump beam spots are visible in the photograph taken with an IR viewer, as shown in Fig. 5.4 (c). This experiment demonstrated the designed multi-pass structure's capability, albeit

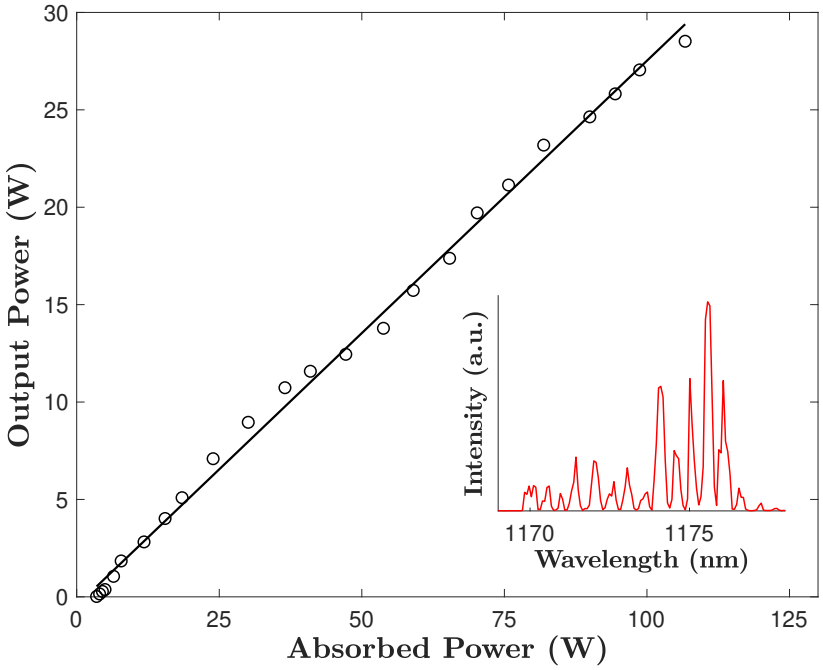

Fig. 5.5 Output power versus absorbed pump power for the multi-pass in-well pumping twenty quantum well MECSEL at 10 °C chiller temperature, with a slope efficiency of 28%. The output spectrum (inset) was measured at the absorbed power of 70 W.

with challenges in achieving optimal beam overlap and setup stability for a large number of passes.

In the multi-pass in-well pumping experiment illustrated in Fig. 5.5, a maximum output power of 28.5 W was achieved without encountering thermal rollover, indicating that the system was limited by the available pump power rather than thermal constraints. The slope efficiency recorded was 28.0%, noticeably lower than that observed in the single-pass in-well pumping setup. This reduction in efficiency is attributed to the less-than-ideal overlap between the multiple pump spots and the laser cavity mode on the MECSEL gain chip as shown with the Zemax simulation, which compromised the efficiency of the energy transfer. The output spectrum, as captured by an OSA at 70 W of absorbed pump power, exhibited multi-longitudinal-mode operation with a center wavelength at 1174 nm and a linewidth (FWHM) of 3 nm. The

mode separation, measured at approximately 0.5 nm, matches the FSR of a 500 µm thick SiC heat spreader, suggests that etalon effect within the gain chip contributes in shaping the laser's output spectrum. This etalon consists of one surface at the membrane/SiC interface and the other at the external facet of the SiC heat spreader. To further eliminate this etalon effect, the current 1070 nm AR coating needs to be adjusted to also be AR at the 1178 nm laser wavelength. The rule of thumb for an effective AR coating is to have less than 0.1% reflection at the design wavelengths.

5.4 Wavelength Tuning

A 2 mm thick quartz BRF placed on a rotation mount was integrated into the laser cavity of the twenty quantum well MECSEL to facilitate wavelength tuning and narrow the linewidth, aiming to achieve the 1178 nm output necessary for LGS applications. The resulting normalized laser output spectra, measured with 40 W of absorbed pump power at 1070 nm, are depicted in Fig. 5.6. The spectral tuning range achieved spanned 71 nm, from 1124 nm to 1195 nm, aligning with the tuning capabilities observed in the previous experiments with the 808 nm barrier pumped eleven quantum well MECSEL [113]. The peak emission under these conditions occurred at approximately 1160 nm, deviating from the target wavelength of 1178 nm. This shift can be attributed to the thermal characteristics of the MECSEL gain chip, which was specifically designed to reach peak emission at 1178 nm only upon approaching the thermal rollover temperature around 100 °C [93, 94].

With the chiller temperature set to 10 °C, the laser output wavelength was tuned to 1178 nm by adjusting the BRF within the cavity. The relationship between the output power at this wavelength and the absorbed pump power is plotted in Fig. 5.7. The maximum output recorded was 17.9 W with 100 W of absorbed pump power, marking a considerable improvement over

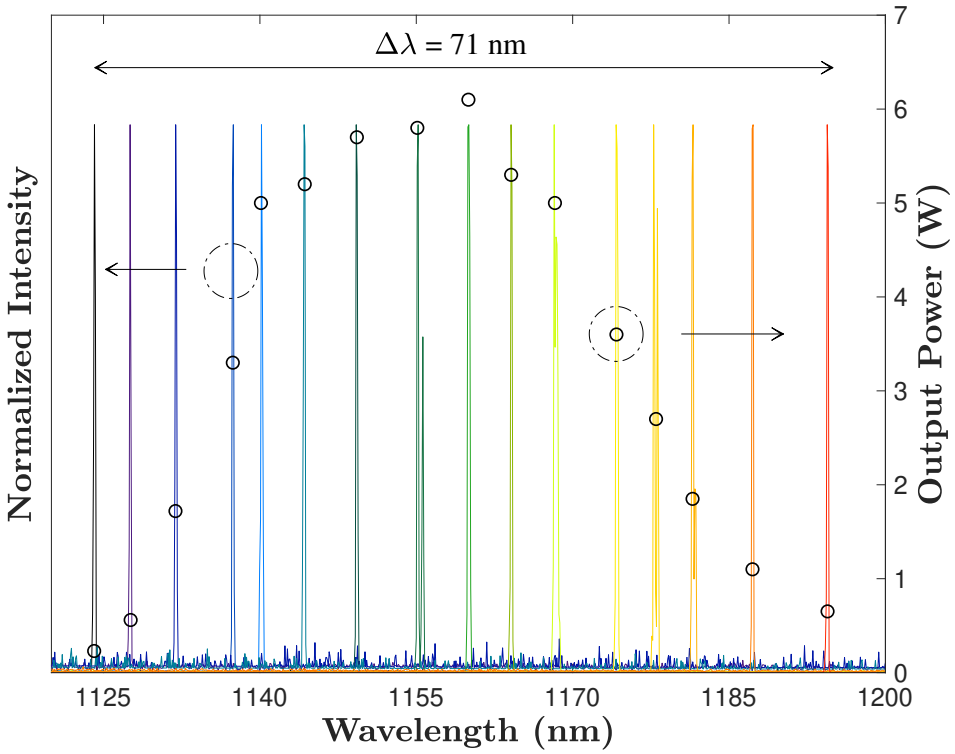

Fig. 5.6 Normalized spectra for the twenty quantum well MECSEL gain chip with 40 W absorbed pump power and a chiller temperature of 10 °C [112]. Wavelength tuning was achieved by rotating a 2 mm thick quartz BRF.

the 12.8 W output at 1178 nm achieved previously with the eleven quantum well MECSEL employing barrier pumping [113]. The observed slope efficiency of 21.3% is reduced from that in free-running operation, attributed to the extra intracavity losses imposed by the quartz BRF. The insets, captured at 75 W of absorbed pump power, provide additional insights. The bottom right inset displays the laser output spectrum with a linewidth (FWHM) of 0.4 nm, as measured by an OSA with a resolution of 0.06 nm. The top left inset shows the transverse mode profile of the laser beam, captured using an Ophir beam profiler, which reveals an asymmetric shape, which can result from the non-ideal ratio between the pump and cavity mode [135]. The wavy slope of the output curve suggests the presence of a pump power-related thermal lens within the

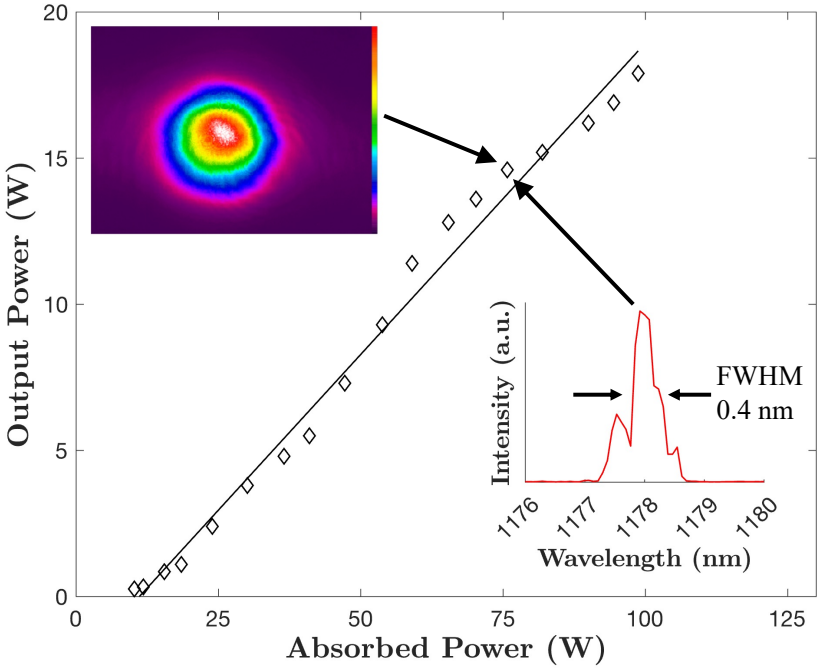

Fig. 5.7 Output power at 1178 nm versus absorbed pump power at 10 °C chiller temperature. The beam profile (top-left) and spectrum (bottom-right) were recorded at 75 W of absorbed pump power [112].

MECSEL gain chip. As the thermal lens power changes, the cavity mode size on the gain chip adjusts accordingly, leading to a mismatch between the pump and cavity modes as pump power increases. A thorough analysis of the thermal lens within the gain chip is necessary to optimize the laser cavity design.

5.5 Conclusion

This chapter presents a detailed experimental investigation of in-well pumping for reducing the quantum defect and improving the thermally-limited output power of MECSELs in LGS applications. The experiments compared twenty quantum well MECSEL gain chips using in-well pumping at 1070 nm and barrier pumping at 808 nm. The slope efficiency for barrier

pumping was 22.4%, while in-well pumping achieved a significantly higher slope efficiency of 39.5% for a single pass. With an aspheric-lens-based multi-pass in-well pumping design, a 28.5 W output was delivered with a slope efficiency of 28.0% at a chiller temperature of 10 °C. This system demonstrated pump power limitation without thermal rollover even at higher chiller temperatures and achieved a 17.9 W output at 1178 nm with a 2 mm thick BRF for wavelength tuning. The enhanced output at 1178 nm through in-well pumping significantly advanced the development of semiconductor-based LGS. However, challenges such as aligning the multi-pass pumping scheme necessary for further simplification of the design.

In addition, the asymmetric beam profile needs to be improved to meet LGS specifications. Achieving precise mode matching between the pump and the laser cavity mode is essential for optimizing the laser's output and ensuring a symmetric beam profile, a important factor for the consistent performance of LGS systems. The presence of a pump power-related thermal lens challenges maintaining good mode matching as pump power increases. A rigorous analysis of thermal lens within the gain chip is necessary. Using these results, a thermal lens-insensitive laser cavity can be designed to address the mode mismatch problem.

Chapter 6

Hybrid Membrane External-Cavity Surface-Emitting Laser

To address the thermal limitation that curtails the maximum achievable output power of MECSELs, the in-well pumping method was proposed and implemented experimentally. This method reduces heat generation within the MECSEL structure but introduces the challenge of low absorption of the incident pump beam. To enhance the efficiency of the system given the low absorption, pump beam recycling was employed for a transmissive MECSEL gain chip. Although this setup effectively recycled the pump beam, thereby satisfying the output power requirements for LGS applications, the multi-pass pumping scheme is time-consuming to align and is not ideal for practical use. Furthermore, the thermal lensing effect within the gain chip necessitates thorough investigation, with the goal of designing a laser cavity less sensitive to thermal lensing and solving the transverse mode issues.

Reflective samples like VECSEL gain chips, as analyzed in the simulations from Chapter 4, typically allow for simpler and more robust multi-pass pumping designs compared to their transmissive counterparts. Traditional VECSELs inherently include a DBR, which simplifies

multi-pass pumping designs. This raises the question of why a DBR would be reintroduced into a MECSEL, given that MECSELs are designed to be DBR-free. The rationale for integrating a DBR back into a MECSEL lies in enhancing specific capabilities. By growing the gain structure and DBR separately and having a heat spreader between active region and DBR, issues such as lattice mismatching between the gain structure and DBR, and a fixed global laser mode near the gain structure, are resolved. MECSELs excel in heat dissipation due to the direct contact between the membrane and heat spreaders, allowing higher output power before reaching thermal rollover compared with conventional VECSELs. By adding a DBR to a MECSEL gain chip outside the heat spreader, the design retains this heat dissipation while also utilizing the reflective feature that potentially could simplify the multi-pass pumping scheme. This is important for improving light absorption in the gain medium as discussed in Chapter 4. This hybrid approach combines the good heat dissipation ability of MECSELs with the reflective feature of VECSELs. Thus, including a DBR in a MECSEL is a strategic move to harness the best attributes of both designs: MECSELs' thermal advantages and VECSELs' simple optical design. This new MECSEL variant, termed Hybrid Membrane External-cavity Surface-emitting Laser (H-MECSEL), is introduced in this chapter. This H-MECSEL design was introduced at the SPIE Photonics West Conference [74] and the OPTICA CLEO Conference [115]. This chapter provides a more detailed analysis of the design.

6.1 H-MECSEL Gain Chip

As depicted in Fig. 6.1, the H-MECSEL sample resembles a traditional MECSEL but incorporates an additional DBR or HR coating directly bonded to one external facet of the gain heat spreader sandwich. The active region of H-MECSEL is the same as Fig. 5.1, with the same fabrication procedure to directly bond in between two 500 µm-thick SiC heat spreaders [105].

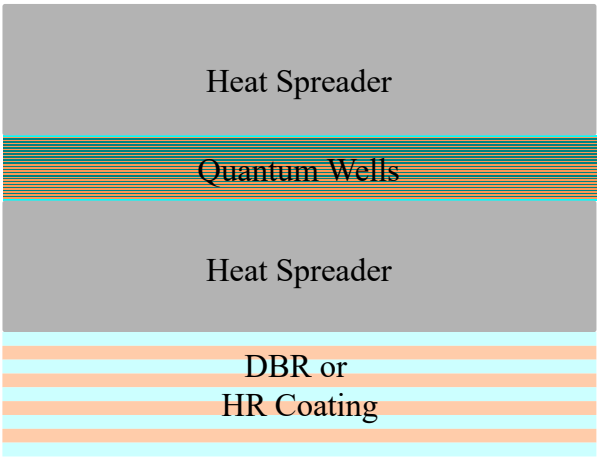

Fig. 6.1 Schematic diagram of a H-MECSEL gain chip.

The distance between the gain structure and the DBR is much shorter than the distance between a cavity mirror and gain structure in a standard MECSEL. However, comparing the optical path length of the 500 µm SiC heat spreader to the laser wavelength of 1.178 µm, there remains sufficient flexibility in the laser mode. Thus, the H-MECSEL is a modified MECSEL rather than a VECSEL, even though a DBR has been integrated onto the heat spreader sandwich.

The structural differences between VECSELs, MECSELs, and H-MECSELs significantly influence their thermal management and efficiency, as depicted in Fig. 6.2 [20]. VECSELs traditionally use a heat sink positioned directly behind the DBR, with a heat spreader sandwiched between. The heat flow must travel from the active region through the high thermal impedance DBR before reaching the heat spreader, significantly reducing the effectiveness of thermal management. This arrangement facilitates 1D heat flow from the gain region to the heat sink, which motivates power scaling by increasing the spot size. In contrast, MECSELs have open apertures at the front and back of the heat sink, causing heat in the active region and heat spreader to transfer laterally before reaching the heat sink. However, MECSELs improve the heat transfer by omitting the DBR, which in VECSELs can absorb pump light and generate additional heat. Without the DBR, the active region in MECSELs is closer to the heat spreader,

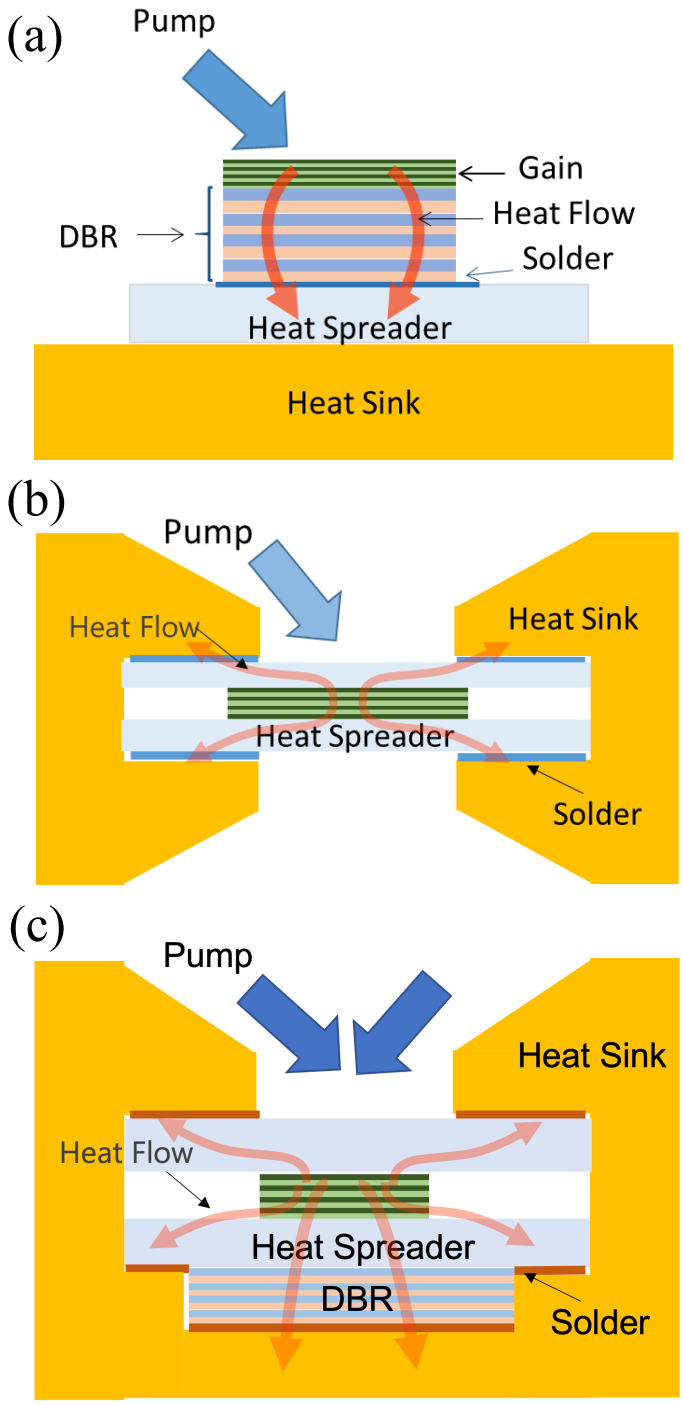

Fig. 6.2 Schematic diagrams of (a) VECSEL [20], (b) MECSEL [20], and (c) H-MECSEL gain chips [20] that are mounted on their heat sinks.

allowing heat to dissipate more effectively in both directions into the heat spreaders towards the heat sink. The direct contact with the active region reduces the thermal barrier between the heat-generating components and the heat sink. As a result, even without 1D heat flow from the gain region to the heat sink, MECSELs still exhibit better heat dissipation compared to VECSELs.

H-MECSELs modify thermal management by reintroducing a DBR outside a heat spreader. Although adding the DBR increases thermal impedance and worsens heat transfer from the heat spreader to the heat sink, and the DBR may absorb some pump power and generate extra heat, this modification still improves heat management for the following reasons. First, closing the aperture on the back of the heat sink makes 1D heat flow possible again on one side of the gain chip, while the other side retains the MECSELs' lateral heat transfer within the active region and heat spreader before reaching the heat sink. Second, the active region maintains direct contact with the heat spreader, effectively dissipating heat within the gain area. Lowering the maximum temperature within the active region is important for preventing thermal rollover, and the temperature increase within the heat spreader does not contribute to this issue. Additionally, with a heat spreader between the DBR and the active region, the small amount of heat generated within the DBR does not significantly contribute to the maximum temperature in the active region. Thus, H-MECSELs can surpass both VECSELs and traditional MECSELs in thermal management, supporting higher power outputs.

6.2 Dual-Band DBR

Building upon the expertise of our collaborator at THORLABS CRYSTALLINE SOLUTIONS, renowned for their proficiency in high-performance DBR design and fabrication [136], a dual-band DBR was integrated onto the H-MECSEL heat spreader/gain structure sandwich. This

dual-band DBR [137] was designed to provide HR at both the 1070 nm pump wavelength and the 1178 nm laser emission wavelength. The DBR's design is rooted in the methodologies established by C.P. Lee, utilizing an $Al_{0.92}Ga_{0.08}As$/GaAs multi-layer structure [138]. The DBR is HR at both wavelengths by incorporating a bi-periodic function derived from the periodic functions of these two targeted wavelengths. This dual periodicity is described by the equation

$$\sin\left(\frac{\pi x}{d_1}\right) + \sin\left(\frac{\pi x}{d_2}\right), \tag{6.1}$$

where d_1 and d_2 represent the quarter-wavelength thicknesses of the AlGaAs and GaAs layers for the 1070 nm and 1178 nm wavelengths, respectively. This expression can be transformed into:

$$2\sin\left(\frac{\pi x}{d}\right)\cos\left(\frac{\pi x}{D}\right), \tag{6.2}$$

where d is the average of the quarter-wavelengths, defined as $\frac{1}{d} = \frac{1}{2}\left(\frac{1}{d_1} + \frac{1}{d_2}\right)$, and D is the difference between these wavelengths, defined as $\frac{1}{D} = \frac{1}{2}\left(\frac{1}{d_1} - \frac{1}{d_2}\right)$.

The resultant bi-periodic structure, if translated from sine and cosine functions into square waveforms, provides a practical blueprint for experimental fabrication. The smaller period d correlates to the quarter-wavelength of an intermediary wavelength, λ_{new}, which lies between 1070 nm and 1178 nm. If the larger period D is set to be an integer multiple C times the smaller period d, the structure will exhibit two distinct reflective peaks at:

$$\lambda_1 = \frac{C}{C+1}\lambda_{\text{new}}, \tag{6.3}$$

and

$$\lambda_2 = \frac{C}{C-1}\lambda_{\text{new}}. \tag{6.4}$$

These peaks correspond precisely to the design wavelengths, ensuring optimal performance of the H-MECSEL across both the pump and emission wavelengths. Researchers in the MECSEL community have also explored the use of a single band to cover both the pump and laser wavelengths [139], but it cannot achieve the same high reflectance on both wavelengths as this dual-band DBR could offer.

The dual-band DBR structure, specifically designed and fabricated by Dr. Garrett Cole, a collaborator in the project, was optimized to provide high reflectivities at the laser and the pump wavelengths. Utilizing an intermediary wavelength of $\lambda_{\text{new}} = 1108.5\,\text{nm}$ and setting $C = 10$. This DBR comprises five identical stacks, with each stack containing ten pairs of $Al_{0.92}Ga_{0.08}As$/GaAs quarter-wavelength layers. These layer pairs are specifically designed to match the quarter-wavelength optical thickness at 1108.5 nm. To effectively separate each of these stacks and to match the thickness of large period D, a half-wavelength layer of GaAs was incorporated between each stack. Additionally, to improve the thermal contact between these optical layers and the copper heat sink, the entire structure was backed with a metal layer consisting of Ti/Au, which also serves to enhance the reflectivity. As depicted in Fig. 6.3, the reflectance diagram of this dual-band DBR shows an extraordinarily high reflectance at the pump wavelength of 1070 nm (blue) at 99.997%. This high reflectance is crucial for ensuring efficient recycling of the pump beam within the multi-pass pumping structure of the H-MECSEL. The reflectance at the laser emission wavelength of 1178 nm (red) also achieves a very high level at 99.93%, which is critical for maintaining low losses. The design was purposely blueshifted, to account for parasitic heating that would cause the mirror to redshift on both bands for pump and laser wavelengths.

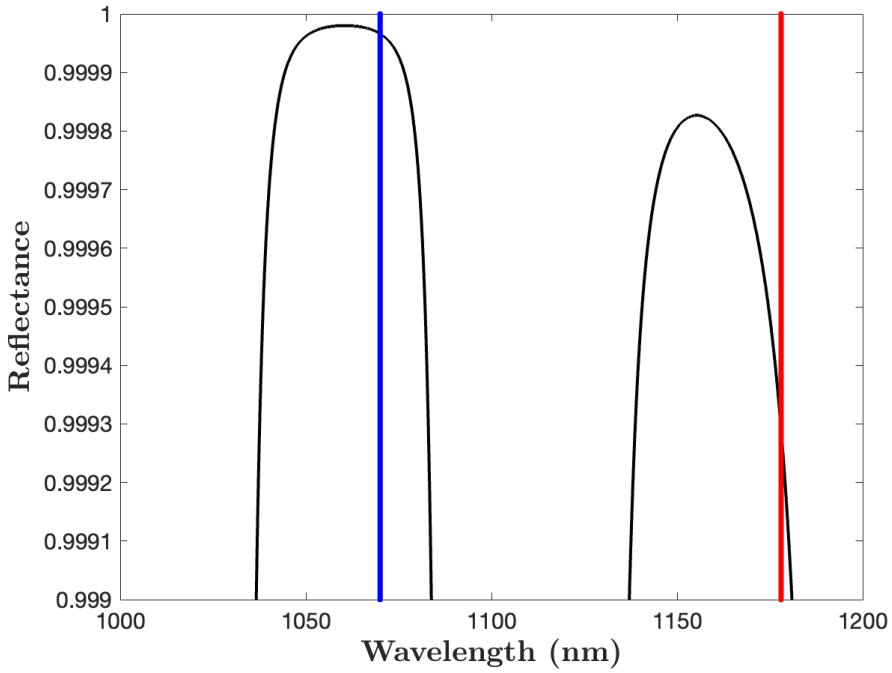

Fig. 6.3 Reflectance of a dual-band DBR that was experimentally used for constructing H-MECSEL LGS. The structure achieves high reflectivity (>99.9% reflectance) at both 1070 nm (blue) pump wavelength and 1178 nm (red) laser wavelength.

6.3 Thermal Analysis

Finite element method (FEM) simulations were conducted using the commercial software COMSOL to analyze the thermal performance of various configurations, including the H-MECSEL. As depicted in Fig. 6.4 (a), the simulated H-MECSEL structure featured two 500 µm thick SiC heat spreaders and heat sinks positioned on both sides of the gain sandwich structure. A more detailed view of the internal structure is shown in Fig. 6.4 (b), where the meshing strategy is highlighted. A finer mesh was employed for thin layers such as the active region and the DBR to capture detailed thermal gradients, while normal mesh was applied to intermediate thickness regions like the indium layers and heat spreaders. Coarse mesh was utilized in the

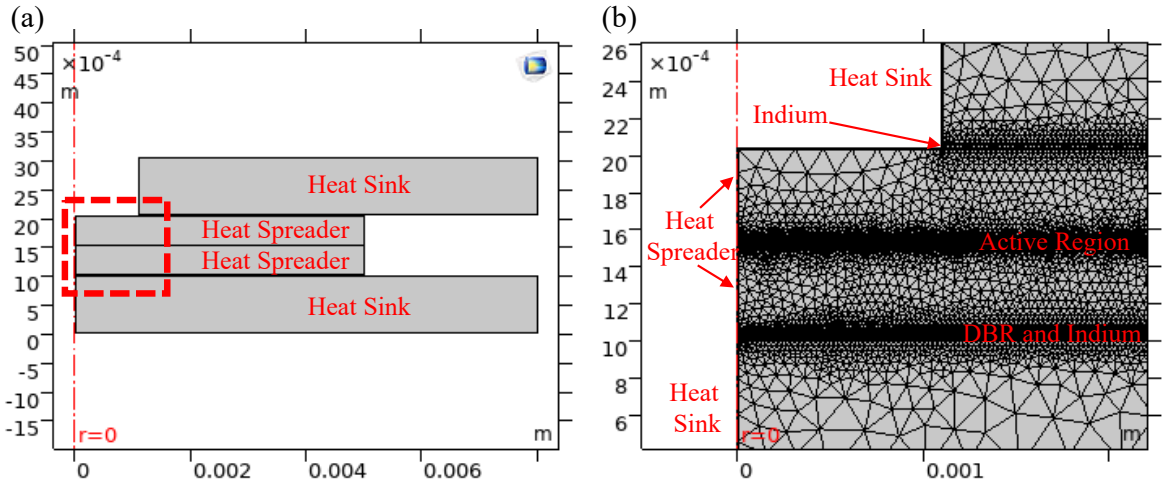

Fig. 6.4 (a) COMSOL structure of a H-MECSEL sample with two 500 µm thick SiC heat spreader, and the area within the red box was detailed with mesh structure in (b).

heat sink regions to optimize computational resources without compromising the accuracy in less thermally active areas.

The heat transfer within the system was modeled using the heat transfer equation [4]:

$$\rho c_p \frac{\partial T}{\partial t} - \nabla \cdot (\kappa \nabla T) = H, \tag{6.5}$$

where ρ represents the material density, c_p is the specific heat capacity, T denotes the temperature, κ is the thermal conductivity, and H is the heat supplied to the system. The simulation aimed to reach a steady state condition, defined by $\frac{\partial T}{\partial t} = 0$, under a boundary condition that maintained a constant temperature at a specific layer inside the heat sink, positioned 1 mm from the interface between the heat spreader and the heat sink. This boundary condition was based on the experimental setup, where the copper heat sink was liquid-cooled, ensuring adequate removal of heat from the system. These simulations are important for understanding thermal behavior within H-MECSEL gain chips. By modeling the temperature distribution within the

laser structure, potential hot spots can be identified and the effectiveness of the heat spreaders and the overall design can be evaluated.

Several approximations were implemented to enhance computational efficiency and focus on key thermal behaviors in FEM simulations. Material properties such as density (ρ) and thermal conductivity (κ) were assumed to be temperature-independent to avoid the complexities associated with their variation. The heat source was modeled to emulate the Gaussian distribution of the pump beam's intensity, formulated as $P_{\text{heat}}(r) = P_0 e^{-\frac{2r^2}{w_{\text{p}}{}^2}}$, where P_0 is the pump power, r is the radial distance from the beam center, and w_{p} is the beam radius. This model simplifies the actual heat generation mechanisms, and multi-layer structures were approximated as single layers to reduce the simulation's complexity, ignoring the variations within layers but maintaining an overall assessment of thermal behavior. Perfect bonding was assumed between interfaces such as the active region and heat spreader, and between the DBR and heat spreader, eliminating potential defects or roughness that could affect thermal contact.

The model was simplified to cylindrical symmetry with the assumption that the Gaussian-shaped pump beam was centrally incident. This assumption significantly reduces computational demands by transforming a potentially three-dimensional problem into a two-dimensional one. The steady-state heat transfer equation was adapted to these simplifications and expressed as:

$$\frac{1}{r}\frac{\partial}{\partial r}\left(\kappa r\frac{\partial T}{\partial r}\right)+\frac{\partial}{\partial z}\left(\kappa\frac{\partial T}{\partial z}\right)+H(r,z)=0, \tag{6.6}$$

where $H(r,z)$ denotes the heat generated per unit volume, dependent on the radial position r and depth z.

And $H(r,z)$ can be written as a combination of the heat generation within the active region (H_{g}) and DBR (H_{d}) was detailed by [72]:

$$H_{\mathrm{g}}(r,z) = \frac{2\eta_{\mathrm{g}}P}{\pi {w_{\mathrm{p}}}^2} e^{-\frac{2r^2}{{w_{\mathrm{p}}}^2}} e^{-\alpha_{\mathrm{g}}(z_{0\mathrm{g}}-z)}, \tag{6.7}$$

and

$$H_{\mathrm{d}}(r,z) = \frac{2\eta_{\mathrm{d}}P}{\pi {w_{\mathrm{p}}}^2} e^{-\frac{2r^2}{{w_{\mathrm{p}}}^2}} e^{-\alpha_{\mathrm{d}}(z_{0\mathrm{d}}-z)} e^{-\alpha_{\mathrm{g}}d_{\mathrm{g}}}, \tag{6.8}$$

highlighting the spatial distribution of heat generation with efficiency factors η_{g} and η_{d}, and absorption coefficients α_{g} and α_{d}, $z_{0\mathrm{d}}$ is the depth of DBR top surface, and d_{g} is the thickness of the active region.

In the computational analysis of the H-MECSEL structure, certain assumptions were made regarding the absorption coefficients in different layers to simplify the thermal modeling. The ratio of absorbed power converting to heat in gain (η_{g}) was set to 0.4 for 808 nm pump slightly higher than the quantum defect to account for additional heat generated from non-radiative recombination and fabrication imperfection. The ratio of absorbed power converting to heat in the DBR (η_{d}) of 100% was initially considered, assuming complete absorption of any residual pump energy within this layer. However, this assumption is typically not valid in scenarios employing in-well pumping, where the majority of the residual pump beam is reflected rather than absorbed, contributing minimally to heat generation within the DBR. Given these considerations, the heat generation equations were modified to incorporate parameters for heat intensity (I_{H}) and beam area (A)

$$H_{\mathrm{g}}(r,z) = \frac{2I_{\mathrm{H}}A}{\pi {w_{\mathrm{p}}}^2} e^{-\frac{2r^2}{{w_{\mathrm{p}}}^2}} e^{-\alpha_{\mathrm{g}}(z_{0\mathrm{g}}-z)}, \tag{6.9}$$

and

$$H_{\mathrm{d}}(r,z) = \frac{2\eta_{\mathrm{DBR}} I_{\mathrm{H}} A}{\pi {w_{\mathrm{p}}}^2} e^{-\frac{2r^2}{{w_{\mathrm{p}}}^2}} e^{-\alpha_{\mathrm{d}}(z_{0\mathrm{d}}-z)}, \tag{6.10}$$

where η_{DBR} is the relative efficiency of heat generation in the DBR compared to the active region. In the simulations, η_{DBR} was conservatively set to 5% of the heat generated in the active region. This equates to 0.25% of the input pump power if 50% of the pump is absorbed and 10% of that is converted into heat within the active region. Despite the DBR being over 99.9% HR at the pump wavelength, the multi-pass pumping scheme can result in more than 0.1% absorption within the DBR. This thermal analysis is conservative and may underestimate the thermal management capacity, but considering the DBR's small contribution to the overall thermal load within the structure, it is a reasonable estimation. The maximum temperature point consistently occurs within the active region from the author's simulation and other previous work [4]. With a 500 µm thick heat spreader between the DBR and the active region, the DBR's contribution to the maximum temperature within the gain chip is minimal. Simulation results indicated that varying η_{DBR} from 5% to 10% only marginally increased the maximum temperature by less than 5 °C for H-MECSEL samples equipped with 500 µm thick SiC heat spreaders under a heat dissipation condition of 100 W. The dissipated heat can be described by

$$P_{\mathrm{diss}} = P_{\mathrm{abs}} - P_{\mathrm{out}}, \tag{6.11}$$

where P_{abs} is the absorbed pump power and P_{out} is the laser output power.

In the thermal modeling of H-MECSEL structures using COMSOL, effective thermal conductivities for various material layers were calculated to ensure accurate simulation of heat transfer within the device. This calculation integrates the thickness and thermal conductivity of

each constituent material layer using the following formula:

$$\frac{d_{\mathrm{g}}}{\kappa_{\mathrm{g}}} = \frac{d_{\mathrm{GaAs}}}{\kappa_{\mathrm{GaAs}}} + \frac{d_{\mathrm{GaAsP}}}{\kappa_{\mathrm{GaAsp}}} + \frac{d_{\mathrm{InGaAs}}}{\kappa_{\mathrm{InGaAs}}}, \tag{6.12}$$

where d and κ represent the thickness and thermal conductivity, respectively, for GaAs, GaAsP, and InGaAs layers within the gain structure. This method overlooks the nonuniform and fine structures within the active region, thus ignoring the interfaces of these fine structures, which is a primary reason for the low thermal conductivity of DBRs. However, this approximation is necessary to save calculation time. Based on this calculation, the effective thermal conductivity of the gain area was approximated to be $35\,\mathrm{W}/(\mathrm{m}\cdot\mathrm{K})$. The thermal conductivity of the dual-band AlGaAs/GaAs DBR was similarly computed, resulting in an approximate value of $25\,\mathrm{W}/(\mathrm{m}\cdot\mathrm{K})$.

The specific parameters used in the COMSOL simulations were systematically organized into two modules, Module A and B, as detailed in Tables 6.1. If not explicitly listed separately, parameters are the same for both Module A and B. Module A corresponds to the parameters matching those of the H-MECSEL sample tested experimentally, featuring a twenty quantum well active region designed for in-well pumping and equipped with a thick dual-band DBR. Module B, on the other hand, represents a configuration typical of a standard VECSEL or MECSEL, with a thinner active region and DBR, typically used in structures pumped by diodes [4]. Consistent with previous thermal simulations for similar structures, Module B used a relatively high thermal conductivity for the DBR [67, 140]. This assumption, while an overestimation, aligns with potential realizations in hybrid semiconductor/metal structures [66]. All simulations within this chapter employed a Gaussian heat source with a constant heat intensity of $40\,\mathrm{kW}/\mathrm{cm}^2$, unless specified otherwise, to model the heat distribution across

Table 6.1 Parameters for COMSOL thermal simulation of gain Module A and B [4, 114].

Parameter	Description	Value	Unit
α_{g}	absorption coefficient of active region	1	$\mu\mathrm{m}^{-1}$
α_{DBR}	absorption coefficient of DBR	0.457	$\mu\mathrm{m}^{-1}$
$\mathrm{C}_{\mathrm{InGaP}}$	thermal capacity of window layer	368.8	$\mathrm{J/kg\cdot K}$
C_{g}	thermal capacity of active region	330	$\mathrm{J/kg\cdot K}$
$\mathrm{C}_{\mathrm{DBR}}$	thermal capacity of DBR	394.7	$\mathrm{J/kg\cdot K}$
$\mathrm{C}_{\mathrm{SiC}}$	thermal capacity of SiC	670	$\mathrm{J/kg\cdot K}$
$\mathrm{C}_{\mathrm{diamond}}$	thermal capacity of diamond	520	$\mathrm{J/kg\cdot K}$
$\mathrm{C}_{\mathrm{copper}}$	thermal capacity of copper	385	$\mathrm{J/kg\cdot K}$
κ_{InGaP}	thermal conductivity of window layer	10	$\mathrm{W/(m\cdot K)}$
κ_{g}	thermal conductivity of active region	A: 35 B: 24	$\mathrm{W/(m\cdot K)}$
κ_{DBR}	thermal conductivity of DBR	A: 25 B: 61	$\mathrm{W/(m\cdot K)}$
κ_{In}	thermal conductivity of indium	84	$\mathrm{W/(m\cdot K)}$
κ_{SiC}	thermal conductivity of 4H-SiC	390	$\mathrm{W/(m\cdot K)}$
$\kappa_{\mathrm{diamond}}$	thermal conductivity of diamond	1800	$\mathrm{W/(m\cdot K)}$
κ_{copper}	thermal conductivity of copper mount	400	$\mathrm{W/(m\cdot K)}$
ρ_{InGaP}	mass density of window layer	4.482×10^{3}	$\mathrm{kg/m^3}$
ρ_{g}	mass density of active region	5.320×10^{3}	$\mathrm{kg/m^3}$
ρ_{DBR}	mass density of DBR	4.479×10^{3}	$\mathrm{kg/m^3}$
ρ_{SiC}	mass density of SiC	3.210×10^{3}	$\mathrm{kg/m^3}$
ρ_{diamond}	mass density of diamond	3.515×10^{3}	$\mathrm{kg/m^3}$
ρ_{copper}	mass density of copper	8.700×10^{3}	$\mathrm{kg/m^3}$
ρ_{In}	mass density of indium	7.310×10^{3}	$\mathrm{kg/m^3}$
d_{InGaP}	thickness of window layer	214	nm
d_{g}	thickness of active region	A: 3.56 B: 2.25	µm
d_{DBR}	thickness of DBR	A: 9.07 B: 3.72	µm
d_{In}	thickness of indium	20	µm
d_{SiC}	thickness of SiC	500	µm
d_{SiC}	thickness of diamond	500	µm
$\frac{dn}{dT}\vert_{\mathrm{SiC}}$	thermo-optic coefficient of 4H-SiC	3.5×10^{-5}	$1/\mathrm{K}$
$\frac{dn}{dT}\vert_{\mathrm{diamond}}$	thermo-optic coefficient of 4H-SiC	9.6×10^{-6}	$1/\mathrm{K}$

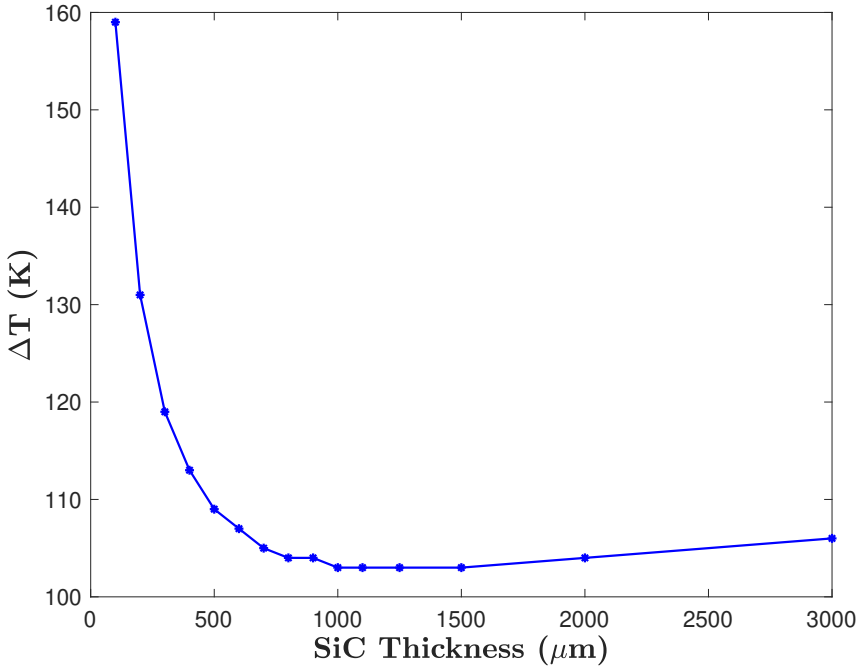

Fig. 6.5 Maximum temperature increase versus thickness of one of the two identical SiC (Dual-heat spreader H-MECSEL) for gain module A under 80 W of dissipated heat.

the device effectively. To change the pump power, a standard power scaling method was implemented by adjusting the pump beam mode size while maintaining constant intensity.

In a detailed simulation conducted to investigate the thermal management capabilities of a dual-SiC heat spreader H-MECSEL gain element, the impact of SiC thickness on the maximum temperature within the gain structure was thoroughly analyzed. The simulation utilized the gain module A configuration, 80 W of dissipated heat was implemented. The resulting data is depicted in Fig. 6.5, which illustrates the temperature variation in relation to the SiC heat spreader thickness. The graph demonstrates a distinct trend where increasing the thickness of SiC initially leads to a reduction in the maximum temperature within the gain structure. This trend continues favorably until the SiC thickness reaches approximately 1 mm. Beyond this point, further increases in thickness do not enhance thermal performance; instead, resulting in a

higher maximum temperature. For the specific SiC heat spreader thickness of 500 µm used in the experimental setup, the simulation predicted an increase in temperature of approximately 110 °C, and this temperature rise nears the thermal rollover even under 0 °C cooling conditions.

In a comprehensive analysis conducted using FEM simulations, the thermal management of eight different SDL structures was examined. This analysis included a variety of VECSELs, MECSELs, and H-MECSELs, each depicted in Fig. 6.6. These configurations were specifically chosen to explore different approaches optimizing thermal performance within these systems. The study encompassed VECSELs with three distinct arrangements: a single bottom heat spreader, an intracavity heat spreader, and dual heat spreaders positioned on each side of the active region. For MECSELs, configurations with either one or two heat spreaders were evaluated. H-MECSEL configurations included setups with a single heat spreader accompanied by two heat sinks, and variations with one or two heat spreaders coupled with dual heat sinks. The simulations highlighted the thermal behavior of these configurations under operational conditions, with orange lines in the figures indicating the surfaces where the temperature remained constant at 10 °C.

In the analysis of module A using FEM simulations, the thermal performance of various structures equipped with either diamond or SiC heat spreaders was evaluated. The results, illustrated in Fig. 6.7, reveal that the H-MECSEL (iii) configuration consistently achieves superior thermal management compared to other structures under all tested conditions of dissipated heat, for both types of heat spreaders. The simulation clearly demonstrates that diamond heat spreaders possess a significantly higher thermal conductivity than SiC, allowing them to dissipate up to five times more heat before reaching the thermal rollover range, defined as $90\,^{\circ}\mathrm{C} < T_{\mathrm{max}} < 110\,^{\circ}\mathrm{C}$ [93, 67]. This enhanced capability makes diamond an ideal material for heat spreaders in high-performance laser applications due to its high thermal conductivity. Despite diamond's superior performance, SiC was chosen for the heat spreaders in this disserta-

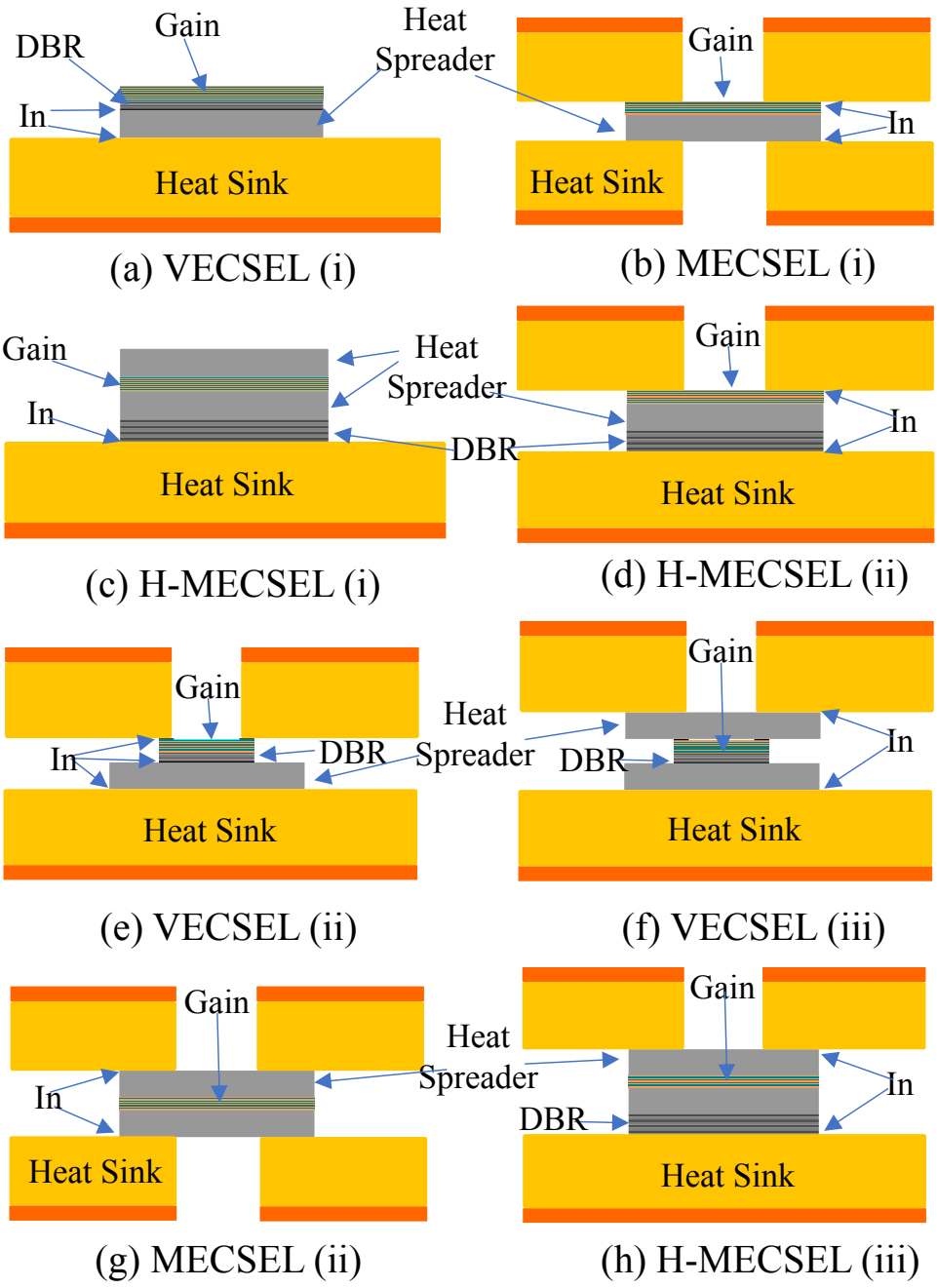

Fig. 6.6 Eight different VECSEL, MECSEL, and H-MECSEL geometries that were employed in the COMSOL simulations.

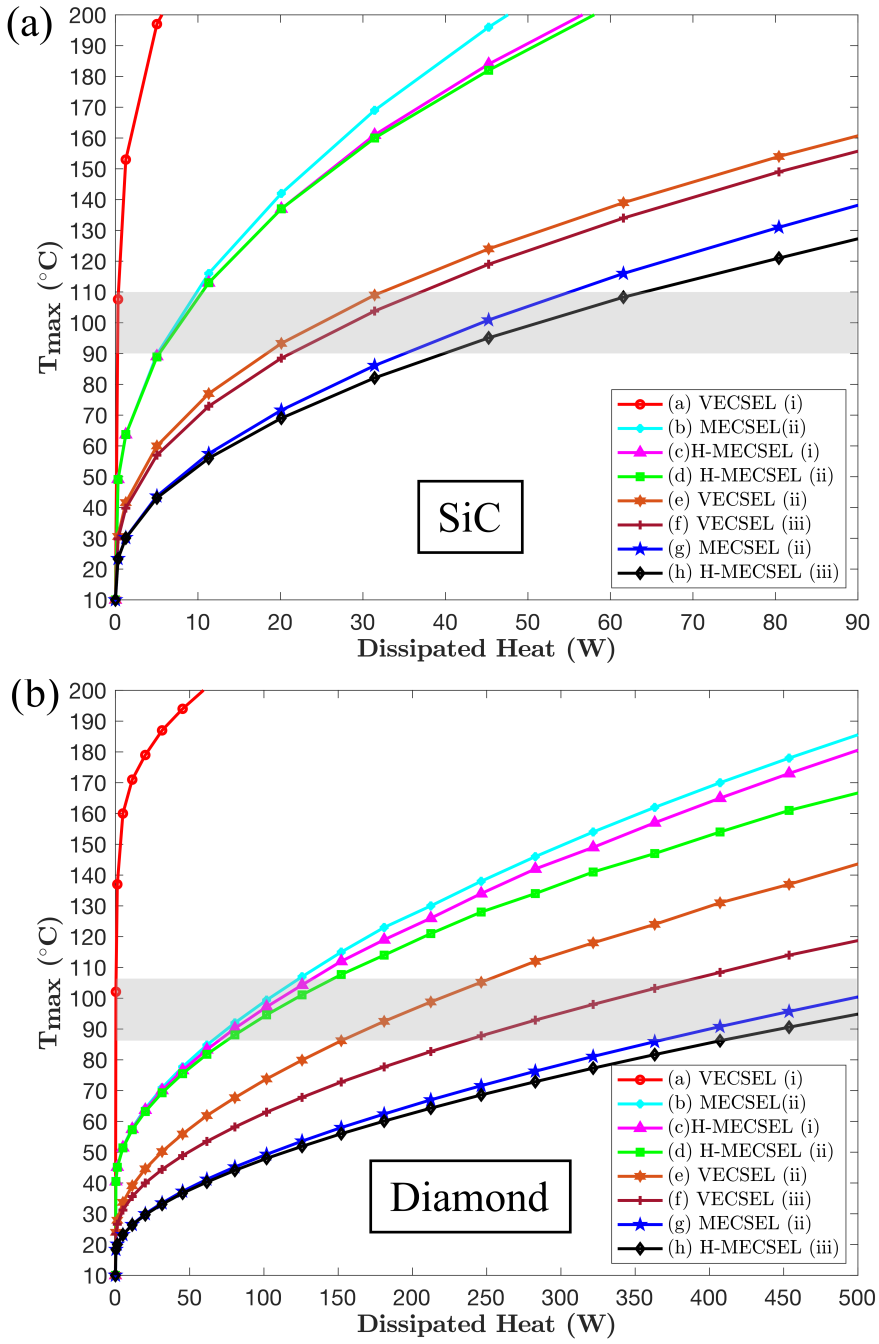

Fig. 6.7 Maximum temperature within the gain chip for eight different structures for Module A parameters versus dissipated heat, with two different heat spreader materials, (a) SiC and (b) diamond [114]. The shaded temperature range indicates the region where thermal rollover is expected to occur.

tion project due to considerations of cost and ease of fabrication. Based on the simulations, it is estimated that the H-MECSEL (iii) structure with SiC heat spreaders can effectively dissipate up to 50 watts of heat without surpassing the thermal rollover temperature threshold of 100 °C.

The simulation results for module B, as depicted in Fig. 6.8, corroborate the findings from module A, further establishing that the H-MECSEL (iii) structure with dual heat spreaders outperforms all other configurations examined. When diamond is employed as the heat spreader material, the capacity for heat dissipation can be increased by up to tenfold before nearing the thermal rollover range. Module B's superior thermal performance is partly attributed to its thinner active region and DBR, which collectively lead to a lower maximum temperature ($T_{\max}$) under identical conditions of heat dissipation. This configuration not only aligns with, but also expands upon previous studies regarding the thermal management in VECSELs and MECSELs [4].

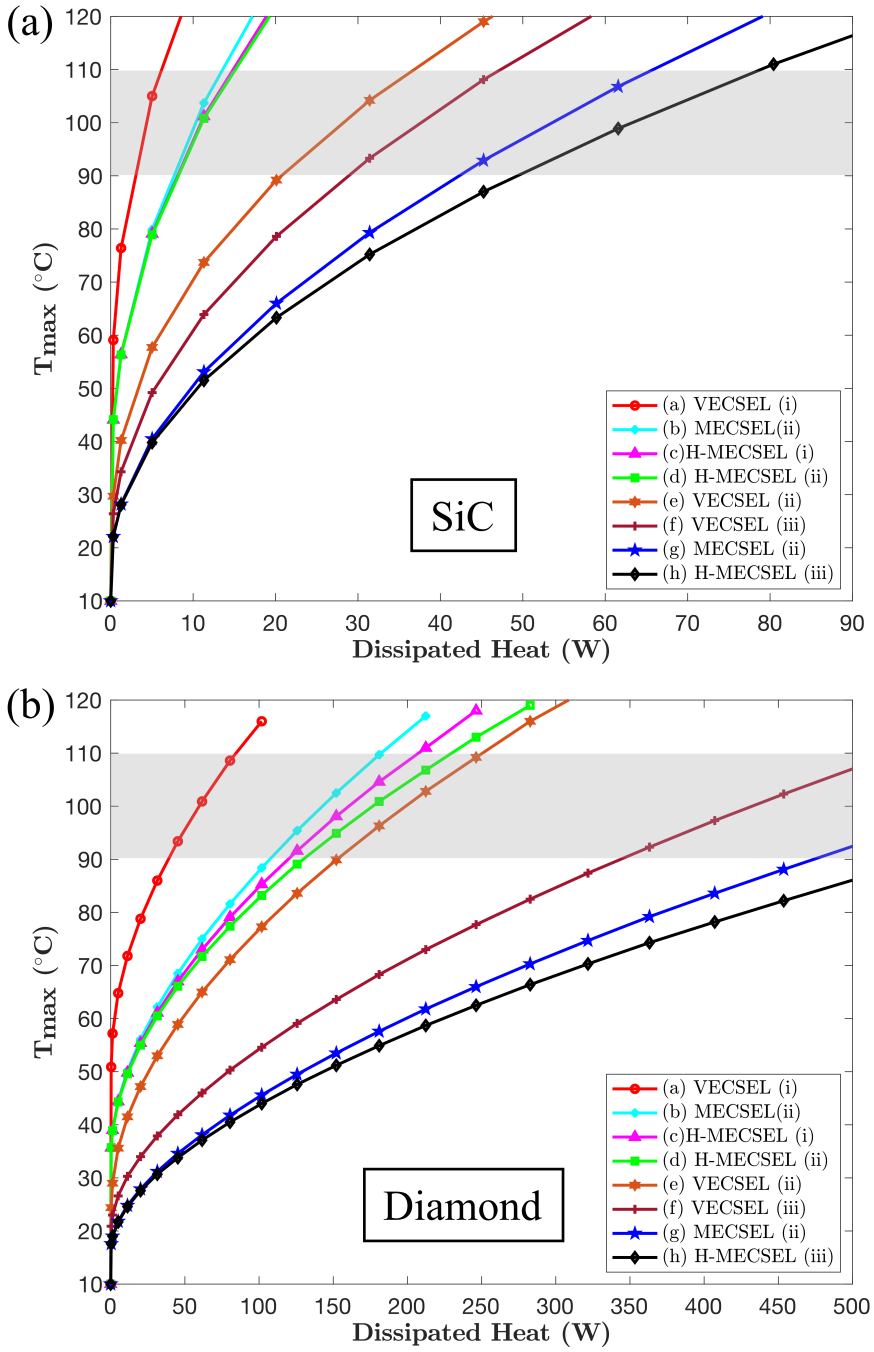

Fig. 6.8 Maximum temperature within the gain chip for eight different structures for Module B parameters versus dissipated heat, with two different heat spreader materials, (a) SiC and (b) diamond [114]. The shaded temperature range indicates the region where thermal rollover is expected to occur.

6.4 Thermal Lens

An important consideration arising from these simulations is the temperature gradient observed within the active region and heat spreaders, which introduces a thermal lensing effect. For semiconductor disk lasers, including VECSELs, MECSELs, and H-MECSELs, this effect is critical because the active regions are intracavity components. Heat spreaders are also intracavity components for all MECSELs, H-MECSELs, and some variations of VECSELs. Thermal lensing could potentially alter the cavity mode size, impacting the alignment and overlap of the pump and laser modes on the gain chip. Such changes might compromise the stability of the laser cavity, potentially rendering it unable to sustain lasing. The experimental results discussed in Chapter 5 indicated the negative influence of laser output from this thermal lensing effect. Addressing these thermal dynamics is essential for ensuring the reliability and effectiveness of H-MECSELs under high thermal load conditions. One solution is to incorporate the thermal lens into the laser cavity design to create a thermal lens-insensitive cavity.

In the numerical analysis using FEM, the radial temperature distribution across the heat spreaders was studied in detail. The average temperature variation along the r-axis, $\Delta T_{\mathrm{HS}}(r)$, was represented by the yellow line in Fig. 6.9, highlighting the predominant thermal lensing effect contributed by the heat spreaders. The temperature effects within the thin active region and any associated thermal expansion were considered negligible for this analysis. A parabolic approximation [141, 142] was applied to this radial temperature profile, illustrated by the red dashed line in the figure. The fit was described by the equation:

$$\Delta T_{\mathrm{HS}}(r) = a\left(1 - \frac{br^2}{{w_{\mathrm{P}}}^2}\right) \tag{6.13}$$

where w_{P} denotes the radius of the pump beam, where a and b are two fitting parameters with SI unit. This fit was focused solely on the region covered by the pump beam to achieve an accurate

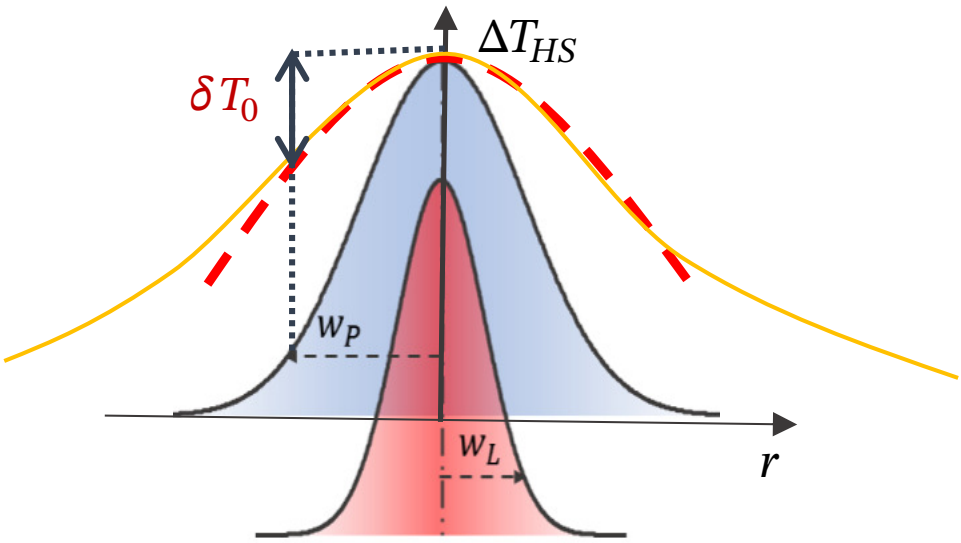

Fig. 6.9 Schematic diagram for δT_0 calculation, in this figure w_P and w_L are radius for the pump beam and the laser beam, ΔT_{HS} is the maximum temperature change within the gain structure [74].

parabolic fit. Also the cavity mode size is smaller than the pump mode size, temperature variations outside the pump beam area are less significant to the thermal lensing effects that influence the laser cavity. From this analysis, a specific temperature factor, δT_0, was derived. This factor represents the temperature difference between the maximum value of ΔT_{HS} and the value at the outer boundary of the pump beam ($r = w_{\mathrm{P}}$ at $1/e^2$ intensity).

The temperature variation across the radial position can be described by the following expression

$$\Delta T_{\mathrm{HS}}(r) \approx -\delta T_0 \frac{r^2}{{w_{\mathrm{p}}}^2}. \tag{6.14}$$

This equation models how the average temperature change diminishes radially outward from the center of the pump beam, associates with the heat spreader's effective focal length due to thermal lensing. The power of the resultant thermal lens is then given by:

$$\frac{1}{f_{\mathrm{th}}} = 2\delta T_0 \frac{d}{{w_{\mathrm{p}}}^2} \frac{dn}{dT}, \tag{6.15}$$

where f_{th} is the focal length of the thermal lens, d is the thickness of the heat spreader, and $\frac{dn}{dT}$ is the thermo-optic coefficient, which is a measure of how the refractive index of the material changes with temperature.

In the simulation of a high-power laser system utilizing a H-MECSEL design with dual 500 µm thick SiC heat spreaders, the thermal response under a condition of 50 W of absorbed pump power (corresponding to around 34 W dissipated heat) was analyzed to determine the temperature distribution and the resultant thermal lens. The radial temperature profile for H-MECSEL as this absorbed pump power was depicted in Fig. 6.10 (a). A parabolic fit was applied to the averaged temperature data, as shown by the red line in Fig. 6.10 (b). The Gaussian shaped pump beam, with a radius of 530 µm, is overlaid as the blue line, illustrating the spatial distribution of the pump power within the laser structure. The temperature factor δT_0, derived from this analysis, was found to be approximately 3 K. Based on this factor and the known properties of the SiC heat spreaders, the focal length of thermal lens was calculated be $f_{\text{th}} \approx 2.6$ m. This relatively long focal length indicates a mild thermal lensing effect, suggesting that the laser system maintains good beam quality and stability under the expected operational conditions.

In solid-state lasers, where the excitation and boundary conditions maintain cylindrical symmetry, the power of the thermal lens has been demonstrated to correlate directly with the dissipated heat power P_{heat}, following the relation $\frac{P_{\text{heat}}}{\pi {w_{\text{p}}}^2}\left[\frac{dn}{\kappa dT}\right]$ [143]. For the H-MECSEL design using parameters in Table 6.1, incorporating both SiC and diamond as heat spreader materials, a generalized formulation can be articulated to estimate the thermal lens power as [114]

$$\frac{1}{f_{\text{th}}} \approx K \frac{P_{\text{heat}}}{{w_{\text{p}}}^{\beta}}, \tag{6.16}$$

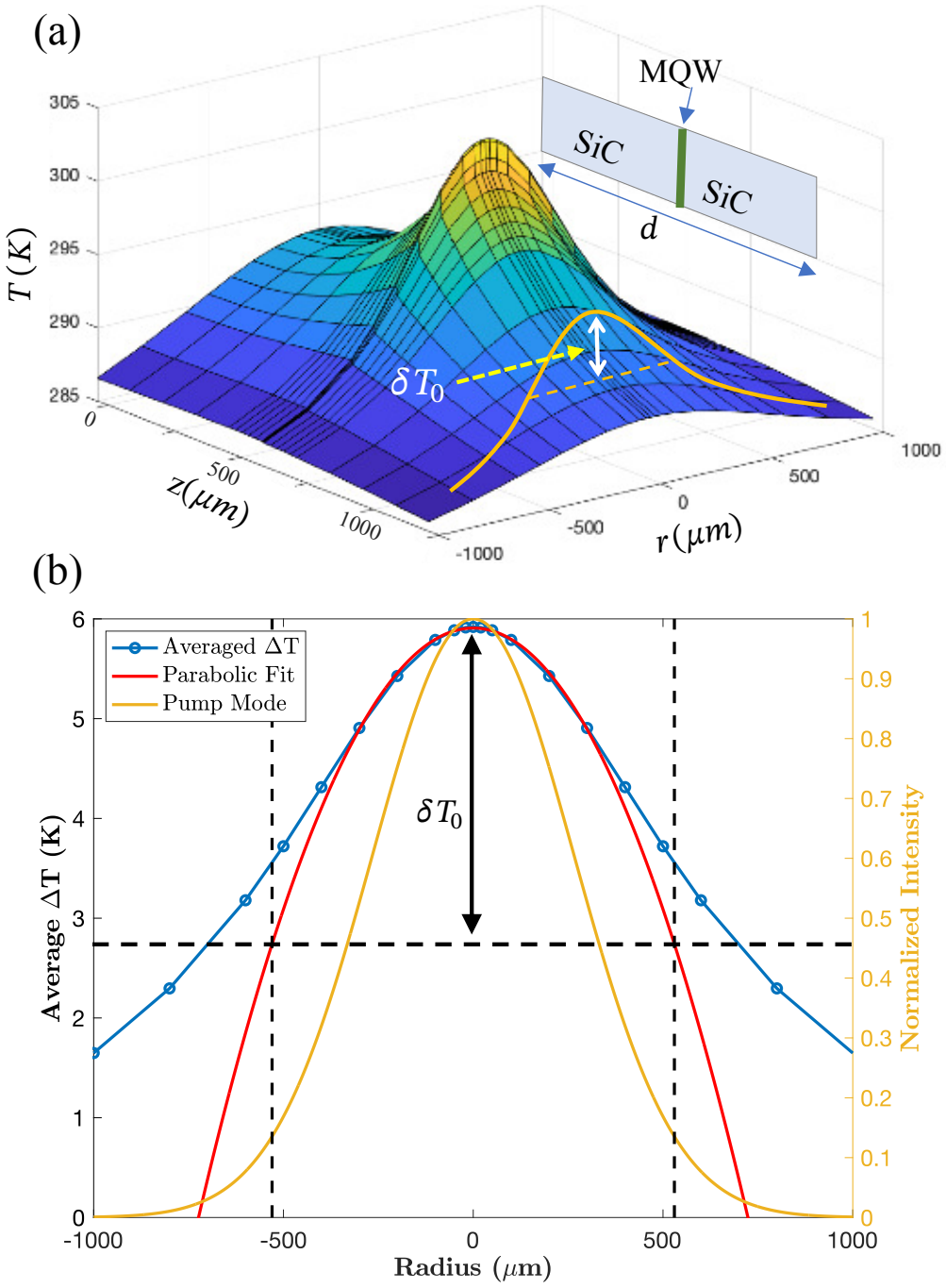

Fig. 6.10 (a) Temperature profile of a dual SiC heat spreader H-MECSEL with 50 W absorbed pump power, the yellow curve represents $\Delta T(r)$. (b) Averaged ΔT (blue) extracted from (a), parabolic fit (red) of ΔT, and a 530 µm radius pump beam profile [74].

where K encapsulates the influence of material properties such as thermal conductivity (κ), the thermo-optic coefficient ($\frac{dn}{dT}$), and the effective layer thickness of the heat spreader (d). For SiC heat spreaders, K is quantified at 5.7×10^{-7} (SI unit), reflecting its satisfactory thermal handling albeit lower thermal conductivity relative to diamond. Conversely, for diamond heat spreaders with better thermal conductivity, K is significantly lower at 2.9×10^{-8}. This lower value reflects diamond's enhanced capability to mitigate thermal lensing effects. Fitting parameter β (unitless) is 1.4 for both SiC and diamond heat heat spreaders.

FEM simulations were performed to validate Equation 6.16 across various scenarios, employing different materials and heat spreader thicknesses. The COMSOL simulation model for a H-MECSEL structure incorporated two 500 µm thick heat spreaders and utilized material parameters from Table 6.1. Various pump beam radii, including 300 µm, 500 µm, and 1000 µm, were simulated in conjunction with both SiC and diamond as heat spreader materials under multiple heat dissipation scenarios driven by differing pump intensities.

The results from the simulations, detailing the thermal lens power, are graphically represented in Fig. 6.11. Data points for diamond heat spreaders are indicated with red diamonds, while those for SiC heat spreaders are denoted with black circles. These data align well with the theoretical predictions of Equation 6.16, depicted by the red dotted line for diamond and the black solid line for SiC. This alignment underscores the equation's robustness across a range of operational conditions and material choices. The findings from Fig. 6.11 suggest that thicker heat spreaders generally mitigate the strength of the thermal lens. While the effect of diamond as a heat spreader minimizes the lensing to negligible levels, the use of SiC requires considerations for thermal lensing within the laser cavity due to its more pronounced impact. The insights from Equation 6.16 facilitate precise predictions of thermal lens effects based on varying pump powers, serving as a foundational element for the laser cavity design of H-MECSEL. This aspect, essential for ensuring optimal performance and stability, will receive detailed discussion

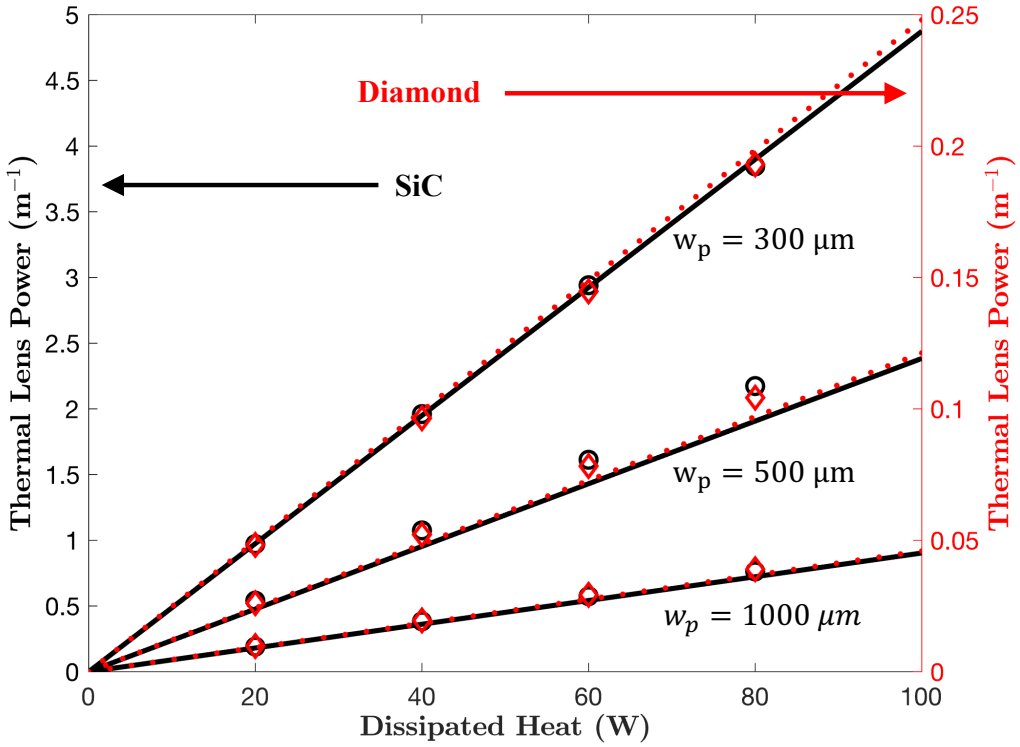

Fig. 6.11 Thermal lens power versus dissipated heat for SiC (black) and diamond (red) heat spreaders [114].

later, where the integration of these design principles into practical device configurations will be explored.

6.5 Experimental Verification

The FEM simulations demonstrated a modest enhancement in thermal performance for the H-MECSEL compared to the standard MECSEL, despite the inclusion of an additional 9 µm DBR layer. The inclusion of the dual-band DBR significantly simplifies the design of multi-pass pumping schemes. As discussed in Chapter 4, the elements of the multi-pass pumping scheme for H-MECSEL can be reduced to half of what was used for standard MECSEL. The

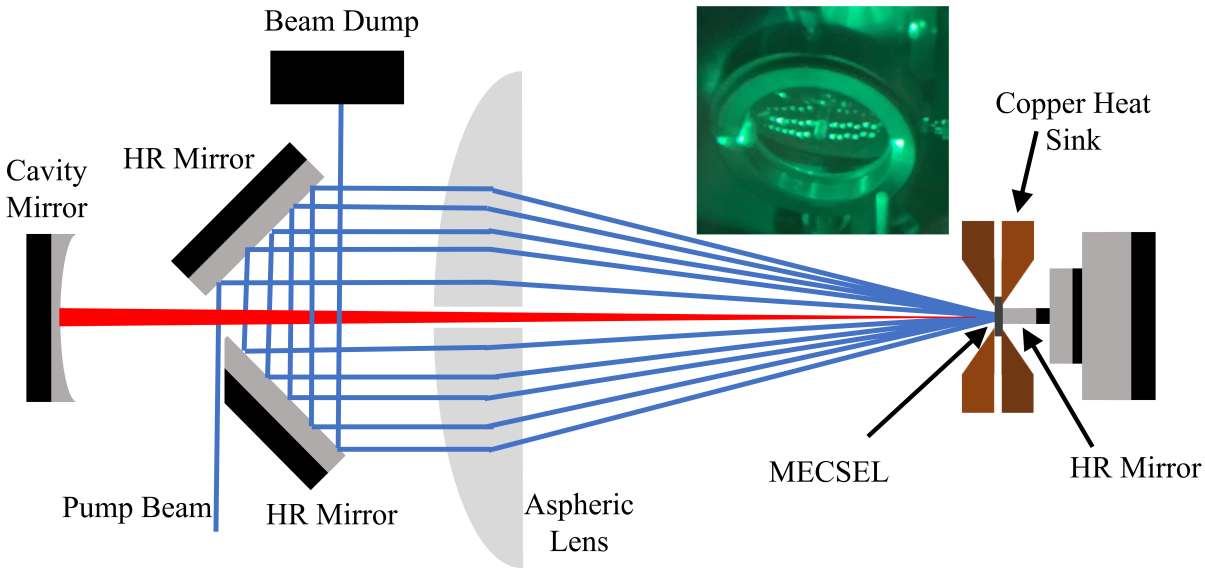

Fig. 6.12 Schematic diagram of H-MECSEL demonstration with HR mirror and MECSEL sample. The inset illustrates multiple pump spots on the aspheric lens.

ray tracing analysis indicates that this simplified design still can achieve good pump beam overlap on the gain chip. Given these promising simulation results, an experimental trial was undertaken using a dummy sample. This preliminary step was crucial to validate the theoretical models and practical feasibility before committing to the costly process of wafer growth and device fabrication. The trial aimed to ensure that the theoretical advantages of the H-MECSEL structure—particularly its simplified pumping mechanism—could indeed be realized in practice.

In the laboratory, a readily available MECSEL sample was utilized for a H-MECSEL demonstration, involving a broadband coated HR mirror compatible with both 1070 nm in-well pumping and 1178 nm laser wavelengths. As depicted in Fig. 6.12, the HR mirror was custom-fitted within the MECSEL copper mount's aperture, positioned as close as possible but not touching the MECSEL gain chip to avoid potential damage. This was achieved by affixing the HR mirror to an adapter that mounted on a translation stage for fine adjustment of the mirror position. The copper mount itself was cooled by a chiller set to 15 °C. To allow passing of the laser cavity beam, a 3 mm hole was drilled at the center of a 2-inch diameter aspheric lens (focal

length = 100 mm), which was positioned 100 mm from the MECSEL sample. A pair of HR plane mirrors configured as a retro-reflector was placed an equal distance from the aspheric lens. One of these plane mirrors was specifically modified to permit the entry of the 1070 nm pump beam into the circulator without obstruction. Any residual pump beam was safely terminated at a beam dump.

The laser cavity was constructed using an ROC=500 mm concave HR mirror, chosen for its spatial accommodation and threshold reduction capabilities. Another key component of the cavity was the specially adapted HR plane mirror positioned at the rear of the MECSEL sample. Initially, an 808 nm diode pump laser was employed to initiate lasing. Once the cavity was aligned, the 808 nm pump was removed and the parts for the 1070 nm pump were installed. And adjustments were made to the aspheric lens and retro-reflector to facilitate multiple pump passes and maintain lasing solely with the 1070 nm pump. According to the author's ray tracing analysis, a larger than expected 2 mm separation between the HR mirror and the MECSEL gain chip resulted in a highly elliptical pump beam overlap across twelve passes on the sample. Despite this non-ideal beam shape, it was sufficient to demonstrate the concept and proceed with the fabrication of actual H-MECSEL samples. An infrared viewer captured an image of the twelve pump spots on the aspheric lens as the inset of Fig. 6.12, highlighting the experimental setup's effectiveness for achieving multiple passes. This H-MECSEL setup was experimentally validated, paving the way towards the fabrication of H-MECSEL gain chips.

6.6 Conclusion

In this chapter, the H-MECSEL was introduced as an evolution of the MECSEL, aimed at providing a reflective sample. This design simplifies the multi-pass in-well pumping structure, addressing the issues of distorted output beam profiles due to imperfect mode matching between

the cavity mode and the pump mode on the sample, which was elaborated in Chapter 5. The design and functionality of a dual-band DBR for the H-MECSEL were reviewed. Further, FEM simulations substantiated the thermal efficiency of the H-MECSEL, affirming its ability to maintain excellent thermal management. The thermal lens effect, a critical factor in the design of laser cavities, was quantitatively analyzed, leading to the derivation of a general formula that will underpin the laser cavity design for the H-MECSEL in subsequent studies. A demonstrative experiment was conducted using an existing MECSEL sample paired with a custom-engineered high reflectance mirror to establish a proof-of-concept for the H-MECSEL before proceeding with the fabrication of dedicated samples.

With the foundational elements now established, all necessary components are in place to construct a semiconductor-based LGS that meets the design criteria outlined in Chapter 1. The forthcoming chapters will delve into the experimental setup, detailed implementation, and the outcomes of an H-MECSEL-based LGS.

Chapter 7

In-Well Pumped H-MECSEL

This chapter details the development of a twenty quantum well H-MECSEL gain chip, which integrates a high-reflectance membrane designed to reflect unabsorbed pump light back into the multi-pass in-well pumping structure. The design of multi-pass pumping structure and laser resonator, as well as the experimental results, will also be presented. The original experimental results presented in this chapter were documented in [114]. This chapter provides a more detailed reevaluation of those results.

7.1 H-MECSEL Gain Chip

Reflective samples, such as those used in standard VECSELs, can reduce the number of elements required in a multi-pass in-well pumping structure by half compared to the configurations necessary for transmissive samples like those in MECSELs. This simplification could significantly streamline the construction of multi-pass pumping setups, as noted in Chapter 4. However, VECSELs, while advantageous for their reflective nature, generally do not match MECSELs in terms of thermal management [1, 72]. The superior heat dissipation capability of MECSELs

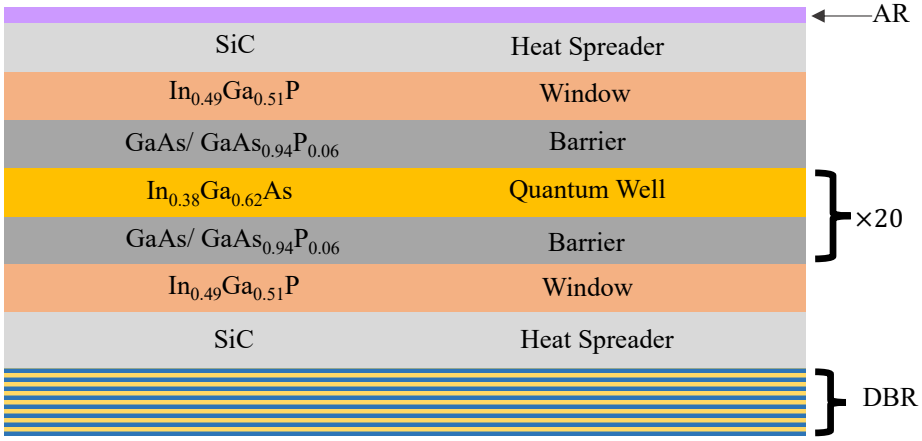

Fig. 7.1 Schematic of the H-MECSEL gain chip [114].

is crucial for high-power applications. In response to these challenges, the introduction of the H-MECSEL in Chapter 6 represents a significant advancement. The H-MECSEL combines the benefits of MECSELs and VECSELs by incorporating a reflective element into a structure that retains the excellent thermal management properties of MECSELs. This approach enables the use of simplified multi-pass pumping structures while ensuring that the thermal performance necessary for high-output applications is not compromised.

The epitaxial sample for the H-MECSEL, same as studied in Chapter 5, consists of twenty InGaAs quantum wells and GaAs barrier layers with GaAsP strain compensation layers as illustrated in Fig. 7.1. These are arranged in a RPG structure, where the InGaAs layers are placed at the anti-nodes and GaAsP layers at the nodes of the cavity's standing wave. InGaP window layers are employed to reduce surface recombination and safeguard the active region during the substrate removal process. This active region is encapsulated between two 500 µm thick, double-side polished, single-crystalline SiC heat spreaders, directly bonded to the epitaxial active material. Subsequently, one outer facet of the heat spreader sandwich is AR coated at 1070 nm to minimize reflecting losses associated with the multi-pass pumping beam. A dual-band DBR, highly reflective at both 1070 nm and 1178 nm as detailed in Chapter 6, is

attached to the other outer facet of this structure using a direct-bonding-based substrate-transfer coating process. After assembly, the complete H-MECSEL device is mounted between two water-cooled copper heat sink plates, with a 50 µm thick layer of indium foil sandwiched in between to enhance thermal contact.

7.2 Multi-Pass Pumping Design

The multi-pass pumping structure designed for the H-MECSEL experiment incorporated an aspheric lens with a 100 mm focal length and two plane mirrors, as depicted in Fig. 7.2 (a). For the ray tracing simulations, both plane mirrors were presumed to reflect 100% of the pump wavelength, and the data including aberration for the aspheric lens was sourced directly from THORLABS, where the aspheric lenses used in the experiment were purchased from. The gain chip assembly, highlighted in Fig. 7.2 (c), comprised two 500 µm thick SiC layers, an AR coating on the front and a HR coating on the rear. Additionally, the quantum wells (QWs) were represented by a 5% absorption layer sandwiched between the SiC heat spreaders. In this setup, the pump beam was focused between the two plane mirrors, reflected and collimated onto the gain chip by the aspheric lens. The beam was then reflected off the HR-coated back of the sample, refocused by the aspheric lens, and the cycle was repeated. Each pass introduced a slight lateral shift in the beam position due to a small shift between the two plane mirrors. This setup facilitated ten round-trips of the pump beam before it was terminated by a beam dump.

The simulation output is plotted in Fig. 7.2 (b), displaying the beam profile at the quantum well position after twenty passes. The simulation indicated that reducing the number of passes could increase the system's tolerance to alignment errors without compromising the overlap of multiple pump spots on the quantum wells. It was noted that the ideal AR coating assumed for the aspheric lens in the simulation does not perfectly reflect real-world conditions, particularly

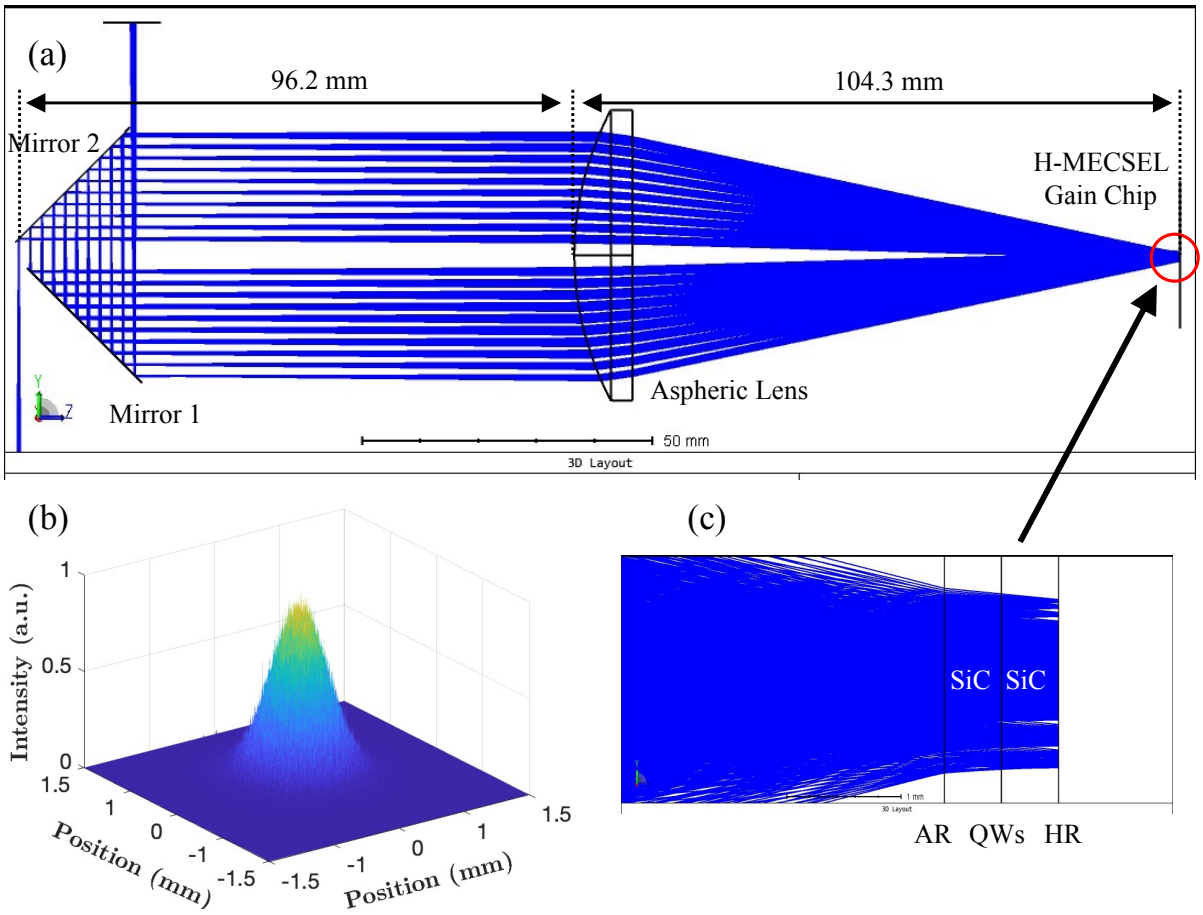

Fig. 7.2 (a) Zemax simulation setup for H-MECSEL multi-pass pumping scheme. (b) The beam profile on the quantum well layer. (c) Detailed H-MECSEL structure setting in the simulation.

for beams striking the lens edge at steep angles where the AR coating is less effective. For practical reasons, including ease of alignment and reduced scattering losses, the experimental setup was adjusted to utilize only ten passes of the pump beam. This setup allowed for simpler alignment and maintenance of effective pump spot overlap compared with the MECSEL multi-pass pumping design.

7.3 H-MECSEL Cavity Design

For the H-MECSEL-based experimental setup, a V-cavity configuration was employed, optimized to incorporate the H-MECSEL gain chip along with linewidth narrowing elements such as a BRF and a FP etalon in one arm of the cavity. The other arm was designated for housing the frequency doubling LBO crystal, and the end mirror was mounted on a piezo actuator for frequency stabilization. The cavity design utilized the DBR on the rear side of the H-MECSEL gain chip as one of the cavity end mirrors, selecting another plane mirror as the opposite cavity end mirror. This choice was driven by the need for simplification in the setup of second harmonic generation (SHG) and frequency locking mechanisms, ensuring that the wavefronts at these mirrors remain planar for optimal interaction with intracavity components. A concave folding mirror was selected to link the two arms of the cavity, set at a folding angle α as marked in Fig. 7.4 to accommodate the intra-cavity elements and optimize the cavity's stability and mode-matching.

The objective was to achieve a cavity beam size of approximately 350 µm in radius at the gain chip. This design also aims to minimize the difference in beam size between the tangential and sagittal planes. Furthermore, the design focused on reducing the sensitivity of the system to thermal lensing effects that might arise within the SiC heat spreaders of the H-MECSEL gain chip. Thermal lensing can distort the cavity mode and affect the overall performance of the laser system. By optimizing the geometry and placement of the cavity components, the design sought to mitigate these effects, ensuring stable and efficient laser operation suitable for LGS systems.

In the design of the H-MECSEL laser cavity, a folding mirror with a ROC of 500 mm was chosen to facilitate the appropriate redirection of the laser beam. The folding angle was set at 15°, positioning the H-MECSEL gain chip 520 mm away from the turning mirror and the plane

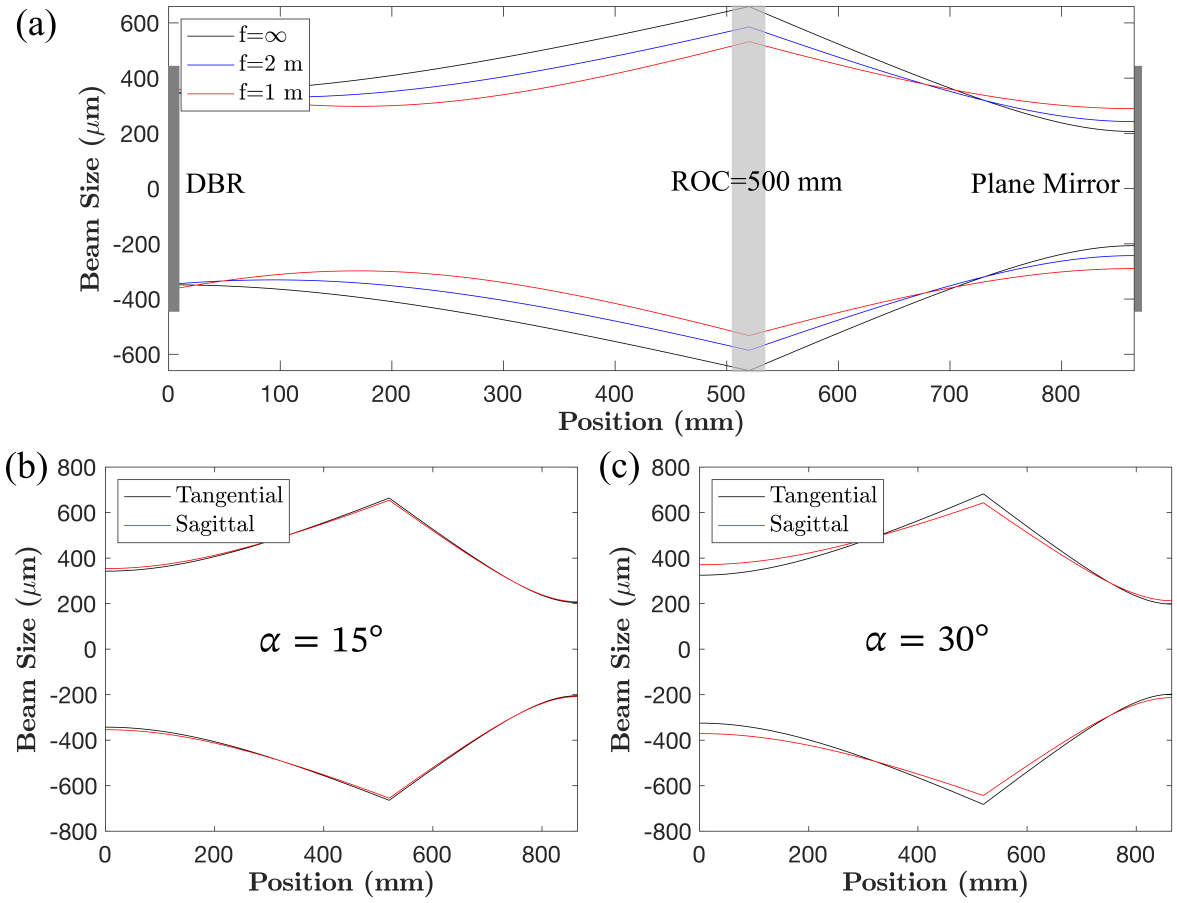

Fig. 7.3 (a) Cavity mode size calculation with a V-cavity configuration for three thermal lens conditions with f = ∞, f=2 m, and f=1 m. Cavity beam size for tangential and sagittal planes for turning angle of (b) 15°, and (c) 30°.

end mirror 345 mm from the turning mirror. The cavity mode size under various thermal lensing conditions was examined, as depicted in Fig. 7.3 (a). This figure illustrates the cavity mode size for three scenarios: no thermal lens effect, a thermal lens with a focal length f of 2 m, and f of 1 m. The analyses assumed an ideal scenario with a 0° folding angle, showing the beam size at the sample position remains at approximately 350 μm in radius regardless of the thermal lensing effect, which this thermal lens-insensitive cavity design, the mode mismatching issue mentioned in Chapter 5 could be resolved. Further analysis, as shown in Fig. 7.3 (b), reveals

that at a 15° folding angle and assuming no thermal lensing in the gain chip, the cavity beam size on the sample remains nearly identical between the sagittal and tangential planes. However, increasing the folding angle to 30° introduces significant discrepancies in the cavity beam size between the sagittal and tangential planes, as demonstrated in Fig. 7.3 (c). Such a disparity can lead to inefficiencies in the laser system, as the beam profile becomes more elliptical, potentially impacting the overlap with the pump mode and reducing the overall system performance.

7.4 Experiment Results

The experimental setup for the H-MECSEL laser system is detailed in Fig. 7.4. The system utilizes a 1070 nm fiber laser as the pump source, which is focused using a lens with a focal length f_p of 750 mm. This configuration positions the focal point between two plane mirrors, which are HR at 1070 nm and form a retro-reflector. These mirrors along with an aspheric lens facilitate a multi-pass pumping scheme, allowing the pump beam to circulate within the setup for ten passes before being terminated by a beam dump. The 2-inch diameter aspheric lens that was AR-coated at 1070 nm and a focal length of 100 mm, incorporates a 3 mm diameter central hole. This design permits the unimpeded passage of the laser cavity beam through this hole. The aspheric lens is positioned 100 mm away from both the H-MECSEL gain chip and the retro-reflector.

This cavity design aims to achieve a cavity beam radius of approximately 350 µm at the sample position, accommodating a thermal lens effect with an estimated focal length of 2 m. The chiller was set at 10 °C to maintain the required thermal stability. The inset shows the cross-section of the overlapped pump beam profile on the gain chip, captured using a CCD camera. It illustrates the pump beam profile with ten passes on the gain chip has a beam radius of 590 µm.

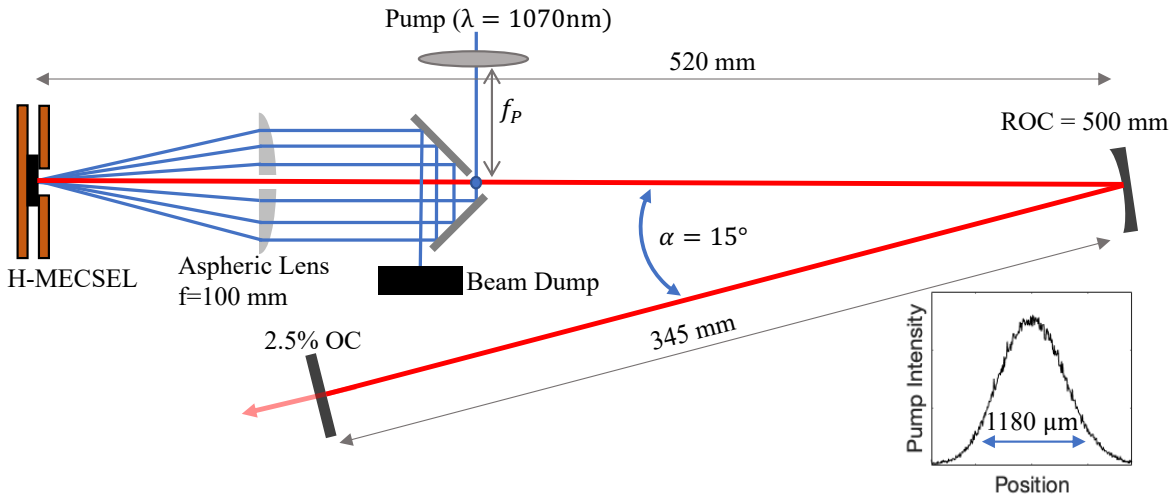

Fig. 7.4 Schematic diagram (not in scale) of the multi-pass in-well pumped H-MECSEL setup [114]. The inset is the profile of ten passes of pump beam on the sample measured by a CCD camera.

The free-running output power of the H-MECSEL setup as a function of absorbed pump power is plotted in Fig. 7.5. The power before and after all multi-pass components—plane mirrors, the aspheric lens, and the H-MECSEL gain chip—at low pump powers was measured to determine absorption and reflection rates for each component. The H-MECSEL gain chip was found to absorb 39% of the pump power over ten passes, a figure derived from these measurements. The laser exhibited a threshold of approximately 10 W and successfully avoided noticeable thermal rollover up to the maximum tested absorbed power of 86 W. Thermal modeling, as discussed previously in Chapter 4, predicted a maximum temperature within the sample of about 105 °C under a heat load of 58 W, approaching the thermal rollover threshold. However, this model was conservative and likely overestimated the temperature within the active region. The maximum output power reached was 28 W, demonstrating a slope efficiency of 38%. This represents a significant improvement over the 28.0% slope efficiency observed in the multi-pass in-well pumping setup for the twenty quantum well MECSEL gain chip [112].

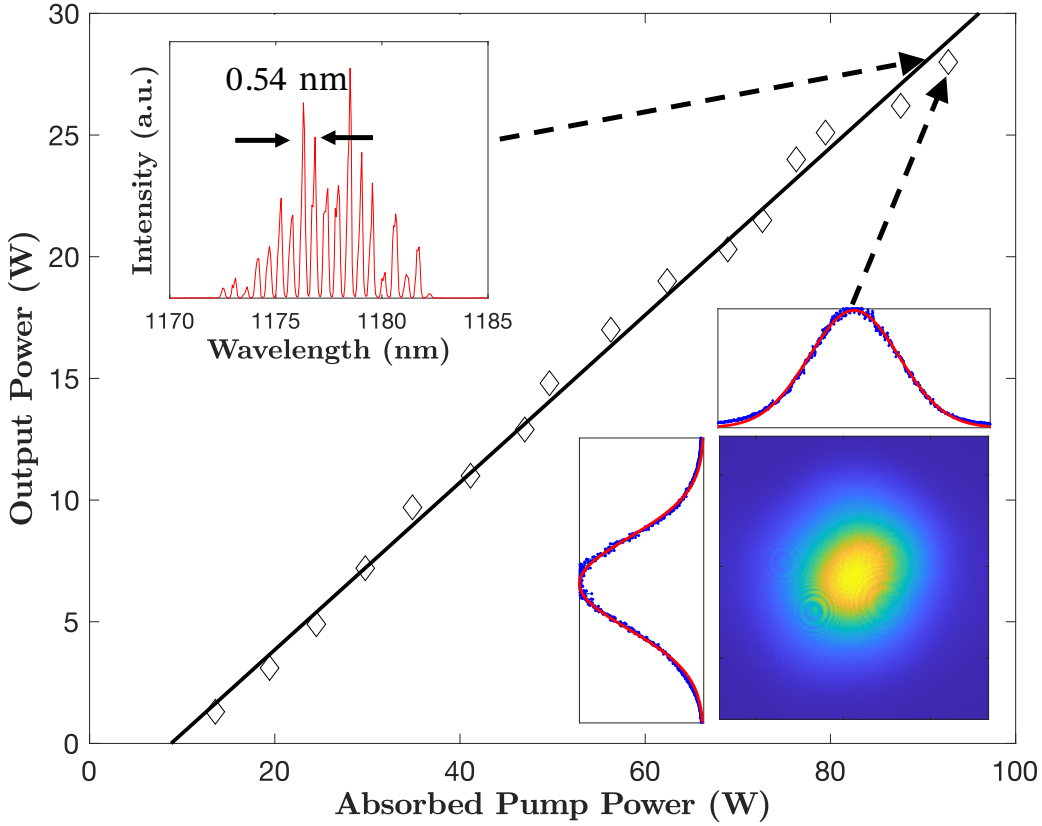

Fig. 7.5 H-MECSEL output power versus absorbed pump power [114]. Both insets were measured at maximum output power of 28 W, the top left inset of free-running multi-mode spectrum was measured by an OSA, and the bottom right right inset of beam profile with Gaussian fit was measured by a commercial beam profiler.

The enhanced performance here can be attributed to a superior alignment of the multiple pump spots on the sample.

Further insights into the laser operation are provided by the insets included in Fig. 7.5 which were both measured at maximum output power point. The spectrum in the top left inset, obtained using an OSA with a resolution of 0.06 nm, showed multiple longitudinal mode operation with a mode spacing of 0.54 nm, corresponding to the FSR of a 500 µm thick SiC etalon, assuming a refractive index (n) of 2.57. Additionally, the bottom right inset, captured by

a commercial beam profiler positioned 500 mm from the output coupler, confirmed the emission of a TEM_{00} mode. The beam profile was symmetric in both x and y axes, fitting Gaussian distributions well. The system was ready for further steps such as linewidth narrowing and frequency doubling aimed at achieving the targeted 589 nm output.

7.5 Conclusion

To simplify the multi-pass pumping structure, a H-MECSEL design was employed, demonstrating a well-aligned ten-pass 1070 nm pump beam on the gain chip. This resulted in a free-running output of 28 W with a TEM_{00} transverse mode. This result is sufficient for further linewidth narrowing and frequency doubling to meet the design criteria for LGS applications and will be discussed in the next chapter.

Chapter 8

Semiconductor-Based Laser Guide Star

In this chapter, the continued advancements based on the H-MECSEL platform will be discussed to finalized the semiconductor-based LGS design. The laser output wavelength is tuned to 1178 nm using a quartz BRF, and the linewidth is further narrowed by employing an FP etalon. The intracavity frequency doubling process to achieve laser output at 589 nm and the preparation for on-sky testing will also be detailed. Part of the experimental results in this chapter were reported at the SPIE Photonics West Conference [75].

8.1 Wavelength Tuning

The Z-shaped laser cavity design for the H-MECSEL gain chip was configured with optics available. The H-MECSEL gain chip was positioned 550 mm from a ROC=250 mm concave mirror (M1) as illustrated in Fig. 8.1 (a). The space between M1 and another ROC=150 mm mirror (M2) was set at 245 mm. The segment stretching from M2 to a plane end mirror (M3) measured 240 mm. The folding angle for each mirror was determined to be 14°, minimizing the divergence between beam size on tangential and sagittal planes. Calculated beam sizes within

this cavity are plotted in Fig. 8.1 (b), the plot indicated that the beam radius on the H-MECSEL gain chip was 298 µm on the tangential plane and 307 µm on the sagittal plane. At M3, the beam radii were 240 µm for the tangential plane and 278 µm for the sagittal plane. The same gain chip and multi-pass pumping scheme as in Chapter 7 was used. The chiller was set to 15 °C for thermal management. A CCD camera was used to study the overlapped pump beam size on the gain chip. A comparison of the cross section of 2 passes and 10 passes of the overlapped pump spot on the gain chip is shown in Fig. 8.1 (c). For 2 passes, the beam radius is 338 µm (FWHM), and it increases by less than 5% to 349 µm (FWHM) for 10 passes. This indicates good beam overlap between different passes.

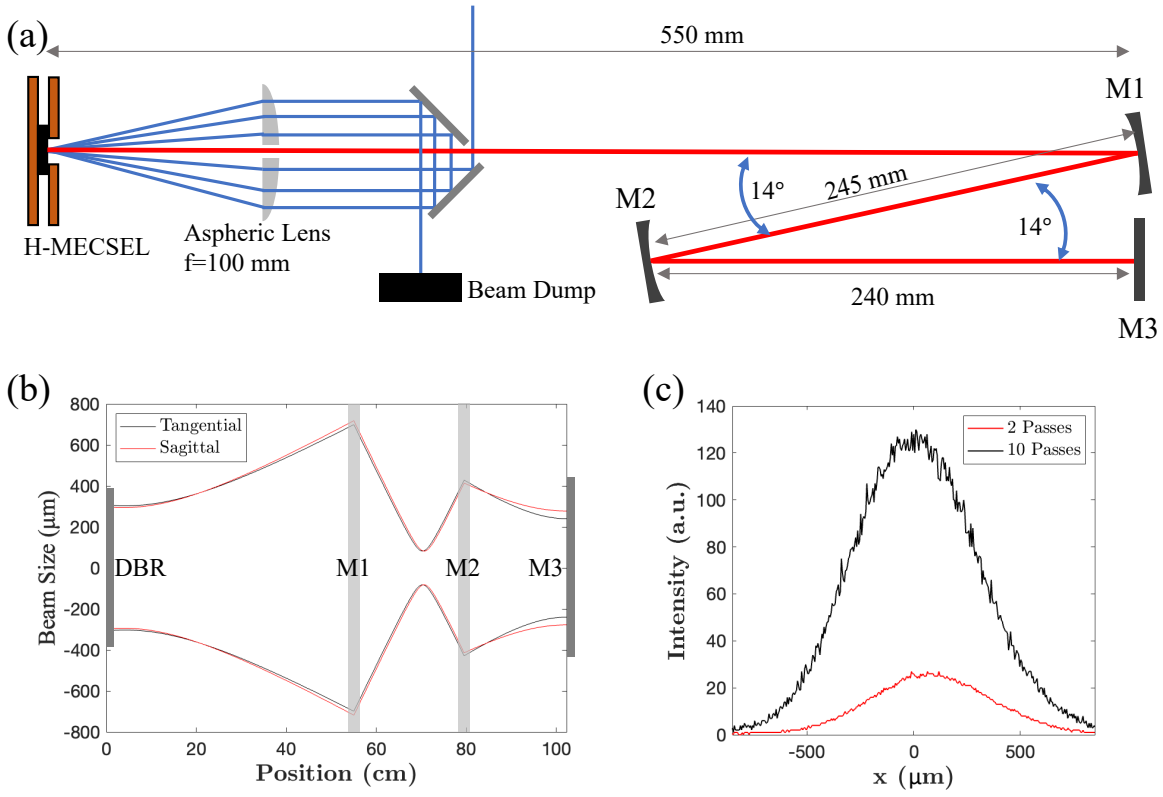

Fig. 8.1 (a) Schematic diagram of the Z-cavity configuration for H-MECSEL experiments [74]. (b) Intra-cavity beam size calculated for this Z-cavity configuration on both tangential and sagittal planes. (c) Cross section of 2 passes and 10 passes of the overlapped pump spot on the gain chip.

An intracavity BRF was first inserted in the gain chip arm to stabilize the fundamental wavelength at 1178 nm and to narrow the laser output linewidth. The laser cavity was composed of HR mirrors at 1178 nm, except for the plane end mirror which served as a 2.5% OC at this wavelength. A 2 mm thick quartz BRF placed on a rotation mount was first introduced into the cavity, positioned at Brewster's angle to minimize losses and adjusted to align the laser output precisely at 1178 nm. The laser was characterized by measuring the output spectra with an OSA as plotted in Fig. 8.2, revealing a tuning range of 61 nm from 1133 nm to 1193 nm under an absorbed pump power of 44 W at 1070 nm.

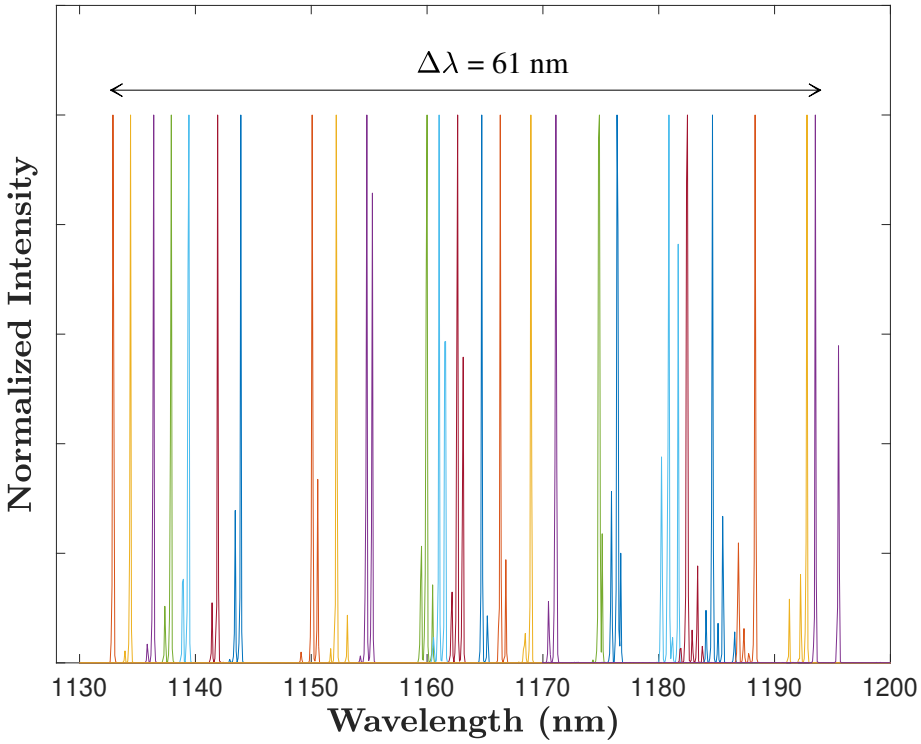

Fig. 8.2 Normalized emission spectra for the twenty quantum well H-MECSEL gain chip utilizing a 2 mm thick quartz BRF for wavelength tuning with 44 W of absorbed pump power and 15 °C chiller temperature.

This observed range was narrower compared to the previously discussed 1124 nm to 1195 nm tuning range for a similar twenty quantum well MECSEL gain chip, primarily due to the significant drop in reflectance of the dual-band DBR around 1135 nm. This limitation can be seen in Fig. 6.3, which shows that the operational wavelength range with reflectance exceeding 99% is confined between 1131 nm and 1194 nm, thereby correlating well with the experimental findings and being limited by the reflectance properties of the cavity mirror coatings.

8.2 Linewidth Narrowing

A 100 µm thick YAG etalon was mounted on a high-precision mirror mount to facilitate precise angular adjustments for wavelength tuning to achieve the desired emission at 1178.32 nm. Precise angle adjustment of the etalon is critical because even a slight deviation from the correct angle can result in 100% transmission at a non-targeted wavelength, leading to an unwanted shift in the emission wavelength. The transmission characteristics of the YAG FP etalon at 1178.32 nm for various incidence angles are illustrated in Fig. 8.3, where perfect transmission is attainable at angles of 7.2° and 11.1°. For this experiment, the angle of 7.2° was selected to ensure optimal transmission at the target wavelength.

Three distinct operational modes of the H-MECSEL were explored: free-running operation, operation with a BRF only, and operation with both a BRF and a FP etalon. These modes are depicted in Fig. 8.4, with free-running operation shown in black, operation with BRF in blue, and with both BRF and FP etalon in red. The results in Fig. 8.4 (b) conclusively demonstrate the effective narrowing of the linewidth. Due to the instrument's limited resolution of 0.06 nm which equivalent to 1.3 GHz at 1178 nm, and the laser cavity's FSR of 200 MHz, single longitudinal mode operation cannot be conclusively determined, even though the spectrum appears to show a single mode. The highest power achieved during free-running operation was 24.1 W, which

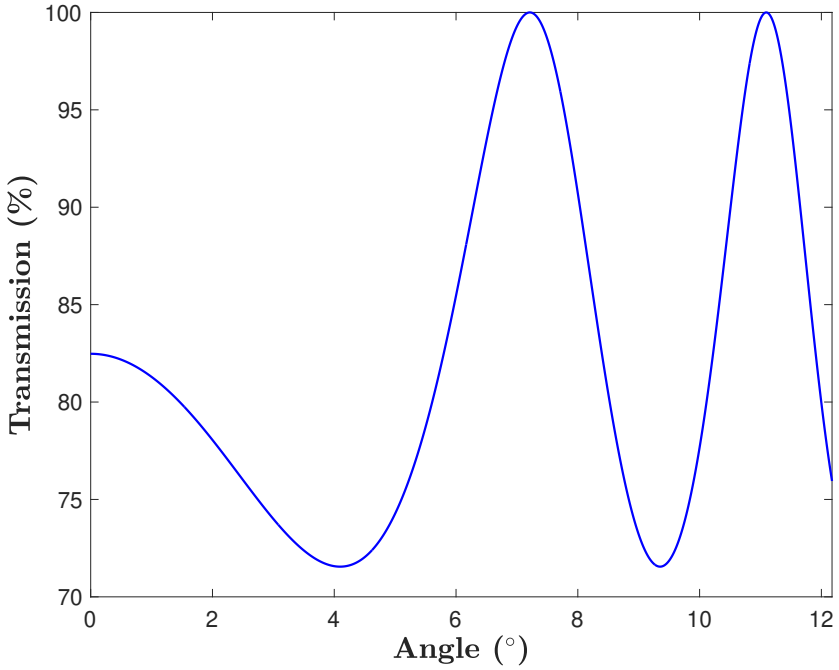

Fig. 8.3 Transmission versus incidence angle at room temperature for a 100 µm thick YAG etalon at 1178.32 nm [122].

decreased to 16.4 W with the addition of the BRF, and further to 11.8 W with both the BRF and FP etalon, indicating a slope efficiency of 30.0%, 23.9%, and 22.7% respectively. Although this performance can potentially generate over 10 W of yellow light after nonlinear conversion, it is suboptimal, necessitating further enhancements. A key issue was the reduced mode size at 1178 nm on the H-MECSEL gain chip, which compromised the mode overlap between the pump and cavity beam. Optimizing the slope efficiency and output power at 1178 nm requires enlarging the cavity mode size at the sample while maintaining the desired beam size near the cavity end mirror where the LBO crystal will be placed for optimal nonlinear conversion efficiency.

A comparative study employing 808 nm barrier pumping was conducted using the same experimental setup to validate the effectiveness of the in-well pumping strategy. For the barrier

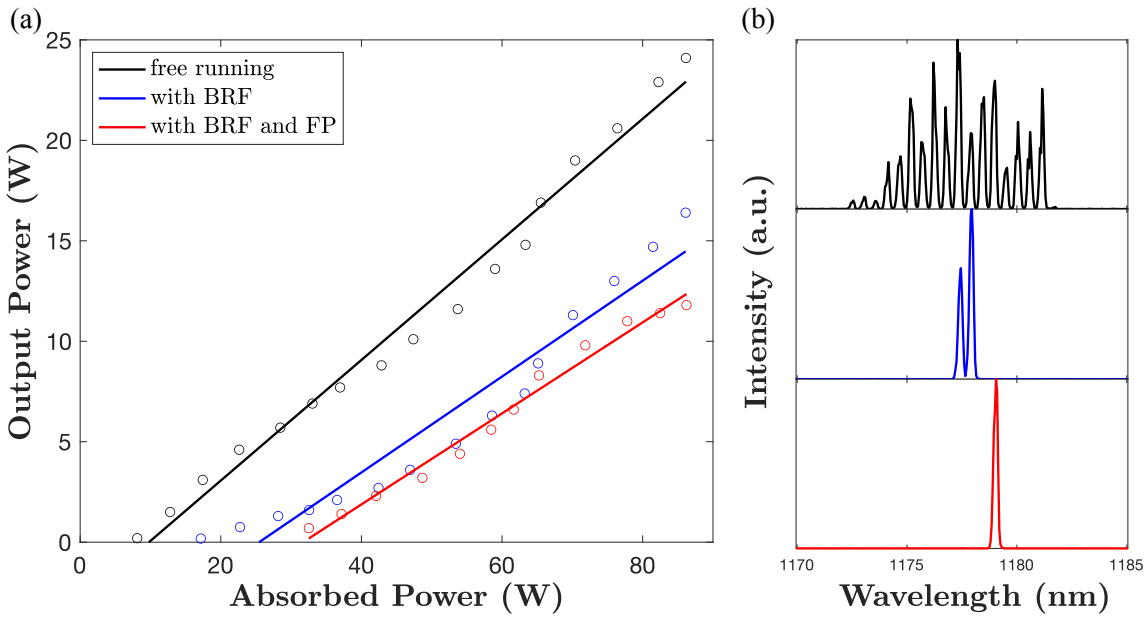

Fig. 8.4 H-MECSEL with the Z-cavity configuration using 1070 nm in-well pumping, (a) output power versus absorbed pump power and (b) spectra measured by an OSA for free running operation (black), with BRF and tuned to near 1178 nm (blue), and with BRF and FP etalon for linewidth narrowed operation at 1178 nm (red) [74].

pumping approach, maximum output powers of 5.8 W, 4.3 W, and 1.9 W were recorded for free-running, operation with a BRF, and operation with both BRF and a FP etalon, respectively. These results are presented in Fig. 8.5 (a), with the corresponding spectra at the highest output power shown in Fig. 8.5 (b) to illustrate the effects of linewidth narrowing. In-well pumping demonstrated a more than four-fold increase in output power without signs of thermal rollover, compared to the maximum output achieved by barrier pumping at its thermal rollover point, underscoring the superiority of the in-well pumping method. Also it needs to be noted that DBR would be strongly absorbing at 808 nm, even though most 808 nm pump is absorbed by the active region. Experimental results using the same active structure described in Chapter 5 indicate that 98% of the the incident 808 nm pump power is absorbed by the active region, leaving approximately 2% of pump power to be absorbed by the DBR and converted into

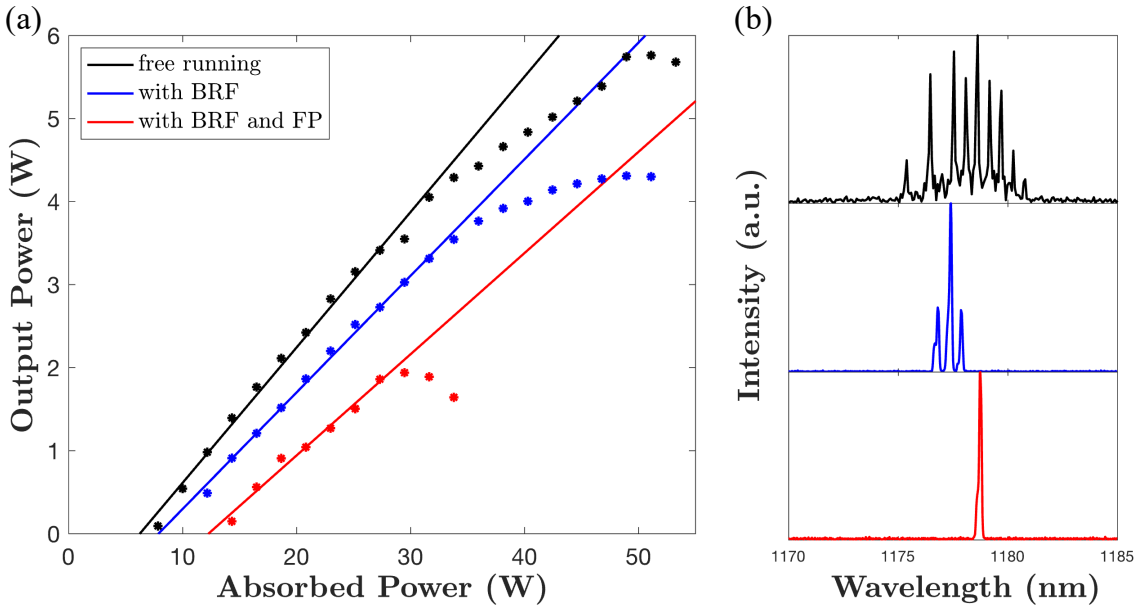

Fig. 8.5 H-MECSEL with the Z-cavity configuration using 808 nm barrier pumping, (a) output power versus absorbed pump power and (b) spectra measured by an OSA for free running operation (black), with BRF and tuned to near 1178 nm (blue), and with BRF and FP etalon for linewidth narrowed operation at 1178 nm (red).

heat. This additional heat contributes to the overall thermal load within the gain chip, slightly increasing the maximum temperature.

The slope efficiencies for barrier pumping were 16.3%, 14.0%, and 12.2%, respectively, significantly lower than those achieved with in-well pumping, which nearly doubled these figures. This stark contrast highlights the enhanced performance of in-well pumping in improving MECSEL output power. Additionally, the onset of thermal rollover observed, particularly when both BRF and FP etalon were utilized, can be attributed to multiple factors. Primarily, the reduced output power extraction could lead to increased heat accumulation within the gain chip, thus accelerating the thermal rollover. Secondly, the impact of a thermally non-stabilized FP etalon could also play a role. During the experiments, incidental light striking the FP etalon mount might have caused temperature variations, misaligning the etalon's mode-selective

tuning with the BRF. This misalignment could introduce extra intracavity losses, consequently lowering the output power and precipitating an earlier thermal rollover.

8.3 On-Sky Test Preparation

The complete system was prepared for an on-sky test at an observatory and was required to be mounted on a single breadboard to facilitate shipping. All mechanical components used in the setup were selected for their robustness against mechanical vibrations. A commercial CAD software (Fusion 360) was utilized to design the experimental setup, ensuring it fit within the dimensions of a breadboard measuring $47" \times 23" \times 1\frac{7}{8}"$ (119.4 cm×58.4 cm×4.8 cm) available in the laboratory.

The schematic representation of the setup is illustrated in Fig. 8.6. The experiment began with a 1070 nm output from a pump laser which first passed through a polarizing beamsplitter (PBS) to convert the unpolarized pump beam into a polarized one, with half of the pump power was dumped into the beam trap. The beam then traveled through a half wave plate followed by another PBS, which allowed for fine control of the pump power based on polarization adjustments. Following these elements, the beam was focused into the multi-pass pumping setup using a lens with a focal length of 750 mm. The beam path incorporated three HR plane mirrors to guide the beam into the multi-pass pumping scheme, and four apertures were placed for alignment of the pump beam. The output beam size from the fiber laser is 3.8 mm (FWHM), and combining this f=750 mm lens and the f=100 mm lens within the multi-pass pumping scheme, the laser beam size is around 0.5 mm (FWHM) on the H-MECSEL gain chip

The MECSEL gain chip, housed in a copper heat sink, was mounted on a translation stage allowing for precise position adjustments. The multi-pass pumping setup, as previously described, included an aspheric lens with a focal length of 100 mm featuring a 3 mm central

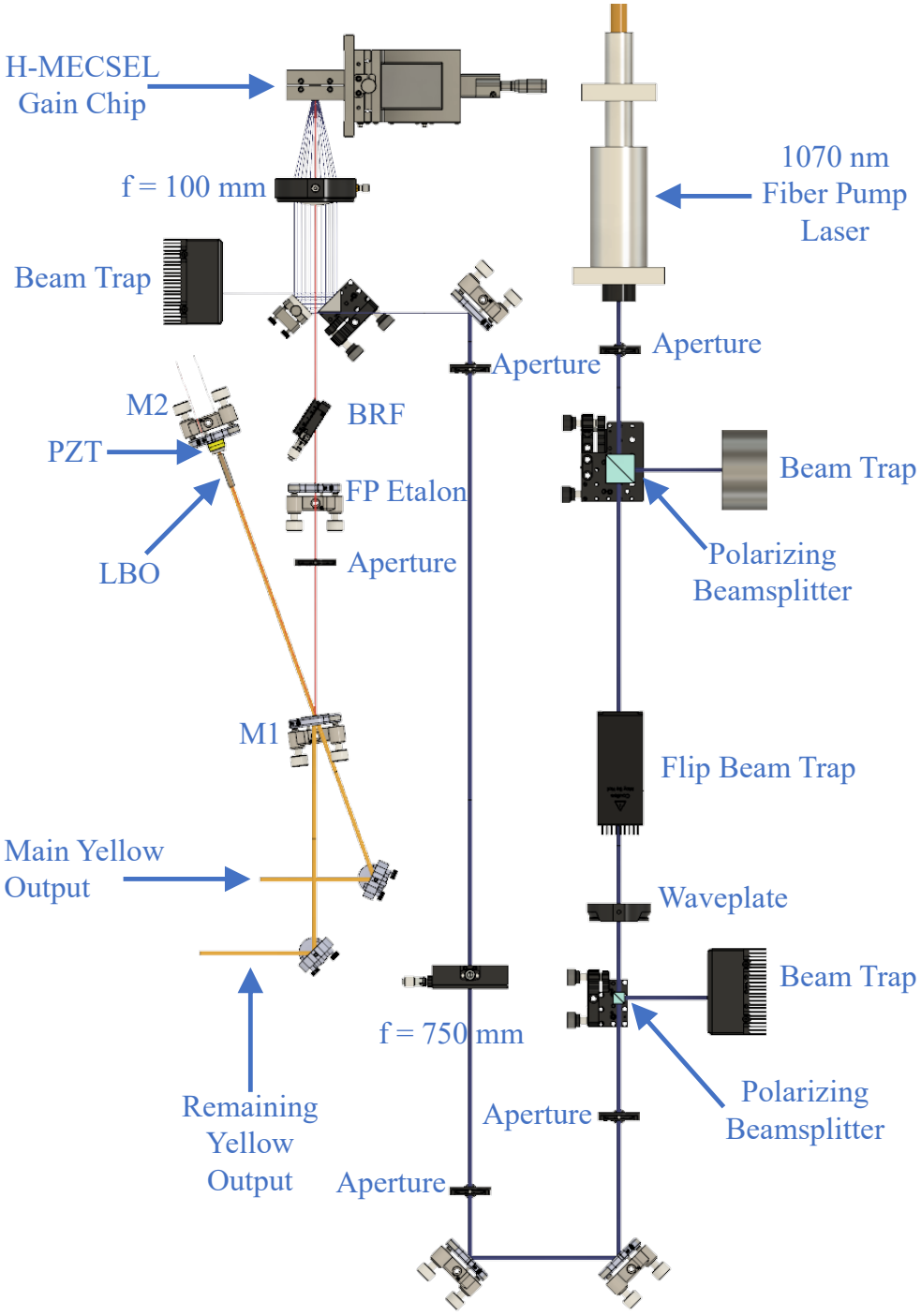

Fig. 8.6 Schematic diagram of the experimental setup, including pump beam optics, multi-pass scheme, H-MECSEL cavity and frequency reference.

aperture and a retro-reflector made up of two plane HR mirrors. After ten passes, the remaining pump was blocked by a beam trap. This setup can be improved in the future by adding an isolator at 1070 nm between the second PBS and the aperture. With this additional isolator, an HR mirror can be used to reflect the remaining pump beam back into the multi-pass pumping scheme, increasing absorption efficiency, rather than using a beam trap.

Additional cavity mirrors were coated for HR at 1178 nm and AR at 589 nm with various ROCs. A newly coated ROC=500 mm mirror was selected, enabling the replication of the V-cavity configuration as previously illustrated in Fig. 7.4. The cavity beam sizes at the gain chip and the plane end mirror were computed to be 347 µm and 243 µm, respectively, assuming a thermal lens with a 2 m focal length, calculated using the thermal lens equation (Eq. 6.16) with 30 W of dissipated heat. The experimental setup depicted in Fig. 7.4 was constructed, and a 4 mm thick quartz BRF along with a 100 µm thick YAG etalon were integrated into the laser cavity on the gain chip arm, with the chiller temperature maintained at 15 °C. The use of a thicker BRF allowed for finer wavelength adjustments albeit at the expense of a reduced wavelength tuning range of 41.9 nm, though extensive tuning was not the primary objective of this experiment. An aperture was also positioned in this arm to potentially shape the beam if needed. In the cavity, the LBO crystal was positioned near the plane cavity end mirror (M2) for intracavity frequency doubling, and a piezoelectric ring was attached to the back of this mirror for active frequency control. The folding mirror (M1) was mounted on a three-axis piezo mirror mount, which can also be used for laser output frequency control.

The main yellow output was directed through M1, which was AR coated at 589 nm. However, a small amount of yellow light remained in the cavity. Upon reflection from the H-MECSEL gain chip, this residual yellow light exited the cavity through the same folding mirror but in a different direction. This remaining yellow output was designed as a reference beam to generate the error signal used for feedback control to stabilize the laser output wavelength.

A box was constructed on the breadboard to cover the entire system, minimizing disturbances from surrounding air flows that could destabilize the laser operation. Additionally, the optical table beneath the breadboard is floated to isolate any ground variations that may disrupt the laser operation. This comprehensive setup ensured that all components were robustly integrated and prepared for field deployment.

8.4 Experimental Results at 1178 nm

The YAG etalon exhibits a temperature-dependent refractive index change and can experience a temperature increase during high-power operation. And because the etalon is an intra-cavity element, even a small change is sufficient to cause a shift in the laser output wavelength. Considering the aim of LGS is to target an atomic transition and the wavelength accuracy is in the range of 10 pm (12 pm corresponding to 10 MHz at 589 nm), the inclusion of a temperature maintaining element is essential. To ensure precise wavelength control, a ring heater was attached to the YAG etalon to maintain a constant temperature. This ring heater also allows for fine adjustments of the laser output wavelength through temperature tuning. The etalon angle was adjusted to achieve 100% transmission at 1178.32 nm with an etalon temperature of 40 °C. The transmission characteristics of this YAG etalon at 1178.32 nm across an achievable temperature range from 20 °C to 50 °C was plotted in Fig. 8.7. Since a complete tuning cycle was calculated to exceed 200 °C, the transmission change was less than 3% for this 30 °C tuning range. However, since this etalon is an intracavity element, even a small change in transmission can shift the laser output wavelength. Given that the goal of this laser is to target an atomic transition with high wavelength precision, temperature control of the etalon is necessary to maintain wavelength stability.

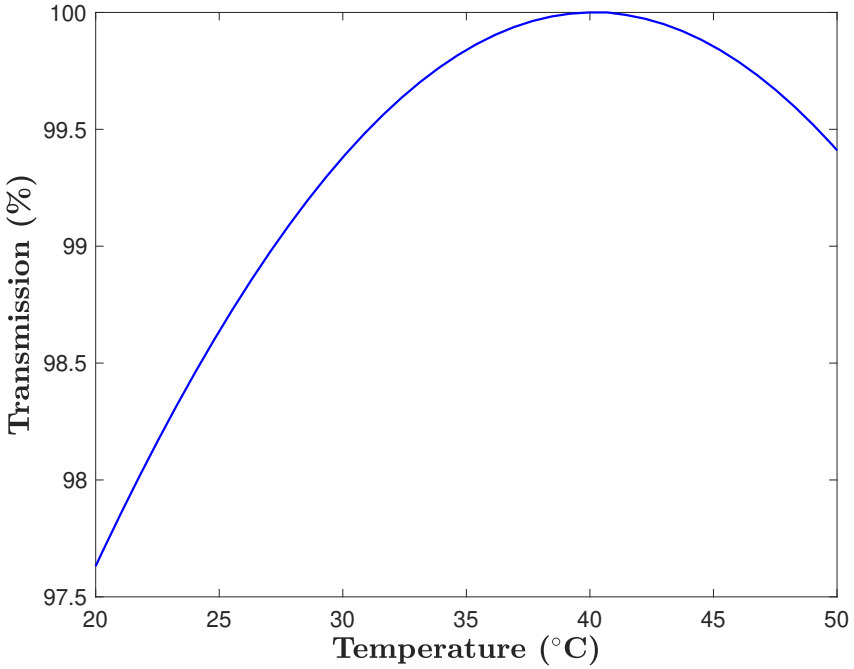

Fig. 8.7 Transmission versus etalon temperature at 1178.32 nm for a 100 µm thick YAG etalon [122].

The updated experimental results utilizing the V-cavity configuration tailored for linewidth narrowing are documented in Fig. 8.8. This configuration was tested under three operational conditions: free-running (black), with a BRF only (blue), and with a BRF and a FP etalon (red). During free-running operation, the system produced 28.9 W of output. When a 4 mm thick quartz BRF was introduced, the output power decreased to 21.4 W, and further insertion of a FP etalon, resulted an a linewidth below the spectrometer resolution with a power of 17.2 W at 1178 nm. The FP etalon heater was maintained at 40 °C during these measurements. Throughout these experiments, no thermal rollover was observed, and the slope efficiencies were 37.8%, 26.4%, and 24.2%, respectively, for the three setups. The decrease in slope efficiency across the setups can be attributed to increased intracavity loss due to the additional spectral shaping elements. The recorded spectra at maximum output power for each setup confirmed the

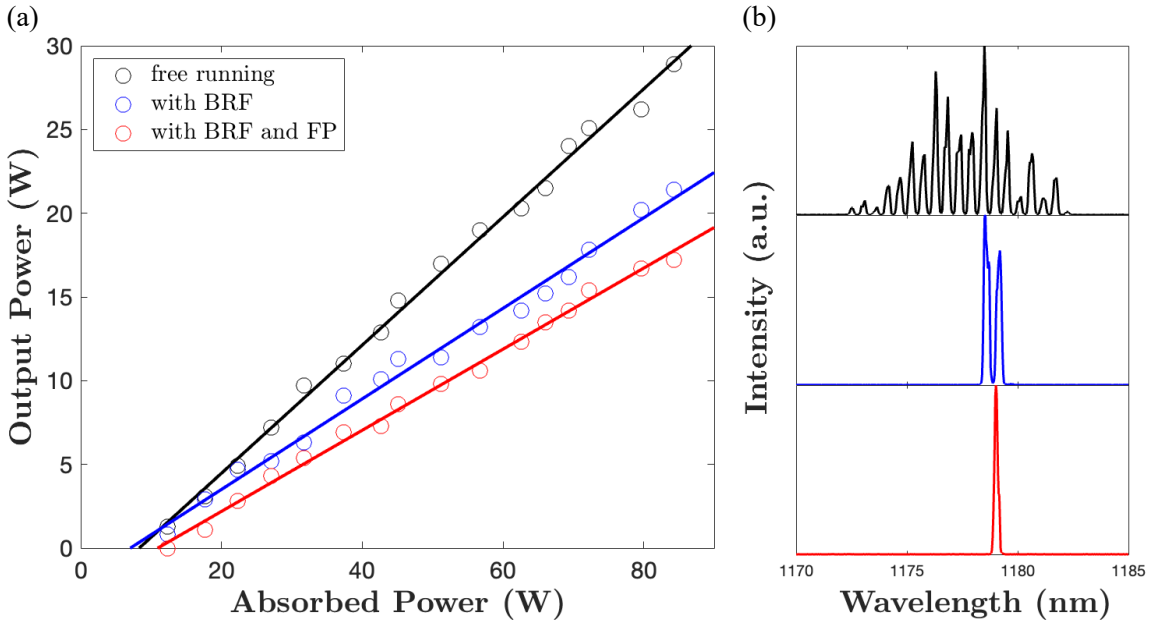

Fig. 8.8 H-MECSEL with the V-cavity configuration, (a) output power versus absorbed pump power and (b) spectra measured by an OSA for free running operation (black), with BRF and tuned to near 1178 nm (blue), and with BRF and FP etalon for linewidth narrowed operation at 1178 nm (red).

effectiveness of the linewidth narrowing strategy employed. The adjustment that led to an increase in the cavity beam size at the H-MECSEL gain chip position facilitated a recovery to higher power levels.

8.5 Experimental Results at 589 nm

In order to achieve the requirements for a semiconductor-based LGS, the H-MECSEL's wavelength must be converted to the appropriate wavelength near 589 nm. Using intracavity frequency doubling, a $\chi^{(2)}$ nonlinear process. A specially coated mirror, which exhibits HR at 1178 nm and AR at 589 nm, was employed as the OC for the yellow output. The remaining external mirrors are HR at both 589 nm and 1178 nm. Considering the optical components

available during the designing phase, the OC for the yellow output was constrained to either a plane mirror or a concave mirror with a ROC of 150 mm. This limitation necessitated a creative approach to the cavity design to accommodate the physical and operational parameters essential for LGS applications. Thus a Z-cavity configuration was initially adopted first, and later with the availability of more optics, the laser was switched back to a V-configuration as discussed in the previous section.

For achieving optimal performance in the conversion of 1178 nm to 589 nm using a LBO crystal, detailed optical planning and efficiency calculations were necessary. With a maximum output power of 28 W demonstrated from the H-MECSEL gain chip under free-running conditions with a 2.5% OC, the intracavity power was estimated to be approximately 1120 W. However, when considering the additional intracavity losses introduced by the insertion of a BRF and a FP etalon for wavelength tuning and linewidth narrowing, a more conservative estimate of 200 W intracavity power at 1178 nm was used for further calculations. This represents an underestimation in the design phase, considering the experimental results in the previous section indicate that the intracavity power exceeds 650 W. To maximize the SHG efficiency, the LBO crystal was placed near the cavity end mirror. Using the previously established nonlinear conversion efficiency equation

$$\eta_{\mathrm{SHG}} = \frac{2\omega^2 d_{eff}^2 l^2}{n_{2\omega} n_{\omega}^2 c^3 \varepsilon_0} \mathrm{sinc}^2\left(\frac{1}{2}\Delta k l\right) I^2(\omega), \tag{8.1}$$

the relationship between the beam radius and conversion efficiency for a 30 mm long LBO crystal was analyzed, as plotted in Fig. 8.9. This analysis demonstrated that the conversion efficiency increases as the fundamental beam size decreases. An optimal coupling efficiency of 3% was assumed, which required the cavity beam to have a radius of 257 µm at the position of the LBO crystal.

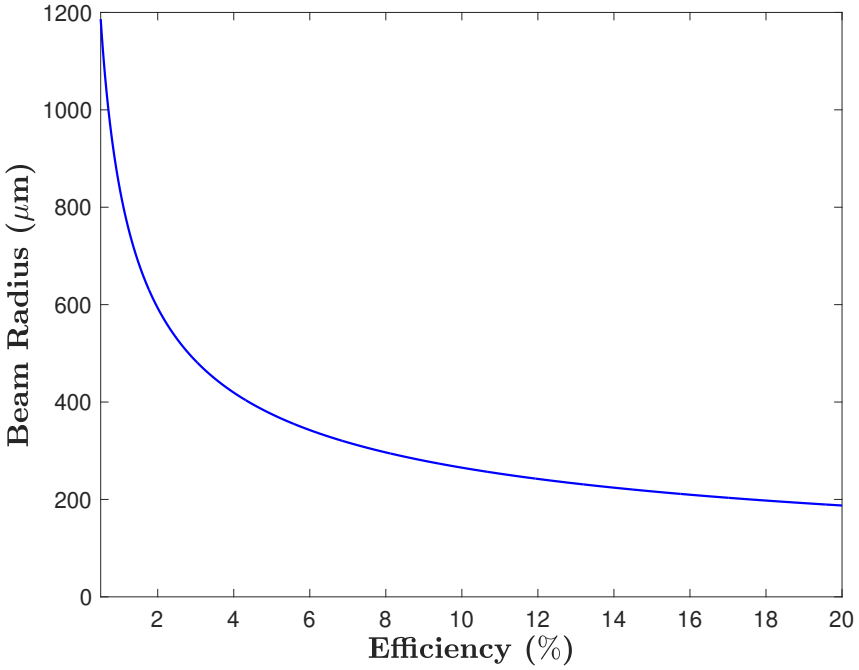

Fig. 8.9 Nonlinear conversion efficiency in a 30 mm long LBO crystal versus beam radius of 200 W of 1178 nm fundamental light.

The non-critical phase matching (NCPM) technique, as discussed in Chapter 2, was implemented for efficient frequency doubling from 1178 nm to 589 nm using a LBO crystal. NCPM is a preferred method to achieve phase matching between the fundamental and SHG wavelengths, as it allows the use of a long crystal without experiencing beam walk-off, thus facilitating high conversion efficiency. For LBO crystals, Type I NCPM involves having the fundamental light polarized along the y-axis (ordinary ray, o-ray), resulting in the SHG polarized along the z-axis (extraordinary ray, e-ray). In Type II NCPM, the LBO crystal is typically rotated 45° to have the fundamental light polarized along both the y-axis (o-ray) and the z-axis (e-ray), with the SHG polarized along the x-axis (o-ray). The refractive index of the crystal can be calculated using the Sellmeier equation, which depends on the wavelength and the temperature for all three axes. By adjusting the temperature of the LBO crystal, phase matching can be

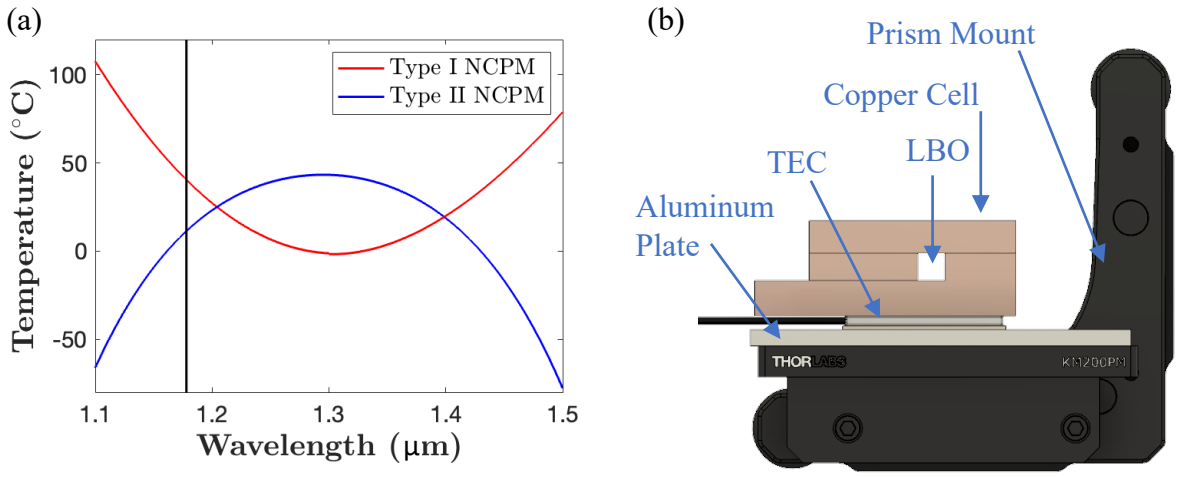

Fig. 8.10 (a) Temperature requirements for type I (red) and type II (blue) NCPM of a LBO crystal at different fundamental wavelengths. (b) CAD drawing of the home-made copper cell for LBO crystal temperature control on top of a prism mount.

achieved at different wavelengths. The temperature requirements for achieving SHG using an LBO crystal are presented in Fig. 8.10 (a), detailing both Type I (red) and Type II (blue) NCPM configurations. This figure was plotted using the LBO specifications and equations provided by EKSMA Optics. At the target wavelength of 1178 nm, the required temperatures are 40.49 °C for Type I NCPM and 11.37 °C for Type II NCPM. Type I NCPM was chosen for its ease of implementation, as opposed to Type II NCPM, which requires rotating the crystal by 45° to achieve two orthogonally polarized components in the fundamental light.

The LBO crystal employed for the experiments measured 5 mm×5 mm×30 mm, oriented at θ=90° and ϕ=0° for optimal Type I NCPM performance. Both facets of the crystal were coated with AR layers at 1178 nm and 589 nm to minimize losses. The crystal was housed in a custom-designed copper cell, shown in Fig. 8.10 (b), which utilized 50 μm thick indium foil to enhance thermal contact between the LBO crystal and the copper cell. A thermoelectric cooler (TEC), sandwiched between the copper cell and an aluminum plate, facilitated precise temperature adjustments, with thermal paste improving the thermal linkage. The entire assembly was

mounted on a prism mount, allowing fine adjustments to the crystal's orientation. Temperature regulation was achieved by integrating a thermistor within the cell for accurate temperature readings, connected alongside the TEC to a temperature controller. This setup ensured the LBO crystal was maintained at the precise temperature necessary for efficient SHG. The crystal's positioning within the laser cavity was adjusted to place one facet just 2 mm from the cavity's end mirror, optimizing the interaction with the intracavity light for maximum conversion efficiency to 589 nm.

In the experimental setup, the initial 2.5% OC was substituted with a plane mirror featuring HR coatings at both 1178 nm and 589 nm. This mirror was mounted onto a piezoelectric transducer ring to facilitate active frequency control during the experiment. Additionally, the ROC=500 mm folding mirror was specifically coated to be highly reflective at 1178 nm while allowing anti-reflection at 589 nm, thus serving as the output coupler for the yellow 589 nm beam generated by frequency doubling. To accommodate the nonlinear crystal within the laser cavity, adjustments were necessary for the LBO arm's length to ensure that the cavity beam sizes on the sample and the cavity end mirror remained consistent with previous configurations. Although it might seem intuitive to shorten the LBO arm to compensate for the optical path length difference due to the LBO crystal's higher refractive index than air, the ray transfer matrix analysis used for calculating cavity beam size indicated that an increase in arm length was required instead.

Initially, the LBO arm of the laser cavity without the LBO crystal had a length d_{initial}. The ABCD matrix for light propagation through this arm is:

$$\begin{bmatrix} 1 & d_{\text{initial}} \\ 0 & 1 \end{bmatrix}$$

When the LBO crystal is introduced, it alters the effective optical path within the arm. The ABCD matrix for light propagation through the LBO crystal, taking into account the refraction at the air-crystal interfaces and the travel through the crystal, is given by:

$$\begin{bmatrix} 1 & \frac{n_{\text{air}} d_{\text{LBO}}}{n_{\text{LBO}}} \\ 0 & 1 \end{bmatrix}$$

The total ABCD matrix for the new arm length d_{new} after introducing the LBO crystal is then:

$$\begin{bmatrix} 1 & d_{\text{new}} - \frac{n_{\text{LBO}} - n_{\text{air}}}{n_{\text{LBO}}} d_{\text{LBO}} \\ 0 & 1 \end{bmatrix}$$

To ensure that the beam properties are not altered, the new ABCD matrix in the LBO arm must remain equivalent to the original ABCD matrix. This means:

$$d_{\text{initial}} = d_{\text{new}} - \frac{n_{\text{LBO}} - n_{\text{air}}}{n_{\text{LBO}}} d_{\text{LBO}}$$

From this equation, the change in cavity length needed to accommodate the LBO crystal, denoted as Δd, is determined by:

$$\Delta d = d_{\text{new}} - d_{\text{initial}} = \frac{n_{\text{LBO}} - n_{\text{air}}}{n_{\text{LBO}}} d_{\text{LBO}},$$

which indicates that for LBO crystal that has refractive index larger than air, after insertion of the crystal, the LBO arm length needs to be increased.

To integrate the 30 mm LBO crystal into the laser cavity, the length of the LBO arm was increased by 11 mm to account for the crystal's refractive index of 1.55 at 1178 nm. This modification ensured that the cavity beam size on the cavity end mirror M2 was unchanged,

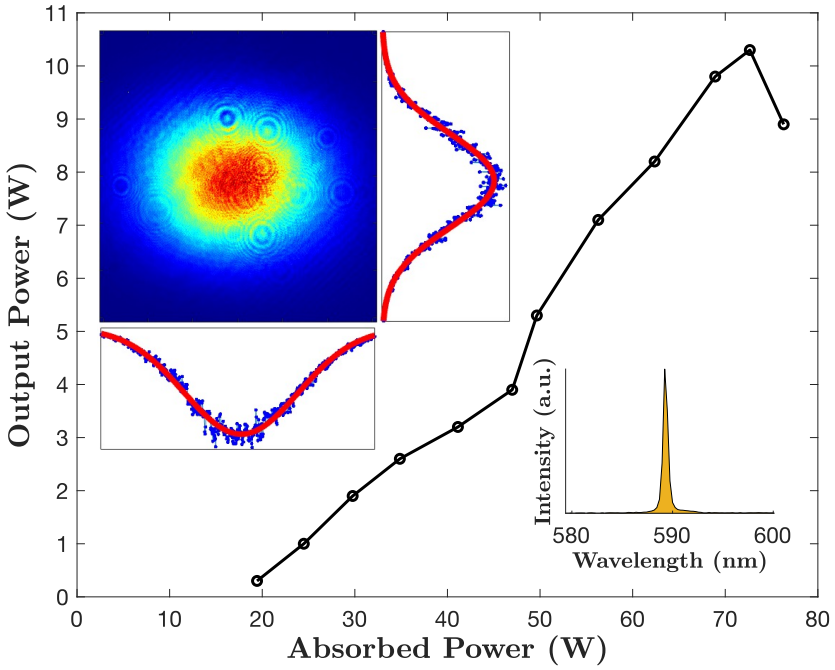

Fig. 8.11 Output power at 589 nm versus absorbed pump power. The top left inset is the beam profile with Gaussian fit, and the bottom right inset is the output spectrum, both insets measured at 10.3 W.

facilitating efficient frequency doubling. The LBO crystal was positioned 2 mm away from M2, aligning with the optical design to optimize the overlap of the fundamental and second harmonic waves. The experimental setup was carefully controlled with the chiller set at 15 °C. The temperature of the LBO cell was precisely adjusted to 41.77 °C to achieve phase matching, the temperature experimentally tested to yield highest output power at 589 nm.

The experimental outcomes at 589.2 nm were quantified and the resulting data were plotted in Fig. 8.11, where an output power of 10.3 W at 589.2 nm was achieved with 73 W of absorbed pump power. The top left inset of the figure illustrates the yellow beam profile with Gaussian fitting, measured at maximum output using a commercial beam profiler, confirming a TEM_{00} mode. The bottom right inset displays the output beam spectrum at maximum output, captured using an Ocean Optics HR4000 spectrometer. Upon attaining the peak output of 10.3 W at

589.2 nm, a subsequent increase in pump power led to a decrease in output power. This phenomenon was initially hypothesized to be thermal rollover, as per the thermal model described in Chapter 6, which predicted a temperature of approximately 100 °C under a heat load of 49 W (equivalent to 73 W of absorbed pump power). In addition, as the maximum output power of the H-MECSEL significantly decreases from free-running operation at 1178 nm to linewidth-narrowed operation at 589 nm, this reduction in laser output extraction leads to increased heat generation. Consequently, the actual temperature may higher than predicted by the thermal model.

However, the laser with similar experimental setups did not exhibit thermal rollover even at higher pump powers, as shown in Fig. 8.8 (a). At 1178 nm, the linewidth narrowed H-MECSEL produced 6.9 W more output power with an additional 11.6 W of absorbed pump power compared to 589 nm operation, which is an extra 4.7 W of heat in the gain chip at 1178 nm operation but there was no thermal rollover. This disparity suggests that the observed decline in 589 nm output may stem from an excessively high nonlinear conversion efficiency rather than thermal effects. For the conversion efficiency calculations, an intracavity power of 200 W at 1178 nm was presumed, which established the optimal cavity beam size in the LBO crystal. However, the actual intracavity power, post-linewidth narrowing with BRF and FP etalon, reached 712 W, corresponding to a 12% conversion efficiency for a 30 mm long LBO crystal at maximum pump power. The exponential increase in nonlinear conversion efficiency with the intensity of the fundamental wavelength implies that when the conversion efficiency surpasses the optimal output coupling efficiency of the laser, the output power may decrease as pump power increases. The intracavity beam size in the LBO crystal needs to be altered to control the nonlinear conversion process to avoid efficiency losses at high pump powers.

The resolution of the Ocean Optics HR4000 (4C4754) spectrometer, at 0.26 nm (corresponding to 225 GHz at 589 nm), was insufficient for the precise linewidth measurement required for

LGS applications. Consequently, a commercial scanning Fabry-Pérot interferometer (SFPI), with a FSR of 1 GHz and a resolution of 2.5 MHz, was employed to obtain a more accurate determination of the spectral linewidth. The linewidth (FWHM) of the 10.3 W output at 589 nm was measured to be 7 MHz, confirming single longitudinal mode operation, as depicted in Fig. 8.12. The experiment successfully demonstrated over 10 W of linewidth-narrowed, single longitudinal TEM_{00} transverse mode laser output at 589.2 nm. This achievement marks a significant milestone towards meeting the spectral requirements of LGS applications. However, active frequency stabilization remains the final technical challenge to address before the system is ready for deployment in on-sky testing at an observatory.

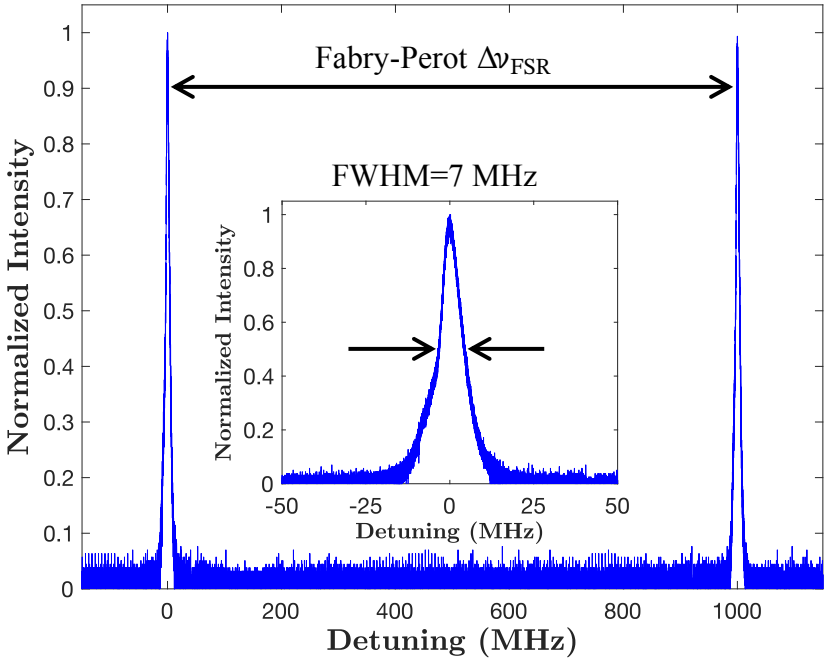

Fig. 8.12 The linewidth (FWHM) of the 589 nm output was measured to be 7 MHz using a SFPI with FSR of 1 GHz.

8.6 Conclusion

The experimental investigations presented in this chapter detailed the wavelength tuning and linewidth narrowing with intracavity BRF and FP etalon for H-MECSEL setup. This H-MECSEL assembly was mounted on a breadboard incorporating pump optics, the laser cavity, the multi-pass pumping structure, and a frequency reference, preparing the system for observatory deployment. Wavelength tuning and linewidth narrowing were achieved using a 4 mm thick quartz BRF and a 100 µm thick YAG etalon, culminating in a single longitudinal mode output of 17.8 W at 1178 nm. Subsequently, a 30-mm long type I non-critical phase matching LBO crystal was integrated within the laser cavity, set to an optimal temperature of 41.66 °C, which supported the generation of 10.3 W at 589.2 nm with a TEM_{00} transverse mode and single longitudinal mode. A scanning Fabry-Pérot interferometer measured the laser output linewidth at 7 MHz (FWHM). This system thus achieved all design specifications calculated in Chapter 1, except for laser frequency stabilization as the last piece of the puzzle, which will be the focus of the subsequent chapter.

Chapter 9

Laser Frequency Stabilization

Ensuring the laser output wavelength aligns with the sodium D_2 transition is essential to optimize sodium atom absorption and maximize the detection of backscattered photons by ground-based telescopes. If the laser output frequency deviates significantly from the absorption peak of sodium atoms, the H-MECSEL setup detailed in previous chapters may not generate an artificial beacon with adequate fluorescence for LGS applications. This chapter introduces the fundamentals of laser frequency stabilization, followed by discussions on frequency reference preparation, error signal generation, and feedback implementation. Finally, preliminary experimental results will be presented before the conclusion of this chapter. Part of the experimental results in this chapter were reported at the SPIE Photonics West Conference [76], but they have not yet been published in a peer-reviewed journal.

9.1 Laser Frequency Stabilization Fundamentals

Frequency stabilization encompasses four essential components: A laser that is incident on a frequency reference, creating a signal to be analyzed by a frequency discriminator, and a

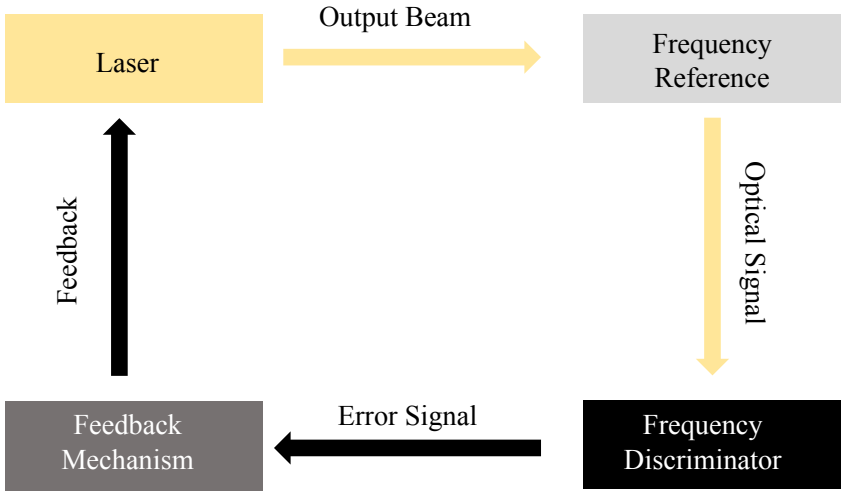

Fig. 9.1 Schematic diagram of a laser frequency stabilization system.

feedback mechanism to reduce wavelength deviations [144] as illustrated in Fig. 9.1. Typically, the frequency reference is a reference cavity or an atomic transition line that aligns with the desired frequency to which the laser is intended to be synchronized. The frequency discriminator facilitates a comparison between the wavelength of the laser output and the desired wavelength, transforming the optical signal from the laser beam into an electrical signal compatible with the feedback loop. The feedback mechanism uses this error signal, with various methods of feedback control being employed to accurately adjust the laser wavelength.

The frequency reference may be provided by a wavemeter, which also supplies the error signal. This method is currently used by some commercial vendors of LGS systems, is straightforward and operates at a repetition rate around 1 kHz, which is a typical requirement for AO systems. However, the implementation requires an expensive wavemeter to have a 10 MHz level resolution at the D_{2a} transition of sodium atoms. Operation at the repetition rate in kHz level is necessary for real-time aberration correction, implying that the wavemeter must also function at this speed. Only a few wavemeters can meet both requirements simultaneously, and they are all cost-prohibitive. Alternatively, a stable reference cavity can serve as the frequency

reference, with the signal (after frequency reference) detection facilitating the generation of a discriminant signal. Lastly, a sodium vapor cell can be employed as a frequency reference, utilizing its wavelength-specific absorption features. The transmitted signal can be detected by a photodiode and used to generate the discriminant signal. The later implementation will be explored in this chapter.

The Pound-Drever-Hall (PDH) method [145] is a widely used technique for laser frequency stabilization. Locking to the peak is typically challenging, a sideband on the side of the peak is necessary for locking. The PDH method employs an electro-optic modulator to generate two sidebands near the laser wavelength outside the laser cavity bandwidth, to facilitate the locking process. Zero error signal can be achieved at the locking point, and the error signal has a non-zero slope with opposite signs on either side of the locking point, indicating the direction of the feedback needed for stabilization. The PDH method can achieve sub-Hertz levels of laser frequency stabilization [146]. However, the equipment required for this technique, along with the necessity for external frequency modulation, renders this method less favorable for our experiment.

Dither locking [147] presents a simpler alternative to the PDH method. Although it may be less sensitive and have a narrower locking range, these limitations do not pose significant concerns in light of our system's stabilization requirements. The implementation of the dither locking method is particularly suited for future updates to the system, as the components required for laser frequency sweeping are already integrated into this frequency stabilization system. Consequently, there is no need to add additional components, making it a preferred choice for future systems where dynamic wavelength shifts may be employed to avoid saturating the absorption of atmospheric sodium. To construct a dither locking system for the experiment, a PZT was attached to the rear of one laser cavity mirror to modulate the laser frequency. By applying varying voltages to the PZT, its thickness undergoes changes, resulting in adjustments

to the length of the laser cavity, and the laser wavelength correspondingly adjusts. A sodium vapor cell was utilized as the frequency reference due to its frequency-sensitive absorption characteristics.

For dither locking, the laser frequency ω is modulated at the dither frequency ω_d, it is modulated by $\Delta\omega$. The frequency reference exhibits a Gaussian-shaped absorption spectrum in Fig. 9.2 (a). This Gaussian shape is assumed to account for Doppler broadening, which inherently follows a Gaussian distribution. However, if only the natural broadening due to the finite lifetime of the excited state of the atom is considered, the absorption spectrum would instead exhibit a Lorentzian shape. When the laser frequency is modulated at various parts of this absorption spectrum, the same frequency change $\Delta\omega$ results in different amplitude changes ΔA. With the same frequency modulation, the amplitude change ΔA observed on the slope of the absorption spectrum is significantly larger than that at the absorption peak. This variation in amplitude response is due to the steeper gradient of the absorption profile on the slope compared to the relatively flat peak, which affects the sensitivity of the detection system to frequency changes. In addition, if the laser frequency is modulated solely on the slope of the absorption spectrum, the resulting signal modulation frequency is ω_d. Conversely, if the laser frequency modulates around the peak of the absorption spectrum, the signal modulation frequency doubles to $2\omega_d$. A photodiode was employed to detect the transmitted laser light, converting the optical signal into an electrical signal. This detected signal was then routed to a lock-in amplifier for phase-sensitive detection.

The generated error signal is depicted in Fig. 9.2 (b), which shares the same x-axis as Fig. 9.2 (a). Three red lines connect these two figures, demonstrating that at the peak of the absorption position, the error signal reaches zero with a non-zero slope, exhibiting error signals of opposite signs on either side of the peak. Additionally, the peaks and valleys of the error signal occur where the gradient of the absorption slope is maximal, defining the effective

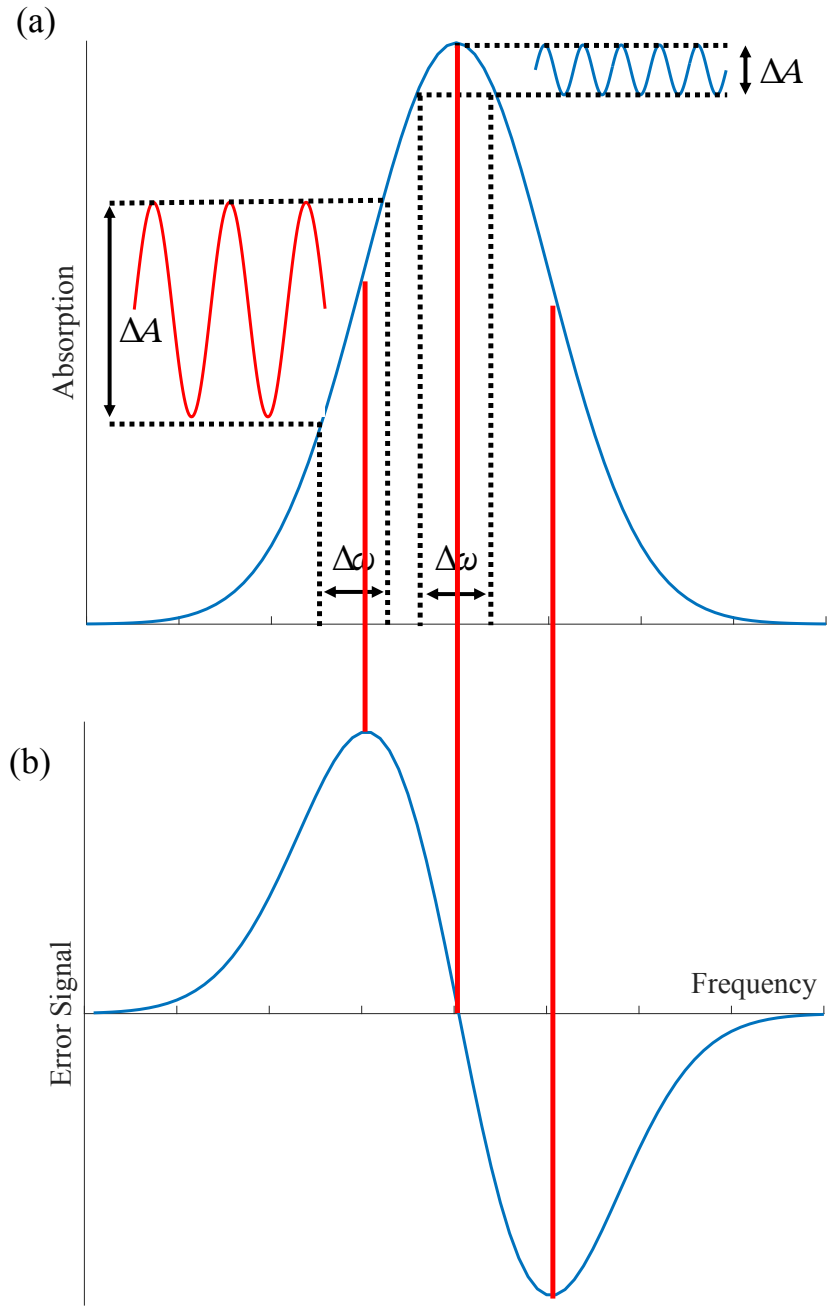

Fig. 9.2 (a) Absorption versus frequency for an atomic frequency reference. (b) Error signal generated from the frequency reference.

locking range. The shape of the generated error signal corresponds to the derivative of the absorption curve of the frequency reference.

To generate the desired error signal as illustrated in Fig. 9.2 (b), the measured optical signal, characterized by frequency ω_{sig}, phase θ_{sig}, and amplitude A_{sig}, is expressed as:

$$S(t) = A_{\text{sig}} sin(\omega_{\text{sig}} t + \theta_{\text{sig}}), \tag{9.1}$$

which represents the absorption feature of the frequency reference. This signal will be sent to a lock-in amplifier for phase-sensitive measurement. The lock-in amplifier utilizes a reference sine signal, which is defined by frequency ω_{ref}, phase θ_{ref}, and amplitude A_{ref}, and can be written as:

$$R(t) = A_{\text{ref}} sin(\omega_{\text{ref}} t + \theta_{\text{ref}}). \tag{9.2}$$

This setup enables the lock-in amplifier to detect the phase and amplitude differences between $S(t)$ and $R(t)$, thus facilitating the extraction of the error signal. The multiplication of the two signals $S(t)$ and $R(t)$ yields an output signal $V_{\text{out}}(t)$:

$$V_{\text{out}}(t) = S(t) \times R(t), \tag{9.3}$$

where the AC terms are filtered out by a low-pass filter, leaving a non-zero DC component only when $\omega_{\text{sig}} = \omega_{\text{ref}}$. This condition simplifies the equation to:

$$V_{\text{out}}(t) = \frac{A_{\text{sig}} A_{\text{ref}}}{2} \cos(\theta_{\text{sig}} - \theta_{\text{ref}}), \tag{9.4}$$

Through the manipulation of the phase delay of the reference signal, the resultant output can be effectively simplified to:

$$V_{\text{out}}(t) = \frac{A_{\text{sig}} A_{\text{ref}}}{2},$$

where A_{ref} remains constant, as determined by the lock-in amplifier's settings, and A_{sig} is contingent upon the laser's output frequency, correlating with the slope of the absorption spectrum of the frequency reference. This setup ensures that the generated error signal is proportionate to the derivative of the absorption spectrum.

The generated error signal $e(t) = V_{\text{out}}(t)$ is subsequently directed to a proportional-integral-derivative (PID) controller [148], which produced a feedback signal to the PZT, thereby controlling the laser frequency. The control signal generated by the PID controller, $u(e,t)$, can be expressed as [149]:

$$u(e,t) = K_{\text{p}} e(t) + K_{\text{i}} \int e(t)\, dt + K_{\text{d}} \frac{de(t)}{dt},$$

where K_{p}, K_{i}, and K_{d} represent the proportional, integral, and derivative gains, respectively. This formulation allows the controller to adjust the control signal based on the current error, the accumulated past errors, and the rate of change of the error, facilitating effective stabilization of the system [149]. In this dissertation project, a proportional-integral (PI) controller was utilized, as only low-frequency noise was present. The derivative component for correcting high-frequency noise was therefore omitted.

9.2 Frequency Reference

The preparation of the frequency reference is the initial step in constructing the laser frequency stabilization system. For on-sky operation of a deployed LGS, the laser power is utilized to interact with a 10 km thick sodium layer. In contrast, only a milliwatt-level yellow leakage

is employed with a 2-inch long sodium vapor cell for stabilization, while the bulk of the yellow output power is dedicated to creating the LGS. As a result, the sodium vapor cell must be controlled to generate a sufficient laser frequency-related discriminant for error signal generation.

All atoms are continuously in motion, and the varying velocities of these atoms lead to different Doppler shifts. This phenomenon results in an effect known as Doppler broadening [150]. The root mean square (RMS) width of this broadening, denoted as δ_{D}, can be expressed as:

$$\delta_{\mathrm{D}} = \nu_0 \sqrt{\frac{k_{\mathrm{B}} T}{M c^2}}, \tag{9.5}$$

where ν_0 represents the center resonance fluorescence frequency, k_{B} is the Boltzmann constant, T denotes the temperature in Kelvin, M is the atomic mass, and c is the speed of light. This equation quantifies the effect of thermal motion on the spectral linewidth due to Doppler broadening. For interested sodium atoms, at room temperature (300 K), this broadening is approximately 567 MHz. If the sodium atoms are heated to 400 K, the broadening increases to 655 MHz. Conversely, for atoms within the mesospheric sodium layer at a reduced temperature of $\sim$200 K [40], the Doppler broadening is reduced to 463 MHz.

The backscattering mechanism for sodium atoms operates as follows: atoms transition to a higher energy level upon absorbing incident photons. This higher energy state is unstable and characterized by a short effective lifetime, typically on the order of tens of nanoseconds. Subsequently, the excited atoms return to their original energy level, simultaneously scattering resonance fluorescence photons. This process, in which all absorbed photons are eventually scattered, is known as resonance fluorescence scattering [151]. The probability of an incident photon being absorbed by sodium atoms is described by the absorption cross-section. The peak

Table 9.1 Parameters for sodium D_2 line.

	Hyperfine Number	$^2S_{\frac{1}{2}}$	$^2P_{\frac{3}{2}}$	Offset (GHz)	Relative Strength (f_i)
D_{2a}	1	F=2	F=1	-0.7150	1/32
D_{2a}	2	F=2	F=2	-0.6806	5/32
D_{2a}	3	F=2	F=3	-0.6216	14/32
D_{2b}	4	F=1	F=0	-1.0408	2/32
D_{2b}	5	F=1	F=1	-1.0566	5/32
D_{2b}	6	F=1	F=2	-1.0911	5/32

value of the absorption cross-section can be calculated using the following equation [152]:

$$\sigma_{\text{peak}} = \frac{1}{\sqrt{2\pi}} \frac{e^2}{4\varepsilon_0 m_e c \delta_D} f, \tag{9.6}$$

here, e represents the electron charge, ε_0 denotes the vacuum permittivity, m_e is the electron mass, δ_D refers to the Doppler broadening, and f is the oscillator strength associated with the sodium atoms. The frequency-dependent absorption cross-section can be expressed as follows:

$$\sigma(\nu) = \sigma_{\text{peak}} \exp\left(-\frac{(\nu-\nu_0)^2}{2{\delta_D}^2}\right), \tag{9.7}$$

where ν is the frequency of the incident light, and ν_0 is the center resonance frequency. For sodium atoms, the center resonance frequency (ν_0) is 509.2 THz, the atomic mass is 3.705×10^{-26} kg, and the oscillator strength (f) is 0.6408 [153].

For the sodium D_2 line, there are six hyperfine transitions, the parameters of which are detailed in Table 9.1 [152, 154]. This table includes the hyperfine number, initial hyperfine states in $^2S_{\frac{1}{2}}$, final hyperfine states in $^2P_{\frac{3}{2}}$, the frequency offset relative to the central frequency, and the relative line strength for each transition.

The total absorption cross-section of sodium is determined by summing the absorption cross-sections of each individual transition line within the hyperfine structure. This relationship

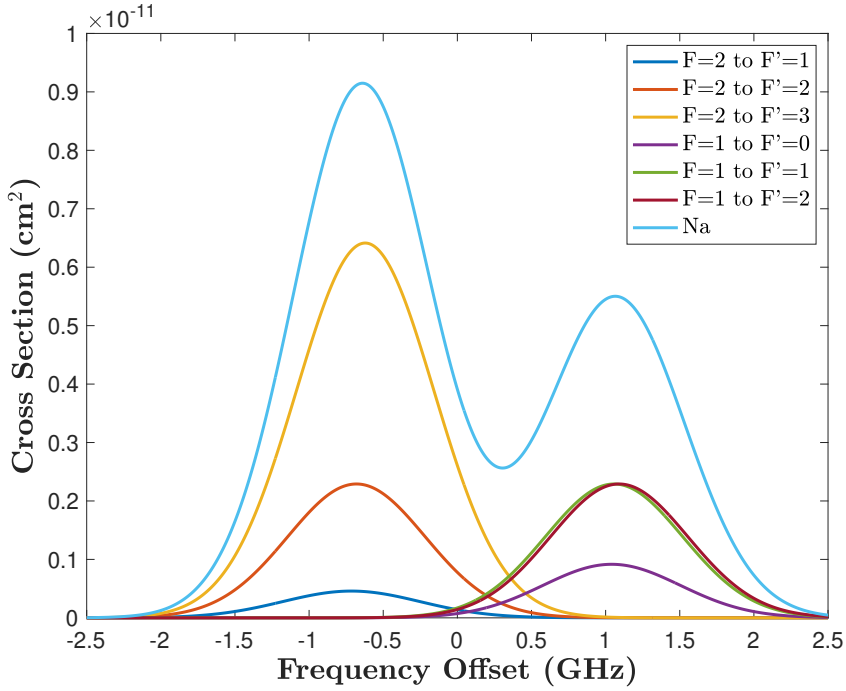

Fig. 9.3 The total absorption cross-section of sodium with the individual hyperfine transition lines at 200 K.

is expressed as [152]:

$$\sigma_{\mathrm{Na}}(\nu) = \sum_{i=1}^{6} f_{\mathrm{i}} \sigma^{i}(\nu), \tag{9.8}$$

where f_{i} represents the relative line strength and $\sigma^{i}(\nu)$ denotes the absorption cross-section for the i-th hyperfine transition line.

The total cross-section of sodium at 200 K (sodium layer temperature [40]), encompassing the individual hyperfine transition lines, is depicted in Fig. 9.3. This graphical representation illustrates the contribution of each transition line to the overall absorption profile. Using the Beer-Lambert law, the absorption coefficient of a sodium cell can be expressed as follows:

$$\alpha_{\mathrm{Na}} = -\frac{1}{z_{\mathrm{Na}}} \ln\left(\frac{P(z_{\mathrm{Na}})}{P_0}\right) = -\frac{1}{z_{\mathrm{Na}}} \ln(T_{\mathrm{Na}}), \tag{9.9}$$

where z_{Na} represents the thickness of the sodium gas cell, and P_0 and $P(z_{\mathrm{Na}})$ are the powers of the laser beam before entering and after passing through the cell, respectively, and T_{Na} refers to the transmittance of the sodium cell. The absorption coefficient α_{Na} can be directly related to the absorption cross section σ_{Na} through the number density N_{Na} of sodium atoms, as follows:

$$\alpha_{\mathrm{Na}} = \sigma_{\mathrm{Na}} N_{\mathrm{Na}}. \tag{9.10}$$

The temperature-dependent number density of alkali metals, such as sodium, can be expressed as follows [155]:

$$N_{\mathrm{Na}}(T) = N_{\mathrm{Na}}^{0} \frac{T_0}{T} e^{b\left(1-\frac{T_0}{T}\right)}, \tag{9.11}$$

where N_{Na}^{0} is the reference number density at reference temperature, T_0, and b is a parameter that characterizes the temperature sensitivity of the number density. For sodium, these parameters are given as $N_{\mathrm{Na}}^{0} = 10^8\,\mathrm{cm}^{-3}$, $T_0 = 336.79\,\mathrm{K}$, and $b = 38.306$ [155]. The transmission through a 2-inch long sodium cell at various temperatures is shown Fig. 9.4. This plot demonstrates that the absorption decreases significantly as the cell temperature is reduced, with negligible frequency-related absorption changes observed below 360 K. It is imperative to heat the sodium cell adequately to generate a sufficient frequency-related discriminant signal, which is essential for the system to produce a clear error signal. The sodium cell was housed within a homemade cell, with a maximum achievable temperature of 405 K due to the limited heating power of the cell. Despite this limitation, the temperature is sufficient to induce appreciable frequency-related transmission changes within the sodium cell.

Saturated absorption spectroscopy (SAS, also known as Lamb dip spectroscopy) is a method for generating Doppler-free signals [156], offering a sharper change in the transmitted signal within a confined dither frequency range. In the SAS technique, two laser beams—commonly designated as the pump and probe beams—are directed through a vapor cell in opposite direction.

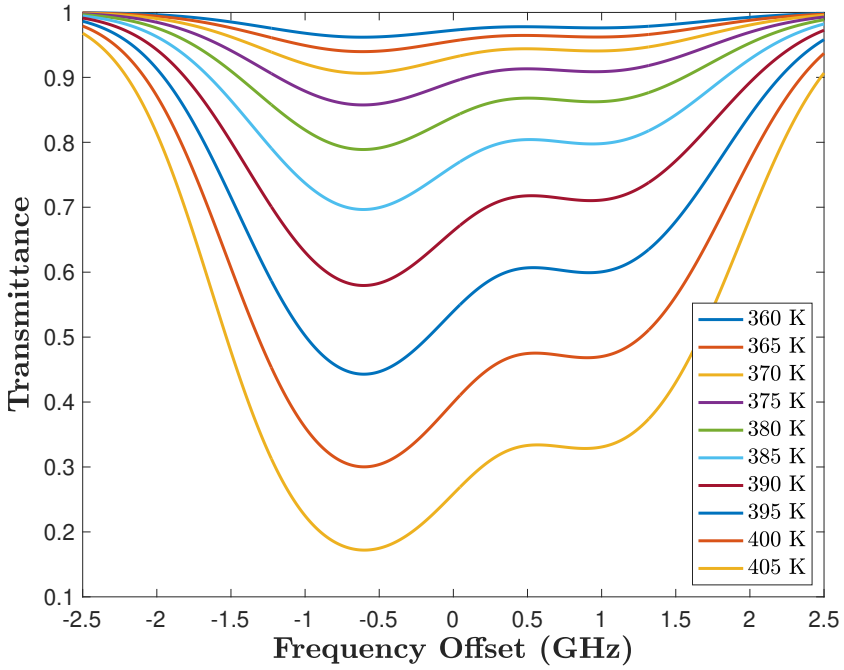

Fig. 9.4 Temperature related transmission of a 2-inch long sodium cell.

The pump beam's intensity is sufficient to saturate the absorption of specific atomic transitions, while the probe beam is employed to measure the resulting absorption. Saturation induced by the pump beam alters the population distribution across energy levels, thereby reducing the absorption features detectable by the probe beam on atoms with minimal velocity along the probe beams' direction. This reduction yields narrow, Doppler-free peaks that stand out against the Doppler-broadened background typical of standard absorption spectroscopy. Using a SAS setup, researchers reported Doppler-free spectroscopy of the Na D_2 line as shown in Fig. 9.5 [157]. The author's experiment aimed to replicate these results.

The experimental setup for SAS is depicted in Fig. 9.6. The linearly polarized laser light first passes through a half-wave plate (HWP), which adjusts its polarization. The light then encounters a polarizing beam splitter (PBS), where part of it is reflected towards photodiode 1 (PD1). This photodiode functions as a reference detector to monitor output power and compensate for

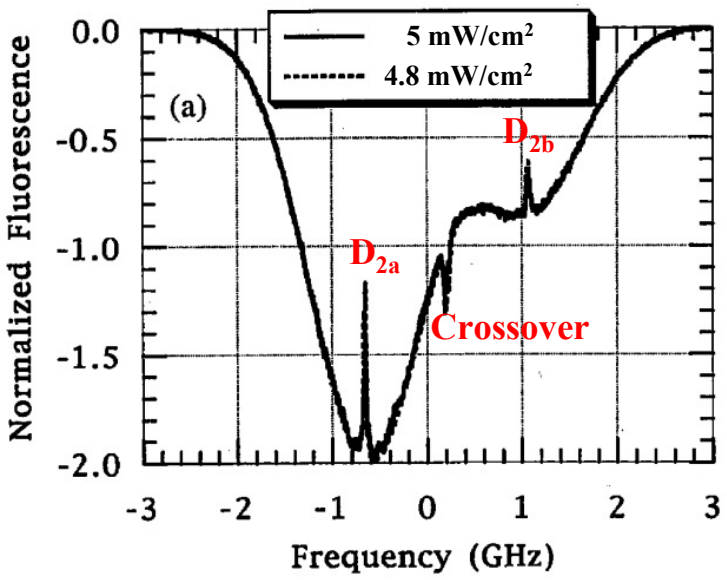

Fig. 9.5 Doppler free spectroscopy results of Na D_2 line [157]. The solid line is the experimental result with laser intensity of 5 mW/cm^2, and the dash line is the simulation result with laser intensity of 4.8 mW/cm^2.

any power fluctuations. The transmitted light from the PBS is modified by a quarter-wave plate (QWP) that converts its polarization from linear to circular before it passes through a sodium cell heated to 405 K, which absorbs approximately 80% of the incident light at the absorption peak of sodium D_{2a}. After the sodium cell, the beam passes through a neutral density (ND) filter, which further modulates the intensity difference between the pump and probe beams. The now weakened pump beam is directed onto a HR mirror, which not only reflects but also reverses the polarization from left-hand to right-hand, transforming it into the probe beam. This probe beam is then further attenuated by the ND filter as it retraces its path through the sodium cell.

Upon exiting the cell, the QWP converts the probe beam's polarization back to linear but perpendicular to the input beam polarization. The linearly polarized probe beam is subsequently reflected by the PBS towards photodiode 2 (PD2), which detects the transmitted signal. Through-

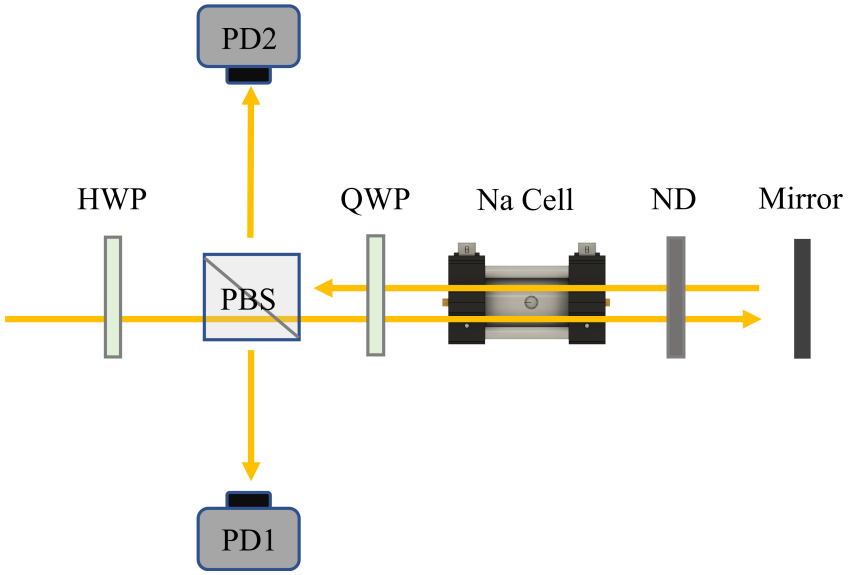

Fig. 9.6 Schematic diagram of SAS setup for LGS frequency reference generation. The pump and probe beams are shown separately for clarity, though they need to be overlapped in the experiment.

out the experiment, fine adjustments are made to the QWP to maximize the detected signal at PD2, and the HWP is tuned to ensure that the signals at PD1 and PD2 are balanced, allowing for the effective removal of intensity fluctuations by subtracting the two signals. Components typically involved in managing beam size and preventing detector saturation or beam clipping, such as telescopic systems, attenuator rings, and lenses, are omitted from the schematic to present a clear and concise conceptual understanding.

In the experiment, a laser beam with a diameter of 3 mm and a power of 0.4 mW was directed into the sodium cell, resulting in an intensity of 6 mW/cm^2. This intensity is close to the theoretically calculated steady-state saturation intensity of 6.26 mW/cm^2 for circularly polarized light on the sodium D_2 line [33]. An ND=0.3 filter was applied to the probe beam, reducing its power to approximately 10% of the pump beam accounting for the absorption by the sodium cell. The spectroscopic outcomes of the SAS experiment are depicted in Fig. 9.7, with (a) displaying repeated scan results and (b) offering a detailed view within the 300 MHz

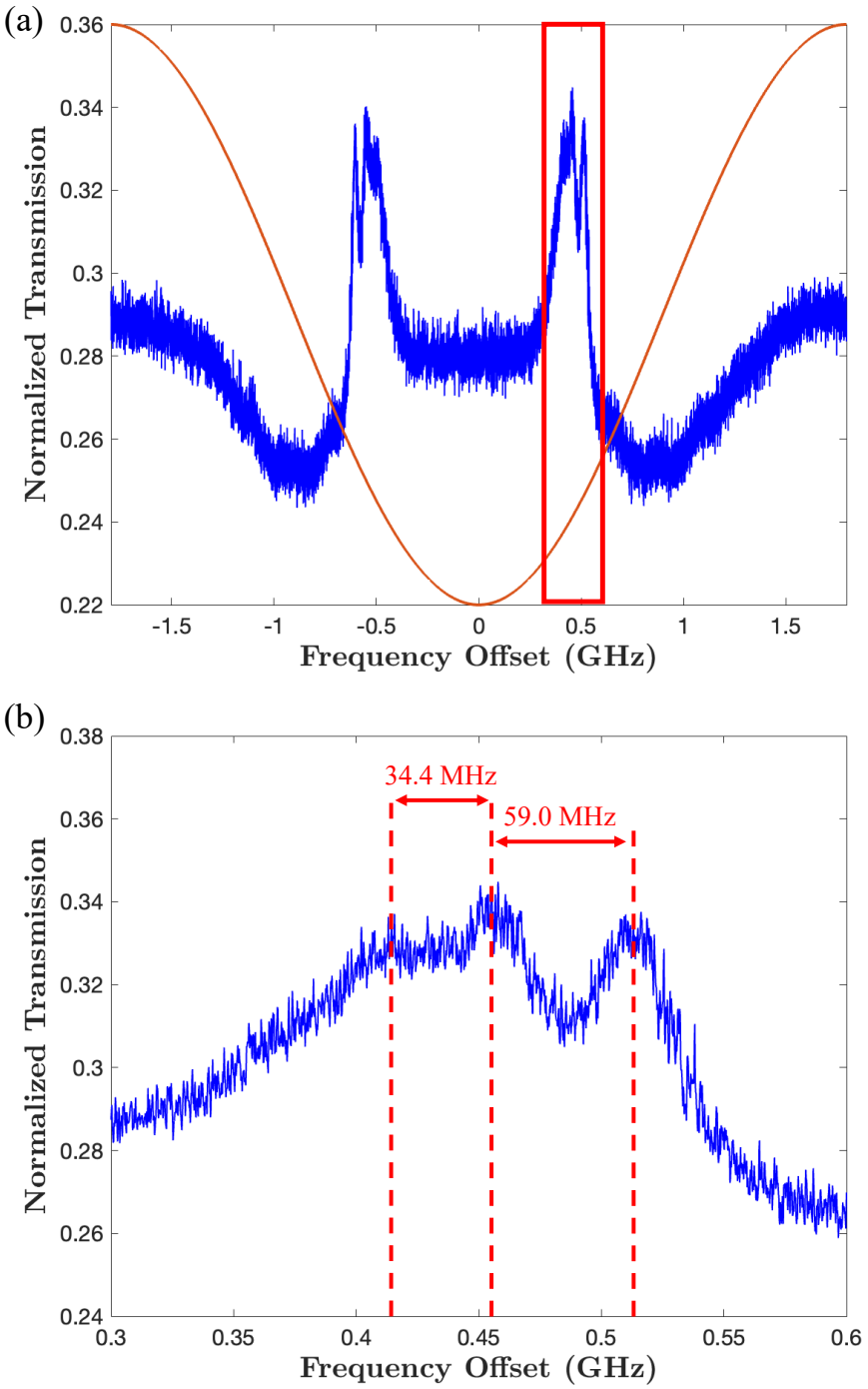

Fig. 9.7 (a) A complete scan cycle in a SAS experiment, with the red curve indicating the scanning signal and the blue curve representing the normalized transmission detected by photodiodes. (b) Detailed view of the frequency range from 300 MHz to 600 MHz.

to 600 MHz frequency range. In this setup, a sine wave signal from a function generator, represented by the red curve in Fig. 9.7 (a), was applied to a PZT attached to the back of a cavity mirror. This signal modulated the cavity length, enabling a complete scan of the cavity from its peak expansion through to its minimal point—set as the 0 GHz frequency offset—and back to the maximum. This scan cycle produced a symmetrical response in the scanning signal at points equidistant from the minimum, suggesting that the cavity length—and consequently the laser output frequency—was also symmetrically modulated.

The blue lines in the graph represent normalized transmission signals detected by photodiodes, demonstrating that the scanning results are symmetric around the minimum point of the scan. Three hyperfine transition peaks, symmetric about the zero-frequency offset, are evident on both sides of the scan. A closer inspection of the zoom-in section in Fig. 9.7 (b) reveals that the separation between these transitions corresponds to 34.4 MHz and 59 MHz, respectively. As detailed in Table 9.1, the relative strengths of these transitions are 1/32, 5/32, and 14/32. This ratio explains why the first peak is almost indiscernible and the final peak is markedly pronounced.

9.3 Feedback Mechanism

In the laser frequency stabilization experiment, a similar setup that previously achieved 10 W of yellow output at 589 nm was utilized, as depicted in the CAD drawing shown in Fig. 9.8. This configuration employed a V-cavity layout incorporating an H-MECSEL sample coupled with a multi-pass structure that included an aspheric lens and two plane mirrors mounted on a dedicated small breadboard. For wavelength stabilization and linewidth narrowing, the system integrated a 4 mm thick quartz BRF and a 100 µm thick YAG etalon, with the etalon temperature control via a ring heater attached to the etalon mount. The LBO crystal AR coated for 1178 nm

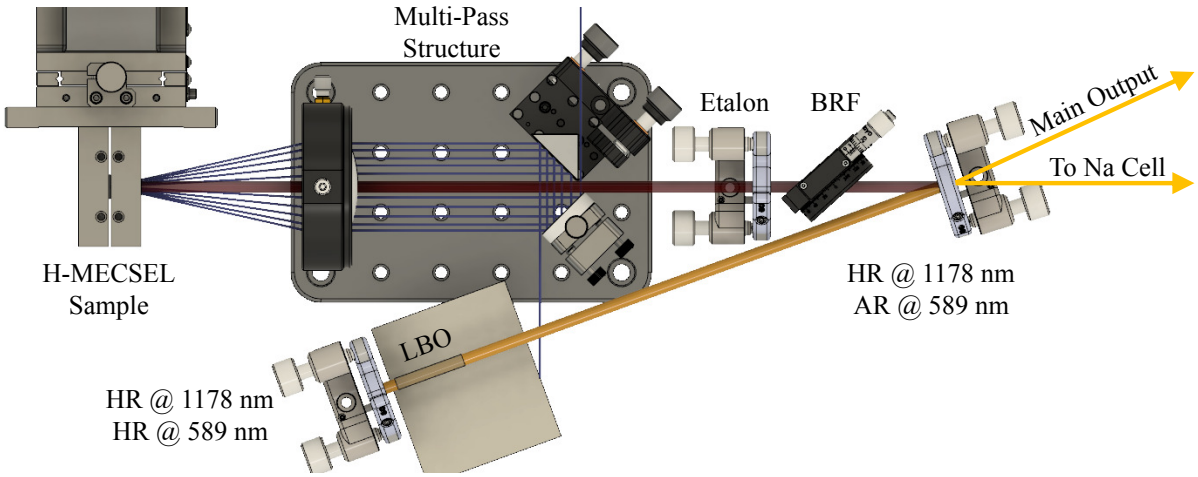

Fig. 9.8 H-MECSEL setup was used for laser frequency stabilization experiment.

and 589 nm on both facets is 20 mm in length and was positioned near the plane cavity end mirror inside a homemade cell, which was omitted in the schematic for clarity. The cavity end mirror was specially coated for high reflectance at both 1178 nm and 589 nm, while the 500 mm radius of curvature folding mirror was HR coated at 1178 nm and AR coated at 589 nm.

Most of the yellow light was directed out of the cavity via this 589 nm AR coated folding mirror, although some remained within the cavity. This remnant yellow light was redirected toward the sodium cell after a second reflection by the H-MECSEL sample and transmitted through the folding mirror. The leakage light was still too intense for direct application in the SAS setup and required attenuation before use for measuring frequency-related transmission signals. Additionally, a PZT was affixed to the back of the cavity end mirror for fine-tuning the laser wavelength, complemented by a 3-axis PZT system on the folding mirror mount that provided a broader wavelength tuning range due to its positioning behind a curved mirror. The entire system underwent a rebuild due to a catastrophic failure of the pump laser, which was then replaced with another pump laser of the same model. This updated setup was capable of producing up to 6.6 W of yellow light at 589 nm with 5 MHz linewidth (FWHM), which is still adequate for demonstrating frequency stabilization capabilities for watt-level LGS.

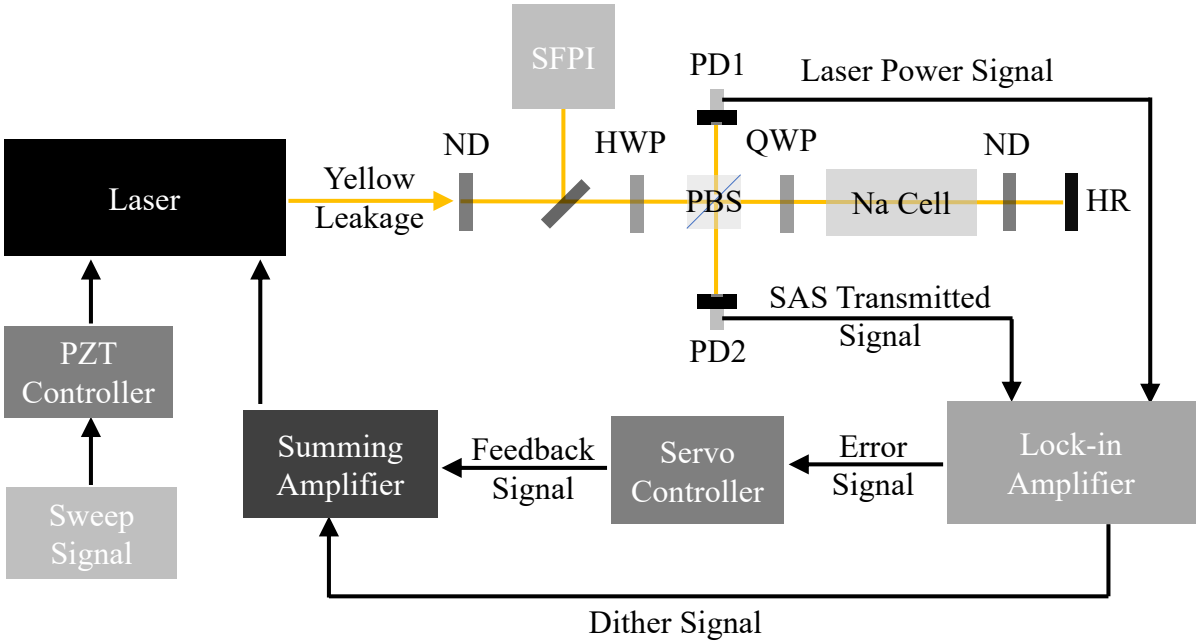

Fig. 9.9 Schematic diagram of laser frequency stabilization system for the H-MECSEL developed in the course of this dissertation research.

The schematic diagram of the laser frequency stabilization system is illustrated in Fig. 9.9. This diagram outlines the optical and electrical signal paths used in the experiment. Optical signals are represented by yellow lines and arrows, while electrical signals are denoted by black lines and arrows. Initially, the yellow leakage from the laser is attenuated by a ND filter, and a portion of this attenuated beam is directed into a scanning Fabry-Perot interferometer (SFPI) for measuring the laser linewidth. The remainder of the beam first passes through a HWP, after which a fraction of it is reflected towards PD1 to monitor laser power fluctuations. As mentioned in the previous section, the signal that passes through the HWP is then sent through a SAS setup before detected by PD2. The difference in signals from PD1 and PD2 is used to create a laser power fluctuation-free input for the lock-in amplifier. The generated error signal is then routed to a servo controller. The controller functions effectively as a PI controller, omitting

the differential component, which is deemed unnecessary for correcting low frequency noise in this specific experiment.

The feedback signal produced by the servo controller is combined with a dither signal from the reference channel of the lock-in amplifier using a summing amplifier. This combined signal is subsequently fed into a PZT attached to the back of the cavity end mirror for both dither and feedback control of the laser frequency. Additionally, an external PZT controller connected to the mount of the folding mirror allows for 3-axis control, enabling fine tuning of the laser wavelength to optimally align with the absorption peak of the sodium D_{2a} transition. A function generator connected to this PZT system facilitates frequency sweeping, enabling precise identification of the transmitted signal patterns necessary for locating the exact laser wavelength.

Before configuring the parameters for the frequency stabilization system, it was imperative to identify the sources of noise present in this complex optomechanical system. The optical table was floated to minimize vibrations, and potential external noise sources, such as vacuum pumps in the lab, were isolated from the system to prevent interference. For precise noise analysis, the signal input for the lock-in amplifier was monitored by an oscilloscope, and a fast Fourier transform (FFT) function was employed to conduct a frequency domain analysis. A typical result of this analysis is shown in Fig. 9.10, which highlights pronounced noise occurring from 200 Hz to 400 Hz, accompanied by low-frequency noise. The peak at 1026 Hz is the applied dither frequency utilized in this noise identification experiment. The low-frequency noise (<1 Hz) was suspected to be linked variations over hours due to slower temperature changes in the environment or long-term heating effects within the laser system. However, the measurement system's sensitivity does not extend to such low frequencies.

The noise occurring at a few hundred Hertz could originate from multiple sources. One potential source is the mechanical vibrations within the system; however, finding better vibration-

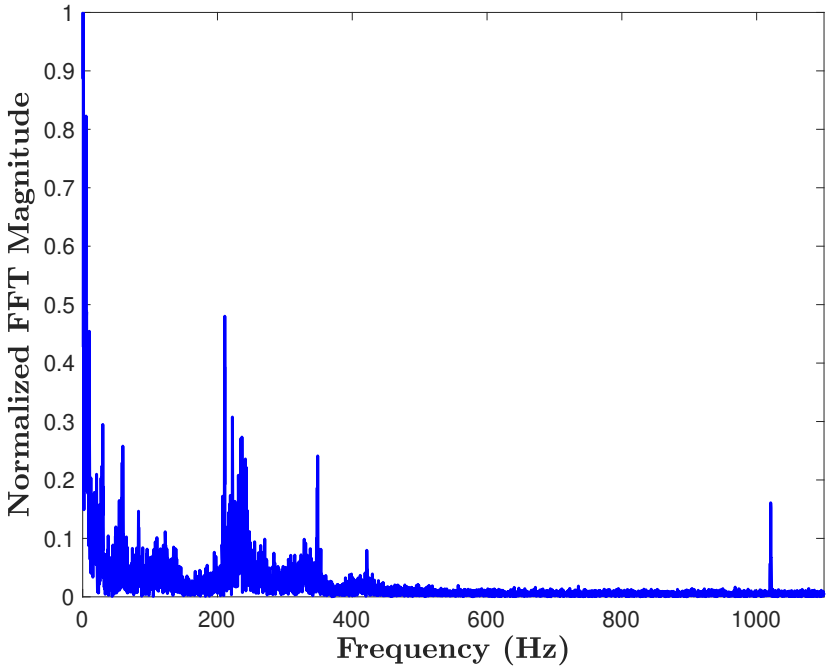

Fig. 9.10 FFT result for precise noise source identification, 1026 Hz was used as dither frequency for this measurement.

resistant alternatives based on the parts currently stored in the lab proved challenging. Noise could also emanate from the power supply, with limited options available to effectively filter them out within the lab setting. Additionally, the HVAC system in the lab, despite efforts to mitigate its impact by constructing a protective box around the laser, might still contribute to the noise. The most suspected source of noise, however, was the water flow from the chiller, which routes cooling water to the copper cooling mount of the H-MECSEL sample. This component is slated for future upgrades to reduce noise. Given the equipment available, both the low-frequency noise and the noise at several hundred Hertz need to be suppressed by the frequency stabilization system to ensure its effective operation.

The performance of the ring piezoelectric transducer located near the end mirror, as well as the PZT mirror mount, was evaluated to determine their respective frequency sweeping

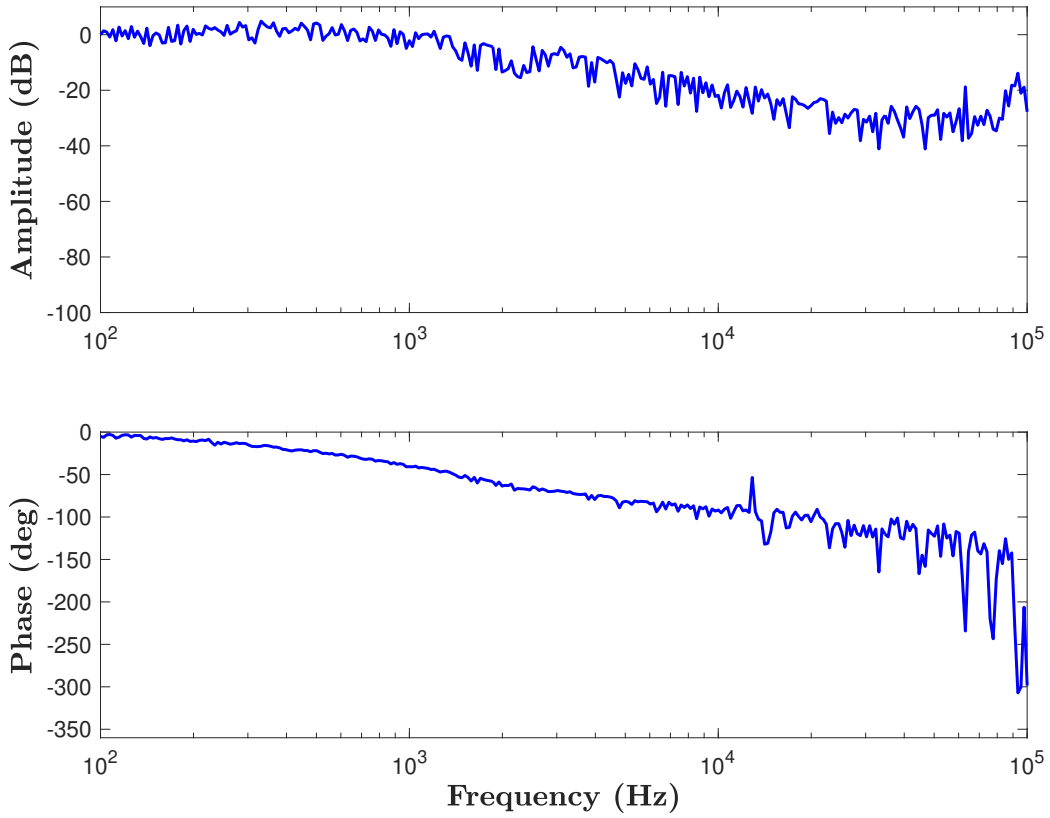

Fig. 9.11 Amplitude and phase change for the ring PZT with increase of dither frequency.

capabilities. To facilitate a comprehensive evaluation for the PZTs for their frequency related performance, a LabVIEW script was developed by the author to automate the experimental procedures through control of the lock-in amplifier. This script was designed to adjust the dither frequency applied to the PZT and to capture corresponding amplitude and phase information across a frequency range extending from 100 Hz to 100 kHz.

The experimental results for the ring PZT positioned on the back of the cavity mirror are presented in Fig. 9.11, which captures both the amplitude and phase responses of the system across a range of frequency inputs. The figure is divided into two subfigures that have the same frequency range from 100 Hz to 100 kHz, displayed on a logarithmic scale. The amplitude

changes are denoted in decibels (dB), while the phase changes are measured in degrees. Analysis of the data reveals a continuous and gradual decrease in the response amplitude as the dither frequency increases. Additionally, the results show a slow but steady phase shift with increasing dither frequency. Within the 200 Hz to 400 Hz range—where noise correction is most urgently needed for achieving reasonably fast stabilization—the phase shift remains modest, with only a 10-degree difference observed. This relatively stable phase response within the targeted frequency range indicates that this PZT is well-suited for noise correction tasks.

A similar experiment was conducted using the PZT mirror mount, with the results presented in Fig. 9.12. In contrast to the smoother amplitude response observed with the ring PZT, the amplitude changes for the PZT mirror mount exhibited some fluctuations, characterized by increases and decreases as the dither frequency increased. However, these variations were generally moderate and deemed acceptable. Regarding the phase response, the mirror mount showed significant limitations. Beyond 1 kHz, the device exhibited numerous abrupt phase changes, indicating phase wrapping around 0 and 360 degrees. Even after unwrapping these changes, the rapid phase transitions rendered the device unsuitable for high-frequency applications. Most critically, within the frequency range of 200 Hz to 400 Hz—where noise correction is crucial—the phase shift reached a maximum of 114 degrees. This phase lag limits the bandwidth of the servo loop and prevents effective noise correction in the most critical frequency range.

Based on the performance tests of the PZTs, it was concluded that both the dither signal and the feedback signal should be directed to the ring PZT located near the cavity end mirror. And since the maximum scanning range of the PZT mount is larger than the ring PZT, the PZT mirror mount will be designated for frequency sweeping at frequencies below 100 Hz. This decision leverages the large frequency tuning range, making it particularly suited for fine-tuning the laser frequency before start the laser frequency stabilization. The objective is to center the

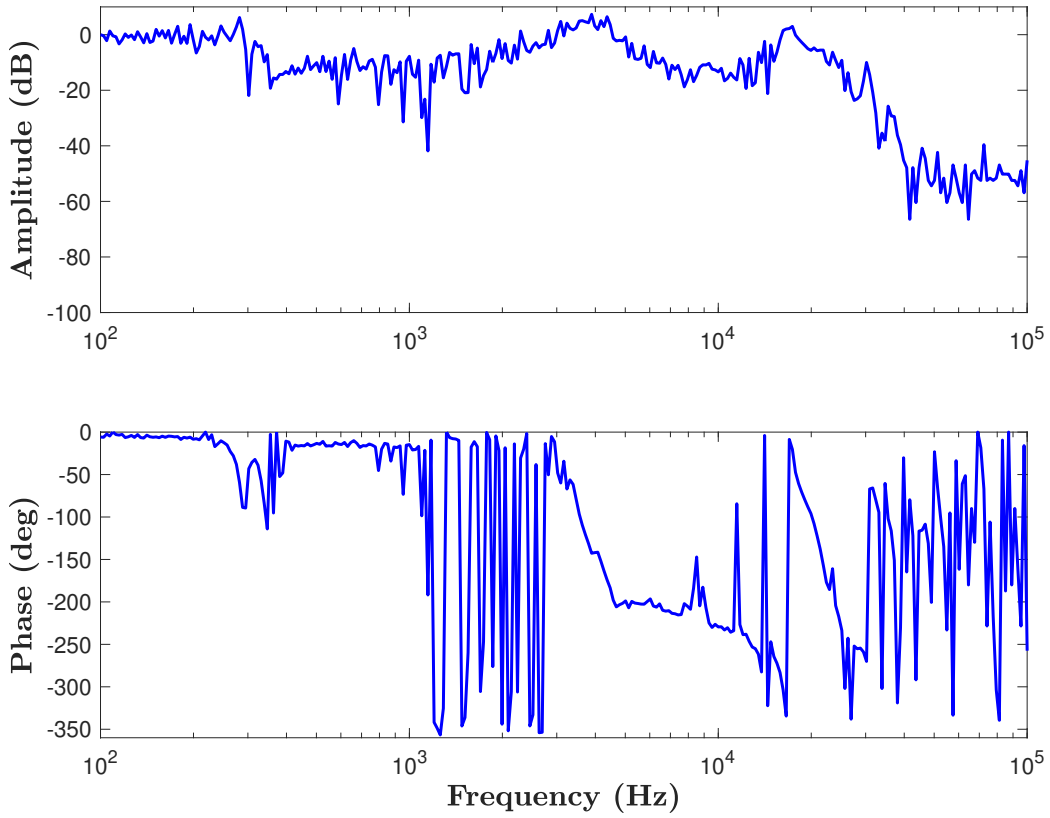

Fig. 9.12 Amplitude and phase change for the PZT mirror mount with increase of dither frequency.

laser frequency at the sodium D_{2a} transition absorption peak, which is near the Doppler-free Lamb dips. Once the frequency stabilization process begins, the mirror mount PZT will not be adjusted or involved further. This ensures that the initial tuning provided by the mirror mount PZT remains stable and undisturbed.

The normalized transmission (blue curve) and the generated error signal (red curve) for scanning through the sodium D_2 line are displayed in Fig. 9.13. The black dash line indicates the scanning sinusoidal signal applied to the PZT. Throughout the entire scan cycle, the figure displays the Doppler-free transitions in sodium D_{2a}, D_{2b}, and the crossover resonance. The x-

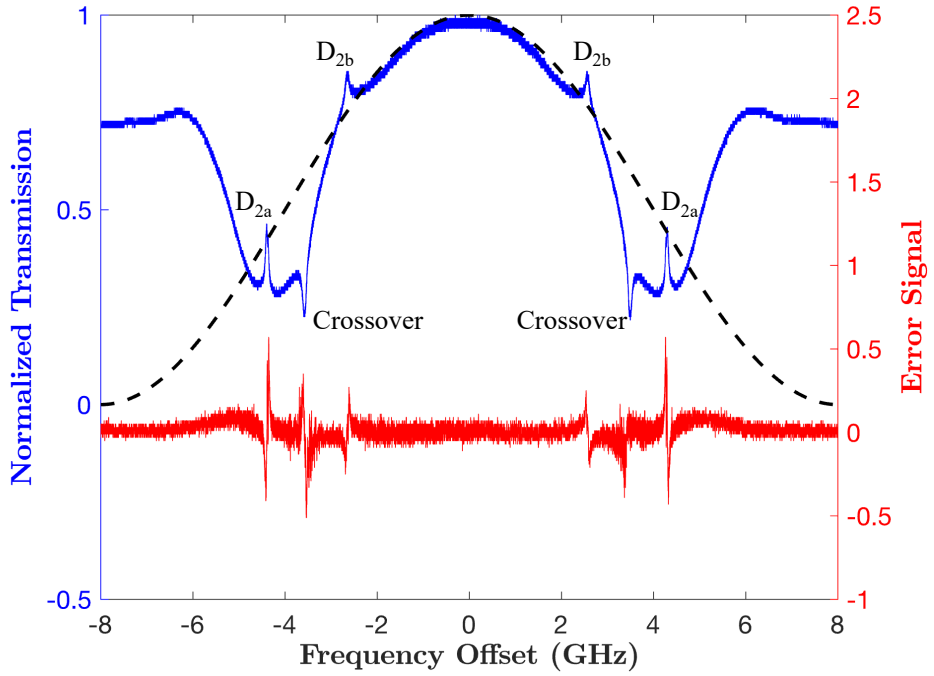

Fig. 9.13 The normalized transmission (blue), the generated error signal (red) for scanning through Doppler-free peaks within the sodium D_2 line, and the scanning signal applied to the PZT (black).

axis of this figure represents frequency offset, calibrated by the frequency difference 1.772 GHz between D_{2a} and D_{2b} [154]. For this calibration, a linear relationship was assumed. However, because the PZT does not respond well to triangle signal, a sinusoidal signal was used in the experiment. This resulted in inaccuracies in the calibrated x-axis near the peaks and troughs of the scan signal.

The y-axes are designated for different purposes: the left y-axis measures the normalized transmitted signal, while the right y-axis corresponds to the error signal. This figure demonstrates that the error signal performs as expected; it mirrors the derivative of the transmitted signal. At the peak of the transmitted signal, the error signal crosses zero and exhibits opposite signs on either side, indicating the direction for necessary corrections. The error signal's nearly linear slope from the peak to the valley delineates the range within which the laser frequency

should ideally be locked. This range is around the linewidth (FWHM) of the Doppler-free peak targeted within the sodium D_{2a} transition. Given the additional data from Fig. 9.7, where three hyperfine transition peaks are identifiable, the dither range during the experiment should be confined to less than 5 MHz considering the linewidth of the laser itself. From the experimental results, it has been determined that for the planned implementation of a 10 kHz dither frequency, the dither range, denoted as $\Delta\nu_{\text{dither}}$, can be approximately related to the input voltage amplitude of the dither signal, V_{dither}, through the relationship $\Delta\nu_{\text{dither}} \approx a_{\text{dither}} V_{\text{dither}}$. Here, a_{dither} is the proportionality constant derived from experimental fitting, calculated to be $10.38\,\text{MHz}/\text{V}$.

To optimize the dithering process while ensuring effective error signal generation, a dither signal amplitude of 100 mV was selected. This amplitude is sufficiently robust to produce a discernible error signal for frequency stabilization. In pursuit of refining the dither locking outcomes, several key parameters were systematically evaluated and adjusted to enhance system performance. One parameter adjusted was the lowpass filter time constant that filters out the second harmonic and higher harmonics, which was set to 100 µs with an 18 dB/octave roll-off on the Stanford Research Systems SR830 DSP lock-in amplifier. Additionally, the sensitivity was configured to 100 mV, and high reserve mode was enabled to optimize the amplifier's response to signal variations. Furthermore, on the New Focus LB1005 servo controller, the PI corner frequency was set at 1 kHz. This setting is for balancing long-term error correction with immediate error response capabilities. The PI corner frequency serves to delineate the crossover point in the control system where the proportional component is dominant at higher frequencies, while the integral component becomes more significant at lower frequencies. Additionally, the low-frequency gain limit on the servo controller was set to 50 dB, representing the gain limit for low frequencies as measured from the proportional gain value. The integrator is turned off for frequencies lower than the corresponding 3-dB corner frequency, making this mode useful for acquiring lock and situations where limiting the DC gain is necessary. This gain limit is

disabled when switching to "Lock On." In the experiment, the gain limit was used to search for the best parameters for the locking system, but the data were collected with the "Lock On" setting, where no low-frequency gain limit is applied. The gain was adjusted to -25 dB (2.5 on the dial).

9.4 System Stabilization Results

Using the setup and parameters outlined in the previous section, the laser stabilization process was conducted with the main laser output set at 1.3 W to demonstrate watt-level stabilization. For this demonstration, a Thorlabs OSA 203B OSA was employed to measure the 1178 nm fundamental wavelength. This measurement involved capturing some of the light leakage after it passed through the laser cavity end mirror, facilitated by a long-pass filter. The wavelength data was recorded by the OSA at a rate of one data point per second. Such a slow measurement rate can degrade the resolution of the wavelength measurement if there are any power fluctuations within this one-second period. Simultaneously, both the transmitted signal from the SAS setup and the error signal output from the lock-in amplifier were monitored using an oscilloscope.

The error signal before and after activating the locking mechanism on the servo controller is detailed in Fig. 9.14, where a red dashed line marks the moment the switch is engaged, initiating the laser wavelength stabilization. Prior to activation, the error signal exhibits large fluctuations characteristic of the laser operating in free-running mode. This instability results in significant deviations from the desired frequency, as the system lacks any corrective feedback to maintain the laser at a steady state. Upon engaging the locking switch, there is a noticeable and immediate reduction in the magnitude of the error signal, which stabilizes to a value close to zero. This dramatic improvement signifies that the servo controller's locking mechanism stabilizes the laser frequency to a Doppler-free peak within the sodium D_{2a} transition.

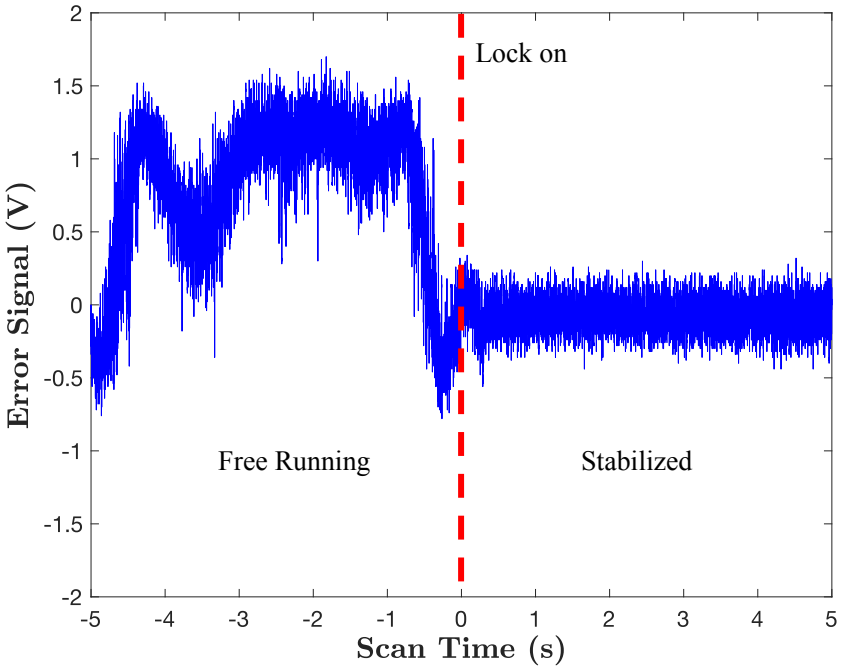

Fig. 9.14 The error signal behavior before and after activating the locking mechanism, where a red dashed line marks the moment the switch is engaged to initiate the lock.

The FFT analysis was employed to delve deeper into the noise cancellation capabilities of the system. Figure 9.15 offers a comparison to earlier noise profile visualizations like those shown in Fig. 9.10, with both axes displayed on a logarithmic scale. On this graph, the x-axis delineates frequency, while the y-axis indicates the normalized amplitude, using the DC noise level from the laser's free-running operation as the reference point. In this analysis, the red trace represents the laser in free-running mode, and the blue trace shows the laser's behavior when the stabilization system is engaged. The analysis clearly demonstrates that low-frequency noise is drastically reduced, diminishing by more than three orders of magnitude. Also the noise around 200 Hz—a primary target for mitigation—shows a significant reduction.

The system's ability to maintain laser frequency stabilization using a sodium reference over an hour was demonstrated, as shown in Fig. 9.16. In this figure, the free-running operation of

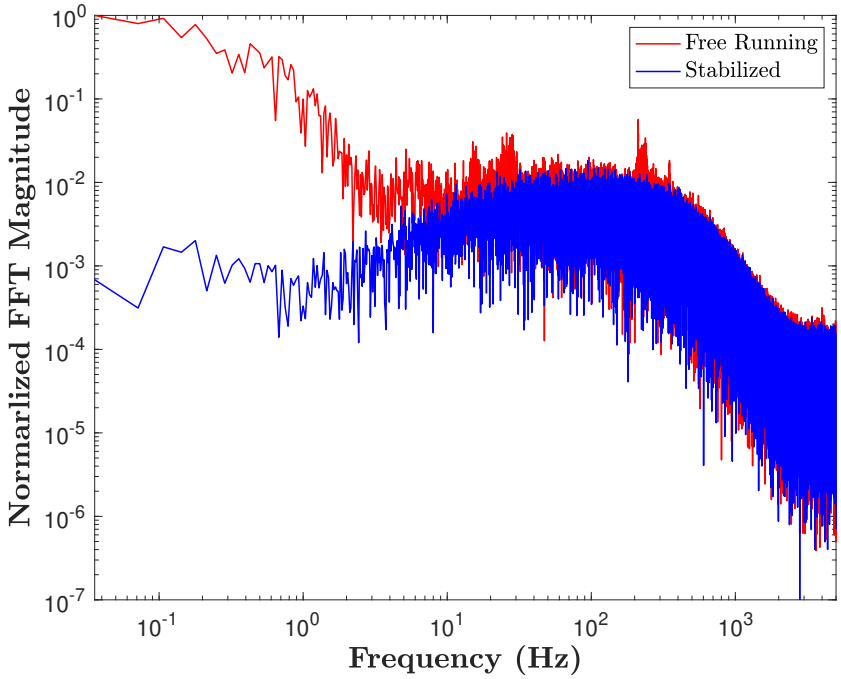

Fig. 9.15 Noise cancellation analysis of the system between free running (red) and stabilized operation (blue).

the laser is represented by a red trace, while the stabilized operation is depicted in blue. The x-axis of the graph measures time in minutes, and the y-axis indicates the frequency offset from the sodium reference in MHz. To generate this plot, the value of the fundamental wavelength was first converted to optical frequency. The frequency offset was then calculated by subtracting this optical frequency from half of the optical reference frequency. The observed behavior of the free-running laser operation, as depicted in Fig. 9.16, reveals a slow drift with occasional mode hops, which is suspected to be caused by a slow thermal drift within the system. This drift leads to frequency variations that cause the laser to hop after reaching the maximum allowable optical frequency shifts. From the graph, it is evident that the hopping-free range spans approximately 800 MHz. This range exceeds the laser's longitudinal mode spacing of 170 MHz, which was calculated based on a cavity length of 0.88 m. The inset within the figure provides a detailed

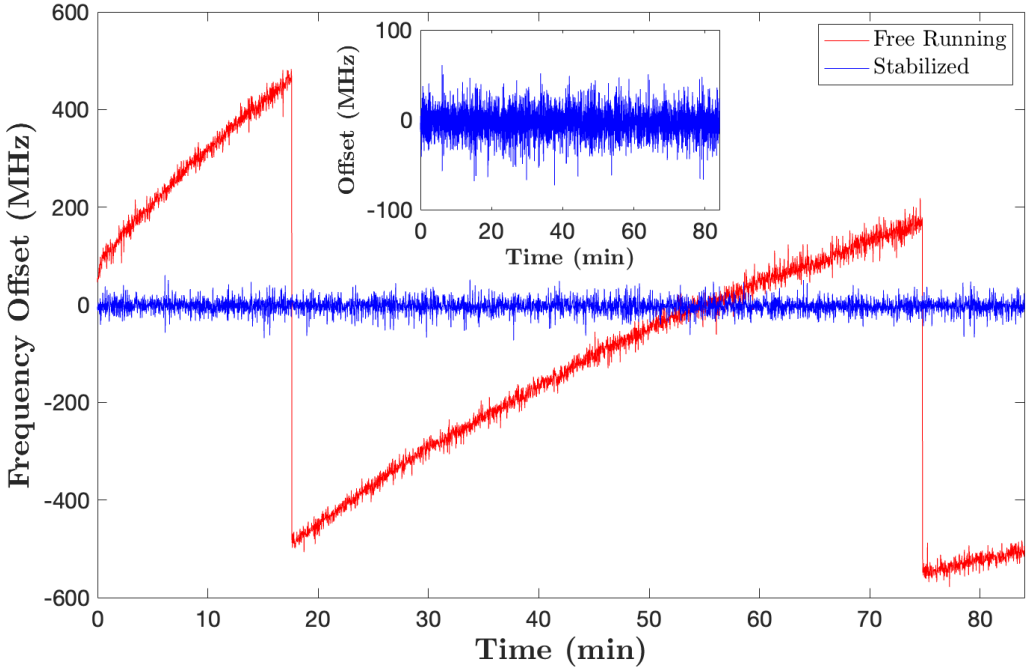

Fig. 9.16 Long term frequency offset from 254.4237 THz (1178.3197 nm) measurement for free running (red) and stabilized (blue) conditions.

view of the y-axis, ranging from -100 MHz to 100 MHz. This closer look demonstrates that once the stabilization system is engaged, the laser frequency is tightly maintained within this much narrower range. However, the precision of the measurement is constrained by the resolution of the measuring device, which has a resolution of 0.1 parts per million (ppm). This level of resolution translates to approximately 25.5 MHz at a wavelength of 1178 nm. Additionally, the absence of power stabilization equipment, such as a noise eater, before the input of the OSA further complicates the measurement. Power fluctuations in the timescale within a single sweep of the Fourier transform infrared spectroscopy-based OSA can introduce excess noise to the short timescale wavelength measurement, and degrade the effective resolution.

The square root of Allan variance, or Allan deviation, is a statistical measure commonly used to analyze the stability of frequencies over time [158]. Initially developed to quantify

the frequency stability of precision oscillators, including atomic clocks, quartz oscillators, and other high-stability frequency sources, it has also become a powerful tool in laser physics for evaluating the temporal stability of a laser's frequency [159]. For the calculation of Allan deviation, the sampling interval τ starts with the sampling period of 1.04 s used in the experiment as the minimum sampling interval. The interval τ is then increased gradually to the maximum duration for which sufficient experimental data are available for reliable calculation. For the stabilized laser operation, the maximum τ_{max} was set to 533 s, while for the free-running case, τ_{max} was limited to 266 s. This limitation for the free-running case arises because only the data from periods without mode hopping are considered reliable for stability analysis. The calculation process involves averaging the data over each interval τ as follows:

$$\bar{y}_{\mathrm{k}}(\tau) = \frac{1}{\tau} \sum_{i=(k-1)\tau+1}^{k\tau} y_{\mathrm{i}}, \tag{9.12}$$

where $\bar{y}_{\mathrm{k}}(\tau)$ represents the average of the k-th interval of length τ. The Allan deviation is then computed using the averaged values [159]:

$$\sigma(\tau) = \sqrt{\frac{1}{2(N-1)} \sum_{k=1}^{N-1} (\bar{y}_{\mathrm{k}+1}(\tau) - \bar{y}_{\mathrm{k}}(\tau))^2}, \tag{9.13}$$

where N is the total number of intervals that can be accommodated within the total duration of the measured data. The error bar of the calculated Allan deviation can be derived from the degrees of freedom (ν_{Allan}). For a 68.3% confidence interval (one standard deviation), the error bars can be approximated as:

$$\mathrm{Error}_{\mathrm{Allan}} = \sigma(\tau) \sqrt{\frac{2}{\nu_{\mathrm{Allan}}}}, \tag{9.14}$$

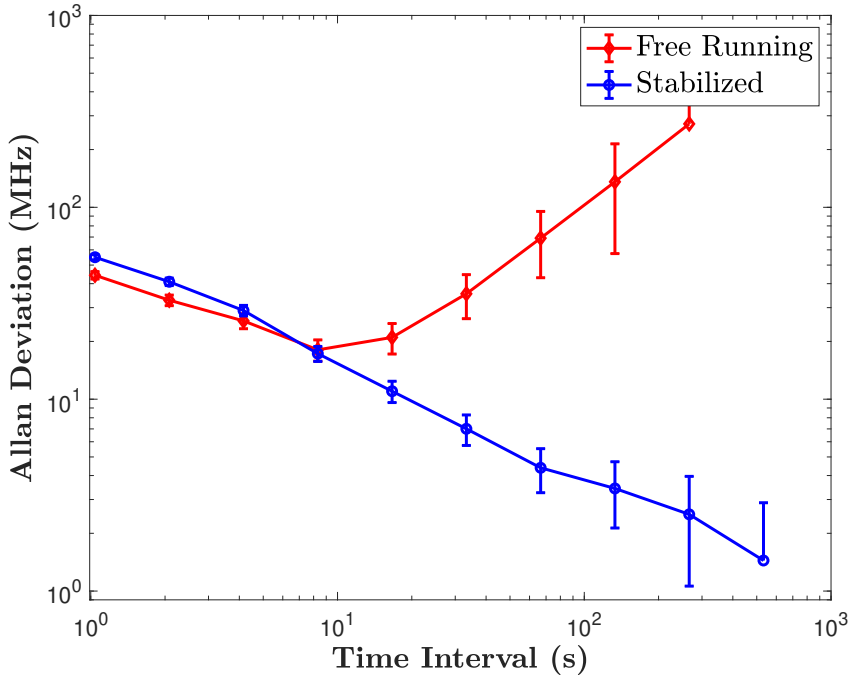

Fig. 9.17 Noise cancellation behavior of the system comparing free running (red) and stabilized operation (blue).

where an approximation of $\nu_{\text{Allan}} \approx N - 1$ can be applied [160].

The results of the Allan deviation calculation, utilizing the data from Fig. 9.16, are illustrated in Fig. 9.17. The x-axis represents the time interval τ, and the y-axis shows the frequency offset from the frequency reference. In this graph, the red curve represents the free-running operation, while the blue curve indicates the frequency-stabilized operation. An error bar calculated from Eq. 9.14 was utilized. The graph illustrates a significant improvement in frequency stability as the time interval increases. At higher frequencies with shorter integration times, the performance of the free-running operation appears slightly better than that of the frequency-stabilized operation, though the difference is not substantial. This discrepancy could be due to measurement errors, particularly since the OSA has a spectral resolution of 7.5 GHz. In wavelength meter mode, the resolution can be improved to a theoretical limit of 25.5 MHz,

but it is constrained by detector noise, reference laser drift, interferometer alignment, and other systematic errors. For wavelength meter mode with a slow scanning rates below 1 Hz, fluctuations in laser output power increase the actual resolution beyond this theoretical limit. And even the instrument resolution in ideal case exceeds the 10.5 MHz difference at the shortest time interval in Allan deviation calculation. Additionally, when measuring the wavelength in free-running operation, the dither signal was turned off. However, a high-frequency dither is necessary for laser frequency stabilization. While low-frequency noise is suppressed, the introduction of high-frequency dither could worsen stabilization at higher frequencies.

9.5 Conclusion

In this chapter, the dither locking method was introduced as an active approach to stabilize laser frequency. The SAS technique, recognized for its Doppler-free spectroscopic capabilities, was employed in conjunction with a sodium cell. This setup provided sub-Doppler hyperfine transition lines as a frequency reference for the stabilization system. The construction and functionality of the feedback loop were then explored, covering aspects such as noise source identification, implementation of feedback mechanisms using piezoelectric transducers, generation of error signals, and the optimization of settings on both the lock-in amplifier and the servo controller.

Subsequently, a demonstration of laser frequency stabilization was conducted, showcasing watt-level output power at 589 nm. The comparative analysis between free-running and frequency-controlled operations was detailed, highlighting distinctions in error signal patterns, noise patterns using Fast Fourier Transform, and wavelength measurements. While the short-term stability at the 1-second level was limited by the resolution of the OSA, the long-term stability of the system was markedly improved with the active feedback loop. The experiment

successfully maintained the laser frequency within a 100 MHz bandwidth for over an hour. Additionally, Allan deviation calculations were performed using data from long-term stabilization tests, validating the system's successful locking behavior. The successful demonstration of long-term frequency stabilization to the sodium D_{2a} transition, coupled with watt-level output power, has effectively proven the feasibility of deploying semiconductor-based laser guide star systems in astronomical observatories.

Chapter 10

Conclusion and Future Work

10.1 Conclusion

This dissertation was centered around the development of a semiconductor-based LGS system. The H-MECSEL was designed to achieve this goal, it leverages superior heat dissipation capabilities [114], simplified multi-pass pumping construction [127], and the potential for wafer-scale manufacturing [105]. This structure has achieved several performance milestones, including approximately 30 W of output at 1178 nm [114], over 10 W at 589 nm [75], and watt-level output at 589 nm with frequency stabilization to the sodium D_{2a} transition [76].

Chapter 1 extensively reviewed LGS technology and semiconductor lasers, focusing on the design of a CW LGS system. It detailed calculations for the minimum power, linewidth, and wavelength necessary for effective LGS operation, and highlighted saturation power that potentially requires chirping of the laser wavelength in the future update. To the author's knowledge, this represents the first instance where all these criteria have been integrated into a single framework for designing a CW LGS system. These parameters were subsequently

used as foundational requirements in the development of a semiconductor-based LGS, setting a benchmark for future implementations.

Chapter 2 explored the design and characterization of the MECSEL gain structure. This included a thorough analysis of the epi structure, temperature-dependent energy levels of quantum wells, and the optimal number of quantum wells for achieving high performance in a single MECSEL gain chip. Experimental measurements of foundry-supplied epitaxial material validated these theoretical calculations. Additionally, the chapter delved into laser resonator design, introducing a custom MATLAB script. This script, which utilizes paraxial Gaussian solutions and the matrix transfer method, not only corroborated the results from commercially available software but also introduced a parameter sweeping function for complex cavity calculations involving multiple beam size requirements. Furthermore, techniques for linewidth narrowing using BRF and FP etalon were reviewed, alongside discussions on intracavity frequency doubling using NCPM with an LBO crystal.

Chapter 3 focused on the experimental investigations the performance of an eleven quantum well MECSEL gain chip, which achieved a record output of 20.2 W not only at 1178 nm but across all MECSEL implementations up to that point [113]. This was accomplished using a 808 nm barrier pumping strategy. To explore the capabilities of wavelength tuning, a 2 mm thick quartz BRF was utilized, demonstrating a tuning range of 75 nm. The peak performance of this setup yielded 12.8 W at 1178 nm with a linewidth of 0.3 nm, setting a benchmark for MECSELs in high-power applications. However, thermal limitations observed with this MECSEL led to further study on thermal behavior of MECSELs.

Chapter 4 introduced the in-well pumping method, a strategy devised to mitigate thermal restrictions on high-power laser output, notably advantageous due to its lower quantum defect compared to more conventional barrier pumping. To address the challenges of low absorption inherent in in-well pumping, due to the reduced thickness of the quantum well layers, a

detailed examination and development of a multi-pass pumping strategy were undertaken. This strategy focused on recycling unabsorbed pump power to enhance overall absorption efficiency. In this chapter the author discussed and evaluated three distinct types of multi-pass pumping structures [127] aimed at enhancing the robustness and compactness required for LGS applications. These include parabolic mirror-based configurations, OAP mirror-based configurations, and aspheric lens-based configurations. Each configuration was verified using Zemax ray tracing software. The OAP mirror-based design was experimentally validated using a He-Ne laser and a silver mirror instead of real gain chip in the laboratory setting. Additionally, aspheric lens-based multi-pass pumping designs were implemented for the practical construction of a semiconductor-based LGS. This chapter contributes to the field by detailing the design, verification, and application of multi-pass pumping structures in semiconductor-based laser systems.

Chapter 5 detailed experiments with a twenty quantum well MECSEL gain chip using a 1070 nm in-well pumping strategy. Direct comparisons were made between 808 nm barrier pumping and 1070 nm in-well pumping on the same gain chip. Single-pass in-well pumping showed a slope efficiency of 39.5%, nearly doubling the 21.6% efficiency achieved with single-side barrier pumping. By integrating a ten-pass in-well pumping structure, a new output record of 28.5 W was established without any indication of thermal rollover [112]. Additionally, wavelength tuning facilitated by a 2 mm thick quartz BRF exhibited a range of 71 nm, and a 1178 nm output of 17.9 W with a linewidth of 0.4 nm was successfully demonstrated. This direct experimental comparison between barrier and in-well pumping provided clear evidence of the superior performance of in-well pumping. Despite these achievements, challenges such as alignment difficulties in the multi-pass pumping configuration that distorted the output beam profile due to imperfect mode matching between the cavity mode and pump mode persisted.

Chapter 6 introduced the H-MECSEL, a configuration that synthesizes the advantages of VECSELs and MECSELs. This hybrid structure not only retains the superior thermal management capabilities characteristic of MECSELs but also the simpler multi-pass pumping configuration associated with VECSELs. The chapter begins with a detailed review of the H-MECSEL structure, including the dual-band DBR designed for the experiment. Following this, the chapter employs COMSOL FEM simulations to conduct a comprehensive comparison of thermal management capabilities across eight different semiconductor disk laser structures, demonstrating that the H-MECSEL provides superior heat dissipation [114]. From these FEM simulations, a general equation for calculating thermal lens effects in H-MECSELs was derived, enhancing the precision of laser cavity designs. The chapter concludes with an experimental demonstration that highlights the ease of constructing multi-pass pumping structures using a specially machined mirror alongside a MECSEL gain chip.

Chapter 7 presented the experimental results associated with the twenty quantum well H-MECSEL gain chip. This chapter details the initial demonstration of the H-MECSEL platform, showcasing its capability to achieve high output power with good beam quality and without thermal limitations. Utilizing a V-cavity configuration, a simplified multi-pass in-well pumping structure was implemented, successfully yielding a similar 28 W output at 1178 nm with a 1070 nm pump laser [114]. This output demonstrated the effectiveness of the H-MECSEL design as no thermal rollover was observed even at high pumping levels.

Chapter 8 dived further into the H-MECSEL design, covering wavelength tuning and linewidth narrowing. Using a 2 mm BRF, a wavelength tuning range of 61 nm was achieved, with the slight reduction in range arising from the narrower reflectance spectrum of the semiconductor-based dual-band DBR. To achieve single longitudinal mode operation, a 100 µm thick YAG etalon was incorporated into the laser cavity, enabling further refinement of the laser linewidth. A comparison was conducted between 1070 nm in-well pumping and 808 nm

barrier pumping on the same sample. Results demonstrated that while barrier pumping could only yield outputs of 5.8 W, 4.3 W, and 1.9 W for free-running, with BRF, and with BRF and FP etalon scenarios before encountering thermal rollover, in-well pumping exhibited no such thermal limitations. Although most of the pump power is absorbed within the active region, the absorption within the dual-band DBR for 808 nm pump light still contributes to this low output power. In-well pumping delivered substantially higher outputs of 24.1 W, 16.4 W, and 11.8 W respectively, under similar conditions. It showcased the first successful demonstration of linewidth narrowing to a single longitudinal mode at 1178 nm with a MECSEL for LGS applications. The entire experimental setup was mounted on a dedicated breadboard as shown in Fig. 10.1, preparing it for transportation to an observatory for future on-sky testing. In reverting to a V-cavity configuration, experimental efforts yielded a free-running output power of 28.9 W. This setup was modified by incorporating a 4 mm thick quartz BRF, achieving an output of 21.4 W at 1178 nm. With the addition of a 100 µm thick YAG etalon, thermally stabilized at 40 °C, the output power reached 17.2 W, with a linewidth narrowed to less than 0.06 nm. This achievement set a new record for output power from a MECSEL and successfully met the single-longitudinal-mode output power requirements for LGS applications. Subsequently, an intracavity frequency doubling experiment was conducted using non-critical phase matching of a LBO crystal, temperature-stabilized at 41.77 °C. This setup yielded 10.3 W output at 589.2 nm, exhibited in a TEM_{00} transverse mode. The linewidth of this output was measured to be 7 MHz using a scanning Fabry-Pérot interferometer. This series of experiments marked the first instance of a MECSEL-based LGS achieving a 589.2 nm output.

Chapter 9 delved into the laser frequency stabilization, focusing on dither locking. The chapter commenced by outlining the preparation of a frequency reference using a sodium gas cell, employing the SAS method. This setup allowed for the resolution of three hyperfine lines within the sodium D_{2a} transition, marking the first instance of achieving Doppler-free

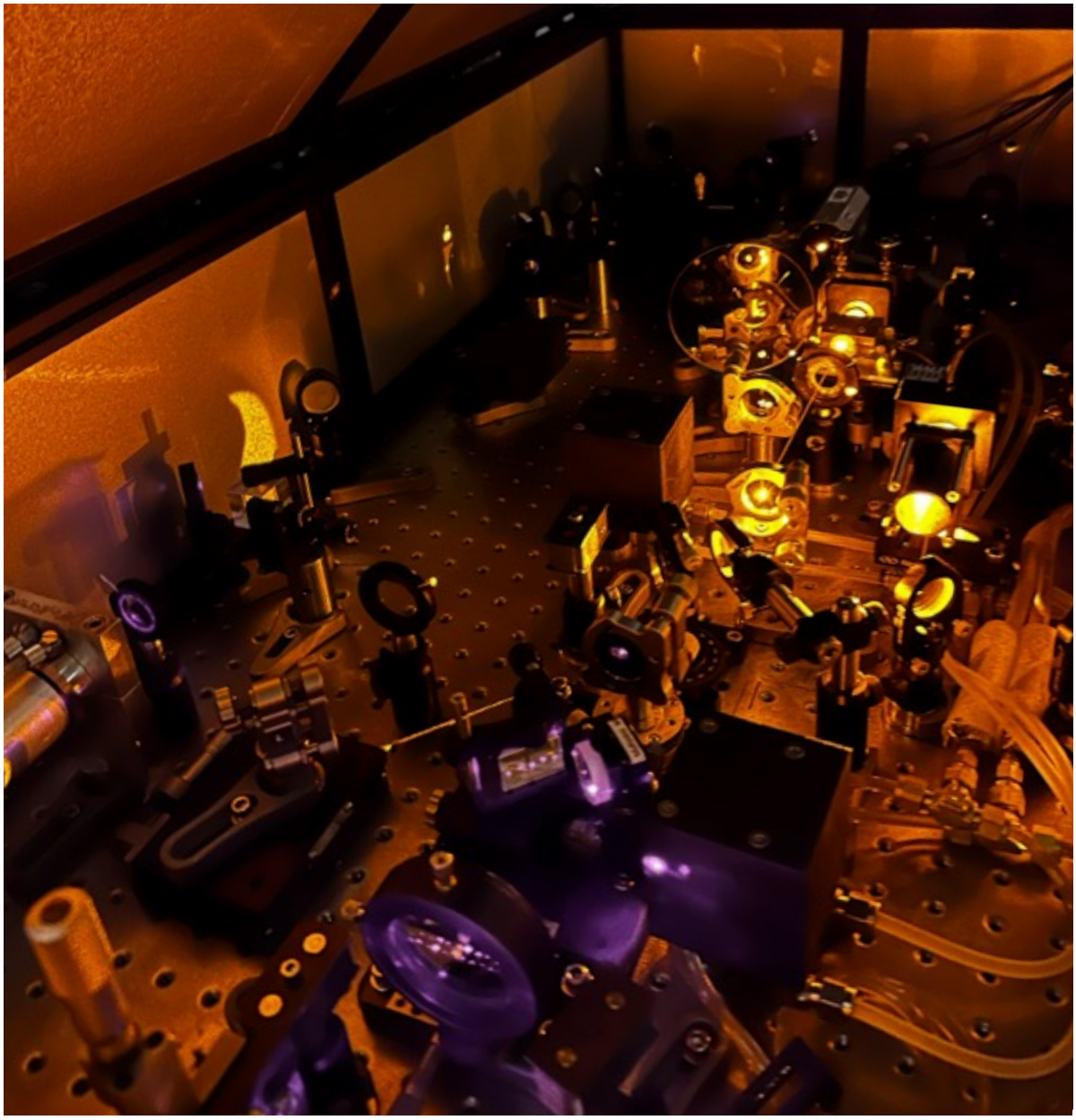

Fig. 10.1 A photography of the experimental setup for the H-MECSEL-based LGS. The setup's illumination by the 1070 nm pump laser appears as a purple hue, while the 589 nm output generates a yellow color, demonstrating the operation of the system.

spectroscopy resolution with a MECSEL. The core of the chapter detailed a demonstration of frequency stabilization of the MECSEL, maintaining stability over an hour at Watt-level output. This involved wavemeter measurements and Allan deviation analysis, both of which confirmed the efficacy of the laser stabilization approach. This demonstration represented the first long-duration, high-power semiconductor based system stabilized using a sodium reference cell targeting LGS applications.

10.2 Future Work

With the preliminary results achieved in laser frequency stabilization, further experiments are essential to demonstrate long-term locking at a 10 W output power at 589 nm, which is anticipated to be accomplished shortly using the current experimental setup. There are several potential future upgrades for the MECSEL LGS system that are either currently under construction or under consideration.

10.2.1 Repumping and Frequency Chirping

Using power scaling method by increasing the cavity mode size on the H-MECSEL gain chip, over 20 W output power potentially could be achieved at 589 nm. As this approaches the saturation intensity of sodium atoms, it is essential to consider factors that reduce the return signal from an LGS. The three major factors, in order of decreasing importance, are Larmor precession, recoil, and transition saturation [39]. The likelihood of stimulated emission increases with higher laser intensity, meaning the emitted photons are more likely to be directed into space rather than returning to the telescope. However, this transition saturation effect contributes less to the decrease in returned photon flux compared to Larmor precession and

recoil. Therefore, no special treatment is planned in the MECSEL-based LGS system to mitigate this effect.

Larmor precession must be considered when the angle between the laser beam and the geomagnetic field lines in the sodium layer is large [161]. The fluorescence from the sodium layer weakens when using a single-frequency laser targeting Na D_{2a} because this precession redistributes the atomic populations and can depopulate the $F = 2$ upper ground state in favor of the $F = 1$ state [161]. To address this issue, an additional repumping laser with a frequency offset of +1.713 GHz from the D_2 line can be employed [41]. Previous studies have shown that this approach can enhance the LGS return flux by a factor of three [39]. The MECSEL-based LGS offers a broad wavelength tuning range, providing a straightforward solution to address Larmor precession-related issues by using an additional identical laser for repumping.

For high brightness single-frequency LGS with a bandwidth of less than 10 MHz, like the system discussed in this dissertation, the spectral hole burning effect will depopulate the corresponding velocity group [162]. This depopulation is caused by atomic recoil. When a sodium atom spontaneously emits a photon after absorbing a photon from the laser beam, the conservation of momentum results in a velocity change of the sodium atom given by [41]

$$\Delta v = \frac{\hbar k}{M}, \tag{10.1}$$

where $\hbar$ is the reduced Planck constant, $k = \frac{2\pi}{\lambda}$ is the wavenumber of the laser photon, λ is the laser wavelength, and M is the mass of a sodium atom. This velocity change leads to a Doppler shift of

$$\Delta \nu_{\text{recoil}} = \frac{\Delta v}{\lambda} \approx 50\,\text{kHz}. \tag{10.2}$$

This Doppler effect will accumulate since all laser photons originate from the same direction, continuing until the velocities of sodium atoms in the mesosphere are randomized due to collisions [41].

Atoms in the sodium layer typically experience collisions with a time interval t_c of 35 µs between two collisions [41]. This results in a frequency shift for sodium atoms of

$$\delta\nu = \frac{\mathrm{t_c} \times \Delta\nu_{\mathrm{recoil}}}{\mathrm{t_a}} \approx 28\,\mathrm{MHz} \tag{10.3}$$

before collision, which is larger than the natural linewidth of sodium atoms. To eliminate the effects of recoil, the optical frequency of the laser needs to be periodically chirped in a sawtooth manner towards higher frequency. The laser system discussed in this dissertation has a unique advantage for implementing this frequency chirping, as all necessary elements are already integrated into the system, and this chirp could also be used to generate the error signal for stabilization. The optimal chirping range and speed depend on the laser intensity. For operations near sodium saturation intensity, a chirping range of 150 MHz with a repetition rate of 7 kHz is recommended [41].

10.2.2 Improved Multi-Pass Configuration

The current multi-pass pumping scheme used for H-MECSEL has been significantly improved compared to the one used for MECSEL. However, further enhancements could potentially be made. In Chapter 4, an OAP mirror-based multi-pass design was discussed, which can simplify the design and make it more robust and compact.

A multi-pass pumping design, as illustrated in Fig. 10.2, was planned. With similar H-MECSEL gain chip, the focused pump beam enters the system through a hole in the first OAP mirror (OAP1) and is collimated onto the gain membrane by the second OAP mirror (OAP2).

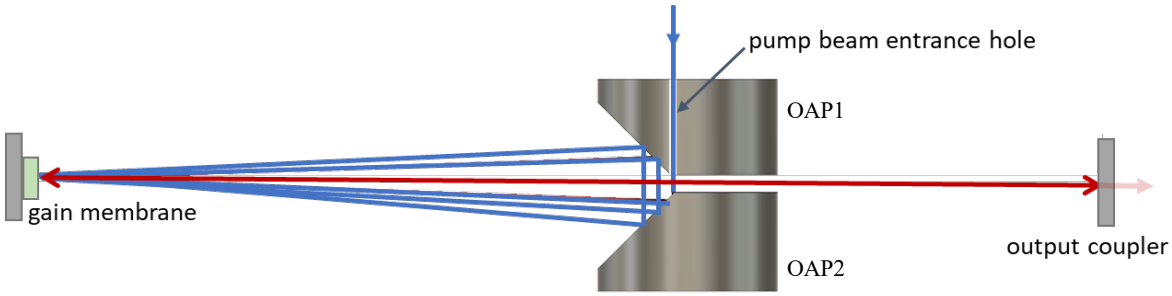

Fig. 10.2 Schematic drawing of OAP mirror-based multi-pass pumping scheme.

The gain chip is slightly tilted to laterally shift the pump beam with each round trip. The reflected pump beam is then refocused by OAP1, hitting a slightly shifted position on OAP2 before being collimated onto the gain chip again. This process continues until the pump is blocked or escapes from the system.

Reducing the number of elements by 33% could simplify alignment and enhance system robustness. Removing the aspheric lens addresses concerns about AR coating quality at pump wavelengths, particularly for passes near the lens edge. It also eliminates the need for custom-drilling a hole in the lens center. The new prototype requires minor modifications to the off-the-shelf OAP mirrors. In the future, these mirrors could be directly sourced from manufacturers with the desired parabolic surface, thus eliminating the need for laboratory modifications.

10.2.3 Diamond Heat Spreader

Based on the FEM analysis discussed in Chapter 6, diamond is a potentially superior candidate compared to SiC for use as a heat spreader. Diamond's superior heat dissipation ability enables the use of traditional barrier pumping to achieve high output power without thermal concerns. The diamond heat spreader would allow the barrier pumping method from a diode laser to

focus directly onto the H-MECSEL sample without the need for a complex multi-pass pumping scheme for implementation of in-well pumping. A simplified pumping design can significantly enhancing the compactness and robustness of the system. Additionally, the use of a diode laser in this setup could reduce costs dramatically compared to fiber lasers, offering a more economical yet efficient solution for laser systems.

A compact H-MECSEL taking advantage of simple barrier pumping was considered, by utilizing a dielectric coating on the H-MECSEL to be HR at the laser wavelength and transparent at the pump wavelength, and by employing a heat sink design with open apertures on both sides as in standard MECSELs, the system can be directly pumped from the back side using a diode laser as shown in Fig. 10.3. This setup allows the laser cavity to be constructed on the opposite side of the H-MECSEL sample. Moreover, this direct pumping approach prevents the issues associated with elliptical pump spots on the gain chip that typically arise due to the angle of the pump beam.

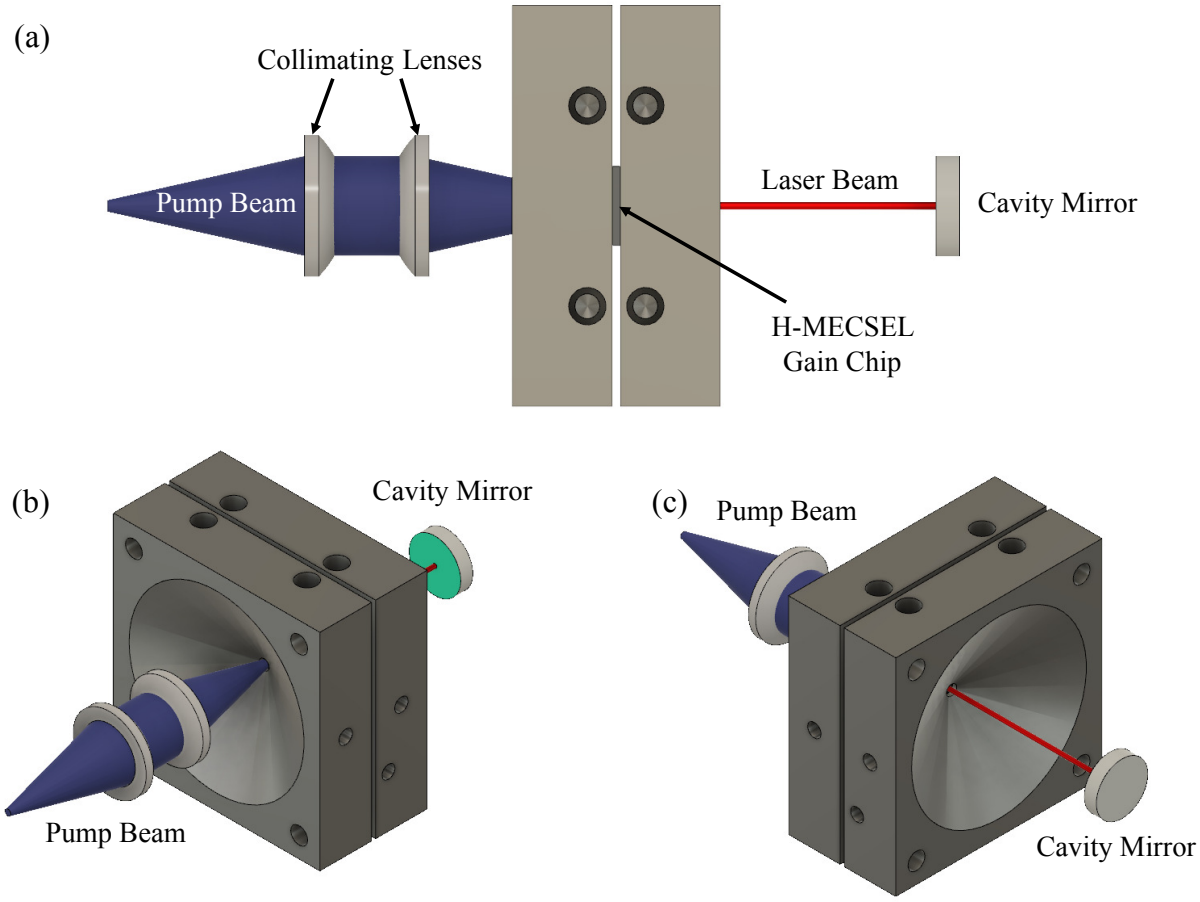

Fig. 10.3 Schematic drawing of backside barrier pumping H-MECSEL structure with (a) top view, (b) pump side side view, and (c) laser cavity side view.

10.2.4 Other Applications with MECSEL

In addition to applications in LGS, MECSELs also show great potential for ultrashort pulse generation [163]. The author demonstrated mode-locked short pulse operation in a VECSEL configuration without relying on a semiconductor saturable absorber mirror (SESAM) [164]. The short pulse demonstration combined with a previous publication from the author's research group [165], highlight the potential of MECSEL in ultrafast area.

When considering nonlinear effect, the refractive index can be expressed as:

$$n(I) = n_0 + n_2 I, \tag{10.4}$$

where n_0 is the linear refractive index, n_2 is the nonlinear refractive index coefficient that can be measured using the z-scan technique [166] developed by Sheik-Bahae et al., and I is the intensity of the light. When the laser operates in CW mode, the contribution of the nonlinear refractive index is small and the cavity beam size remains largely unaffected. However, in mode-locking operation, the laser peak intensity increases significantly, which substantially alters the refractive index of the materials due to the n_2 term. Consequently, the cavity beam size deviates from its low-intensity values. This nonlinear effect can be utilized to achieve Kerr lens mode-locking (KLM) [167] with careful cavity design.

The experimental setup was designed to facilitate KLM, as shown in Fig. 10.4 (a). The laser cavity includes a plane mirror (M1) and a concave mirror (M2), and a VECSEL gain chip effectively serving as a plane folding mirror. A high n_2 ZnS plate was placed near M1, where the cavity beam waist is located, to maximize the cavity beam intensity. An aperture was positioned near M2, where the cavity beam size is largest. Hard-aperture KLM was facilitated by closing the aperture slightly, forcing the laser to operate in pulsed mode and utilizing the nonlinear effect to reduce the cavity beam size at the aperture position. This reduction in beam size

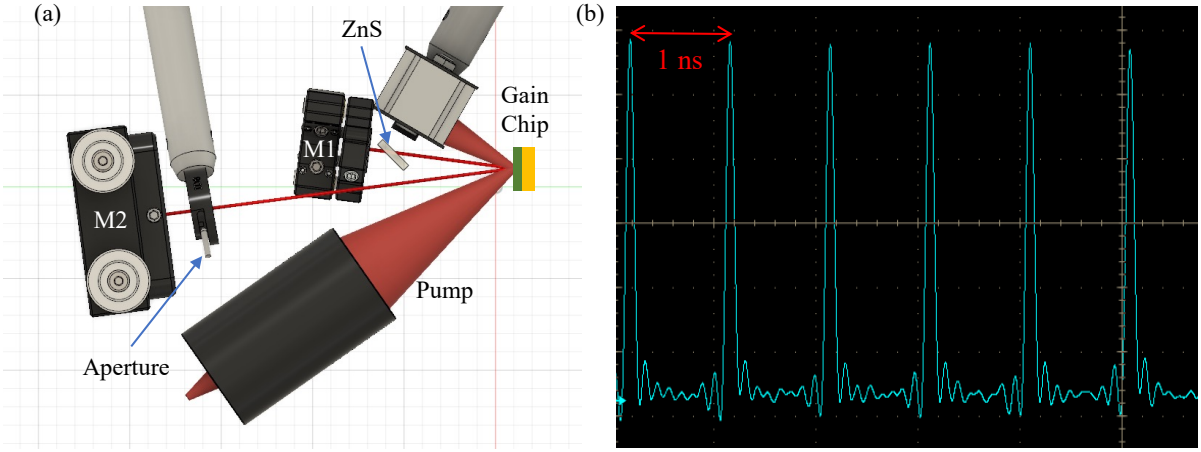

Fig. 10.4 (a) Schematic diagram of Kerr lens mode-locking VECSEL and (b) laser pulses generated from the experiment.

decreases optical losses at the slightly closed aperture where the beam must pass in each cavity round trip. For soft-aperture KLM experiments, the aperture was left wide open, relying solely on the ZnS plate. In these experiments, the pump beam size on the gain chip was purposely reduced. In pulsed operation, the nonlinear effect leads to a smaller cavity beam size on the gain chip, resulting in better overlap of the laser and pump beams at the gain chip position, thus achieving higher gain. Time domain data measured by a fast detector from the soft-aperture Kerr lens experiment as shown in Fig. 10.4 (b), indicate the generation of mode-locked laser pulses. Such findings not only expand the operational capabilities of VECSELs but also provide a foundation for future explorations into similar mode-locking semiconductor lasers without the use of SESAMs.

MECSELs are distinguished by their unique architecture, which exhibits a two-fold gain bandwidth enhancement compared with VECSELs [73]. Figure 10.5 (a) presents a comparative analysis, illustrating the gain enhancement factor for both VECSELs and MECSELs [163]. This broad gain bandwidth is particularly advantageous for short pulse generation. Additionally, the SiC heat spreaders integrated into MECSEL gain chips have a relatively high n_2 and can trigger

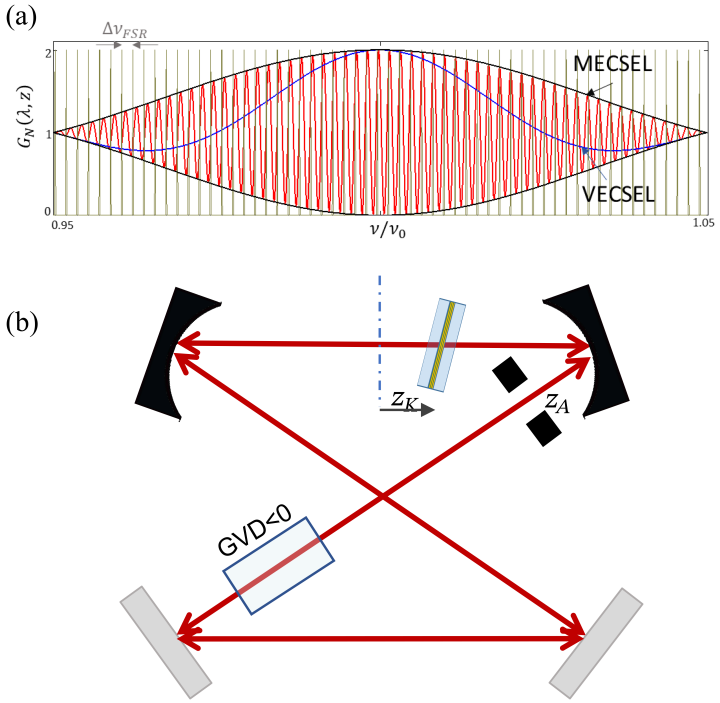

Fig. 10.5 (a) Gain enhancement factor plots for VECSELs and MECSELs [163]. (b) Ring cavity MECSEL with a hard-aperture KLM operation and dispersion management [163].

KLM without additional intracavity elements. Exploiting these advantages, a traveling wave ring cavity design for MECSELs, depicted in Fig. 10.5 (b), has been proposed to potentially generate sub-50 fs pulses. This pioneering approach demonstrates the adaptability of MECSELs to ultrafast laser applications, aiming to push the limits of pulse duration achievable with a KLM MECSEL, potentially replacing the current bulky and expensive Ti:Sapphire lasers.

Beyond the realm of ultrafast lasers, MECSELs demonstrate substantial potential in fields such as quantum information science. Recent studies have indicated that VECSELs are pivotal in generating wavelengths that traditional laser platforms struggle to produce, thereby broadening their applicability in cutting-edge scientific research [168]. As an advanced iteration of VECSELs, MECSELs not only match but may surpass the performance of their predecessors in these innovative quantum research applications.

References

[1] Z. Yang, A. R. Albrecht, J. G. Cederberg, and M. Sheik-Bahae. Optically pumped DBR-free semiconductor disk lasers. *Optics express*, 23(26):33164–33169, 2015.

[2] H. Kahle, C. M. N. Mateo, U. Brauch, P. Tatar-Mathes, R. Bek, M. Jetter, T. Graf, and P. Michler. Semiconductor membrane external-cavity surface-emitting laser (MECSEL). *Optica*, 3(12):1506–1512, 2016.

[3] W. Happer, G. J. MacDonald, C. E. Max, and F. J. Dyson. Atmospheric-turbulence compensation by resonant optical backscattering from the sodium layer in the upper atmosphere. *JOSA A*, 11(1):263–276, 1994.

[4] Z. Yang. *Novel concepts in semiconductor disk lasers*. PhD thesis, The University of New Mexico, 2016.

[5] S. Hackett. *High Power Optically Pumped Semiconductor Lasers for Sodium Guidestar Applications*. PhD thesis, The University of New Mexico, 2016.

[6] R. Epstein, D. Seletskiy, and E. Van Stryland. Mansoor Sheik-Bahae (1956–2023). *Nature Photonics*, 17(10):833–834, 2023.

[7] Zemax LLC. *Zemax*. Zemax LLC., Kirkland, Washington, United States, 2018.

[8] COMSOL Inc. *COMSOL Multiphysics*. COMSOL, Inc., Burlington, Massachusetts, United States, 2020.

[9] The MathWorks Inc. *MATLAB*. The MathWorks Inc., Natick, Massachusetts, United States, 2022.

[10] Gore Photonics. *Vertical Structure Design*. Gore Photonics, Lompoc, California, United States, 2002.

[11] Autodesk Inc. *Autodesk Fusion 360*. Autodesk, Inc., San Francisco, California, United States, 2021.

[12] National Instruments. *LabVIEW*. National Instruments, Austin, Texas, United States, 2019.

[13] J. P. Gardner, J. C. Mather, M. Clampin, R. Doyon, M. A. Greenhouse, H. B. Hammel, J. B. Hutchings, P. Jakobsen, S. J. Lilly, K. S. Long, J. I. Lunine, M. J. Mccaughrean, M. Mountain, J. Nella, G. H. Rieke, M. J. Rieke, H.-W. Rix, E. P. Smith, G. Sonneborn, M. Stiavelli, H. S. Stockman, R. A. Windhorst, and G. S. Wright. The James Webb Space Telescope. *Space Science Reviews*, 123:485–606, 2006.

[14] Saturn (NIRCam). Webb Space Telescope, July 2024. https://webbtelescope.org/contents/media/images/01H3X9BMPCX165ZK9RA49J2416.

[15] Gemini North Infrared View of Jupiter. International Gemini Observatory, July 2024. https://noirlab.edu/public/images/noirlab2116a/.

[16] J. C. Wyngaard. *Turbulence in the Atmosphere*. Cambridge University Press, 2010.

[17] R. Horowitz and H. E. LaGow. Upper air pressure and density measurements from 90 to 220 kilometers with the Viking 7 rocket. *Journal of Geophysical Research*, 62(1):57–78, 1957.

[18] P. Juncar, J. Pinard, J. Hamon, and A. Chartier. Absolute determination of the wavelengths of the sodium D1 and D2 lines by using a cw tunable dye laser stabilized on iodine. *Metrologia*, 17(3):77, 1981.

[19] R. M. Clare, M. Le Louarn, and C. Béchet. Laser guide star wavefront sensing for ground-layer adaptive optics on extremely large telescopes. *Applied Optics*, 50(4):473–483, 2011.

[20] M. Zhang, A. R. Albrecht, G. D. Cole, and M. Sheik-Bahae. Igniting Artificial Stars with Semiconductor Disk Lasers. *UNM Shared Knowledge Conference*, 2021.

[21] R. W. Duffner and R. Q. Fugate. *The adaptive optics revolution: a history*. University of New Mexico Press, 2009.

[22] C. A. Denman, J. D. Drummond, M. L. Eickhoff, R. Q. Fugate, P. D. Hillman, S. J. Novotny, and J. M. Telle. Characteristics of sodium guidestars created by the 50-watt FASOR and first closed-loop AO results at the Starfire Optical Range. In *Advances in Adaptive Optics II*, volume 6272, pages 508–519. SPIE, 2006.

[23] L. A. Thompson and C. S. Gardner. Experiments on laser guide stars at Mauna Kea Observatory for adaptive imaging in astronomy. *Nature*, 328(6127):229–231, 1987.

[24] X. Huo, Y. Qi, Y. Zhang, B. Chen, Z. Bai, J. Ding, Y. Wang, and Z. Lu. Research development of 589 nm laser for sodium laser guide stars. *Optics and lasers in engineering*, 134:106207, 2020.

[25] FASOR Handbook. *SOR FASOR Handbook*. SOR Internal Communications, 2013.

[26] C. Vergien, I. Dajani, and C. Zeringue. Theoretical analysis of single-frequency Raman fiber amplifier system operating at 1178nm. *Optics express*, 18(25):26214–26228, 2010.

[27] L. Zhang, H. Jiang, S. Cui, J. Hu, and Y. Feng. Versatile Raman fiber laser for sodium laser guide star. *Laser & Photonics Reviews*, 8(6):889–895, 2014.

[28] Y. U. Peter and M. Cardona. *Fundamentals of semiconductors: physics and materials properties*. Springer Science & Business Media, 2010.

[29] B. Heinen, T. L. Wang, M. Sparenberg, A. Weber, B. Kunert, J. Hader, S. W. Koch, J. V. Moloney, M. Koch, and W. Stolz. 106 W continuous-wave output power from vertical-external-cavity surface-emitting laser. *Electronics letters*, 48(9):1, 2012.

[30] M. Fallahi, L. Fan, Y. Kaneda, C. Hessenius, J. Hader, H. Li, J. V. Moloney, B. Kunert, W. Stolz, S. W. Koch, J. Murray, and R. BedfoRd. 5-W yellow laser by intracavity frequency doubling of high-power vertical-external-cavity surface-emitting laser. *IEEE Photonics Technology Letters*, 20(20):1700–1702, 2008.

[31] R. Davies, S. Rabien, C. Lidman, M. L. Louarn, M. Kasper, N. M. Schreiber, V. Roccatagliata, N. Ageorges, P. Amico, C. Dumas, and F. Mannucci. Laser Guide Star Adaptive Optics without Tip-tilt. *arXiv preprint arXiv:0801.3738*, 2008.

[32] T. H. Jeys. Development of a Mesospheric Sodium Laser Beacon for Atmospheric Adaptive Optics. *Lincoln Laboratory Journal*, 4(2), 1991.

[33] D. A. Steck. Sodium D line data. *Report, Los Alamos National Laboratory, Los Alamos*, 124:74, 2000.

[34] Y. Lu, L. Zhang, X. Xu, H. Ren, X. Chen, X. Wei, B. Wei, Y. Liao, J. Gu, F. Liu, L. Xu, J. Wang, T. Chen, M. Wan, W. Zhang, C. Tang, and G. Fan. 208 W all-solid-state sodium guide star laser operated at modulated-longitudinal mode. *Optics Express*, 27(15):20282–20289, 2019.

[35] J. W. Hardy. *Adaptive optics for astronomical telescopes*, volume 16. Oxford University Press, USA, 1998.

[36] S.-H. Baik, S.-K. Park, C.-J. Kim, and B. Cha. A center detection algorithm for Shack–Hartmann wavefront sensor. *Optics & Laser Technology*, 39(2):262–267, 2007.

[37] P.-Y. Madec. Overview of deformable mirror technologies for adaptive optics and astronomy. In *Adaptive optics systems III*, volume 8447, pages 22–39. SPIE, 2012.

[38] G. Rousset, F. Lacombe, P. Puget, N. N. Hubin, E. Gendron, T. Fusco, R. Arsenault, J. Charton, P. Feautrier, P. Gigan, P. Y. Kern, A.-M. Lagrange, P.-Y. Madec, D. Mouillet, D. Rabaud, P. Rabou, E. Stadler, and G. Zins. NAOS–the first AO system of the VLT: on-sky performance. In *Adaptive Optical System Technologies II*, volume 4839, pages 140–149. SPIE, 2003.

[39] R. Holzlöhner, S. M. Rochester, D. B. Calia, D. Budker, J. M. Higbie, and W. Hackenberg. Optimization of cw sodium laser guide star efficiency. *Astronomy & Astrophysics*, 510:A20, 2010.

[40] J. Li, B. P. Williams, J. H. Alspach, and R. L. Collins. Sodium resonance wind-temperature lidar at PFRR: Initial observations and performance. *Atmosphere*, 11(1):98, 2020.

[41] F. P. Bustos, R. Holzlöhner, S. Rochester, D. B. Calia, J. Hellemeier, and D. Budker. Frequency chirped continuous-wave sodium laser guide stars: modeling and optimization. *JOSA B*, 37(4):1208–1218, 2020.

[42] A. Einstein. *Zur quantentheorie der strahlung*. Verlag u. Druck Gebr. Leemann, 1916.

[43] N. G. Basov and A. M. Prokhorov. Application of molecular beams for the radiospectroscopic study of rotational molecular spectra. *Zh. Eksp. Teor. Fiz*, 27:431–438, 1954.

[44] N. G. Basov and A. M. Prokhorov. About possible methods for obtaining active molecules for a molecular oscillator. *Sov. Phys.-JETP*, 1:184–185, 1955.

[45] J. P. Gordon, H. J. Zeiger, and C. H. Townes. Molecular microwave oscillator and new hyperfine structure in the microwave spectrum of NH3. *Physical Review*, 95(1):282, 1954.

[46] J. P. Gordon, H. J. Zeiger, and C. H. Townes. The maser—new type of microwave amplifier, frequency standard, and spectrometer. *Physical review*, 99(4):1264, 1955.

[47] A. L. Schawlow and C. H. Townes. Infrared and optical masers. *Physical review*, 112(6):1940, 1958.

[48] The Nobel Prize in Physics 1964. NobelPrize.org. Nobel Prize Outreach AB 2024, May 2024. https://www.nobelprize.org/prizes/physics/1964/summary/.

[49] T. H. Maiman. Stimulated optical radiation in ruby. *Nature*, 187(4736):493–494, 1960.

[50] R. N. Hall, G. E. Fenner, J. D. Kingsley, T. J. Soltys, and R. O. Carlson. Coherent light emission from GaAs junctions. *Physical Review Letters*, 9(9):366, 1962.

[51] M. I. Nathan, W. P. Dumke, G. Burns, F. H. Dill, and G. Lasher. Stimulated emission of radiation from GaAs p-n junctions. *Applied Physics Letters*, 1(3):62–64, 1962.

[52] T. M. Quist, R. H. Rediker, R. J. Keyes, W. E. Krag, B. Lax, A. L. McWhorter, and H. J. Zeigler. Semiconductor maser of GaAs. *Applied Physics Letters*, 1(4):91–92, 1962.

[53] H. Kroemer. A proposed class of hetero-junction injection lasers. *Proceedings of the IEEE*, 51(12):1782–1783, 1963.

[54] Z. I. Alferov, V. M. Andreev, D. Z. Garbuzov, Y. V. Zhilyaev, E. P. Morozov, E. L. Portnoi, and V. G. Trofim. Investigation of the influence of the AlAs–GaAs heterostructure parameters on the laser threshold current and the realization of continuous emission at room temperature. *Fiz. Tekh. Poluprovodn*, 4(9):1826, 1970.

[55] The Nobel Prize in Physics 2000. NobelPrize.org. Nobel Prize Outreach AB 2024, May 2024. https://www.nobelprize.org/prizes/physics/2000/summary/.

[56] A. Baranov and E. Tournié. *Semiconductor lasers: Fundamentals and applications*. Elsevier, 2013.

[57] K. Iga, F. Koyama, and S. Kinoshita. Surface emitting semiconductor lasers. *IEEE Journal of Quantum Electronics*, 24(9):1845–1855, 1988.

[58] R. Paschotta. Bragg Mirrors. RP Photonics Encyclopedia, July 2024. https://www.rp-photonics.com/bragg_mirrors.html.

[59] M. H. MacDougal, P. D. Dapkus, A. E. Bond, C.-K. Lin, and J. Geske. Design and fabrication of VCSELs with AlxOy-GaAs DBRs. *IEEE Journal of Selected Topics in Quantum Electronics*, 3(3):905–915, 1997.

[60] H.-T. Cheng, Y.-C. Yang, T.-H. Liu, and C.-H. Wu. Recent advances in 850 nm VCSELs for high-speed interconnects. *Photonics*, 9(2):107, 2022.

[61] M. Kuznetsov, F. Hakimi, R. Sprague, and A. Mooradian. High-power (> 0.5-W CW) diode-pumped vertical-external-cavity surface-emitting semiconductor lasers with circular TEM/sub 00/beams. *IEEE Photonics Technology Letters*, 9(8):1063–1065, 1997.

[62] N. Basov, O. Bogdankevich, and A. Grasyuk. Semiconductor lasers with radiating mirrors. *IEEE Journal of Quantum Electronics*, 2(9):594–597, 1966.

[63] M. Kuznetsov, F. Hakimi, R. Sprague, and A. Mooradian. Design and characteristics of high-power (> 0.5-W CW) diode-pumped vertical-external-cavity surface-emitting semiconductor lasers with circular TEM/sub 00/beams. *IEEE Journal of Selected Topics in Quantum Electronics*, 5(3):561–573, 1999.

[64] E. Kantola, J.-P. Penttinen, A. Ranta, and M. Guina. 72-W vertical-external-cavity surface-emitting laser with 1180-nm emission for laser guide star adaptive optics. *Electronics Letters*, 54(19):1135–1137, 2018.

[65] E. Kantola, T. Leinonen, S. Ranta, M. Tavast, and M. Guina. High-efficiency 20 W yellow VECSEL. *Optics express*, 22(6):6372–6380, 2014.

[66] J. Piprek, T. Troger, B. Schroter, J. A. K. J. Kolodzey, and C. S. Ih. Thermal conductivity reduction in GaAs-AlAs distributed Bragg reflectors. *IEEE Photonics Technology Letters*, 10(1):81–83, 1998.

[67] Y. Huo, C. Y. Cho, K. F. Huang, Y. F. Chen, and C. C. Lee. Exploring the DBR superlattice effect on the thermal performance of a VECSEL with the finite element method. *Optics Letters*, 44(2):327–330, 2019.

[68] J.-F. Carlin, J. Dorsaz, E. Feltin, R. Butté, N. Grandjean, M. Ilegems, and M. Laügt. Crack-free fully epitaxial nitride microcavity using highly reflective AlInN/ GaN Bragg mirrors. *Applied Physics Letters*, 86(3), 2005.

[69] H. M. Ng, T. D. Moustakas, and S. N. G. Chu. High reflectivity and broad bandwidth AlN/GaN distributed Bragg reflectors grown by molecular-beam epitaxy. *Applied Physics Letters*, 76(20):2818–2820, 2000.

[70] V. Iakovlev, J. Walczak, M. Gębski, A. K. Sokół, M. Wasiak, P. Gallo, A. Sirbu, R. P. Sarzała, M. Dems, and T. Czyszanowski. Double-diamond high-contrast-gratings vertical external cavity surface emitting laser. *Journal of Physics D: Applied Physics*, 47(6):065104, 2014.

[71] Z. Yang, D. Lidsky, and M. Sheik-Bahae. Gain-embedded meta mirrors for optically pumped semiconductor disk lasers. *Optics Express*, 27(20):27882–27890, 2019.

[72] H.-M. Phung, P. Tatar-Mathes, A. Rogers, P. Rajala, S. Ranta, H. Kahle, and M. Guina. Thermal behavior and power scaling potential of membrane external-cavity surface-emitting lasers (MECSELs). *IEEE Journal of Quantum Electronics*, 58(2):1–11, 2022.

[73] Z. Yang, A. R. Albrecht, J. G. Cederberg, and M. Sheik-Bahae. 80 nm tunable DBR-free semiconductor disk laser. *Applied Physics Letters*, 109(2), 2016.

[74] M. Zhang, D. Priante, A. R. Albrecht, G. D. Cole, and M. Sheik-Bahae. High-power in-well pumped MECSEL emitting at 1178 nm for sodium guide star applications. In *Vertical External Cavity Surface Emitting Lasers (VECSELs) XI*, volume 11984, pages 9–16. SPIE, 2022.

[75] M. Zhang, A. R. Albrecht, G. W. Truong, G. D. Cole, and M. Sheik-Bahae. A single-mode high-power in-well pumped hybrid-MECSEL at 589 nm. In *Vertical External Cavity Surface Emitting Lasers (VECSELs) XII*, volume 12404, page 124040A. SPIE, 2023.

[76] M. Zhang, N. Giannini-Hutchin, G. W. Truong, G. D. Cole, A. R. Albrecht, and M. Sheik-Bahae. Advances in MECSEL technology. In *Vertical External Cavity Surface Emitting Lasers (VECSELs) XIII*, page PC1286809. SPIE, 2024.

[77] M. Imada, S. Noda, A. Chutinan, T. Tokuda, M. Murata, and G. Sasaki. Coherent two-dimensional lasing action in surface-emitting laser with triangular-lattice photonic crystal structure. *Applied physics letters*, 75(3):316–318, 1999.

[78] S. Noda, K. Kitamura, T. Okino, D. Yasuda, and Y. Tanaka. Photonic-crystal surface-emitting lasers: Review and introduction of modulated-photonic crystals. *IEEE Journal of Selected Topics in Quantum Electronics*, 23(6):1–7, 2017.

[79] H. Matsubara, S. Yoshimoto, H. Saito, Y. Jianglin, Y. Tanaka, and S. Noda. GaN photonic-crystal surface-emitting laser at blue-violet wavelengths. *Science*, 319(5862):445–447, 2008.

[80] Y. Kurosaka, S. Iwahashi, Y. Liang, K. Sakai, E. Miyai, W. Kunishi, D. Ohnishi, and S. Noda. On-chip beam-steering photonic-crystal lasers. *Nature photonics*, 4(7):447–450, 2010.

[81] W. Zheng, W. Zhou, Y. Wang, A. Liu, W. Chen, H. Wang, F. Fu, and A. Qi. Lateral cavity photonic crystal surface-emitting laser with ultralow threshold. *Optics letters*, 36(21):4140–4142, 2011.

[82] K. Hirose, Y. Liang, Y. Kurosaka, A. Watanabe, T. Sugiyama, and S. Noda. Watt-class high-power, high-beam-quality photonic-crystal lasers. *Nature photonics*, 8(5):406–411, 2014.

[83] M. Yoshida, M. De Zoysa, K. Ishizaki, Y. Tanaka, M. Kawasaki, R. Hatsuda, B. Song, J. Gelleta, and S. Noda. Double-lattice photonic-crystal resonators enabling high-brightness semiconductor lasers with symmetric narrow-divergence beams. *Nature materials*, 18(2):121–128, 2019.

[84] Y. Wang, H. Qu, W. Zhou, A. Qi, J. Zhang, L. Liu, and W. Zheng. Lateral cavity photonic crystal surface emitting laser based on commercial epitaxial wafer. *Optics express*, 21(7):8844–8855, 2013.

[85] M. Yoshida, S. Katsuno, T. Inoue, J. Gelleta, K. Izumi, M. De Zoysa, K. Ishizaki, and S. Noda. High-brightness scalable continuous-wave single-mode photonic-crystal laser. *Nature*, 618(7966):727–732, 2023.

[86] M. Y. A. Raja, S. R. J. Brueck, M. Osinski, C. F. Schaus, J. G. McInerney, T. M. Brennan, and B. E. Hammons. Resonant periodic gain surface-emitting semiconductor lasers. *IEEE Journal of Quantum Electronics*, 25(6):1500–1512, 1989.

[87] J. Xie, T. Lin, C. Wang, J. Shi, C. Xie, D. Liang, and Y. Duan. Study of 589nm GaInP quantum well semiconductor laser on Ge/SiGe substrate. *Applied Physics B*, 130(2):26, 2024.

[88] E. F. Schubert. *Light-emitting diodes (Second Edition)*. Cambridge University Press, 2006.

[89] A. F. Boya and A. I. Abdullah. Study of the influence of the magnetic field on MQW laser through image processing. In *Proceedings of CAOL 2005. Second International Conference on Advanced Optoelectronics and Lasers, 2005.*, volume 1, pages 270–273. IEEE, 2005.

[90] A. David and B. Miller. Optical physics of quantum wells. In *Quantum Dynamics of Simple Systems*, pages 239–266. CRC Press, 2020.

[91] S. Adachi. *Physical properties of III-V semiconductor compounds*. John Wiley & Sons, 1992.

[92] Y. P. Varshni. Temperature dependence of the energy gap in semiconductors. *physica*, 34(1):149–154, 1967.

[93] J. Hader, T.-L. Wang, J. V. Moloney, B. Heinen, M. Koch, S. W. Koch, B. Kunert, and W. Stolz. On the measurement of the thermal impedance in vertical-external-cavity surface-emitting lasers. *Journal of Applied Physics*, 113(15), 2013.

[94] P. P. Baveja, B. Kögel, P. Westbergh, J. S. Gustavsson, Å. Haglund, D. N. Maywar, G. P. Agrawal, and A. Larsson. Assessment of VCSEL thermal rollover mechanisms from measurements and empirical modeling. *Optics express*, 19(16):15490–15505, 2011.

[95] J. Singh. *Physics of Semiconductors and their Heterostructures*. McGraw-Hill, 1993.

[96] R. E. Nahory, M. A. Pollack, W. D. Johnston, and R. L. Barns. Band gap versus composition and demonstration of Vegard's law for In1-xGaxAsyP1-y lattice matched to InP. *Applied Physics Letters*, 33(7):659–661, 1978.

[97] G. B. Stringfellow. The importance of lattice mismatch in the growth of GaxIn1-xP epitaxial crystals. *Journal of Applied Physics*, 43(8):3455–3460, 1972.

[98] N. Tansu and L. J. Mawst. High-performance strain-compensated InGaAs-GaAsP-GaAs (/spl lambda/= 1.17 μm) quantum well diode lasers. *IEEE Photonics Technology Letters*, 13(3):179–181, 2001.

[99] E. D. Palik. *Handbook of optical constants of solids*, volume 3. Academic press, 1998.

[100] S. Ma, H. Sodabanlu, K. Watanabe, M. Sugiyama, and Y. Nakano. Strain-compensation measurement and simulation of InGaAs/GaAsP multiple quantum wells by metal organic vapor phase epitaxy using wafer-curvature. *Journal of Applied Physics*, 110(11), 2011.

[101] P. W. Milonni and J. H. Eberly. *Laser physics*. John Wiley & Sons, 2010.

[102] T. Mikitta, A. Ćutuk, M. Jetter, P. Michler, K. D. Jöns, and H. Kahle. Membrane external-cavity surface-emitting lasers (MECSELs) optimized for double-side-pumping: A first fundamental single-side pumping characterization. In Ursula Keller, editor, *Vertical External Cavity Surface Emitting Lasers (VECSELs) XIII*, volume 12868, page 1286803. International Society for Optics and Photonics, SPIE, 2024.

[103] O. G. Okhotnikov. *Semiconductor disk lasers: physics and technology*. John Wiley & Sons, 2010.

[104] W. Wang, W. Xie, Z. Deng, and M. Liao. Improving output power of InGaN laser diode using asymmetric In0. 15Ga0. 85N/In0. 02Ga0. 98N multiple quantum wells. *Micromachines*, 10(12):875, 2019.

[105] G. D. Cole, C. Nguyen, D. Follman, R. Bek, M. Zimmer, N. Witz, M. Zhang, A. R. Albrecht, and M. Sheik-Bahae. Chip-and Wafer-Scale Manufacturing of High-Power Membrane-External-Cavity Surface-Emitting Laser Gain Elements. In *2022 Conference on Lasers and Electro-Optics (CLEO)*, pages 1–2. IEEE, 2022.

[106] H. Kahle, J.-P. Penttinen, H.-M. Phung, P. Rajala, A. Tukiainen, S. Ranta, and M. Guina. Comparison of single-side and double-side pumping of membrane external-cavity surface-emitting lasers. *Optics Letters*, 44(5):1146–1149, 2019.

[107] H.-M. Phung, H. Kahle, J.-P. Penttinen, P. Rajala, S. Ranta, and M. Guina. Power scaling and thermal lensing in 825 nm emitting membrane external-cavity surface-emitting lasers. *Optics Letters*, 45(2):547–550, 2020.

[108] B. Jeżewski, A. Broda, I. Sankowska, A. Kuźmicz, K. Gołaszewska-Malec, K. Czuba, and J. Muszalski. Membrane external-cavity surface-emitting laser emitting at 1640 nm. *Optics Letters*, 45(2):539–542, 2020.

[109] A. Broda, B. Jeżewski, M. Szymański, and J. Muszalski. High-power 1770 nm emission of a membrane external-cavity surface-emitting laser. *IEEE Journal of Quantum Electronics*, 57(1):1–6, 2020.

[110] A. Broda, B. Jeżewski, I. Sankowska, M. Szymański, P. Hoser, and J. Muszalski. Growth and characterization of InP-based 1750 nm emitting membrane external-cavity surface-emitting laser. *Applied Physics B*, 126(12):192, 2020.

[111] H.-M. Phung, P. Tatar-Mathes, C. Paranthoën, C. Levallois, N. Chevalier, M. Perrin, A. Kerchaoui, H. Kahle, M. Alouini, and M. Guina. Quantum dot membrane external-cavity surface-emitting laser at 1.5 μm. *Applied Physics Letters*, 118(23), 2021.

[112] D. Priante, M. Zhang, A. R. Albrecht, R. Bek, M. Zimmer, C. L. Nguyen, D. P. Follman, G. D. Cole, and M. Sheik-Bahae. In-well pumping of a membrane external-cavity surface-emitting laser. *IEEE Journal of Selected Topics in Quantum Electronics*, 28(1: Semiconductor Lasers):1–7, 2021.

[113] D. Priante, M. Zhang, A. R. Albrecht, R. Bek, M. Zimmer, C. Nguyen, D. Follman, G. D. Cole, and M. Sheik-Bahae. Demonstration of a 20-W membrane-external-cavity surface-emitting laser for sodium guide star applications. *Electronics Letters*, 57(8):337–338, 2021.

[114] M. Zhang, A. R. Albrecht, C. Nguyen, D. Follman, G. D. Cole, and M. Sheik-Bahae. Hybrid membrane-external-cavity surface-emitting laser. *Optics Express*, 30(23):42470–42479, 2022.

[115] M. Zhang, A. R. Albrecht, G. D. Cole, C. Nguyen, D. Follman, and M. Sheik-Bahae. Multipass In-Well Pumped Semiconductor Disk Laser for Sodium Guide Stars. In *2022 Conference on Lasers and Electro-Optics (CLEO)*, pages 1–2. IEEE, 2022.

[116] J. W. Evans. The birefringent filter. *JOSA*, 39(3):229–242, 1949.

[117] X. Wang and J. Yao. Transmitted and tuning characteristics of birefringent filters. *Applied optics*, 31(22):4505–4508, 1992.

[118] G. Ghosh. Dispersion-equation coefficients for the refractive index and birefringence of calcite and quartz crystals. *Optics communications*, 163(1-3):95–102, 1999.

[119] S. Zhu. Birefringent filter with tilted optic axis for tuning dye lasers: theory and design. *Applied optics*, 29(3):410–415, 1990.

[120] G. Shabtay, E. Eidinger, Z. Zalevsky, D. Mendlovic, and E. Marom. Tunable birefringent filters—optimal iterative design. *Optics express*, 10(26):1534–1541, 2002.

[121] J. Hrabovskỳ, M. Kučera, L. Paloušová, L. Bi, and M. Veis. Optical characterization of Y3Al5O12 and Lu3Al5O12 single crystals. *Optical Materials Express*, 11(4):1218–1223, 2021.

[122] Etalon Designer, April 2024. [online] https://lightmachinery.com/optical-design-center/etalon-designer/.

[123] B. W. Boyd. *Nonlinear Optics*. Academic Press, 2008.

[124] M. Zhang. Simpler Ultrashort Pulse Characterisation with a New Type of Frequency-Resolved Optical Gating. Master's thesis, Imperial College London, 2016.

[125] S. Wu, T. Li, Z. Wang, L. Chen, J. Zhang, J. Zhang, J. Liu, Y. Zhang, and L. Deng. Study of Temperature Effects on the Design of Active Region for 808 nm High-Power Semiconductor Laser. *Crystals*, 13(1):85, 2023.

[126] A. R. Albrecht, Z. Yang, and M. Sheik-Bahae. DBR-free Optically Pumped Semiconductor Disk Lasers. *Vertical External Cavity Surface Emitting Lasers: VECSEL Technology and Applications*, pages 175–196, 2021.

[127] M. Sheik-Bahae, M. Zhang, and A. R. Albrecht. Laser beam circulator, July 28 2022. US Patent App. 17/585,775.

[128] A. J. Kemp, G. J. Valentine, J.-M. Hopkins, J. E. Hastie, S. A. Smith, S. Calvez, M. D. Dawson, and D. Burns. Thermal management in vertical-external-cavity surface-emitting lasers: finite-element analysis of a heatspreader approach. *IEEE Journal of Quantum Electronics*, 41(2):148–155, 2005.

[129] O. I. Dosunmu, D. D. Cannon, M. K. Emsley, B. Ghyselen, J. Liu, L. C. Kimerling, and M. S. Unlu. Resonant cavity enhanced Ge photodetectors for 1550 nm operation on reflecting Si substrates. *IEEE Journal of selected topics in quantum electronics*, 10(4):694–701, 2004.

[130] M. Schmid, S. Benchabane, F. Torabi-Goudarzi, R. Abram, A. I. Ferguson, and E. Riis. Optical in-well pumping of a vertical-external-cavity surface-emitting laser. *Applied Physics Letters*, 84(24):4860–4862, 2004.

[131] T. Südmeyer, C. Kränkel, C. R. E. Baer, O. H. Heckl, C. J. Saraceno, M. Golling, R. Peters, K. Petermann, G. Huber, and U. Keller. High-power ultrafast thin disk laser oscillators and their potential for sub-100-femtosecond pulse generation. *Applied Physics B*, 97:281–295, 2009.

[132] C. M. N. Mateo, U. Brauch, H. Kahle, T. Schwarzbäck, M. Jetter, M. A. Ahmed, P. Michler, and T. Graf. 2.5 W continuous wave output at 665 nm from a multipass and quantum-well-pumped AlGaInP vertical-external-cavity surface-emitting laser. *Optics Letters*, 41(6):1245–1248, 2016.

[133] K. Toprasertpong, S. M. Goodnick, Y. Nakano, and M. Sugiyama. Effective mobility for sequential carrier transport in multiple quantum well structures. *Physical Review B*, 96(7):075441, 2017.

[134] J. Guo, W. Liu, D. Ding, X. Tan, W. Zhang, L. Han, Z. Wang, W. Gong, J. Li, R Zhai, Z. Jia, Z. Ma, C. Du, H. Jia, and X. Tang. Analysis of Photo-Generated Carrier Escape in Multiple Quantum Wells. *Crystals*, 13(5):834, 2023.

[135] A. Laurain, J. Hader, and J. V. Moloney. Modeling and optimization of transverse modes in vertical-external-cavity surface-emitting lasers. *JOSA B*, 36(4):847–854, 2019.

[136] G. D. Cole, W. Zhang, B. J. Bjork, D. Follman, P. Heu, C. Deutsch, L. Sonderhouse, J. Robinson, C. Franz, A. Alexandrovski, M. Notcutt, O. H. Heckl, J. Ye, and M. Aspelmeyer. High-performance near-and mid-infrared crystalline coatings. *Optica*, 3(6):647–656, 2016.

[137] C. P. Lee, C.-M. Tsai, and J. S. Tsang. Dual-wavelength Bragg reflectors using GaAs/AlAs multilayers. *Electronics Letters*, 29(22):1980–1981, 1993.

[138] G. D. Cole, S. W. Ballmer, G. Billingsley, S. B. Cataño-Lopez, M. Fejer, P. Fritschel, A. M. Gretarsson, G. M. Harry, D. Kedar, T. Legero, C. Makarem, S. D. Penn, D. H. Reitze, J. Steinlechner, U. Sterr, S. Tanioka, G.-W. Truong, J. Ye, and J. Yu. Substrate-transferred GaAs/AlGaAs crystalline coatings for gravitational-wave detectors. *Applied Physics Letters*, 122(11), 2023.

[139] U. Brauch, C. M. N. Mateo, H. Kahle, R. Bek, M. Jetter, M. A. Ahmed, P. Michler, and T. Graf. Schemes for efficient QW pumping of AlGaInP disk lasers. In *Vertical External Cavity Surface Emitting Lasers (VECSELs) VII*, volume 10087, pages 9–21. SPIE, 2017.

[140] C. Zhang, R. ElAfandy, and J. Han. Distributed Bragg reflectors for GaN-based vertical-cavity surface-emitting lasers. *Applied Sciences*, 9(8):1593, 2019.

[141] W. Koechner. Thermal lensing in a Nd: YAG laser rod. *Applied optics*, 9(11):2548–2553, 1970.

[142] L. M. Osterink and J. D. Foster. Thermal effects and transverse mode control in a Nd: YAG laser. *Applied Physics Letters*, 12(4):128–131, 1968.

[143] M. E. Innocenzi, H. T. Yura, C. L. Fincher, and R. A. Fields. Thermal modeling of continuous-wave end-pumped solid-state lasers. *Applied Physics Letters*, 56(19):1831–1833, 1990.

[144] Z. Fang, H. Cai, G. Chen, and R. Qu. *Single frequency semiconductor lasers*. Springer, 2017.

[145] E. D. Black. An introduction to Pound–Drever–Hall laser frequency stabilization. *American journal of physics*, 69(1):79–87, 2001.

[146] J. Alnis, A. Matveev, N. Kolachevsky, T. Wilken, Th. Udem, and T. W. Hänsch. Sub-Hz line width diode lasers by stabilization to vibrationally and thermally compensated ULE Fabry-Perot cavities. *arXiv preprint arXiv:0801.4199*, 2008.

[147] K. B. MacAdam, A. Steinbach, and C. Wieman. A narrow-band tunable diode laser system with grating feedback, and a saturated absorption spectrometer for Cs and Rb. *American Journal of Physics*, 60:1098–1098, 1992.

[148] K. J. Åström and T. Hägglund. *PID Controllers: Theory, Design, and Tuning*. Instrument Society of America, 1995.

[149] R. P. Borase, D. K. Maghade, S. Y. Sondkar, and S. N. Pawar. A review of PID control, tuning methods and applications. *International Journal of Dynamics and Control*, 9:818–827, 2021.

[150] A. E. Siegman. *Lasers*. University Science Books, 1986.

[151] O. Astafiev, A. M. Zagoskin, A. A. Abdumalikov Jr, Y. A. Pashkin, T. Yamamoto, K. Inomata, Y. Nakamura, and J. S. Tsai. Resonance fluorescence of a single artificial atom. *Science*, 327(5967):840–843, 2010.

[152] K. Wang, Z. Wang, Y. Wu, Y. Xia, Y. Xun, F. Wu, J. Jiao, and L. Du. Calculation of Resonance Fluorescence Scattering Cross Sections of Metal Particles in the Middle and Upper Atmosphere and Comparison of Their Detectability. *Atmosphere*, 14(8):1283, 2023.

[153] G. Megie. Laser measurements of atmospheric trace constituents. *Laser Remote Chemical Analysis*, page 333, 1988.

[154] C. Y. She, J. R. Yu, H. Latifi, and R. E. Bills. High-spectral-resolution fluorescence light detection and ranging for mesospheric sodium temperature measurements. *Applied optics*, 31(12):2095–2106, 1992.

[155] D. R. Lide. *CRC handbook of chemistry and physics*, volume 85. CRC press, 2004.

[156] D. W. Preston. Doppler-free saturated absorption: Laser spectroscopy. *American Journal of Physics*, 64(11):1432–1436, 1996.

[157] C. Y. She and J. R. Yu. Doppler-free saturation fluorescence spectroscopy of Na atoms for atmospheric application. *Applied optics*, 34(6):1063–1075, 1995.

[158] D. W. Allan. Statistics of atomic frequency standards. *Proceedings of the IEEE*, 54(2):221–230, 1966.

[159] J. L. Hall, M. S. Taubman, and J. Ye. Laser stabilization. *OSA Handbook v14*, 1999.

[160] D. A. Howe, D. U. Allan, and J. A. Barnes. Properties of signal sources and measurement methods. In *Thirty Fifth Annual Frequency Control Symposium*, pages 669–716. IEEE, 1981.

[161] N. Moussaoui, R. Holzlöhner, W. Hackenberg, and D. B. Calia. Dependence of sodium laser guide star photon return on the geomagnetic field. *Astronomy & Astrophysics*, 501(2):793–799, 2009.

[162] P. D. Hillman, J. D. Drummond, C. A. Denman, and R. Q. Fugate. Simple model, including recoil, for the brightness of sodium guide stars created from CW single frequency fasors and comparison to measurements. In *Adaptive Optics Systems*, volume 7015, pages 118–130. SPIE, 2008.

[163] M. Sheik-Bahae. Analysis of MECSEL mode-locking. In *Vertical External Cavity Surface Emitting Lasers (VECSELs) XI*, volume 11984, pages 29–36. SPIE, 2022.

[164] U. Keller, K. J. Weingarten, F. X. Kartner, D. Kopf, B. Braun, I. D. Jung, R. Fluck, C. Honninger, N. Matuschek, and J. A. Der Au. Semiconductor saturable absorber mirrors (SESAM's) for femtosecond to nanosecond pulse generation in solid-state lasers. *IEEE Journal of selected topics in QUANTUM ELECTRONICS*, 2(3):435–453, 1996.

[165] A. R. Albrecht, Y. Wang, M. Ghasemkhani, D. V. Seletskiy, J. G. Cederberg, and M. Sheik-Bahae. Exploring ultrafast negative Kerr effect for mode-locking vertical external-cavity surface-emitting lasers. *Optics express*, 21(23):28801–28808, 2013.

[166] M. Sheik-Bahae, A. A. Said, T.-H. Wei, D. J. Hagan, and E. W. Van Stryland. Sensitive measurement of optical nonlinearities using a single beam. *IEEE journal of quantum electronics*, 26(4):760–769, 1990.

[167] T. Brabec, Ch. Spielmann, P. F. Curley, and F. Krausz. Kerr lens mode locking. *Optics letters*, 17(18):1292–1294, 1992.

[168] S. C. Burd, J.-P. Penttinen, P.-Y. Hou, H. M. Knaack, S. Ranta, M. Mäki, E. Kantola, M. Guina, D. H. Slichter, D. Leibfried, and A. C. Wilson. VECSEL systems for quantum information processing with trapped beryllium ions. *JOSA B*, 40(4):773–781, 2023.